UNIVERSITY OF TRENTO

DOCTORAL SCHOOL IN PHYSICS

XXIV cycle

RF plasma synthesis and characterization of thin films for transparent conductors

Supervisor: Dr. Nadhira Bensaada Laidani

PhD candidate: Ioana Luciu

Trento, Italy
March 2012

Acknowledgements

First, I would like to thank my supervisor, Dr. Nadhira Bensaada Laidani, for helping me from the first moment of my arrival in Trento, for teaching me and sharing the professional experience in the moments I did not know what I should do, for motivating me in the moments I was disappointed. I sincerely appreciate the opportunity she gave me to work in her team.

I would like to thank all of my colleagues from Plasma, Advanced Materials and Surface Engineering Laboratory from Fondazione Bruno Kessler for their encouragements in all this period.

During this thesis work, I had the opportunity to collaborate for the Positron Annihilation measurements with the group of Prof. Roberto Sennen Brusa and the persons working with him, at the Department of Physics from Trento University. I wish to thank them for their moral support and encouragements.

Many thanks also for some people back home, in Bucharest, who contributed to my scientific background. In the group of Prof. Dr. Gheorghe Dinescu (Low Temperature Plasma Laboratory, National Institute for Laser, Plasma and Radiation Physics) I have started to learn how to make research. Thank you to all my colleagues from this lab.

Last but not least, I would like to thank my family and all my friends who made even my little free time highly enjoyable during these intense three years in Trento, for their moral support and encouragements.

Table of contents

Acknowledgements

Abstract 6

Chapter 1. Introduction and Motivation 8

Chapter 2. Background 12

2.1 Introduction 13
2.2 Fundamentals of transparent conductive oxides (TCOs) 13
2.2.1 Growth techniques used for preparing TCOs 13
2.2.2 Choice of TCOs 15
2.2.3 A brief introduction to semiconductor physics 16
2.2.4 Electrical properties of TCOs 19
2.2.4.1 Electronic conductivity and band structure 19
2.2.4.2 Scattering mechanisms 19
2.2.5 Optical properties of TCOs 22
2.2.6 Intrinsic and extrinsic doping of TCOs 23
2.2.7 Work function, chemical affinity and ionization potential 24
2.2.8 Figure of merit for TCOs 25
2.2.9 Alternative TCOs and current status 26
2.3 Fundamentals of TiO_2 27
2.3.1 Crystal structures of TiO_2 27
2.3.2 Electronic states of TiO_2 30
2.3.3 Electrical and optical properties of TiO_2 32
2.3.4 Water adsorption on TiO_2 surfaces 33
2.3.5 Oxygen vacancies and other impurities in TiO_2 34
2.4 Fundamentals of ZnO 38
2.4.1 Crystal structure of ZnO 39
2.4.2 Electronic states of ZnO 42
2.4.3 Electrical and optical properties of ZnO 42
2.4.4 Hydrogen and water adsorption on ZnO polar surfaces 43
2.4.5 Native point defects and hydrogen in ZnO 44
2.5 Concluding remarks 46
2.6 References 47

Chapter 3. Synthesis, methods and materials characterization 52

3.1 Thin films preparation 53
3.1.1 RF reactive sputtering technique – basic principle 53
3.1.2 Experimental set-up 53
3.2 Thin films characterization 55
3.2.1 Structure and morphology determination 55
3.2.2 Chemical composition 56
3.2.3 Electrical properties 58
3.2.4 Optical properties 59
3.2.5 Work function determination 59
3.2.6 Positron Annihilation Spectroscopy 61
3.3 Plasma characterization - Optical Emission Spectroscopy (OES) 63
3.4 References 64

Chapter 4. Deposition of TiO_2 films in different plasmas for intrinsic doping 65

4.1 Introduction 66
4.2 Deposition in pure-Ar plasma
4.2.1 Effects of cathode self-bias voltage 66
4.2.1.1 Influence of cathode self-bias voltage variation on the films growth rate 66
4.2.1.2 Influence of cathode self-bias voltage variation on the films chemical composition 67
4.2.2 Effects of substrate temperature 70
4.2.2.1 Influence of substrate temperature on the films chemical composition 70
4.2.2.2 Influence of substrate temperature on the films structural properties 71
4.3 Deposition in Ar-O_2 plasma 72
4.3.1 Influence of O_2 concentration in the gas on the films growth rate 72
4.3.2 Influence of O_2 concentration in the gas on the films chemical composition 72
4.3.3 Influence of O_2 concentration in the gas on the films structure and morphology 77
4.3.4 Influence of O_2 concentration in the gas on the films chemical composition for post-growth annealed in vacuum films 79
4.3.5. Influence of O_2 concentration in the gas on the films structure and morphology for post-growth annealed in vacuum films 80
4.4 Deposition in Ar-H_2 plasma 82
4.4.1 Influence of H_2 concentration in the gas on the films growth rate 82
4.4.2 Influence of H_2 concentration in the gas on the films chemical composition 82
4.4.3 Influence of H_2 concentration in the gas on the films structure and morphology 87
4.4.4 Influence of H_2 concentration in the gas on the films chemical composition for post-growth annealed in vacuum films 88
4.4.5 Influence of H_2 concentration in the gas on the films structure and morphology for post-growth annealed in vacuum films 89
4.5 Concluding remarks 91
4.6 References 92

Chapter 5. Extrinsic doping of TiO_2 films 93

5.1 Introduction 94
5.2 Sputtering from TiO_2-Nb mosaic target 94
5.2.1 Effects of cathode self-bias voltage 94
5.2.1.1 Influence of cathode self-bias voltage variation on the film growth rate 94
5.2.1.2 Influence of cathode self-bias voltage variation on the film chemical composition 95
5.2.2 Structure and morphology of as-grown films at room temperature 97
5.2.3 Influence of post-growth annealing in vacuum on the film chemical composition 97
5.2.4 Influence of post-growth annealing in vacuum on the film structure and morphology 98
5.2.5 Effects of substrate temperature during the films deposition 99
5.2.5.1 Influence of substrate temperature on the film chemical composition 99
5.2.5.2 Influence of substrate temperature on the film structure 100
5.3 Co-sputtering from separate TiO_2 and Nb targets 100
5.3.1 Film growth rate 100
5.3.2 Film chemical composition 101
5.3.3 Film structural properties 102
5.3.4 Influence of post-growth annealing in vacuum on the film chemical composition 102
5.3.5 Influence of post-growth annealing in vacuum on the film structure 104
5.3.6 Effects of substrate temperature during the films deposition 105
5.3.6.1 Influence of substrate temperature on the film chemical composition 105
5.3.6.2 Influence of substrate temperature on the film structure 106
5.4 Concluding remarks 108
5.5 References 109

Chapter 6. TiO_2 film deposition and characterization for intrinsic-extrinsic co-doping 110

6.1 Introduction 111
6.2 Film deposition in Ar-O_2 plasma 111
6.2.1 Sputtering of Nb-TiO_2 films from a mosaic target 111
6.2.1.1 Film growth rate 111
6.2.1.2 Film chemical composition 112
6.2.1.3 Film structure and morphology 115
6.2.1.4 Influence of post-growth annealing on the film chemical composition 115
6.2.1.5 Influence of post-growth annealing on the film structure and morphology 116
6.2.2 Deposition of Nb-TiO_2 films by co-sputtering from two separate targets 117
6.2.2.1 Film growth rate 117
6.2.2.2 Film chemical composition 118
6.2.2.3 Film structure 119
6.2.2.4 Influence of post-growth annealing on the film chemical composition 119
6.2.2.5 Influence of post-growth annealing on the film structure 119
6.3 Film deposition in Ar-H_2 plasma 120
6.3.1 Sputtering of Nb-TiO_2 films from a mosaic target 120
6.3.1.1 Film growth rate 121
6.3.1.2 Film chemical composition 121
6.3.1.3 Film structure and morphology 123
6.3.1.4 Influence of post-growth annealing on the film chemical composition 124
6.3.1.5 Influence of post-growth annealing on the film structure and morphology 125
6.3.1.6 Influence of substrate temperature on the film chemical and structural properties 126
6.3.2 Deposition of Nb-TiO_2 films by co-sputtering from two separate targets 127
6.3.2.1 Film growth rate 127
6.3.2.2 Film chemical composition and structure 127
6.3.2.3 Influence of post-growth annealing on the film chemical composition 128
6.3.2.4 Influence of post-growth annealing on the film structural properties 129

6.4 Concluding remarks 130
6.5 References 131

Chapter 7. Electrical, optical, and electronic properties of doped-TiO_2 films 132

7.1 Introduction 133
7.2 Intrinsically doped-TiO_2 films 133
7.2.1 Electrical properties of as-grown films 133
7.2.2 Influence of post-growth annealing on film electrical properties 133
7.2.3 Influence of substrate temperature on film electrical properties 136
7.2.4 Optical properties of as-grown films 136
7.2.5 Influence of post-growth annealing on film optical properties 137
7.2.6 Influence of substrate temperature on film optical properties 138
7.2.7 Figure of merit of intrinsically-doped TiO_2 films 139
7.2.8 Electronic properties of as-grown films 140
7.2.9 Influence of post-growth annealing on film electronic properties 143
7.3 Extrinsically doped-TiO_2 films 143
7.3.1 Electrical properties of as-grown films 143
7.3.2 Influence of post-growth annealing on film electrical properties 144
7.3.3 Influence of substrate temperature on film electrical properties 145
7.3.4 Optical properties of as-grown films 145
7.3.5 Influence of post-growth annealing on film optical properties 147
7.3.6 Influence of substrate temperature on film optical properties 147
7.3.7 Figure of merit of extrinsically-doped TiO_2 films 148
7.3.8 Electronic properties of as-grown films 149
7.3.9 Influence of post-growth annealing on film electronic properties 150
7.4 Intrinsically-extrinsically co-doped TiO_2 films 151
7.4.1 Electrical properties of as-grown films 151
7.4.2 Influence of post-growth annealing on film electrical properties 151
7.4.3 Influence of substrate temperature on film electrical properties 154
7.4.4 Optical properties of as-grown films 155
7.4.5 Influence of post-growth annealing on film optical properties 156
7.4.6 Influence of substrate temperature on film optical properties 157
7.4.7 Figure of merit of intrinsically-extrinsically co-doped TiO_2 films 157
7.4.8 Electronic properties of as-grown films 158
7.4.9 Influence of post-growth annealing on film electronic properties 160
7.5 Concluding remarks 161
7.6 References 163

Chapter 8. Investigation of structural vacancies in doped-TiO_2 by positron annihilation spectroscopy 164

8.1 Introduction 165
8.2 Intrinsically-doped TiO_2 165
8.2.1 Structural vacancies in as-grown films 165
8.2.2 Structural vacancies in post-growth annealed films 169
8.3 Extrinsically doped-TiO_2 171
8.3.1 Structural vacancies in as-grown films 171
8.3.2 Structural vacancies in post-growth annealed films 173
8.4 Intrinsically-extrinsically co-doped TiO_2 174
8.4.1 Structural vacancies in as-grown films 174
8.4.2 Structural vacancies in post-growth annealed films 176
8.5 S-W plot 179
8.6 Concluding remarks 180
8.7 References 181

Chapter 9. Doping of ZnO films deposited in Ar-H_2 plasma by intrinsic defects 182

9.1 Introduction 183
9.2 Film growth rate in Ar-H_2 plasma 183
9.3 H_2 effect on the film chemical composition 184
9.4 H_2 effect on the film structural properties 185
9.5 H_2 effect on the plasma composition 187
9.6 H_2 effect on the film electrical properties 189
9.7 H_2 effect on the film optical properties 191
9.8 Concluding remarks 192
9.9 References 192

Chapter 10. Concluding remarks and perspectives 193

Abstract

Oxide-based transparent conductors constitute a novel class of materials, which finds applications in many technological fields such as photovoltaics and organic light emitting devices. They can be employed in the new generation solar cells as transparent charge collectors. The transparent and conductive oxide mostly used nowadays is indium tin oxide (ITO), however due to the high cost and scarcity of indium, other materials are under research and development as potential substitutes. Many candidates are currently under study, mainly doped-ZnO, doped-CdO, doped-SnO_2, doped-TiO_2.

The work undertaken in this thesis is a study of the doping processes of thin films of TiO_2 and ZnO, two cheap, chemically stable and non-toxic materials. Two main objectives were pursued in this work: (i) the optimization of the film deposition and doping conditions for a potential replacement of ITO and (ii) the understanding of the factors dominating the doping process as well as its limitations. The approach was to explore three doping methods of the films: intrinsic doping, extrinsic doping and, with the aim to combine the benefits of both, intrinsic-extrinsic co-doping. Since the structural defects (such as oxygen vacancies) are at the basis of the intrinsic doping, a control of their formation was searched through the variation of the growth process conditions of the ZnO and TiO_2 films. Niobium was selected for the extrinsic doping of the TiO_2 films.

The films were grown by RF plasma sputtering in different atmospheres (Argon, Ar-O_2 and Ar-H_2 gas mixtures) and under different plasma power conditions and substrate temperature, onto silicon and quartz substrate. The Nb-containing films were obtained by co-sputtering of either a single composite TiO_2 -Nb target or two distinct niobium and TiO_2 targets.

Many characterization techniques were applied to define the film structural, electronic, electrical and optical properties obtained upon doping. For chemical analysis, X-ray Photoelectron Spectroscopy (XPS) was used. The structure and morphology of the films were analyzed by X-ray Diffraction (XRD) and Scanning Electron Microscopy (SEM). The chemical species present in various plasmas used in deposition process were investigated by Optical Emission Spectroscopy (OES). Further, the defect structure and properties of the obtained films were studied by Positron Annihilation Spectroscopy. Analysis by this technique shed more light on the nature of the vacancies/open volume and on the effect of the latter on the electrical and structural properties of the films. A study based on a joint use of XPS and optical measurements allowed to define the electronic properties of the films (valence band edge, Fermi level position, work function, ionization potential and electron affinity).

Structural analysis results revealed the formation of both anatase and rutile nanocrystalline phases for intrinsic and extrinsic doping of TiO_2, while with the co-doping method only anatase phase was obtained, a phase known to be favorable for Nb incorporation in TiO_2 lattice.

The intrinsic doping of TiO_2 films showed high transparency in the visible range, but resulted in still high resistivity values (10^1-10^3 Ωxcm). The latter could be lowered by using Ar-H_2 gas mixtures during film deposition. The same trend was observed in the case of intrinsically-doped ZnO films, an increase in the electrical conductivity was observed when the concentration of defects was increased.

The lowest resistivity was achieved with niobium doping of TiO_2, $5x10^{-3}$ Ωxcm, with an optical absorption coefficient in the visible range of ~$1x10^4$ cm^{-1}, however the combination of the internal defects and Nb, in co-doping, did not improve the conductivity. Nonetheless, it was found that co-doping method strongly modified the electronic properties of the TiO_2 films, allowing a control of the work function, an important parameter for transparent electrodes.

Low cost transparent conductive oxides were obtained when niobium was successfully incorporated in TiO_2 lattice. By optimization of the deposition process of the films (dopant concentration, RF power, atmosphere, and annealing temperature) the electronic, electrical and optical properties of doped- TiO_2 films can be improved. The obtained results can contribute to the development of transparent electrodes and charge collectors by RF sputtering, a suitable technique for coating on large area substrates.

1. Introduction and motivation

Transparent electronics is becoming an important field in material science. The developments in the field of transparent electronics calls for the need of understanding the basic properties of transparent conducting oxides. This chapter gives an introduction on the recent developments in transparent electronics, the content of the research carried out in this thesis, and the aims of the study.

The first reported transparent conductive oxide (TCO) was cadmium oxide (CdO) in 1907 [1], obtained by thermal oxidation of sputtered cadmium. However, the technological advances in TCOs emerged only after 1940, as the potential applications in industry and research became evident. In 1956 Thelen *et al.* [2] has found transparency and conduction in indium oxide (InO), which was later used in applications for heated windows. Years of extensive research finally led to SnO_2 doped In_2O_3 (known as indium tin oxide or ITO) with excellent electrical and optical properties [3]. The commercial value of TCO films has been recognized, and the list of potential TCO materials has expanded to include ZnO, SnO_2, In_2O_3 CdO etc. One of the advantage of using binary compound as TCO material is that their chemical composition in film deposition is relatively easier to control than that of ternary and multicomoponent oxides.

In addition to these binary compounds, ternary compounds such as Cd_2SnO_4, $CdSnO_3$ $CdIn_2O_4$, Zn_2SnO_4 [4], $MgIn_2O_4$ [5], $ZnSnO_3$ [6] and $GaInO_3$ [7] were also developed prior to 1980 [8,9]. New TCO materials consisting of multicomponent oxides have been developed in 1990s. In 1999, Minami et al [10] reported $Zn_2In_2O_5$-$MgIn_2O_4$ multicomponent oxide as a new TCO material. The advantage of the multicomponent oxide materials is the fact that their electrical, optical, chemical and physical properties can be controlled by altering their chemical compositions.

Nowadays there is a renewed interest in research on TCOs, mainly due to the exponential rise in the applications using the TCO materials [11]. With the advent of flexible displays, high definition TVs (HDTVs), flat panel displays (FPDs) and the several hand-held and smart devices, the demand for TCOs has also increased several folds [12]. Another important application for the TCOs is energy efficient windows, which is gaining significance in the global regions with cold or moderate climates [12,13]. However, the most important application in the present context is that of transparent electrodes for light emitting diodes (LEDs) and for photovoltaic (PV) cells [11,14-16]. With an ever deepening of energy crisis, the demand for alternate and cost-effective energy sources is increasing. There is also a need to improve the efficiency of solid state lighting devices. Although rapid progress is being made in increasing efficiency of the above-mentioned solid state devices through breakthrough results in synthesis of photoactive materials and novel device structures, the research in the field of TCOs has been relatively slow placed [12]. Soon the TCO properties will be the limiting factor in the development of PVs and the solid state lighting devices. Thus there is a considerable interest in developing TCOs with improved properties. Apart from these some of the other applications of TCOs include: window heating, electrochromic windows, electromagnetic shielding, and invisible security circuits [13].

Currently, indium tin oxide (ITO) is the most widely used material for TCO applications. With the steady rise in demand for the applications mentioned earlier, it seems to be difficult to meet the supply requirements because of the rapidly diminishing supply of In. In the recent times the production of indium has dropped and increasing the production is itself a topic of intense research [17]. The primary reason for the limited availability of In is that it is produced as a by-product of Zn, Sn and Pb production. The concentration of In in earth's crust is extremely low (0.1 ppb), which prohibits direct mining of this element [18]. Thus, increasing the output of In would require drastic improvement in the extraction processes and

equipment. This directly translates into addition of cost to the present high prices of In. In 2005 – 06, 70% of the In produced globally was used in the form of ITO coating for various TCO applications. A large fraction of the remaining In is mostly used as an electronic grade material for semiconductor and electrical components. The demand for In based compound semiconductors has been steady over the past few years, it is predicted to pick up in the future. The automotive sector is another huge market for the TCO coatings and can be directly associated with the demand for the commercial vehicles. Thus, it can be seen that substituting ITO with a more economical TCO material would save a large amount of material related costs of the TCO based products. Moreover, this would also assure a stable supply of In for the semiconductor and optoelectronic applications.

In addition to the high cost of In, ITO also suffers from poor chemical stability in hydrogen atmospheres and exhibits relatively poor diffusion barrier characteristics [13]. Stability in hydrogen is a particularly important property for the Si based photovoltaic applications, where H passivation is a key processing step in the solar cell fabrication. These factors and the limited availability of In have motivated researchers all over the world to explore new and relatively inexpensive TCO materials. It is also thought that the new materials can offer more technical advantages, especially in terms of processibility and post-deposition stability [19]. With the improvement in properties of TCOs, the solar cell industry is expected to be benefited the most among all the applications. The performance of solar cells is directly related to the TCO characteristics.

In this thesis, the focus is on preparation and characterization of low-cost TCO films with an eye toward applications in photovoltaics. Two different materials, ZnO and TiO_2, doped intrinsically and extrinsically, have been investigated as alternative TCOs to ITO. In the case of ZnO, the hydrogen effect on the structural, optical, electrical properties is studied, while in the case of TiO_2 more parameters were investigated: different gas mixtures and different doping. The main aim of this study is to gain a better understanding of the fundamentals and the factors affecting the properties of the alternative TCOs.

The thesis is composed of nine chapters, organized as follows. The introduction chapter (Chapter 1) is followed by a chapter describing the TCO fundamentals. This chapter (Chapter 2) will give an overview of the basic phenomena and the processes involved in the materials that exhibit TCO characteristics. In addition, it will also briefly discuss the TCO requirements specific to photovoltaic application. The third chapter describes the experimental details used for synthesis and characterization of all the films. Chapter 4 and 5 describe and discuss in detail the results obtained for intrinsically (via internal defects creation) and extrinsically doped-TiO_2, respectively. A mixed intrinsic-extrinsic doping of TiO_2 films, obtained by Nb incorporation and the creation of internal defects will be investigated in Chapter 6. The effects of the different deposition conditions on the electrical, optical, and electronic properties of doped-TiO_2 films will be described and commented in Chapter 7. Further investigation of the structural defects in un-doped and doped TiO_2 films will be given in Chapter 8, which gives the results obtained by Positron Annihilation Spectroscopy (PAS) analysis. The results of a study of ZnO film deposition in Ar-H_2 plasma for intrinsic

doping will be given in Chapter 9 and in a final chapter the overall conclusions are summarized along with the future directions.

References

1. K. Badeker, Ann. Phys. (Leipzig) 22, 749 (1907)
2. A. Thelen, H. König, Naturwissenschaften, 43, 297, (1956)
3. R. Groth, E Kauer, Philips Technical Review, 26, 105, (1965)
4. H. Enoki, T.Nakayama, J. Echigoya, Phys. Stat. Sol. (a) 29 (1992) 181
5. H. Un'no, N. Hikuma, T. Omata, N. Ueda, T. Hashimoto, H.Kawazoe, Jpn. J. of Appl. Phys. 32 (1993) L1260-L1262
6. T. Minami, H. Sonohara, S. Takata, H. Sato, Jpn. J. Appl. Phys., Part 2, Lett. 33 (1994) L1963
7. R.J. Cava, J.M. Phillips, J.Kwo, G.A. Thomas, R.B. van Dover, S.A. Carter, J.J. Karjewski, W.F. Peck, J.M. Marshall, D.H. Rapkine, Appl. Phys. Lett 64, (1994) 2071
8. T.J. Coutts, X. Wu, W.P. Mulligan, J.M. Webb, J. Electron. Mater. 25 (1996) 935
9. T. Minami, MRS Bulletin (2000) 38
10. T. Minami, S. Takata, T. Kakumu, H. Sonohara, Thin Solid Films 270 (1995) 22
11. T. Minami, Semicond. Sci. 20, S35 (2005)
12. D.S. Ginley and C. Bright, MRS Bull. 25, 15 (2000)
13. R.G. Gordon, MRS Bull. 25, 52 (2000)
14. J. Muller, B. Rech, J. Springer, and M. Vanecek, Sol. Energy 77, 917 (2004)
15. E. Fortunato, D. Ginley, H. Hosono, and D.C. Paine, MRS Bull. 32, 242 (2007)
16. J. Lewis, S. Grego, B. Chalamala, E. Vick, and D. Temple, Appl. Phys. Lett. 85, 3450 (2004)
17. T. Jansseune, Compd. Semicond. 11, 34 (2005)
18. T. Jansseune, Compd. Semicond. 5, 33 (2003)
19. B.G. Lewis and D.C. Paine, MRS Bull. 25, 22 (2000)

2. Background

Optical transparency and electrical conductivity can coexist in a specific class of oxide materials. These so-called transparent conducting oxides are semiconductors that transmit visible light because of a wide band gap. By introducing doping, it is possible to control the conductivity. At very high doping concentration the semiconductor becomes degenerate, and the conductivity is limited by scattering of the charge carriers. Furthermore, the optical properties are affected by the doping concentration.

Doped-titanium dioxide (TiO_2) and doped-zinc oxide (ZnO) are two promising materials for replacing indium tin oxide (ITO) as transparent conductive oxides. Cheap, chemically stable, and non-toxic materials are important criterias to be considered in choosing a TCO for different applications.

Contents

2.1 Introduction
2.2 Fundamentals of transparent conductive oxides (TCOs)
- 2.2.1 Growth techniques used for preparing TCOs
- 2.2.2 Choice of TCOs
- 2.2.3 A brief introduction to semiconductor physics
- 2.2.4 Electrical properties of TCOs
  - 2.2.4.1 Electronic conductivity and band structure
  - 2.2.4.2 Scattering mechanisms
- 2.2.5 Optical properties of TCOs
- 2.2.6 Intrinsic and extrinsic doping of TCOs
- 2.2.7 Work function, chemical affinity and ionization potential
- 2.2.8 Figure of merit for TCOs
- 2.2.9 Alternative TCOs and current status

2.3 Fundamentals of TiO_2
- 2.3.1 Crystal structures of TiO_2
- 2.3.2 Electronic states of TiO_2
- 2.3.3 Electrical and optical properties of TiO_2
- 2.3.4 Water adsorption on TiO_2 surfaces
- 2.3.5 Oxygen vacancies and other impurities in TiO_2

2.4 Fundamentals of ZnO
- 2.4.1 Crystal structure of ZnO
- 2.4.2 Electronic states of ZnO
- 2.4.3 Electrical and optical properties of ZnO
- 2.4.4 Hydrogen and water adsorption on ZnO polar surfaces
- 2.4.5 Native point defects and hydrogen in ZnO

2.5 Concluding remarks
2.6 References

2.1 Introduction

Transparent conducting oxide (TCO) layers are characteristically described as thin films that exhibit simultaneously high visible wavelength transparency and electrical conductivity. The majority of known TCO materials are *n*-type semiconductors where defects such as oxygen vacancies, impurity substitutions and interstitials donate electrons to the conduction band providing charge carriers for the flow of electric current [1].

TCO films useful for most applications must have a wide band gap (>3 *eV*) which requires a degenerate carrier density $\geq 10^{20}$ cm^{-3} and ideally a resistivity $<10^{-3}$ Ωcm. They are highly transparent in the visible region and highly reflective in the near infrared, where the so-called *free carrier absorption* takes place. In general, TCOs are polycrystalline, although, recently, studies on amorphous TCOs have also been performed [2]. The degree of crystallinity (grain size) influences the electron transport, i.e., better crystallinity (larger grains) leads to higher film conductivity. Each of the application already mentioned in *Chapter 1* have different requirements upon the optoelectronic and structural properties of TCO film. For example, for some applications amorphous films are desired because they are normally easier to etch and smoother than the polycrystalline films [2]. Therefore, a profound understanding of the fundamental aspects of transparent semiconductors is required in order to improve either the properties of existing materials, or design new type of TCOs.

Not many materials exhibit this unusual combination of high transmittance and electrical conductivity. Usually, materials that show high electrical conductivity are almost opaque to the visible light owing to their absorption coefficient and/or reflectivity, whereas transparent materials are insulating or semiconducting due to the lack of free carriers at ambient temperatures. A figure of merit is often adopted to qualify a TCO, defined as the ratio of the optical absorption coefficient to the electrical conductivity of the film.

Factors that may influence the choice of TCO for any particular application are: electrical conductivity, physical, chemical and thermal durability, etchability, plasma wavelength, work function, thickness, uniformity, deposition temperature, toxicity, and cost.

In this chapter an overview of the most important fundamental aspects on transparent conductive oxides will be discussed. The structural, electrical, electronic and optical properties of titanium dioxide (TiO_2) and zinc oxide (ZnO), two possible candidates for replacing ITO, are discussed.

2.2 Fundamentals of TCOs

2.2.1 Growth techniques used for preparing TCOs

The properties of a TCO layer depend not only on its chemical composition, but also on the method used for its preparation. A vast amount of literature is available on different TCOs deposited by various growth techniques and their fundamental aspects. Reviews on TCOs concerning these issues have been reported

earlier [1,3-5]. These preparative methods include physical methods (sputtering, evaporation, pulsed laser deposition) and chemical methods (chemical vapor deposition, sol-gel, and spray-pyrolisis).

Sputtering is one of the most extensively used techniques for the deposition of TCOs films. Both reactive and non-reactive forms of DC and RF sputtering, magnetron and ion beam sputtering are used. Ar-O_2, O_2 or H_2 are generally used as the sputtering gas. In order to obtain the optimum transparent conducting properties, the reactively sputtered oxide films normally require a post-deposition heat treatment in either oxidizing or reducing ambients, depending on the initial sputtering conditions. Sputtering from oxide targets renders a better control over the stoichiometry. Films deposited onto unheated substrates tend to be amorphous and increasing the substrate temperature improves the crystallinity and grain size and decreases the density of structural defects, leading to higher mobilities. The application of a negative bias to the substrate can increase the purity of the film, resulting in improved electrical and optical characteristics. Ion beam sputtering involves minimal intrinsic heating and electron bombardment and hence constitutes a low temperature deposition method which can be useful for several applications of TCOs.

Evaporation can be an alternative to sputtering. The important control parameters in evaporation using metallic or oxide sources are the evaporation rate, substrate temperature, source-to-substrate distance and oxygen partial pressure. To obtain highly transparent and conducting films by evaporation, higher partial pressures of oxygen in combination with correspondingly adequate substrate temperatures and fast evaporation rates are necessary.

A technique that is widely used for the production of ZnO films is *pulsed laser deposition (PLD)*. In this technique, pulsed nanosecond or picosecond lasers generally emitting in the near-UV, such as excimer or frequency-tripled Nd:YAG lasers, are focused tightly on a pressed or sintered ZnO target, thus producing a plume of evaporating source material, which is deposited on a heated substrate. The plume is emitted normal to the target surface, independent of the angle of incidence of the laser beam. The angle of aperture of the plume gets narrower with increasing laser pulse energy. The high kinetic energy of the evaporating species results in a high surface mobility on the substrate. A low background pressure of O_2 in the recipient or a post-growth annealing in an O_2 atmosphere helps to improve the stoichiometry of the ZnO layers.

Chemical vapour deposition (CVD) consists of a surface reaction, on a solid surface, involving one or more gaseous reacting species. Metallic oxides are usually deposited by the vaporization of a suitable metal-bearing compound and its *in situ* oxidation with O_2, H_2O or H_2O_2. O_2, N_2 or argon are generally used as carrier gases. In general the quality of TCOs prepared by CVD has been slightly inferior to that of sputtered or reactively sputtered conductors. Better results are expected with the plasma-assisted CVD process.

A variety of the CVD technique is called *spray pyrolysis*. This technique involves spraying of a solution, usually aqueous, containing soluble salts of the constituent atoms of the desired compounds onto heated substrates. Whether or not the process can be classified as CVD depends on whether the liquid droplets vaporize before reaching the substrate or react on it after splashing. Various geometries of the spray set-ups are employed, including an inverted arrangement in which larger droplets and gas phase precipitates are discouraged from reaching the substrate, resulting in better quality films. H_2O is the most common

convenient oxidizing agent, but is usually helpful to dilute the solution by adding ethanol, or, in some cases, methanol, propanol or butyl acetate. N_2, O_2, argon or air are generally used as carrier gases.

Other technologies can be applied without recourse to vacuum. For example, *sol–gel* deposition involves immersion of a substrate in a chemical solution, withdrawal at a controlled rate, and subsequent heat treatment. Alternatively, the chemical solution can be applied by *spray coating*.

In this work intrinsically doped-TiO_2 and ZnO and extrinsically doped-TiO_2 were prepared. Niobium was selected for the extrinsic doping of the TiO_2 films. The films were grown by RF plasma sputtering in different atmospheres (Argon, Ar-O_2 and Ar-H_2 gas mixtures) and under different plasma power conditions and substrate temperature, onto silicon and quartz substrate. The Nb-containing films were obtained by co-sputtering of either a single composite TiO_2-Nb target or two distinct niobium and TiO_2 targets.

2.2.2 Choice of TCOs

It is apparent from the diversity of applications for TCOs presented in first chapter that no one material is most suitable for all uses. Depending on which material property is of most importance, different choices are made. A summary of the advantages and disadvantages of different TCOs with respect to different applications is presented by Gordon [6].

For example, in low-emissivity windows in buildings materials with high transmittance are preferred in cold climates while in hot climates, materials reflecting the near-infrared part of incident sunlight are requested. Low cost materials and with good thermal stability are necessary in solar cells. The many different styles of flat panel displays use TCOs as a front electrode. Etchability is a very important consideration in forming patterns in the TCOs electrode. The materials used in this application must be deposited at low temperature and have a low electrical resistance. Chemical inertness, high transparency and low cost materials are required for electrochromic mirrors widely used in automobiles market and ”smart” windows. For defrosting windows used in freezers, defrosting windows in airplanes or automobiles windshields low cost and durable materials with low resistance are required. Tin oxide coatings are placed on oven windows, where the main criteria for the material are high temperature stability, chemical and mechanical durability, and low cost. TCOs with high resistances and high mechanical and chemical durability are placed on glass to dissipate static charges that can develop on xerographic copiers, television tubes, and computer displays. Another application where the durability and low cost of the TCO are important criterias is touch-panel controls. TCOs-coated glass can be used as part of invisible security circuits for windows or on glass. The materials used for this purpose should have a good UV protection.

There is no one transparent conductor that is best for all applications. All of the commonly used transparent conducting materials nowadays and their production methods have advantages and disadvantages for each application.

2.2.3 A brief introduction to semiconductor physics

Semiconductors are a class of materials which have electrical conductivity in between that of a metal (> 10^4 $\Omega^{-1}cm^{-1}$) and that of an insulator (< 10^{-10} $\Omega^{-1}cm^{-1}$) [7]. However this definition of semiconductor is not completed. Another definition is made by considering the existence of a gap between occupied and empty states: an energy gap with its width larger than 4 eV exists in an insulator (Figure 2.1 *(a)*); an energy gap with its width less than 4 eV exists in a semiconductor (Figure 2.1 *(b)*); no such an energy gap exists in a metal (Figure 2.1 *(c)*).

In semiconductors at zero temperature, the conduction band is completely empty and the valence band is completely filled. As in an empty or full filled band, the electrons do not carry any current, there isn't any conductance in semiconductors at $T = 0\ K$, while with the increase of temperature, the electrons at the top of the valence band are thermally excited to the bottom of conduction band, leaving empty states in the valence band. The valence band with some empty states can be considered as a full filled valence band along with some positive charges ($+e$), called *holes*, occupying the top of the valence band. Therefore, conductance is induced by the motion of electrons in the conduction band and the holes in the valence band.

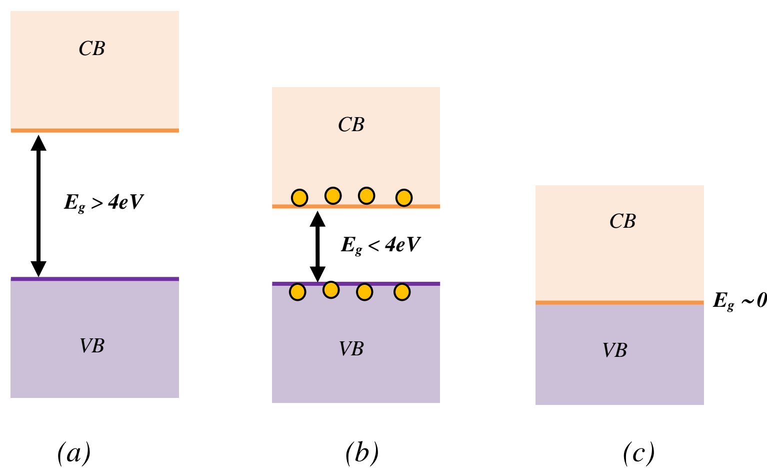

Figure 2.1. Schematic band structures for *(a)* insulator, *(b)* semiconductor, and *(c)* metal

Another effective way to introduce charge carriers (electrons or holes) is to dope with some impurities the host semiconductor. The number of outer shell electrons of the impurity atoms should be different from that of the constituent atoms. If the impurity atoms have more outer shell electrons, they will provide or "donate" extra electrons in the semiconductor, accordingly, they are called *n-type dopants* or *donors*. While if the impurity atoms have less outer shell electrons, they will require or "accept" electrons from the host atoms, or they provide extra holes in the semiconductor, thereby they are called *p-type dopants* or *acceptors*. From a band structure point of view, *n*-type dopants create donor impurity levels below the bottom of the conduction band, while *p*-type dopants create acceptor impurity levels above the top of the valence band as depicted in Figure 2.2. Due to thermal activation, electrons in the donor levels will be excited to the conduction band, or

the holes in the acceptor levels will be excited to the valence band, which can give rise to a large number of charge carriers.

Besides the number of charge carriers, the mobility of carriers determines the conductivity as well. In a simple Drude model, the conductivity is written as [7]:

$$\sigma = \sigma_n + \sigma_p = ne\mu_e + pe\mu_p \quad (2.1)$$

where $n = N_c \exp(-\frac{E_C - E_F}{kT})$ is the electron density in the conduction band, (2.2)

$p = N_V \exp(-\frac{E_F - E_V}{kT})$ is the hole density in the valence band, (2.3)

$E_F = \frac{E_C + E_V}{2} + \frac{kT}{2} \ln\left(\frac{N_V}{N_C}\right)$ is the Fermi energy, (2.4)

e is the electronic charge, k is Boltzmann's constant, T the absolute temperature, μ_e and μ_p are the electron and hole mobility respectively, N_C and N_V are the effective density of states of the conduction and valence band, E_C the energy of the bottom of conduction band, and E_V the energy of the top of valence band.

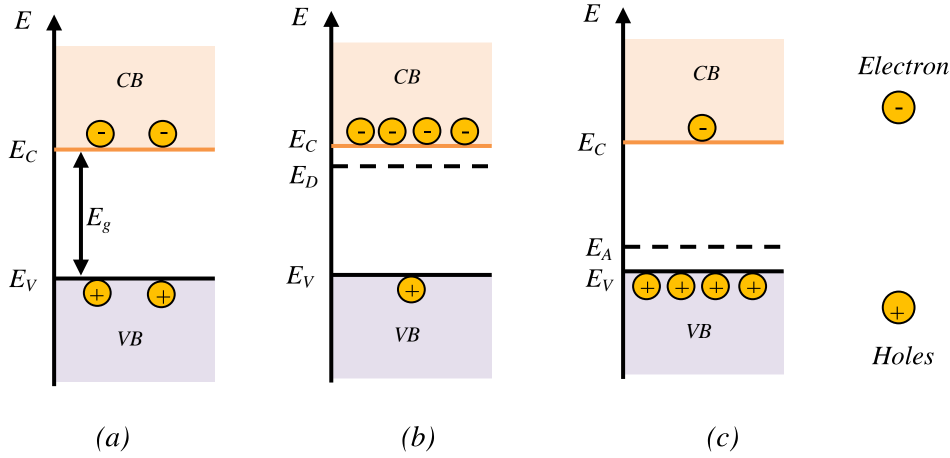

Figure 2.2 Schematic band diagram for *(a)* intrinsic, *(b) n*-type, and *(c) p*-type semiconductors at thermal equilibrium

The *Fermi energy* or *Fermi level* defines the reference energy for the probability of occupation of electron states. Thus, in metals is located within a partially filled allowed band, whereas in semiconductors and insulators is positioned within the forbidden band. In doped semiconductors, *p*-type and *n*-type, the Fermi level is shifted by the impurities. The closer the Fermi Level is to the conduction band, the more mobile electrons are present in that band. Similarly, the closer the Fermi Level is to the valence band, the more mobile holes are present in this band.

As we discussed above, to introduce a large number of carriers into a wide-band gap semiconductor, an extrinsic doping with shallow donors or acceptors is required. Since 1950s, it has been noticed that when the concentration of shallow impurities in a semiconductor increases to a critical value, an abrupt *semiconductor-to-metal transition* occurs. This transition was named *Mott transition* later because of the significant contribution of N. F. Mott in explaining the underlying physics of this phenomenon [8].

Mott pointed out three main features of this transition (n-type semiconductors for example) [8]:

1) When the donor concentration n_d is below a first critical value n_c, the electrons are loosely bound to the donors, and they form a single donor level in the band gap, as shown in Figure 2.3 *(a)*.

2) When n_d is above n_c, the orbit of bounded electron starts to overlap with each other and hence they are delocalized, giving rise to a metallic behavior. From the band structure point of view, the single impurity level spreads into an impurity band (Figure 2.3 *(b)*).

3) When n_d is above a second characteristic concentration n_{cb}, the impurity band overlaps with the conduction band of the host crystal and the Fermi level of the electron system moves up to conduction band as well (Figure 2.3 *(c)*)

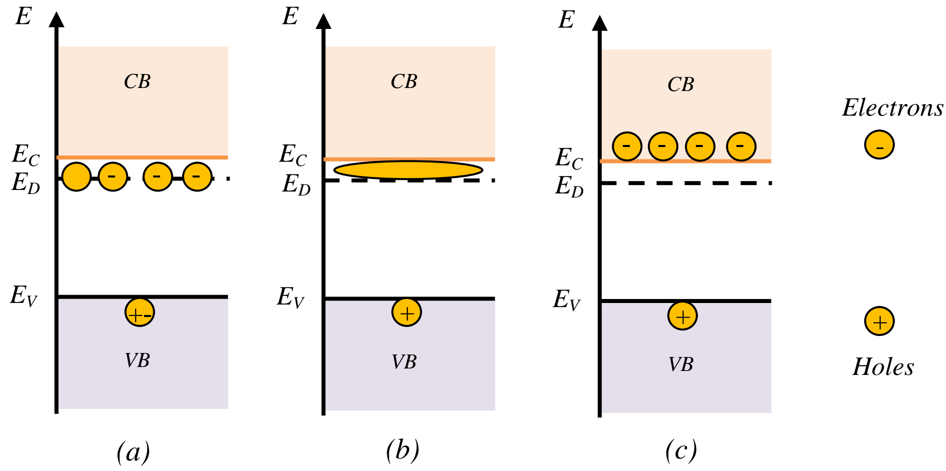

Figure 2.3. Schematic band structure for an extrinsic n-type doped semiconductor when *(a)* $n_d < n_c$; *(b)* $n_c < n_d < n_{cb}$; *(c)* $n_d > n_{c2}$

This Mott-transition picture is a useful guidance for the development of transparent conducting oxides. According to this picture, to achieve good conductivity in a transparent wide-band gap semiconductor, one should have shallow donors or acceptors and considerable high concentration of these shallow impurities.

Joyce and Dixon [9] have obtained a useful approximate expression applicable to degenerate semiconductor, given by:

$$\frac{E_F - E_C}{kT} \cong ln\frac{n}{N_c} + \frac{1}{\sqrt{8}}\frac{n}{N_c} - \left(\frac{3}{16} - \frac{\sqrt{3}}{9}\right)\left(\frac{n}{N_c}\right)^2 + \cdots \tag{2.5}$$

for electrons and by:

$$\frac{E_V - E_F}{kT} \cong ln\frac{p}{N_V} + \frac{1}{\sqrt{8}}\frac{p}{N_V} - \left(\frac{3}{16} - \frac{\sqrt{3}}{9}\right)\left(\frac{p}{N_V}\right)^2 + \cdots \tag{2.6}$$

for holes.

2.2.4 Electrical properties of TCOs

2.2.4.1 Electronic conductivity and band structure

The conductivity σ is a product of the number of charge carriers *n* in a material, and the mobility μ of these charge carriers, times the elementary electron charge *e*. The resistivity ρ (for an n-type semiconductor, for example) is defined as the inverse of the conductivity.

$$\sigma = n\mu e = \frac{1}{\rho} \tag{2.7}$$

For thin films of uniform thickness *d*, the electrical resistance is sometimes expressed as the sheet resistance ($R_s=\rho/d$). Other than the thickness, the sheet resistance is independent of the film dimensions.

In order to promote conductivity, the number of charge carriers can be increased by doping. Dependant on the material this can be done by substitutional doping, creation of vacancies or implantation of interstitials. Dependant on the valence of dopants or vacant sites, acceptor or donor states will induce *p*- or *n*-type conductivity.

Another possibility to enhance the conductivity is to increase the mobility. However, the mobility is dependent on intrinsic scattering mechanisms, and can therefore not be controlled directly. In general these mechanisms limit the mobility as the carrier density increases. As a result, the mobility is the most important parameter influencing the total conductivity.

The presence of a band gap, providing low absorption in the visible range, is an essential feature of TCOs. Metal-oxide semiconductors having a band gap of at least 3 *eV* meet this condition.

In intrinsic stoichiometric oxides, coexistence of electrical conductivity besides visible transparency is not possible. However, substitutional doping by cationic donors or anion vacancies can create charge carriers, i.e. electrons. The donor (or acceptor) states alter the electronic band structure of the material.

2.2.4.2 Scattering mechanisms

Mobilities in thin-film TCOs may be limited by a variety of scattering mechanisms including: ionized impurities, neutral impurities, thermal lattice vibration scattering and grain-boundary scattering, whereas single-crystalline samples are ideally limited only by intrinsic lattice phonon scattering [10]. Owing to the concentration and the scattering cross section of the neutral impurities being much smaller than that of ionized impurities both in undoped and doped oxide films, the neutral impurity scattering can be neglected. The reciprocal mobility of the films can be expressed as [11]:

$$\frac{1}{\mu} = \frac{1}{\mu_i} + \frac{1}{\mu_l} + \frac{1}{\mu_g} \tag{2.8}$$

where μ_i, μ_l and μ_g are mobilities corresponding to ionized impurity, lattice vibration and grain boundary scattering, respectively.

Ionized impurity scattering

The TCO films contain a large amount of point defects. These defects are assumed to be oxygen vacancies or/and excess metallic atoms (in undoped films) or external dopants (in doped films). These point defects are usually ionized and become ionized impurities. The concentration of the ionized impurities is larger than 10^{20} cm^{-3} for practically applied films. These ionized impurities are strong scattering centers for charge carriers.

In a degenerate electron system, only the electrons near Fermi level take part in conduction. According to Conwell-Weisskoft formula when degenerate charge carriers are scattered by impurity ions, the energy dependence of mobility is:

$$\mu_i = \frac{e}{m^*}\tau_i(E_F) = (\frac{2}{m^*})^{1/2}\frac{\varepsilon^{1/2}E_F^{3/2}}{\pi e^3 N_i Z^2}\frac{1}{\ln(1+\frac{\varepsilon E_F}{N_i^{\frac{1}{3}} Z e^2})^2} \tag{2.9}$$

where e is the electric charge, m^* is the effective mass of electrons, $\tau_i$is the relaxation time, which takes into account the scattering events occurring near the Fermi level E_F, ε is the static dielectric constant of the films, Ze is the ion charge and N_i is the concentration of the scattering centers. Formula (2.9) does not contain temperature in an explicit way. This means that ionized impurity scattering mobility is independent of temperature for the degenerate semiconductors.

The effective mass m^* is unique for each particular crystal lattice. Once known, m^* allows for the acceleration of an electron through a known crystal lattice under an applied electric field to be described simply using classical mechanics. The effective mass is usually given in terms of the free electron mass, i.e., m^*/m_o. For different semiconductors, this ratio can be slightly greater or less than unity. For TCOs, this value can be significantly higher than 1.

Grain boundary scattering

Grain-boundary scattering is often assumed to be the dominant mechanism in polycrystalline TCO thin films because of the rather small electron mobility compared with that of single-crystal samples [12-14].

Polycrystalline TCO films are composed of crystallites joined together by grain boundaries which are transitional regions between different orientations of neighbouring crystallites. Among polycrystalline semiconductors, polysilicon has been the most extensively studied material where the grain boundary effects have been analysed with charge-trapping model [15,16]. In this model it is assumed that grain boundaries contain lattice defects-induced trapping states. These states compensate a fraction of charge carriers of ionized, uniformly distributed dopants. This process creates a potential barrier across the depletion region, impeding the carrier motion from one crystallite to another. The influence of the grain boundary scattering becomes very important when the width of the depletion layers becomes commensurate with the grain size of the crystallites. This model has been widely applied to the TCO films in the literature [1,17-22], where it is assumed that grain boundaries between crystallites tend to contain some oxygen which is chemisorbed on the grain boundaries of crystallites. The chemisorbed oxygen atoms (or molecules) can capture electrons from conduction band and makes the grain boundaries negatively charged [23]. Potential barriers are formed between the crystallites, which would strongly scatter conduction electrons.

According to the Petritz model [15], the grain boundary scattering-dependent mobility can be defined as:

$$\mu_g = AT^{-1/2}\exp[-(\frac{eV_B}{kT})] \quad (2.10)$$

where A is a constant for the sample, T is the temperature, e is the electric charge, V_B is the potential barrier between the grain boundaries, and k is the Boltzmann constant. μ_g is mainly determined by the potential barrier V_B. For high resistivity oxide films, the grain boundary scattering is the main scattering mechanism and V_B is very high.

The thickness of depletion layers at grain boundaries can be calculated using the formula:

$$d = \sqrt{\frac{2\varepsilon_0\varepsilon_r V_B}{qn}} \quad (2.11)$$

The grain boundary scattering has a much smaller contribution as compared to other scattering mechanisms. The grain boundary scattering is dominant to limit the mobility only for those samples whose grain sizes are small.

Lattice vibration scattering

In a real crystal atoms are not fixed at rigid sites on a lattice, but are vibrating. Increasing the temperature, the lattice vibration scattering may become dominant. The lattice vibration scattering mobility is formulated as [24]:

$$\mu_l = \frac{e\pi^2\hbar^4 c_{||}}{2m^*(2m^*)^{3/2}\Delta_C^2 N}\frac{E^{-1/2}}{kT} \quad (2.12)$$

where e is the elementary charge, $\hbar$ is the reduced Planck constant, $c_{||}$ is elasticity constant modules, m^* is the effective mass of electrons, Δ is the divergence of strain, N is the concentration of matrix atoms, and k is the Boltzmann constant. Considering the degeneracy for the investigated system, in equation (2.12) $E = E_F$ is a constant. The dependence of the mobility on the temperature can be written as:

$$\mu_i \propto \frac{1}{T} \quad (2.13)$$

Only at high temperatures, thermal lattice vibration scattering can dominate the mobility of a TCO film.

In conclusion, the maximum conductivity of wide band gap semiconductors is restricted by the theoretical upper limit of mobility, depending on each scattering mechanism. Although most authors agree on the mobility limit due to ionized impurity scattering, the mobility due to grain boundary scattering is modeled differently in many cases. The influence of grain boundary scattering in TCOs is still under debate. However, it is commonly accepted that the mobility is only affected if the grain size is considerably small.

2.2.5 Optical properties of TCOs

Usually, the optical properties are studied over a broad range of wavelengths (IR-UV) in order to observe the frequency dependence of these properties. An important feature of TCOs is the existence of a transmission window covering most part of the visible spectrum.

The typical spectral dependence of TCOs is shown in Figure 2.4. The transmission window is defined by two regions where no light is transmitted due to different phenomena. At low wavelengths ($\lambda<\lambda_{gap}$) the absorption due to the fundamental band gap dominates. The photon energy in this near-and deep-UV part of the spectrum is high enough to equal the band gap energy (3 - 4 eV). This energy is absorbed in band to band transitions, and no light is transmitted because of this quantum phenomenon. For longer wavelengths, in the (near) infrared (IR) part of the spectrum no light is transmitted due to the plasma edge ($\lambda>\lambda_p$). Here the light is electronically reflected which can be best described by the classical Drude free electron theory [25].In the free electron model, the electrons may be thought of as a plasma whose density is set into motion by the electric field component of the electromagnetic field. The plasma oscillates at a natural frequency ω_p, the resonance or plasma frequency. This frequency corresponds to the plasma wavelength λ_p and is of the order of 1-4 μm for TCOs [6].

In the range between 400 -1000 *nm* the photon energy is too low and the TCO layer is transparent. If the TCO is sufficiently flat, an interference structure will be seen, dependent on the thickness and refractive index of the TCO layer. The absorption in this region is small.

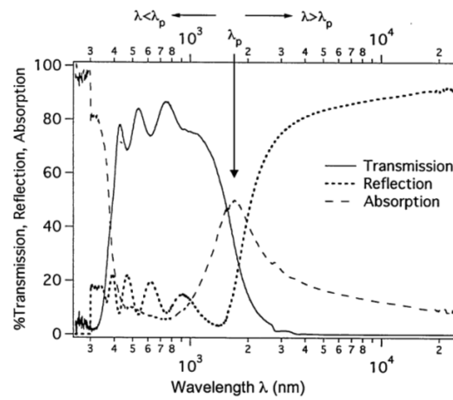

Figure 2.4. Transmission, reflection and absorption spectra of a typical TCO

The transmission can be expressed as [26]:

$$T = (1 - R)e^{-\alpha d} \tag{2.14}$$

where R is the reflectance, d is the film thickness and α is the absorption coefficient.

The optical band gap can be determined from the absorption coefficient:

$$\alpha = 4\pi k/\lambda \tag{2.15}$$

The Tauc model [27] describes α in the high absorbance region of the wavelength range as:

$$\alpha E = A(E - E_g)^{\gamma} \tag{2.16}$$

where E is the incident photon energy, E_g is the energy gap, A is a constant independent of E and γ has four possible numeric values: 1/2, 2, 3, 3/2. Generally an ad hoc assumption is made of a kind of transition (direct allowed when $\gamma = 1/2$, indirect allowed when $\gamma = 2$, indirect forbidden for $\gamma = 3$ and direct forbidden for $\gamma = 3/2$) and the $(\alpha E)^{1/\gamma}$ versus E curve is fitted with a linear function. In order to derive a direct and indirect allowed gap $\alpha E^{1/2} = A(E - E_g)$ and $\alpha E^2 = A(E - E_g)$ respectively are plotted versus E.

For degenerate semiconductors a gradual shift of the band gap towards higher energy as the electron density increases is generally observed. This well-known effect is attributed to the Burstein-Moss shift (BM shift) [28]. The lowest states in the conduction band are filled. Hence transition can only take place to energies above E_F, enlarging the effective optical gap. This effect is of importance at very high carrier concentrations (order 10^{21} cm^{-3}).

One can approximately calculate the effective mass of the charge carrier from the blue shift and conduction electron density. The blue shift can be written as [29]:

$$\Delta E = \frac{\hbar^2 k_F^2}{2m^*} \tag{2.17}$$

where k_F is the Fermi wave vector. The concentration of conduction electrons can be written as [30]:

$$n = \frac{k_F^3}{3\pi^2} = \frac{1}{3\pi^2}\left(\frac{2m^*\Delta E}{\hbar^2}\right)^{3/2} \tag{2.18}$$

The effective mass will be:

$$m^* = \frac{\hbar^2}{2\Delta E}(3\pi^2 n)^{2/3} \tag{2.19}$$

2.2.6 Intrinsic and extrinsic doping of TCOs

Stoichiometric metal oxides have a band gap larger than 3 eV and are therefore practically insulators at room temperature. However, a high charge carrier concentration in TCOs can easily be obtained by use of two doping mechanisms: intrinsic doping and extrinsic doping. Due to this the materials become *n*- or *p*-type.

Intrinsic doping

Intrinsic doping is present due to defects in the crystal lattice, away from stoichiometry. This leads to a small oxygen deficiency and thus to oxygen vacancies in those materials. These oxygen vacancies give rise to shallow donor states just below the conduction band and act as an *n*-type impurity band. It has been postulated for a long time that transparent conductivity is related to the existence of shallow donor levels near the conduction band, formed by a large concentration of oxygen vacancies [30-32]. Having a shallow donor level means that these additional energy levels are not more than $3k_bT$ (0.075 eV at room temperature) away from the lowest conduction band edge, where k_b is the Boltzmann constant.

Extrinsic doping

By replacing the original bulk metal ions (cations) and bulk oxygen ions (anions) with ions having respectively a higher and lower valence, the carrier concentration can be increased further. This increase results eventually in a degenerately doped TCO layer with the Fermi level shifted into the conduction band.

The incorporation of extrinsic defects (aliovalent ions) into the TiO_2 lattice leads to the formation of donors and acceptors when their valency is higher and lower than that of host lattice ions. Several approaches for TiO_2 modification have been proposed: metal-ion implanted TiO_2 (using transition metals: *Cu*, *Co*, *Ni*, *Cr*, *Mn*, *Mo*, *Nb*, *V*, *Fe*, *Ru*, *Au*, *Ag*, *Pt*), reduced TiO_x photocatalysts, non-metal doped-TiO_2 (*N*, *S*, *C*, *B*, *P*, *I*, *F*), composites of TiO_2 with semiconductor having lower band gap energy (e.g. *Cd-S* particles, sensitizing of TiO_2 with dyes (e.g. thionine) and TiO_2 doped with upconversion luminescence agent [33].

n-type doping of ZnO is relatively easy compared to *p*-type doping. Group-III elements *Al*, *Ga*, and *In* as substitutional elements for *Zn* and group-VII elements *Cl* and *I* as substitutional elements for *O* can be used as *n*–type dopants. Known acceptors in ZnO include group-I elements such as *Li*, *Na*, and *K*, *Cu*, *Ag*, *Zn* vacancies, and group-V elements such as *N*, *P*, and *As*. However, many of these form deep acceptors and do not contribute significantly to *p*-type conduction. It has been believed that the most promising dopants for *p*-type ZnO are the group-V elements, although theory suggests some difficulty in achieving shallow acceptor level [34].

2.2.7 Work function, chemical affinity and ionization potential

For thin film solar cells, knowledge of the TCO surface potentials (e.g., ionization potential, Fermi level) provides important benchmarks for interpreting band alignment at TCO/inorganic interfaces.

Figure 2.5 shows schematically the work function for an *n*-type semiconductor. The *work function* (φ) of a TCO is defined as the energy difference between the Fermi level and vacuum. In most *n*-type TCOs the Fermi level lies in the conduction band due to the degenerate nature of these films. Therefore, the work function is essentially the energy required to remove the electron from the conduction band.

The work function has two contributions, the *chemical affinity* (χ) and the value of ($E_F - E_{CB}$):

$$\varphi = \chi + (E_F - E_{CB}) \tag{2.20}$$

Work function is extremely sensitive to the surface characteristics. φ is also a function of the carrier concentration because the value of ($E_F - E_{CB}$) is mainly determined by the carrier concentration. In general the higher the carrier concentration, the lower is the work function of a given sample.

The ionization potential (I_p in Figure 2.5) is the energy necessary to remove an electron from a free unexcited neutral atom (or additional electron from an ionized atom).

Most of the TCO applications require a high work function (>5 *eV*), as the transparent electrodes perform the function of either hole-injection or carrier collection.

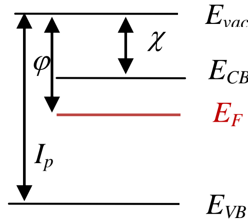

Figure 2.5 Different contributions to work function changes for n-type semiconductor

2.2.8 Figure of merit for TCOs

Because transparent conducting oxides have two important qualities with which they can be judged, optical transmission and electrical conductivity, and because these two parameters are somewhat inversely related, a general method of comparing the properties of different TCOs is used, named figure of merit.

Different equations have been developed and used over the years to compare TCO film properties. One of the earliest equations defining a figure of merit was developed by Fraser and Cook (FC) [35]:

$$F_{FC} = \frac{T}{R_{\square}} \tag{2.21}$$

where T is the transmission and $R_{\square}$ is the sheet resistance of the thin film. This value was often multiplied by 1000 to allow comparisons of numbers greater than one. Higher values of figure of merit indicate superior film properties.

A second figure of merit was developed by Haacke [36], putting more emphasis on the optical transparency because F_{FC} was too much in favor of sheet resistance, resulting in a maximum figure of merit at relatively large film thicknesses. The figure of merit was redefined as:

$$F_H = \frac{T^x}{R_{\square}} \tag{2.22}$$

with $x > 1$. Like Fraser and Cook's figure of merit, the resulting value is multiplied by 1000 and larger numbers indicate superior quality films.

Fraser and Cook and Haacke [] equations are based on the sheet resistance of the films which in turn is thickness dependent. Therefore, a thicker film will have a lower sheet resistance, but will most likely also have a lower transmission due to more absorption in the film.

The third figure of merit was developed by Iles and Soclof [37]. A figure of merit that is independent of film thickness is given by:

$$F_{IS} = R_{\square}(1 - T) = \frac{\alpha}{\sigma} \tag{2.23}$$

where α is the absorption coefficient and σ is the conductivity of the film. The lower numbers correspond to films of higher quality.

Another expression that is thickness independent for the figure of merit was developed by Jain and Kulshreshtha [38]:

$$F_{JK} = -R_{\square} \ln(T) \approx \frac{\alpha}{\sigma} \quad (2.24)$$

Just as with the previous figure of merit, F_{IS}, lower numbers correspond to better film properties.

2.2.9 Alternative TCOs and current status

The most common TCO used nowadays is Sn-doped In_2O_3 (ITO) [39]. However, indium is a relatively scarce, and consequently an expensive element. Consequently, much recent work has been focused on alternative materials [40,41].

Some of the known pure and impurity doped binary materials are TiO_2, ZnO, SnO_2, CdO, and Ga_2O_3. The observation of TCO characteristics in these binary compounds (metal oxides) with no intentional doping is attributed to intrinsic donors such as oxygen vacancies and/or interstitial metal atoms. However, the undoped oxide films are unstable when used at high temperature and when exposed to ambient atmosphere. Doping these films with certain impurity elements improves the long term stability and reliability of these films for transparent electrode applications. It is to be noted that CdO is toxic, which makes it useless for practical application. Recently, it has been found that Nb-doped anatase TiO_2 also exhibit attractive TCO characteristics [42]. In the work of Furubayashi *et al.* $Ti_{1-x}Nb_xO_2$ thin films with a resistivity of 2-3x10^{-4} Ωcm at room temperature, a carrier density in the range 1x10^{19} - 2x10^{21} cm^{-3} and with an internal transmittance of the films of about 97% in the visible light region were grown by pulsed laser deposition technique.

Table 2.1 lists the reported properties of *n*-type TCOs prepared by RF sputtering technique investigated in present as good alternatives to ITO.

Table 2.1. Reported properties of *n*-type TCOs deposited by RF sputtering

TCO	ρ [Ωcm]	T [%]	E_g [eV]	n [cm^{-3}]	μ [cm^2/Vs]	ϕ [eV]	Ref.
ITO	1.56x10^{-4}	~87	3.35–3.47	1.00x10^{21}	20	4.67-5.7	[43-45]
ZnO	3.16x10^{-2}	~80	3.10	7.02x10^{19}	2.81	4.8	[46-48]
ZnO:Al	3.60x10^{-4}	~85	3.21-3.25	7.80x10^{20}	22	3.7–5.1	[48-50]
ZnO:Ga	5.3x10^{-4}	~89	3.40-3.45	1.20x10^{21}	9.9	3.62-4.37	[51,52]
ZnO:In	4.29x10^{-4}	~82	3.80	3.04x10^{20}	47.8	5.12	[53]
TiO_2	~300	~80	3.58-3.79	-	-	3.9	[54-56]
Nb-TiO_2	2.40x10^{-4}	~80	3.67-3.73	3.3x10^{21}	3.35	5.02-5.47	[57]
SnO_2	8.0010^{-3}	~90	3.40-3.65	3.6x10^{20}	1-3	4.7-5.7	[58,59]
SnO_2:Sb	3.30x10^{-3}	~70	3.8-3.9	2.6x10^{20}	4.7	4.7-4.9	[60,61]

2.3 Fundamentals of TiO_2

Titanium dioxide (TiO_2) is a material used in a wide range of common and high-tech applications. It is cheap, chemically stable, non-toxic, and last but not least bio-compatible. Titanium is successfully used as implant material for dental, orthopedic and osteosynthesis application and its native oxide is mostly constituted of titanium dioxide. TiO_2 powder is used as white pigment in paint [62], replacing lead oxide which is toxic, and in toothpaste. Transparent single crystals or thin films have a high refractive index that makes TiO_2 suitable for optical applications [63]. Multi-layers composed of TiO_2 and SiO_2 are designed to make antireflection coatings in the whole visible range [64]. TiO_2 is widely used for photocatalysis [65], for example for water treatment by oxidation of dissolved organic molecules [66]. Electrodes made of TiO_2 are used in electrochromic devices [67] and dye-sensitized solar cells [68]. Solid-state photovoltaic solar cells with porous TiO_2 layer show promising results [69]. Thus, research in many different fields is devoted to titanium dioxide under various forms such as single crystals, ceramics, and thin films.

Because of the high dielectric constant, rutile phase of TiO_2 is investigated as a dielectric material in electronic applications. For optical applications rutile is preferred to anatase because of its higher refractive index. Films should be dense and smooth with as few voids as possible. On the other hand, all the applications related to photocatalytic activity, gas sensing, and solar cells have a preference for anatase due to its higher mobility and its catalytic properties. Here usually porous structures are advantageous because of a large surface to volume ratio. Fabrication techniques of doped or undoped TiO_2 thin films of versatile morphology include sol-gel, chemical vapour deposition (CVD), and physical vapour deposition (PVD) techniques.

In this section the physical, electrical and optical properties of TiO_2 are discussed. An overview on the literature related to the water adsorption at TiO_2 surfaces is given. The effect of oxygen vacancies and impurities on the properties of TiO_2 is discussed in the last part.

2.3.1 Crystal structures of TiO_2

In nature titanium dioxide crystallizes in three common polymorphs: rutile, anatase and brookite [70,71]. Moreover, TiO_2 can be observed in additional crystal structures: TiO_2 II columbite structure [72], TiO_2 III baddeleyite structure [73,74], TiO_2 (H): hollandite structure [75], TiO_2 (R) ramsdellite structure [76], and TiO_2 (B) [77]. Many of these phases occur only at very particular conditions, such as high pressure. The most common and studied structure is rutile, it is also the most stable structure of TiO_2.

Besides an amorphous component, rutile and anatase were the only polymorphs synthesized in the sputtered thin films in this work. Hereafter the description of the properties of titanium dioxide will concentrate on these two phases.

Table 2.2 Physical properties of rutile and anatase TiO_2

	Rutile	**Anatase**
Crystal structure Space group	Tetragonal *P4₂/mnm (136)* [78] *c*=2.9587 *Å*, *a*=4.5937 *Å* [79] *u*=0.3048 *Å*, *c/a*=0.6441	Tetragonal *I4₁/amd (141)* [78] *c*=9.5146 *Å*, *a*=3.7842 *Å* [80] *u*=0.2081 *Å*, *c/a*=2.5143
Heat formation	944.5×10^3 *kJ/kmol* [81]	944.5×10^3 *kJ/kmol* [81]
Most stable surface	*[110]* [82]	*[101]* [83]
Density	4.25 g/cm^3 [78]	3.89 g/cm^3 [78]
Electrical properties at RT	*n*-type semiconductor [84]	*n*-type semiconductor [85]
Band gap	direct 3.04 *eV* indirect 3.05 *eV* [86]	direct 3.42 *eV* indirect 3.46 *eV* [87]
Mobility at RT in crystal	0.1 - 1 cm^2/Vs [88,89] 0.01 cm^2/Vs (high impurity conc.) [88]	15 cm^2/Vs [85,87]
Mobility at RT in polycrystalline thin films	0.1 cm^2/Vs [89,90]	0.1 - 4 cm^2/Vs [87]
Electron effective mass	9 -13m_e [91] 10 - 30m_e [89] 12 - 32m_e [92]	~1m_e [87]

In Table 2.2 a summary of the most important physical properties of anatase and rutile structures of TiO_2 is given. The unit cells of rutile and anatase TiO_2 crystal structures are shown in Figure 2.6. The unit cell parameters at room temperature are given in Table 2.2. The unit cell of rutile contains two Ti atoms situated at (0, 0, 0) and (½a, ½a, ½c), and four oxygen atoms. The oxygen atoms form a distorted octahedron around every Ti cation. The unit cells of anatase contains four Ti atoms located at (0, 0, 0), (½a, ½a, ½c), (0, ½a, ¼c), and (-½a, 0, -¼c), and eight oxygen atoms. In anatase, too, the Ti cation is surrounded by a distorted oxygen octahedron [93]. TiO_6 octahedra constitute the basic building units for anatase and rutile structures of

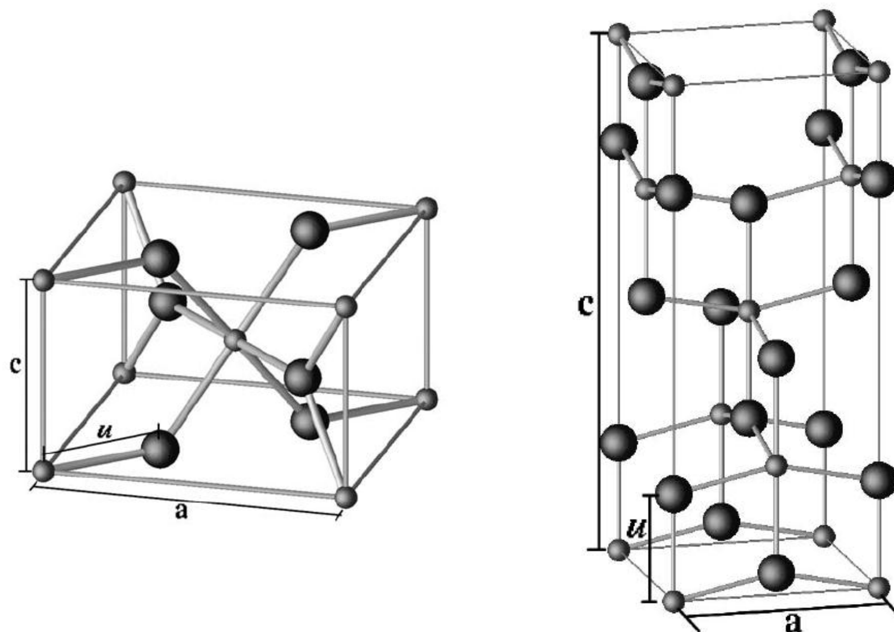

Figure 2.6 Rutile (left) and anatase (right) crystallographic unit cells. Small spheres represent Ti atoms, large spheres represent oxygen atoms

TiO_2. The polymorphs differ from each other by the arrangement and the distortion of the octahedra. In the rutile crystal each octahedron is connected to 10 neighbouring octahedra, among which 2 share an edge and 8 share a corner with it. The edge-shared octahedra are aligned along the *[001]* direction [84]. In the case of anatase, each octahedron shares 4 edges. The edge-shared octahedra are aligned along the *[100]* and *[010]* direction forming zigzag double chains perpendicular to the *c*-axis. These arrangements of TiO_6 octahedra in rutile and anatase give rise to open channels parallel to the *c*-axis in rutile and perpendicular to the *c*-axis in anatase [82]. Amorphous TiO_2 does not have a strict crystallographic structure, often incorporates voids within the material, and has a relatively low density.

Nearly all published results indicate that the transition from an amorphous to anatase film occurs at about $300-365°C$, regardless of whether this is the deposition or annealing temperature. Rutile films are initially observed on silicon substrates at deposition temperatures above $700°C$, and more typically from $900-1100°C$. It should be noted that anatase is a metastable phase of TiO_2, and the conversion to rutile involves a collapse of the anatase structure, which is irreversible [94,95]. The critical temperature can vary from $300°C$ to $1200°C$, depending on the grain size, atmosphere, as well as the nature and amount of impurities [80]. In physical vapour deposition (PVD) systems, such as evaporation, sputtering, and ion-beam deposition, the resulting phase and film structure is determined primarily by the kinetic energy of the impinging atoms. Therefore, the progression through the amorphous, anatase, and rutile phases may not necessarily be expected.

Many researchers have observed that the inclusion of a certain amount of impurities into TiO_2 can drastically alter the physical properties of the film. It has been shown that silicon and phosphorus inhibit the transformation from anatase to rutile, with 100% anatase phase being retained at temperatures as high as $870°C$ for up to $3h$ for thin films and 1500 K for bulk samples [96]. The retardation of the anatase-to-rutile transformation can be achieved with the following impurities: PO_4^{3-}, SO_4^{2-} and Al^{3+} [97]; $AlPO_4$ [94]; SiO_2 [94,96]; Co_3O_4 and MoO_3 [98]; *Ce* and *Nb* [99]; K^+ [100]; WO_3 [101,102]; Na_2O [102]; and P_2O_5 [96]. Conversely, it is well known that other impurities enhance the formation of rutile at lower temperatures. These impurities include CuO_2 [98,102]; V_2O_5 [98]; and *NiO*, *CoO*, MnO_2, Fe_2O_3 [102].

Most researchers agree that oxygen vacancies are responsible for the overall transformation mechanism [94,95,103]. Thus, cations such as Li^{+1},Co^{+2} and Mn^{+4} that assist the transformation can substitute for Ti^{+4} in the anatase lattice, resulting in the creation of oxygen vacancies. On the other hand, the inhibiting effect of other impurities (PO_4^{3-}, SO_4^{2-}, Nb^{5+}) has been explained by the reduction of oxygen vacancies due to the substitution of Nb^{+5} and S^{+6} into the anatase lattice. Oxygen vacancies are also known to be created in hydrogen ambients, thereby favouring the transformation to rutile [95,102,103].

Natural rutile crystals exhibit predominantly *[110]* surfaces [70], and there is agreement on the fact that the *[110]* stoichiometric surface is the most stable surface for rutile [82]. For anatase the *[101]* surface is the most stable [104].

While both rutile and anatase possess a tetragonal crystallographic structure, rutile is more densely packed and thus possesses a greater density (4.25 g/cm^3) than anatase (3.89 g/cm^3). Amorphous TiO_2 films exhibit a

wide range of densities, from 2.4 *g/cm*^{3} for porous films [105] to more typical values of 3.2 − 3.65 *g/cm*^{3} [106] while films deposited with a high kinetic energy have achieved densities in the range 3.6 − 3.8 *g/cm*^{3} [107]. It has been noted that the TiO_2 films with a lower density can favour impurity diffusion [108], so anatase phase is preferred for doping with impurities.

Figure 2.7 shows the phase diagram of titanium oxides. Varying the oxygen content from 0 to 2 oxygen per titanium atom the main phases encountered at room temperature are Ti, Ti_2O, TiO, Ti_2O_3, Ti_3O_5 and finally TiO_2. In addition, in between Ti_3O_5 and TiO_2 a series of Ti_nO_{2n-1} (with $n \geq 4$) phases can be found. This is the Magnéli series of homologous compounds [109,110] where physical properties are changed dramatically, ranging from metallic to insulating depending on *n*. The formation of such reduced oxide phases can be described in terms of the elimination of a plane of oxygen atoms [110].

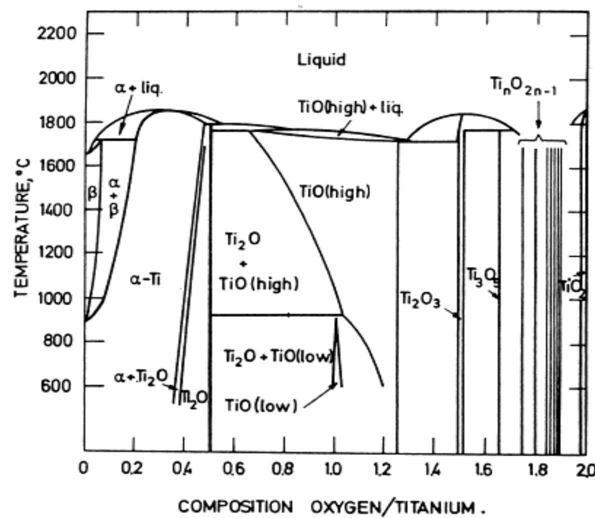

Figure 2.7 The phase diagram of titanium oxides [111]

2.3.2 Electronic states of TiO_2

As mentioned in the previous section, TiO_6 octahedral clusters are basic structural units in anatase and rutile structures of TiO_2. The electronic states associated with such octahedral constitute a determining first approximation for understanding the electronic structures and properties of TiO_2 polymorphs. Electronic states of TiO_6 clusters can be viewed as the atomic states modified by specific crystal fields or as the overlapped atomic state (molecular orbitals) between atoms.

First, the Ti *3d* atomic states are split by the octahedral ligand field of the oxygen ions. For a regular TiO_6 octahedron (O_h symmetry), by approximating the oxygen anions as point charges and by treating the resultant electrostatic potential as a small perturbation, it can be explicitly shown that the Ti *3d* states are split into a two-fold degenerate e_g state and a three-fold t_{2g} state [112,113]. When the octahedron is distorted to lower symmetries such as D_{4h} (tetragonal) and D_{2h} (orthorhombic), the e_g and t_{2g} states are further split (Figure 2.8 *(a)*).

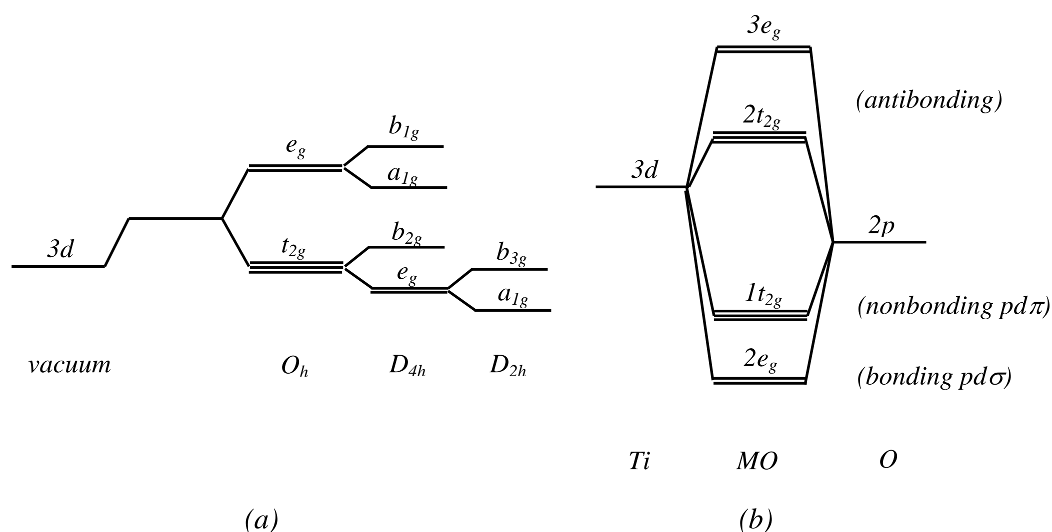

Figure 2.8 *(a)* Splitting of Ti 3d atomic states by the octahedral ligand field of oxygen anions with symmetries O_h (regular octahedron), D_{4h} (tetragonal distortion) and D_{2h} (orthorhombic distortion) respectively; *(b)* Schematic energy level diagram of the molecular orbitals (MO) formed by Ti *3d* and O *2p* atomic levels

To construct the molecular orbitals (MO) of the TiO_6 clusters, however, oxygen anions can no longer be approximated by point charges, because O *2p* orbitals also widely extend in space. In fact Ti *3d* orbitals and O *2p* orbitals overlap in places where they have the same symmetry. Mixing of the atomic orbitals gives rise to the upper antibonding and lower bonding molecular orbitals, as illustrated by the schematic atom-MO-atom energy level diagram in Figure 2.8 *(b)*.

The O *2p* levels are lower than the Ti *3d* levels, so correspondingly the lower bonding molecular orbitals are mainly composed of O *2p* states, whereas the upper antibonding molecular orbitals are mainly derived from Ti *3d* states. The antibonding part of the present diagram corresponds largely to the ligand-field-split Ti *3d* states shown in Figure 2.8 *(a)*.

Though the MO model is a highly empirical approach, it is useful for the interpretation of the X-ray photoelectron spectroscopy valence band spectra presented in the next chapters. Moreover, the MO model links directly the electronic structure and properties to local structural characteristics such as chemical bonds, symmetry distortion, and defects.

2.3.3 Electrical and optical properties of TiO_2

Substoichiometric TiO_{2-x} is both a poor insulator and a modest semiconductor. Therefore several attempts have been made either to control the oxygen vacancy concentration or to introduce charge carriers (doping) inside TiO_2 in order to increase or decrease the electrical conductivity, depending on the desired application. During the last 40 years, almost half the atoms of the periodic table have been incorporated into TiO_2.

The majority of dopants enhance the *n*-type semiconducting properties of TiO_2. These dopants include niobium (*Nb*), tantalum (*Ta*), vanadium (*V*), fluorine (*F*) and hydrogen (*H*). Dopants that change the film to being *p*-type include aluminium (*Al*), iron (*Fe*) and indium (*In*). Additionally, dopants such as aluminium, iron, chromium and cadmium are known to extend the photoactive response from the TiO_2 film under visible light.

As a wide band gap semiconductor TiO_2 crystals have a high resistivity (in the order of 10^{15} *Ωcm* [110]). When TiO_2 is reduced its *n*-type conductivity increases according to the extent of oxygen loss. Oxygen vacancies and/or Ti^{3+} interstitials are interpreted to be the donor centers in reduced TiO_2.

The charge carrier mobility in rutile is low (see Table 2.2), leading to a controversy over the nature of the carriers. Bogomolov *et al.* [114,115] have proposed that charge carriers behave as small polarons. A small polaron is an electron (or hole) self-trapped by the local lattice polarization which itself is generating [116]. As self-trapped localized states, small polarons proceed via hopping from site to site. In rutile a decreasing mobility for higher temperatures is attributed to phonon scattering. This suggests that the carriers are large polarons and not localized small polarons because the latter become more mobile at higher temperatures due to thermally activated hopping between the atoms [113]. However the mobility may decrease if the small polarons diffuse by tunnelling.

In contrast to rutile, anatase shows a significantly higher Hall mobility and a bandlike conduction behavior [87]. Therefore carriers are less likely to be small polarons in anatase than in rutile.

High concentrations of donors lead to the formation of impurity bands in anatase and rutile [87]. When the impurity concentration exceeds a critical value, the impurity-band conduction can become metallic. The impurity-band conduction and the non-metal to metal transition have been experimentally observed and theoretically analyzed for oxide semiconductors [116]. A model of this transition has been developed by Mott, discussed in detail in Section 2.2.3 in this chapter [8]. A transition to metallic behaviour has been observed in heavily reduced/doped anatase thin films [87], but not in similarly reduced rutile films [87,89,92].

Rutile and anatase are wide band-gap semiconductors with the valence band consisting of O *2p* states and the conduction band formed of Ti *3d* states [70]. The values of the band gap are listed in Table 2.2.

Depending on the degree of reduction of rutile TiO_2 the appearance of a blue colour has been reported [89,114]. It has been found that this blue colour arises from the visible tail of an infrared absorption band peaking at about 0.75 to 1.18 *eV* [114]. In anatase the blue colour has been observed, too [83,117]. As in the

case of rutile, it is caused by a wide absorption band with its maximum in the infrared region. In addition, a colour center at 3 *eV* due to an oxygen vacancy has been identified giving rise to a yellow colour [117].

2.3.4 Water adsorption on TiO_2 surfaces

The interaction of water with TiO_2 surface has been of intense interest in recent years. To illustrate, many of the applications, almost all photocatalytic processes, are performed in an aqueous environment. In addition, TiO_2 exposed to air will always be covered by a water film and the presence of water can affect adsorption and reaction processes.

A variety of experimental and theoretical techniques has been used for investigating this interaction [104,116,118-125]. The principal ambiguity in the studies referred to water interaction with TiO_2 surfaces was whether the water is absorbed dissociative or non-dissociative [126].

There are some experimental studies with regard to the surface properties and adsorption mechanisms of water on rutile TiO_2 *[110]* surface. Using synchrotron radiation and photoemission spectroscopy Kurtz *et al.* [123] reported that water molecules adsorbed on the perfect (stoichiometric) rutile *[110]* surface molecularly or dissociatively depending on temperature. Hugenshmith *et al.* [124] studied interaction of H_2O with rutile TiO_2 *[110]* surface by temperature programmed desorption (TPD), x-ray photoelectron spectroscopy (XPS) and work function measurements. They reported that water is mainly molecularly adsorbed and not dissociated on this surface. The same result was reported by Henderson *et al.* [127] by performing high resolution electron energy loss spectroscopy (HREELS) and TPD studies, pointing that dissociation of water may be linked to structural and/or point defects. But Brinkley *et al.* [128] reported molecularly adsorbed H_2O on rutile TiO_2 *[110]* surface using modulated molecular beam scattering and TPD studies. Recent scanning tunneling microscope (STM) studies, most notably the ones published by Brookes *et al.* [129] and Schaub *et al.* [130] support the earlier experimental results that dissociative adsorption occurs at defects or at oxygen vacancies as active sites for water dissociation. Molecular adsorption is more favourable than dissociation on the defect-free surface.

Beside the experimental studies, there are also many theoretical studies about adsorption reactions and surface properties on rutile TiO_2 *[110]*. Goniakowski *et al.* [131] found that dissociative adsorption of water molecule is thermodynamically more stable than molecular adsorption. Lindan *et al.* [132] also indicated that dissociation of the water molecule is thermodynamically favoured on low coverages but both molecular and dissociative adsorption were confirmed at high coverages by use of both density functional theory (DFT) and Hartree-Fock (HF) methods. Casarin *et al.* [133] and Stefanovich *et al.* [125] predicted that molecular water adsorption is more favourable than dissociative chemisorption. Menetrey *et al.* [134] performed periodic DFT calculations to study the effect of oxygen vacancies. They found that the reactivity at reduced surface differs from that on the stoichiometric perfect surfaces. The dissociative adsorption energy for reduced surfaces is lower than on the perfect surface. Perron *et al.* [135] performed periodic DFT calculations and it was determined that molecular adsorption of water is energetically favourable but dissociative one can also

be envisaged because it can be stabilized with hydrogen bonding. Kamisaka *et al.* [136] studied the surface stresses and adsorption energies of clean and water-adsorbed *[110]* and *[100]* surfaces of rutile. Two forms of water, molecularly and dissociatively adsorbed water, and water adsorbed at surface oxygen vacancies, were studied. In their calculations, the H_2O molecular absorbate had larger adsorption energy than that of the H_2O dissociative absorbate.

Only few experimental studies with regard to the surface properties and adsorption reactions of water on TiO_2-anatase surfaces were reported. Srnak *et al.* [137] reported that they observed two states of water desorption from vacuum TPD studies. Vittadini *et al.* [138] investigated structure and energetics of water adsorption on TiO_2-anatase different surfaces by use of DFT calculations. The results support the idea that on the anatase surface, basically two distinct states of the adsorbed water are present, one related to undissociated water on the *[101]* and *[100]/[010]* majority surfaces, and the other to dissociated water on the anatase *[001]* minority surface. The latter can also account for the residual hydroxyl groups observed after heating the surface.

Onal *et al.* [139] have performed a cluster study with regard to water adsorption on anatase TiO_2 *[101]* and *[001]* surfaces. The results indicate that the favorable adsorption mode of water depends on the surface relaxations. Molecular water adsorption is more favorable on relaxed *[101]* than dissociative water adsorption; however, on the fixed cluster it is seen that the opposite situation is valid. Non-activated dissociation of water takes place on relaxed *[001]* cluster while on fixed *[001]* cluster molecular adsorption is found to be more favoured.

2.3.5 Oxygen vacancies and other impurities in TiO_2

TiO_2 is a nonstoichiometric compound, which has been generally considered as an oxygen-deficient compound, TiO_{2-x} [140]. The most notable point defect of pure TiO_2 called native point defects, are oxygen vacancies and interstitial titanium atoms. Recent studies have shown that strong oxidation of TiO_2 (at elevated temperatures) leads to the formation of a metal-deficient oxide [141]. In this case, TiO_2 may be represented by the formula $Ti_{1-x}O_2$ or, more precisely $Ti_{1-x}O_{2-y}$, where $x > y/2$ [142], leading to *p*-type properties. The formation and the transport of titanium vacancies were found to be extremely slow, their concentration remaining practically independent of oxygen activity [142].

The most commonly applied representation of defect disorder is in the form of defect diagrams, which are based on simplified charge neutrality conditions, valid over narrow regimes of nonstoichiometry. Although these diagrams may be used for the verification of defect disorder models they do not inform on defect concentrations.

An oxygen vacancy is formed by the transfer of an oxygen atom on a normal site to the gaseous state. In the Kröger and Vink notation [143], the chemical reaction is written in the following way:

$$O_O \leftrightarrow V_O^x + \frac{1}{2}O_2 \qquad (2.25)$$

where O_O is an oxygen ion on a normal lattice site and V_O^x is a neutral oxygen vacancy.

The two trapped electrons (e') associated with the oxygen vacancy may, depending on the temperature, be excited and freed from the vacancy. In this case, the vacancy acts as a donor and becomes singly ($V_{\dot{O}}$) or doubly ($V_{\ddot{O}}$) charged [144]:

$$V_O^x \leftrightarrow V_{\dot{O}} + e' \quad (2.26)$$

$$V_{\dot{O}} \leftrightarrow V_{\ddot{O}} + e' \quad (2.27)$$

An interstitial titanium is created in the following way:

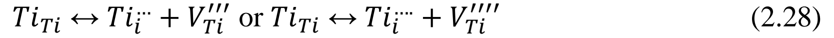

$$Ti_{Ti} \leftrightarrow Ti_i^{\cdot\cdot\cdot} + V_{Ti}''' \text{ or } Ti_{Ti} \leftrightarrow Ti_i^{\cdot\cdot\cdot\cdot} + V_{Ti}'''' \quad (2.28)$$

where Ti_{Ti} is an titanium ion on a normal lattice site, $Ti_i^{\cdot\cdot\cdot}$ or $Ti_i^{\cdot\cdot\cdot\cdot}$ are interstitial titanium (three or four times charges), and V_{Ti}''' or V_{Ti}'''' are titanium vacancy (three or four times charged).

The nonstoichiometric regimes, the related charge neutralities and the effect of oxygen activity on the concentrations of specific defects for undoped TiO_2 have been published in the work of Nowotny *et al.* [142] and is shown in Figure 2.9 *(a)*.

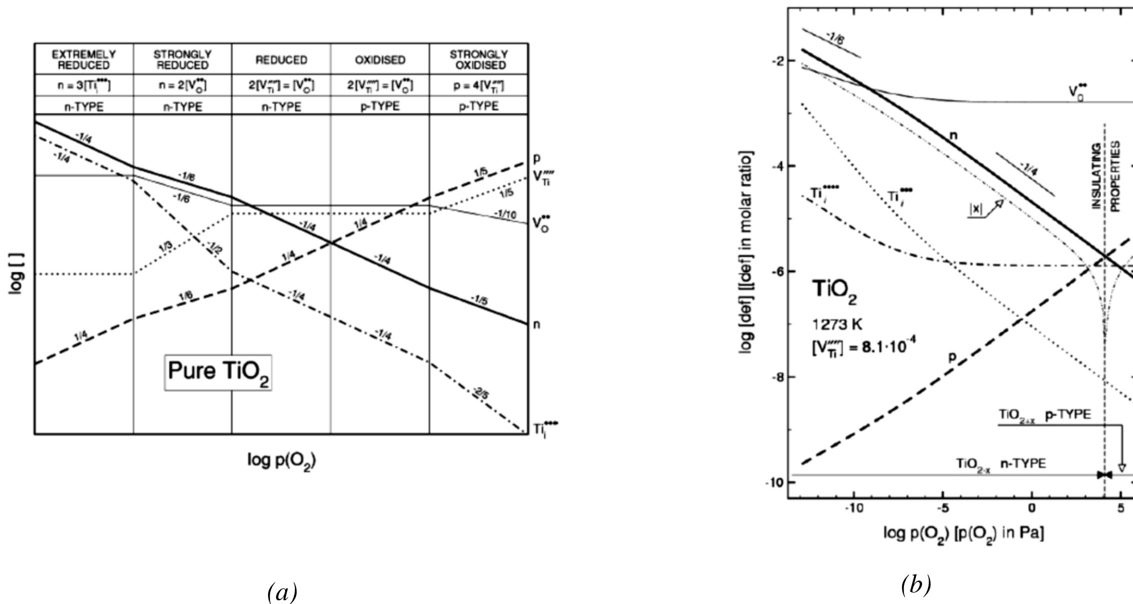

(a) *(b)*

Figure 2.9 *(a)* Defect diagram based on simplified charge neutrality conditions for pure TiO_2; *(b)* Defect disorder diagram for pure TiO_2 at 1273 *K* showing the effect of oxygen activity in the concentration of ionic and electronic defects, where $|x|$ is the absolute value of the deviation from stoichiometry

Figure 2.9 *(b)* shows the defect diagram in terms of the concentration of defects as a function of oxygen activity at 1273 *K* [145]. As seen, the concentration of electronic charge carriers and the related electrical properties of undoped TiO_2 are closely related to oxygen activity, which may be used for the imposition of both *n*- and *p*-type properties as well as mixed conduction.

Nowotny [142] has proposed a band model of TiO_2 showing the energy levels of intrinsic lattice defects, shown in Figure 2.10 *(a)*. As seen in Figure 2.10 *(a)*, both oxygen vacancies and titanium interstitials form donor levels [146,147] and titanium vacancies form acceptors [148].

For years oxygen vacancies have been investigated using a variety of spectroscopic techniques. Whether titanium interstitials or oxygen vacancies are the dominant defects has not been definitively established [104]. It is generally believed that, under weakly reducing conditions or low annealing temperatures (below 870 *K* in vacuum), oxygen vacancies are predominant. In the more reducing conditions and higher annealing temperatures (above 1070 *K* in vacuum) titanium interstitials become more important [110].

When impurities are incorporated into TiO_2, they can dissolve inside the crystallites, or settle in the grain boundaries. They can also agglomerate, if the maximum solubility is exceeded, as precipitates either at the center of crystallites or at the grain boundaries. The diffusion of atoms in solids can take place via a number of mechanisms [149]. For metal oxides in general, diffusion typically occurs via one of three mechanisms: interstitial, vacancy and interstitialcy.

The diffusion of an atom according to the interstitial mechanism takes place when that atom migrates from one interstitial site to a nearest neighbour interstitial site without permanently displacing any of the matrix atoms [149]. In order for such migration to occur, the regular lattice atoms which separate the two interstitial sites involved must dilate sufficiently. Hence, this mechanism proceeds more readily when the diffusing atoms are much smaller than the lattice atoms, and otherwise have a tendency to occupy interstitial positions in the lattice.

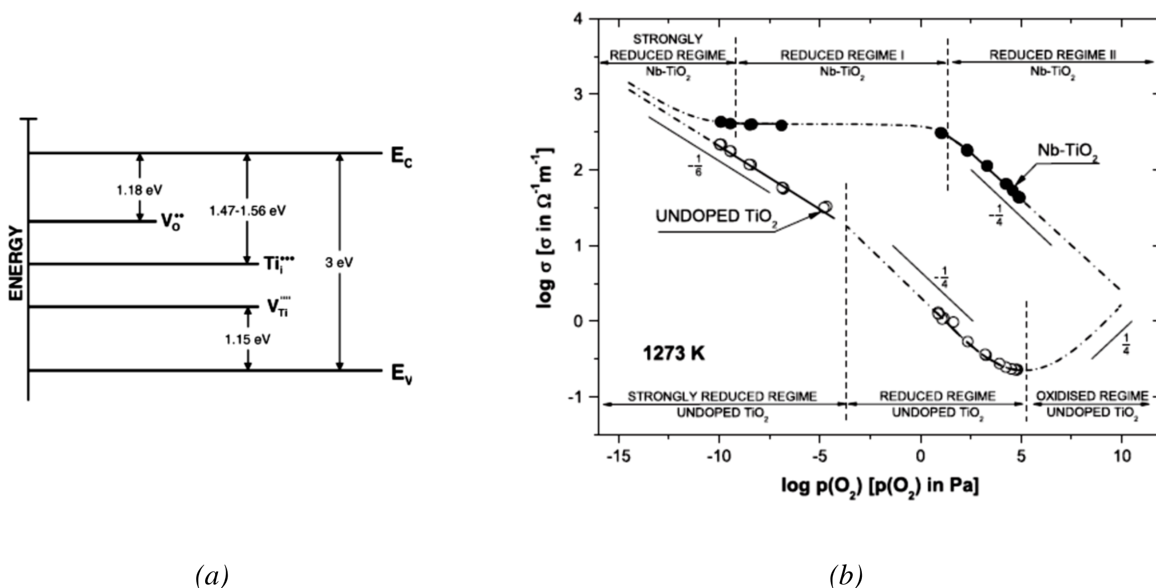

Figure 2.10 *(a)* Band model of TiO_2 showing the energy levels of intrinsic lattice defects; *(b)* The effect of oxygen activity on the electrical conductivity for both undoped TiO_2 and Nb-doped TiO_2 at 1273*K* showing the oxygen activity regimes governed by different charge neutrality conditions

The unavoidable presence of vacant lattice sites in all solids allows for vacancy mechanism. Diffusion via this mechanism involves the jumping of a lattice atom into an adjacent vacancy site, both filling and creating a vacancy in the process. In general, unlike the interstitial mechanism, the required lattice distortion required for diffusion via this mechanism is small [149]. Rather, the probability of such a jump occurring is dependent upon the number of adjacent vacant sites.

The interstitialcy mechanism involves the migration of an atom in an interstitial site to a regular lattice site, whereby it has displaced this lattice atom into a neighbouring interstitial site. This mechanism is favourable over the interstitial mechanism when the interstitial atoms are relatively large (or of comparable size to the host atoms), and so the required distortion for diffusion via the interstitialcy mechanism is similarly very large [149].

The interstitialcy mechanism can occur in several ways [150], depending upon the direction in which the regular lattice atom is displaced.

Donor doping of TiO_2 is achieved by the incorporation of cations of valence greater than 4+ into regular Ti lattice sites. Upon substitution, the excess valence electrons associated with the dopant cation are compensated in order to maintain lattice electroneutrality. In our work, niobium (5+) was used as impurity for donor doping of TiO_2.

The defect disorder of Nb-doped TiO_2 can be divided into several specific regimes of behaviour, depending on the oxygen activity [140]. Under strongly reducing conditions, the concentration of defects related to the incorporation of a dopant (extrinsic defects) is smaller than those associated with a deviation from stoichiometry (intrinsic defects). Consequently, the defect disorder in this regime reflects that of undoped TiO_2. The predominant ionic defects are either doubly charged oxygen vacancies or triply charged titanium interstitials depending upon the donor concentration.

In a first reduced regime, defect disorder is dominated by the electronic compensation of the incorporated donor species. The incorporation can be written in this way:

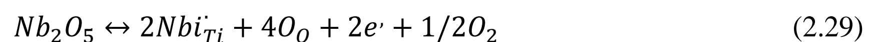

$$Nb_2O_5 \leftrightarrow 2Nbi^{\cdot}_{Ti} + 4O_O + 2e' + 1/2O_2 \quad (2.29)$$

where O_O is an oxygen ion on a normal lattice site, $Nbi^{\cdot}_{Ti}$ is a Nb atom replacing a titanium atom, V''''_{Ti} is a titanium vacancy. In this regime, the concentration of electrons is independent of oxygen pressure.

In a second reduced regime, defect disorder is dominated by the ionic compensation of the donor, via the formation of titanium vacancies. The incorporation of niobium can thus be described by the following equilibria condition:

$$2Nb_2O_5 \leftrightarrow 4Nbi^{\cdot}_{Ti} + V''''_{Ti} + 10O_O \quad (2.30)$$

In an oxidized regime, defect disorder is once again determined by intrinsic defect species, and behaviour reflects that of undoped TiO_2. For a donor-doped metal oxide, the observation of this regime requires the imposition of very high oxygen activity.

Nowotny [140] has proposed a defect disorder diagram for both undoped- and Nb-doped TiO_2 are represented in terms of electrical conductivity data as a function of oxygen activity at 1273 *K*, shown in Figure 2.10 *(b)*. The plot indicate that the $p(O_2)$ range in the strongly reduced regime for un-doped TiO_2 is

much wider than that for Nb-doped TiO_2, the later depending on Nb concentration. Oxidation of undoped TiO_2 results in the transition to reduced regime and to the oxidised regime. The $p(O_2)$ range in the strongly reduced regime for Nb-doped TiO_2 is very narrow. Oxidation of Nb-doped TiO_2 results in the transition to the reduced regime I in which the electrical conductivity is independent of $p(O_2)$, and, ultimately, to the reduced regime II.

It was shown that TiO_2 exhibits a complex defect disorder, involving a number of intrinsic point defects, as well as extrinsic defects. The properties of TiO_2 may be enhanced through the imposition of an optimized combination of the individual lattice species. Oxygen activity is closely related to defect disorder of TiO_2 and the related properties.

2.4 Fundamentals of ZnO

Zinc oxide is a II-VI wide band-gap (~3.4 *eV*) semiconductor which, due to its remarkable properties, has been subject of intensive research in the last decades [151-154]. Zinc oxide (ZnO) has been used in many fields over the years, from rubber and concrete industries to medicine and cosmetics. More recently, ZnO has been implemented in TCO applications, such as solar cells [155], liquid crystal displays (LCDs), or energy saving/heat protecting windows [156].

Other advantages of ZnO are the resistance to high energy radiation, which makes it suitable for space applications, as well as the stability to wet chemical etching, which can be exploited for the fabrication of small size devices. Moreover, the high exciton binding energy (60 *meV*) makes it a strong candidate for UV light emitters. Zinc oxide also proved to be a promising gas sensor, due to the reversible changes encountered by its surface conductivity upon exposure to different gases [157-159]. Ferromagnetism was obtained by doping zinc oxide with various transition metals, such as Mn, Co, V, Sc, Ti, Ni, Cr, Fe or Cu. The ZnO nanostructures can be used in (nano) sensors [160], field effect transistors (FETs) [161], lasing [162], hybrid solar cells [163], or for manufacturing AFM cantilevers [164]. Zn is more abundant than In and Sn and less toxic than Cd, which makes ZnO a desired alternative for ITO.

One of the most popular growth techniques for early ZnO investigations was sputtering (dc sputtering, rf magnetron sputtering, and reactive sputtering). As compared to sol-gel and chemical-vapor deposition the magnetron sputtering was a preferred method because of its low cost, simplicity, and low operating temperature.

Recently, some researchers have drawn attention to the role of hydrogen in the electronic properties of ZnO [165,166]. H-related defects other than oxygen vacancy (V_O) and Zn interstitial (Zn_i) result in the *n*-type conduction of undoped ZnO thin films. Experimental results have confirmed that hydrogen is an effective doping element for improving the conductivity of ZnO films [167-171].The behavior of hydrogen in ZnO is highly unusual. In almost all semiconductors studied to date, interstitial hydrogen has been found (theoretically as well as experimentally) to act as an amphoteric impurity [172]. This amphoteric behavior precludes hydrogen from acting as a dopant, i.e. from being a source of conductivity.

In this section the physical, electrical, electronic and optical properties of ZnO are discussed. Later the adsorption of H_2 and H_2O at ZnO polar surfaces and the effect of native point defects and hydrogen as donor impurity on the properties of ZnO are described.

2.4.1 Crystal structure of ZnO

The possible crystal structures of ZnO are hexagonal wurtzite, cubic zinc blende, and cubic rocksalt. At ambient conditions, ZnO crystallizes in the hexagonal wurtzite-type structure, shown in Figure 2.11 *(a)*. The zinc-blende structure of ZnO can be stabilized only by growth on cubic structure substrates, and the rocksalt (*NaCl*) structure may be obtained at relatively high pressures.

In Table 2.3 a summary of the most important physical properties of wurtzite structure of ZnO is given.

Table 2.3 Properties of wurtzite ZnO [173]

Lattice parameters at 300 K	c=5.2069 $Å$, a=3.2495 $Å$ u=0.345, c/a=1.602
Density (solid)	5.606 g/cm^3
Melting point	1975°C
Refractive index	2.008
Energy gap at 300 K	~3.4 eV, direct
Electron mobility at RT for lightly doped n-type ZnO	200 cm^2/Vs
Electron effective mass	$0.24m_0$

The wurtzite structure has a hexagonal unit cell with two lattice parameters, a and c, in the ratio of $\frac{c}{a} = \sqrt{8/3} = 1.6333$ and belongs to the space group of C_{6v}^4 or $P6_3mc$. The structure is composed of two interpenetrating hexagonal-close-packed (hcp) sublattices, each of which consists of one type of atom displaced with respect to each other along the threefold c-axis by the amount of u =3/8=0.375 (in an ideal wurtzite structure) in fractional coordinates (the u parameter is defined as the length of the bond parallel to the c axis, in units of c). Each sublattice includes four atoms per unit cell and every atom of one kind (group-II atom) is surrounded by four atoms of the other kind (group VI), or vice versa, which are coordinated at the edges of a tetrahedron.

In a real ZnO crystal, the wurtzite structure deviates from the ideal arrangement, by changing the c/a ratio or the u value. It should be pointed out that a strong correlation exists between c/a ratio and the u parameter. When the c/a ratio decreases, the u parameter increases in such a way that those four tetrahedral distances remain nearly constant through a distortion of tetrahedral angles due to long-range polar interactions. These two slightly different bond lengths will be equal if the following relation holds:

$$u = \left(\frac{1}{3}\right)\left(\frac{a^2}{c^2}\right) + \frac{1}{4} \quad (2.31)$$

Since the *c*/*a* ratio also correlates with the difference of the electronegativities of the two constituents in the structure, components with the greatest differences show the largest departure from the ideal *c*/*a* ratio.

The deviation from the ideal values has been related to several factors including: lattice stability, strain, ionicity and carrier density. The presence of defects such as Zn antisites, oxygen vacancies, impurities and dislocations also have been known to contribute to a deviation in the lattice parameter of ZnO. The deformation of ZnO lattice with applied pressure has also been observed. The tetrahedral coordination in ZnO results in a non-central symmetric structure.

Another important characteristic of ZnO structure is that is having polar surfaces. A formal definition for polar surfaces can be obtained by considering the projection of the dipole moment related to the bulk unit cell (which is different from zero because of the non-center symmetric structure) on the surface normal. If, for a given surface orientation, this projection is non-zero, the term ''polar surface'' is used. The presence of a finite dipole moment per surface unit cell for polar surfaces gives rises to an electrostatic field which scales with the thickness of the crystal. As a result, the ''ideal'' surface geometry of a polar surface obtained by a simple truncation of the bulk structure with ions of the same formal charge as in the bulk is not stable.

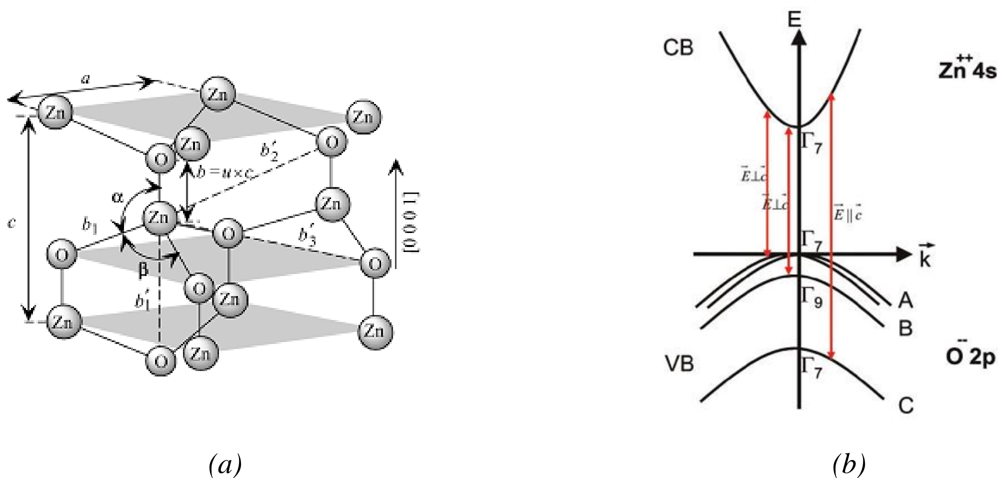

(a) (b)

Figure 2.11 *(a)* Schematic representation of a wurtzitic ZnO structure having lattice constants *a* in the basal plane and *c* in the basal direction; *u* parameter is expressed as the bond length or the nearest-neighbor distance *b* divided by *c* (0.375 in ideal crystal), and α and β (109.47° in ideal crystal) are the bond angles, *(b)* Schematic of the band structure of ZnO.

In wurtzite ZnO, besides the most stable polar plane [0001], two non-polar surfaces [$10\bar{1}0$], [$11\bar{2}0$] and one polar surface [$000\bar{1}$] exist in the structure [151]. The [0001] plane is different from [$000\bar{1}$] plane, where [0001] corresponds to the bond direction from anion to cation along the *c*-axis. It is a common practice to refer the polarity as Zn polarity if the bonds are directed from Zn to O in the *c*-axis and O polarity for the reverse condition.

These stability issues of polar surfaces were first discussed by Tasker, and the algorithm used to decide whether a surface of an ionic crystal is instable or not is referred to as Tasker's rule [174].There are different possibilities to remove this instability. The first one is a charge transfer between the two different polar

surfaces without a significant rearrangement of the geometric positions. The second one is a reconstruction changing the geometry of the surface. The third one involves the adsorption of charged adparticles. This instability of the polar surfaces of ionic crystals scales with the size of the specimens so that, in principle, polar surfaces of very small oxide particles could be stable. For macroscopic samples, however, the electrostatic field referred to above becomes so large that either the electronic or geometric structure of the surface has to change. Most polar metal oxides surfaces undergo a major structural rearrangement, the precise nature of which strongly depends on the particular metal oxide [175].

Surprisingly, most previous studies carried out for the two polar ZnO surfaces, the O-terminated O–ZnO surfaces (or ZnO $[000\bar{1}]$) as well as the Zn-terminated Zn–ZnO surface (or ZnO [0001]), have failed to observe any reconstruction [176-178]. This apparent absence of a reconstruction of the two polar ZnO surfaces, O–ZnO and Zn–ZnO, has led very early [179] to the suggestion that in case of ZnO a stabilization-mechanism different from that seen for other oxide surfaces comes into play. Instead of a removal or repositioning of the zinc or oxygen ions it was proposed that there is a transfer of charge between the Zn–ZnO and the O–ZnO surface. Such a charge transfer would lead to the build up of an electric field which could in principle compensate the electric field giving rise to the electrostatic instability intrinsic to a polar surface. A transfer of electrons from the O–ZnO face to the Zn–ZnO face will also lead to the formation of partially filled surface bands, a situation which is quite common for polar semiconductor surfaces [180]. As a consequence of the presence of partially filled surface states, both polar surfaces would in fact be metallic. Such a charge transfer mechanism has so far not been observed experimentally for any oxide surface.

Donor or acceptor impurities can be introduced in ZnO lattice [154,181]. The group-III impurities *B*, *Al*, *Ga* and *In* when substituted on the Zn site act as shallow donors in ZnO. The extra valence electron of these impurities is loosely bound and occupies effective-mass states near the conduction band minimum at low temperatures. As the temperature rises this extra electron is excited to the conduction band and is free to move. Fluorine has one more electron than O, and when inserted on the O site it acts as a shallow donor in ZnO.

Lithium (*Li*) may behave both as a donor and as an acceptor in ZnO [182]. The donor behavior arises when *Li* occurs as an interstitial impurity; the acceptor behavior is exhibited when *Li* substitutes on a Zn site. Despite the size difference between *Li* and *Na*, it is expected that *Na* also shows an amphoteric behavior, acting as an acceptor when substituting for Zn and as a donor when occupying interstitial sites.

Copper (*Cu*) acts as a deep acceptor in ZnO. It can be used to reduce the carrier concentration in *n*-type ZnO by acting as a compensating center [183].*Cu* has been mentioned as the source of green luminescence [184]. It is likely that *Cu* is one of the causes, noting that not all samples that exhibit green luminescence are shown to contain *Cu* impurities. Nitrogen is thought to be the most suitable *p*-type dopant due to both atomic-size and electronic-structure considerations.

2.4.2 Electronic states of ZnO

The band structure of ZnO was first calculated in 1969 using Greens function and followed up soon after with experimental results from x-ray induced photo-emission spectroscopy and UV photoemission measurements. The results were controversial and remained contradictory for many years [151,185]. More recently, advances in the computational methods allowed for a most detailed calculation of the ZnO band structure, using the linear muffin tin orbital method [186].

The band structure of ZnO is shown schematically in Figure 2.11 *(b)*. The conduction band (CB) with symmetry Γ_7 contains the empty 4*s* levels of Zn^{++}. The valence band (VB) contains the occupied *2p* levels of O^{-}. The VB is split by the hexagonal crystal field and by spin orbit coupling into three, two fold degenerate sub-VBs, which are called from top to bottom A, B and C VB in all wurtzite type semiconductors. The usual ordering is $A\Gamma_7$, $B\Gamma_9$ and $C\Gamma_7$.

2.4.3 Electrical and optical properties of ZnO

The dominating *n*-type character in ZnO has often been attributed to the presence of intrinsic native defects such as O vacancies (V_O) and/or Zn interstitials (Zn_i). However, there is still a great deal of controversy over which of these two defects is the dominant cause of the *n*-type character [187]. Some researchers have suggested that V_O are deep-level states [188] and are therefore not likely to be the dominant cause of *n*-doping in un-intentionally-doped ZnO films. Recently, some researchers have drawn the attention to the role of hydrogen in the electronic properties of ZnO. Hydrogen is usually considered the main cause of *n*-type doping in as-grown, undoped ZnO films [189].

The electron concentration, caused by native point defects and/or hydrogen was reported to be 10^{16}-10^{18} cm^{-3}. For increasing the electron concentration in ZnO, required for degenerately doped ZnO in transparent conducting electrodes, doping with foreign elements is necessary, and the donors can come either from group III, i.e., Al, B, Ga, In, Sn, or from group VII, such as F, Br, Cl. If these atoms are incorporated substitutionally at the Zn and O site, respectively, then they can act as shallow donors and lead to electron concentrations in the order of 10^{21} cm^{-3}.

The mobility in good bulk samples, epilayers or nanorods is about 200 to 500 cm^2/Vs at room temperature. It goes with decreasing temperature through a maximum of 1000 cm^2/Vs around 100 *K* and decays at lower temperature due to scattering with (ionized) impurities. If scattering at grain boundaries comes additionally into play, e.g. in pressed and sintered samples or in epilayers consisting of small grains, the mobility may be significantly reduced, at RT to values as low as 10 cm^2/Vs or even below.

ZnO is a wide band gap semiconductor. The large optical band-gap of ZnO makes it highly transparent to visible light. Defects that affect film electrical properties such V_O, Zn_i and hydrogen incorporation are reported to affect also the film transparency. It is the deviation from stoichiometry as a result of the presence of these intrinsic native point defects that makes ZnO semiconducting.

The band gap of ZnO can be tuned via divalent substitution on the zinc site. For example, cadmium substitution can lower the bandgap to 3.0 *eV* [190] while magnesium alloying can be used to raise the band-gap up to 4 *eV* [191].

2.4.4 Hydrogen and water adsorption on ZnO polar surfaces

On the Zn-terminated [0001] polar surface of ZnO, only Zn-atoms are exposed on a substrate with an ideal (1x1)-structure. As a result, one would expect that the interaction of H atoms with this surface is the weakest among the differently terminated ZnO surfaces, since the binding energy of Zn–H bonds should be considerably weaker than that of O–H bonds. An experimental study using He atom scattering has revealed that, as one might have expected, exposure of this surface to H leads to the formation of a (1x1) overlayer consisting of Zn-hydride species [192]. The presence of OH-species after exposure to H-atoms was observed with XPS (a shoulder at the high-energy side of the O1s XPS peak) and He-TDS [192,193]. The observation of OH-species on the Zn–ZnO surface implies a major restructuring in the surface region and a subsequent subsurface diffusion of H-atoms [192].

Experimentally it was observed that fully hydroxylated O–ZnO surfaces are very stable surfaces exposing to H [194]. In contrast to the experimental findings, general theoretical arguments about the stability of polar surfaces [174,179,180,195] suggest that a perfect H(1x1) OH-terminated O–ZnO surface is instable. These considerations reveal that the structure of the O-terminated polar surface of ZnO, both for the clean and the H covered surface, is not yet fully understood, more work is required to obtain a consistent description of this surface and in particular of its electronic structure. Recently, also results from IR spectroscopy for this H(1x1) O–ZnO surface have become available. The IR-data for a ZnO single crystal substrate studied by Schiek *et al.* [196] reveal a band at 3572 cm^{-1} which is assigned to the stretch frequencies of surface OH species. It is very interesting to note that this frequency does not quite agree with the previous results obtained for ZnO powders exposed to hydrogen, where an OH-induced band at around 3510 cm^{-1} was observed [197].

Exposing a clean, (1x3) – reconstructed O–ZnO surface (an ordered array of O-vacancies which renders the surface a very high reactivity) to water results in the formation of the H(1x1) phase [194,198]. This dissociative adsorption of water already occurs at temperatures as low as 200 *K* indicating that the activation barrier for this dissociation is either very low or completely absent [198]. When heating the surface to temperatures above 550 *K* the H(1x1) O–ZnO-surface is transformed back to the (1x3)-phase, presumably via desorption of H_2O and H_2. In experiments where surfaces resulting from the adsorption of H atoms on the clean (1x3) O–ZnO surface and from H_2O adsorption were compared no differences could be observed. This is a surprising finding, since the atomistic mechanism must be quite different in the two cases. In case of the H_2O adsorption additional oxygen atoms are deposited on the surfaces which are most likely used to fill up the oxygen vacancies in the (1x3)-structure, whereas in the case of H-atom adsorption no additional oxygen is added to the surface. Formally, three H-atoms and one O-atom are needed per unit-cell to transform the

(1x3) O–ZnO surface to the hydroxyl-terminated H(1x1) O–ZnO. Since there are only two H-atoms contained in one H_2O-molecule, an additional source of H-atoms is needed, e.g. water molecules dissociating at defect sites (step edges, additional vacancies). Another possibility is the presence of a residual H-atom per unit cell of the (1x3) O–ZnO surface.

The adsorption of H_2O on the H(1x1) O–ZnO surface has been studied by Jacobi [199] and concluded that on the O–ZnO surface of Zn-doped specimens H_2O molecules adsorb dissociatively and interact more strongly with Zn sites which are present as a result of the doping process than with the oxygen sites. This result was confirmed ten years later by Zhang, Ludviksson and Campbell [200]. In He-atom scattering (HAS) experiments performed by Schiek *et al.* the presence of two different, ordered water adlayers on the HO–ZnO surface was observed [196].

2.4.5 Native point defects and hydrogen in ZnO

The native point defects in ZnO are oxygen vacancies, zinc vacancies, zinc interstitial, zinc antisites, oxygen antisites, and oxygen interstitials.

O vacancies and other native point defects are unlikely to be the predominant cause of unintentional *n*–type conductivity in ZnO [201]. O vacancy is a deep donor, while Zn interstitials are unstable at room temperature. Zn vacancies are present as compensating acceptors in *n*-type ZnO. Other native defects, such as Zn antisites, O antisites, and O interstitials, have high formation energies. Under normal conditions, they are probably not present in large concentrations, although O interstitials may be important in O self-diffusion [202].

The Zn interstitials are shallow donors [203], confirmed experimentally and theoretically with first principles calculations. They have high formation energies in *n*-type ZnO and are fast diffusers with migration barriers as low as 0.57 eV [202]. Therefore, Zn interstitials are not stable at room temperature [204].

First-principles calculations consistently show that the O vacancy is a deep donor. The position of O vacancy level was calculated to be 0.5–0.8 eV above the valence-band maximum [205]. Theorists disagree on whether O vacancies should be present in *n*-type ZnO. For example, Lany and Zunger [206] predicted concentrations of $\sim 10^{17}\ cm^{-3}$ or higher, whereas Janotti and Van de Walle [202] claimed that the formation energy is much too high for significant concentrations to exist at equilibrium.

Zn vacancies are double acceptors. First-principles calculations find the acceptor levels to be 0.1–0.2 and 0.9–1.2 *eV* above the valence-band maximum, respectively [201,202]. Zn vacancies may account for the green luminescence in some ZnO samples.

Experimental results on muonium implanted into ZnO [207] and electron-nuclear resonance measurements [208] on lightly doped *n*-type ZnO provided evidence that H is a shallow donor. In order to determine the microscopic structure of H donors, IR spectroscopy was used to measure O–H vibrational modes arising from these complexes [209].

H can be introduced in two ways in ZnO crystal structure: substitutional or interstitial. Two models were proposed by Van de Walle for *interstitial H* donors [165], shown in Figure 2.12. In one model, H is in the antibonding ($AB_{\perp}$) orientation, attached to a host O atom and pointing away from the Zn–O bond. Another model is the bond-centered ($BC_{\parallel}$) configuration, where H sits between the hosts Zn and O. By measuring the pressure and polarization dependence of the O–H vibrational mode, and comparing it to the predictions of first-principles calculations [210], Jokela and McCluskey [211] attributed an IR peak at 3326 cm^{-1} to H donors in the $AB_{\perp}$ configuration. Muon-implantation experiments and ab initio calculations [212] indicated that H donors should reside in the $BC_{\parallel}$ configuration, not the $AB_{\perp}$ configuration. Experiments by Lavrov *et al.* revealed a peak at 3611 cm^{-1}, attributed to H in the $BC_{\parallel}$ configuration [212].

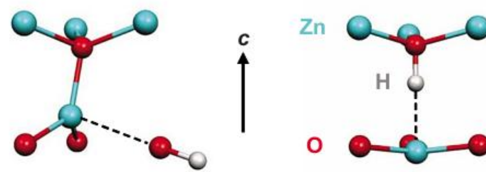

Figure 2.12 Models for interstitial H donors in ZnO. Left: anti-bonding ($AB_{\perp}$) configuration. Right: bond-centered ($BC_{\parallel}$) configuration. The dashed lines indicate broken Zn–O bonds.

The IR peaks at 3326 and 3611 cm^{-1} are unstable, decaying at room temperature with a time constant of several weeks [211]. They form a species of "hidden hydrogen" that remains in the crystal. Shi et al. [213] proposed that the H donors combine to form H_2 molecules, which are electrically neutral and nearly invisible to IR. When the crystal is reheated, the H_2 molecules dissociate and form H donors again. Experimental verification for H_2 molecules in ZnO was achieved using low-temperature Raman spectroscopy [214]. Theoretical work by Karazhanov and Ulyashin [215] suggests that two interstitial H atoms can form a H_2^* defect, where one H attaches to an O while the other attaches to a Zn. Unlike H_2 molecules, however, the H_2^* defect should have clear IR signatures. Until now, H_2^* has not been observed experimentally in ZnO.

First-principles calculations by Janotti and Van de Walle [216] showed that H can occupy an O *substitutional site* and act as a shallow donor. One can think of "substitutional H" as an O vacancy with a single H atom near the center. The predicted vibrational frequency is ~800 cm^{-1}. The mode has not been seen, perhaps because free-carrier and two-photon absorptions are too strong in that region of the IR spectrum. Unlike interstitial H, substitutional H is stable [217]. This makes it a strong candidate for H-related donors in as-grown ZnO [208]. The calculated electron density suggests that H bonds equally with its four Zn neighbours [216].

2.5 Concluding remarks

Coexistence of transparency and conductivity in semiconductors is possible if the band gap is large enough to avoid visible light absorption (~3 *eV*). Intentional doping creates free carriers (electrons or holes) which are responsible for the conductivity. Electron densities are in general high for *n*-type TCOs (order 10^{20} cm^{-3}) resulting in degenerate electron systems. The electrical mobility is dominated by scattering mechanisms, strongly related to the electron concentration. All electronic scattering contributions together influence the mobility, and determine the upper limit of conductivity. For single-crystalline materials the ionized impurity scattering is considered to be the most important. Though, as the structural nature of the thin film decrease, the contribution of grain boundaries becomes ever more important in polycrystalline films. The electrical conductivity of common *n*-type TCO materials is around 10^{-4} Ωcm, whereas the optical transmission can be as high as 90% in the visible range. Many deposition methods can be used to grow TCOs, and varying performances are reported. Each deposition method has its own influence on the intrinsic properties as thin film structure and composition. It is these properties and not the deposition method by itself determining the electrical and optical performance of the TCO.

2.6 References

1. K.L. Chopra, S. Major, D.K. Pandya, Thin Solid Films, 102 (1) 1983, 1-46
2. T. Ashida, A. Miyamura, Y. Sato, T. Yagi, N. Taketoshi, T. Baba, and Y. Shigesato, J. Vac. Sci. Technol., A 25, 1178 (2007)
3. H.L. Hartnagel, A.L. Dawar, A.K. Jain and C. Jagadish, *Semiconducting Transparent Thin Films* (Institute of Physics Publishing, Bristol and Philadelphia, 1995)
4. C. G. Granqvist, Solar Energy Materials & Solar Cells 91 (2007) 1529–1598
5. G. J. Exarhos, X.D. Zhou, Thin Solid Films 515 (2007) 7025–7052
6. R. G. Gordon, MRS Bull., 25 (2000) 52-57
7. H. T. Grahn, *Introduction to Semiconductor Physics* (World Scientific, 1999)
8. N. F. Mott, Proc. Phys. Sot. A 62, 416 (1949); Phil. Mag. 6, 287(1961); Adv. Phys. 16, 49 (1967)
9. W.B. Joyce and R.W. Dixon, Appl. Phys. Lett. 31, 354 (1977)
10. D.S. Ginley *et al*, *Handbook of transparent conductors*, 2010, Springer, chapter 3
11. D.H. Zhang and H.L. Ma, Applied Physics A: Materials Science & Processing 62, Number 5, 487-492 (1996)
12. S. Ghosh, A. Sarkar, S. Chaudhuri, and A.K. Pal, Thin Solid Films 205, 64–68 (1991)
13. H. Kim, C. M. Gilmore, J. S. Horwitz, A. Pique, H. Murata, G. P. Kushto, R. Schlaf, Z. H. Kafafi, and D. B. Chrisey, Applied Physics Letters 76, 259–261 (2000)
14. M.W.J. Prins, D.O. Grosse-Holz, J.F.M. Cillessen, and L.F. Feiner, Journal of Applied Physics 83, 888–893 (1998)
15. R.L. Petritz, Phys. Rev. 104, 1508 (1956)
16. J.Y.W. Seto, J. Appl. Phys. 46, 5247 (1975)
17. E. Shanthi, A. Banerjee, K.L. Chopra, Thin Solid Films, 88, 93 (1982)
18. E. Shanthi, A. Banerjee, V. Dutta, K.L. Chopra, J. Appl. Phys. 53, 1615 (1982)
19. E. Shanthi, V. Dutta, A. Banerjee, K.L. Chopra: J. Appl. Phys. 51, 6243 (1980)
20. T. Pisarkiewicz, K. Zakrzewska, E. Leja, Thin Solid Films 174, 217 (1989)
21. J. Bruneaux, H. Cachet, M. Froment, A. Messad, Thin Solid Films 197, 129 (1991)
22. J.J. PH Elich, E.C. Boslooper, H. Haitjema, Thin Solid Films 177, 17 (1989)
23. D.H. Zhang: J. Phys. D 28, 1273 (1995)
24. P.S. Kireev, *Semiconductor Physics* (Mir, Moscow 1978) p. 442
25. P. Drude, Ann. Phys. 3, 369 (1900)
26. J.C. Manifacier, M. De Murcia, J.P. Fillard, E. Vicario, Thin Solid Films 41, 127 (1977)
27. J. Tauc, R. Grigorovici and A. Vancu, Phys. Status Solidi 15, 627 (1966)
28. E. Burstein, Phys. Rev. Lett. 93, 632 (1954)
29. N.W. Ashcroft and N.D. Mermin, *Solid State Physics* (Saunders College Publishing, 1976)
30. P.D.C. King and T.D. Veal, J. Phys.: Condens. Matter 23 (2011) 334214
31. A. Janotti and C.G.Van de Walle, Rep. Prog. Phys. 72 (2009) 126501
32. C. Kilic and A. Zunger, Appl. Phys. Lett., Vol. 81, No. 1, 2002
33. A. Zaleska, Recent Patents on Engineering 2008, 2, 157-164
34. Ü. Özgür *et al.*, J. Appl. Phys. 98, 041301 (2005)
35. D.B. Fraser and H.D. Cook, J. Electrochem. Soc. 119, 1368, 1972
36. G. Haacke, J. Appl. Phys. 47, 4086, 1976
37. P.A. Iles and S.I. Soclof, Proceedings of the 12th IEEE Photovoltaic Conference, November 1976 (unpublished), p. 978
38. V.K. Jain and A.P. Kulshreshtha, Solid Energy Mater. 4, 151(1981)
39. C.G. Granqvist and A. Hultaker 2002 Thin Solid Films 411 1–5
40. L. Castaneda, Materials Science and Applications, 2011, 2, 1233-1242
41. T. Minami, Semicond. Sci. Technol. 20 (2005) S35–44
42. Y. Furubayashi, T. Hitosugi, Y. Yamamoto, K. Inaba, G. Kinodo, Y. Hirose, T. Shimada and T. Hasegawa, Appl. Phys. Lett. 86, 252101 (2005)
43. W. Zhang, G. Zhu, L. Zhi, H. Yang, Z. Yang, A. Yu, H. Xu, Vacuum (2011)
44. J.-H. Wi, J.-C. Woo, C.-I. Kim, Thin Solid Films 519 (2011) 6824–6828
45. K.J. Patel, M.S. Desai, C.J. Panchal, J. Mater. Sci.: Mater. Electron. (2011) 22:959–965
46. M. Gabas *et al.*, Solar Energy Materials & Solar Cells 95 (2011) 2327–2334

47. V.D. Falcao *et al.*, Prog. Photovolt: Res. Appl.2011; 19:149–154
48. W. Kim,W.J. Maeng, M.-K. Kim, and H. Kim, Journal of The Electrochemical Society, 158 (8) D495-D499 (2011)
49. Z. Zhang, C. Bao, W. Yao, S. Ma, L. Zhang, S. Hou, Superlattices and Microstructures 49 (2011) 644–653
50. R. Jaramillo, S. Ramanathan, Solar Energy Materials & Solar Cells 95 (2011) 602–605
51. K. Jung, W. K. Choi, S. J. Yoon, H. J. Kim, J. W. Choi, Ceramics International 38S (2012) S605-608
52. E. Nam, Y.-H. Kang, D. Jung, Y. S. Kim, Thin Solid Films 518 (2010) 6245-6248
53. G. Goncalves *et al.*, Plasma Process. Polym. 2011, 8, 340–345
54. P.B. Nair *et al*, Applied Surface Science 257 (2011) 10869– 10875
55. C.M. Maghanga *et al.*, Solar Energy Materials & Solar Cells 94 (2010) 75–79
56. R. Konenkamp, Physical Review B, 61, 16, 2000, 11057-11064
57. T. Ishida, M. Okada, T. Tsuchiya, T. Murakami, M. Nakano, Thin Solid Films 519 (2011) 1934–1942
58. B.S. Tosun *et al.*, Thin Solid Films 2011
59. A. Klein *et al.*, Materials 2010, 3, 4892-4914
60. J. Montero, C. Guillen, J. Herrero, Solar Energy Materials & Solar Cells 95 (2011) 2113–2119
61. Q. Tang, Y. Tong, W. Hu, Q. Wan, T. Bjørnholm, Adv. Mater. 2009, 21, 4234–4237
62. W. Clark and P. Broadhead, Journal of Physics C 3 (1970), 1047
63. M. Dekker, *Practical design and production of optical thin films*, R. R. Willey, New York (1996)
64. R. E. Hummel and K. H. Guenther, *Handbook of optical properties*, vol. 1: *Thin films for optical coatings*, CRC, (1995)
65. M. Schiavello, *Heterogeneous Photocatalysis*, John Wiley & Sons, New York (1997)
66. D. Dumitriu, A.R. Bally, C. Ballif, V.I. Parvulescu, P.E. Schmid, R. Sanjinés, and F. Lévy, Preparation of Catalysts VII (1998), 485
67. P. Bonhôte, J.E. Moser, N. Vlachopoulos, L. Walder, S.M. Zakeeruddin, R. Humphry-Baker, P. Pechy, and M. Graetzel, Journal of Chemical Society, Chemical Communication (1996), 1163
68. M. Grätzel and K. Kalyanasundaram, Current Science 66 (1994), 706
69. K. Tennakone, G.R.R.A. Kumara, I.R.M. Kottegoda, V.P.S. Perera, and G.M.L.P. Aponsu, Journal of Physics D: Applied Physics 31 (1998), 2326
70. V.E. Henrich and P.A. Cox, *The surface science of metal oxides*. 1st ed., Cambridge Unversity Press, Cambridge (1994)
71. J.F. Banfield, B.L. Bischoff, and M.A. Anderson, Chemical Geology 110 (1993), 211
72. P.Y. Simons and F. Dachille, Acta Cryst. 23 (1967), 334
73. J. Tang and J. Endo, J. Am. Ceram. Soc. 76 (1993), 796
74. J.S. Olsen, L. Gerward, and J.Z. Jiang, Journal of Physics and Chemistry of Solids 60 (1999), 229
75. M. Latroche, R. Brohan, R. Marchand, and M. Tournoux, J. Solid State Chem. 81 (1989), 78
76. J. Akimoto, Y. Gotoh, Y. Oosawa, N. Nonose, T. Kumagai, and K. Aoki, J. Solid State Chem. 113 (1994), 27
77. R. Marchand, R. Brohan, and M. Tournoux, Mat. Res. Bull. 15 (1980), 1129
78. *PDF-database*. JCPDS, International centre for diffraction data (ICDD), 1601 Park Lane, Swarthmore, PA 19081, USA
79. S.C. Abrahams and J.L. Bernstein, J. Chem. Phys. 55 (1971), 3206
80. M. Horn, C.F. Schwerdtfeger, and E.P. Meagher, Zeitschrift für Kristallographie 136 (1972), 273
81. G.V. Samsonov, *The Oxide Handbook* (IFI/Plenum, new York 1982)
82. V.E. Henrich, Rep. Prog. Phys. 48 (1985), 1481
83. N. Hosaka, T. Sekiya, M. Fujisawa, C. Satoko, and S. Kurita, Journal of Electron Spectroscopy and Related Phenomena 78 (1996), 75
84. D.C. Cronemeyer, Phys. Rev. 87 (1952), 876
85. L. Forro, O. Chauvet, D. Emin, L. Zuppiroli, H. Berger, and F. Lévy, J. Appl. Phys. 75 (1994), 633
86. M. Grätzel and F.P. Rotzinger, Chemical Physics Letters 118 (1985), 474
87. H. Tang, Thèse EPFL N° 1311, Lausanne (1994)
88. Z.M. Jarzebski, *Oxide Semiconductors*. Permagon Press, (1973)
89. R.G. Breckenridge and W.R. Hosler, Phys. Rev. 91 (1953), 793
90. H. Tang, K. Prasad, R. Sanjinés, P.E. Schmid, and F. Lévy, J. Appl. Phys. 75 (1994), 2042
91. G.A. Acket and J. Volger, Physica 32 (1966), 1680
92. H.P.R. Frederikse, J. Appl. Phys. suppl. 32 (1961), 2211

93. R.W.G. Wyckoff, *Crystal Structures Handbook*. 2nd ed., Interscience Publishers, New York (1963)
94. R. Debnath and J. Chaudhuri, Journal of Materials Research, vol. 7, no. 12, pp. 3348–3351, 1992
95. F.C. Gennari and D.M. Pasquevich, Journal of the American Ceramic Society, 82, no. 7, pp. 1915–1921, 1999
96. M.K. Akhtar, S.E. Pratsinis, and S.V.R. Mastrangelo, Mat. Res. Symposium Proceedings, 271, 951–956, 1992
97. C.N.R. Rao, A. Turner, and J.M. Honig, The Physics and Chemistry of Solids, 11, 173–175, 1959
98. J.M.G. Amores, V.C. Escribano, and G. Busca, Journal of Material Chemistry, vol. 5, no. 8, pp. 1245–1249,1995
99. D. Mardare and P. Hones, Materials Science and Engineering B, vol. 68, pp. 42–47, 1999
100. D. Bersani, R. Capelletti, P.P. Lottici, G. Gnappi, and A. Montenero, Mat. Sci. Forum, 239-241, 87–90, 1997
101. K. Kenevey *et al.*, Key Engineering Materials, 118-119, 303–310, 1996
102. Y. Iida and S. Ozaki, Journal of the American Ceramic Society, vol. 44, no. 3, pp. 120–127, 1961
103. R.D. Shannon and J.A. Pask, Journal of the American Ceramic Society, vol. 48, no. 8, pp. 391–398, 1965
104. U. Diebold, Surface Science Reports 48 (2003), 53
105. M. Yokozawa, H. Iwasa, and I. Teramoto, Japanese Journal of Applied Physics, vol. 7, pp. 96–97, 1968
106. P. Lobl, M. Huppertz, and D. Mergel, Thin Solid Films, vol. 251, pp. 72–79, 1994
107. A. Bendavid, P.J. Martin, and H. Takikawa, Thin Solid Films, vol. 360, pp. 241–249, 2000
108. H. Tang, H. Berger, P.E. Schmid, and F. L´evy, Solid State Communications, vol. 92, no. 3, pp. 267–271, 1994
109. L. Kihlborg and I. Olovsson, Acta Cryst. A 53 (1997), 103
110. H.K. Ardakani, Thin Solid Films 248 (1994), 234
111. P.G. Wahlbeck and P.W. Gilles, Journal of the American Ceramic Society 49 (1966), 180
112. S. Sugano, Y. Tanabe, and H. Kamimura, *Multiplets of transition-metal ions in crystals* (Academic Press, new York and London) 1970 p. 6
113. N. Tsuda, K. Nasu, A. yanase, and K. Siratori, *Electronic conduction in oxides* (Springer-Verlag, Berlin Heidelberg 1991) p. 5
114. V.N. Bogomolov, E.K. Kudinov, D.N. Mirlin, and Y.A. Firsov, Soviet Physics - Solid State 9 (1968), 1630
115. V.N. Bogomolov, Y.A. Firsov, E.K. Kudinov, and D.N. Mirlin, Physica Status Solidi 35 (1969), 555
116. P.A. Cox, *Transition Metal Oxides*. 1st ed., Clarendon press, Oxford (1992)
117. T. Sekiya, K. Ichimura, M. Igarashi, and S. Kurita, Journal of Physics and Chemistry of Solids 61 (2000), 1237
118. A.A. Bonapasta, F. Filippone, G. Mattioli and P. Alippi, Catalysis Today, 144 (2009), 177
119. S. Eriksen, P.D. Naylor and R.G. Egdell, Spectrochimica Acta 43A (1987) 1535
120. L.M. Liu, P. Crawford and P. Hu, Prog. Surf. Science 84 (2009) 155
121. C.A. Muryn, G. Tirvengadum, J.J. Crouch, D.R. Warburton, G.N. Raiker, G. Thornton and D.S.L. Law, J. Phys.: Condens. Matter 1 (1989) SB127
122. C.A. Muryn, P.J. Hardman, J.J. Crouch , G.N. Raiker, G. Thornton and D.S.L. Law, Surface Science 251-252 (1991) 747
123. R.L. Kurtz, R.S. Bauer, T.E. Msdey, E. Román and J. De Segovia, Surf. Sci. 218 (1989) 178
124. M.B. Hugenschmidt, L. Gamble and C.T. Campbell, Surf. Sci. 302 (1994) 329
125. E.V. Stefanovich and T.N. Truong, Chem. Phys. Lett. 299 (1999) 623
126. M.A. Henderson, Surf. Sci. Rep. 46 (2002) 1
127. M.A. Henderson *et al.*, Surf Sci 355 (1996) 151
128. D. Brinkley, M. Dietrich, T. Engel, P. Farrall, G. Gantner, A. Schafer, A. Szuchmacher, Surf Sci, 395 (1998) 292
129. I.M. Brookes, C.A. Muryn, G. Thornton, Phys Rev Lett, 87 (2001) 266103/1
130. R. Schaub, P. Thostrup, N. Lopez, E. Lægsgaard, I. Stensgaard, J.K. Nørskov, F. Besenbacher, Phys Rev Lett 2001, 87, 266104
131. J. Goniakowski, M.J. Gillan, Surf Sci, 350 (1996) 145
132. P.J.D. Lindan, N.M. Harrison, M. J. Gillan, Phys Rev Lett, 80 (1998) 762
133. M. Casarin, C. Maccato, J Phys Chem B, 102 (1998) 10745
134. M. Menetrey, M.A. Markovits, C. Minot, Surf Sci, 524 (2003) 49
135. H. Perron *et al.*, Surf Sci, 601 (2007) 518
136. H. Kamisaka, K. Yamashita, Surf Sci, 601 (2007) 4824
137. T.Z. Srnak, J.A. Dumesic, B.S. Clausen, E. Tornqvist, N.Y. Topsoe, J Catal, 135 (1992) 246
138. A. Vittadini, A. Selloni, F.P. Rotzinger, M. Gratzel, Phys Rev Lett, 81 (1998) 2954
139. I. Onal, S. Soyer, S. Senkan, Surf Sci, 600 (2006) 2457
140. J. Nowotny, L.R. Sheppard, T. Bak, M.K. Nowotny, Int. J. Hydrogen Energy, *32* (2007) 2630-2643
141. M.K. Nowotny, T. Bak, J. Nowotny, C.C. Sorrell, Phys. Status Solidi B 2005, *242*, R88-R90

142. M. K. Nowotny, L. R. Sheppard, T. Bak, and J. Nowotny, J. Phys. Chem. *C* 2008, *112,* 5275-5300
143. F.A. Kröger and H.J. Vink, *Solid State Physics*, vol. 3, p. 273–301 (1956)
144. P. Kofstad, *Nonstoichiometry, diffusion, and electrical conductivity in binary metal oxides*, Wiley-Interscience, 1972
145. T. Bak, J. Nowotny, M.K. Nowotny, J. Phys. Chem. B, 110 (2006) 21560-21567
146. D.C. Cronemeyer, Phys. ReV., 113 (1959) 1222
147. A.K. Ghosh, F.G. Wakim, Jr. R. R. Addiss, Phys. ReV., 184 (1969) 979
148. F.M. Hossain, G.E. Murch, L.R. Sheppard, J. Nowotny, AdV.Appl. Ceram. 106 (2007) 95
149. P.G. Shewmon, *Diffusion in Solids*, McGraw-Hill Book Co. Inc., New York, 1963
150. S. Mrowec, *Defects and Diffusion in Solids*, Chapter 2, Elsevier Scientific Publishing Co., Amsterdam, 1980
151. Ü. Özgür, Ya. I. Alivov, C. Liu, A. Teke, M. A. Reshchikov et al., J. Appl. Phys. 98, 041301 (2005)
152. C. Klingshirn, ChemPhysChem 2007, 8, 782–803
153. C. Klingshirn, R. Hauschild, H. Priller, M. Decker, J. Zeller, H. Kalt, Superlattices and Microstructures, 38, 4–6 (2005) 209-222
154. A. Janotti and C. G. van de Walle, Rep. Prog. Phys. 72 (2009) 126501
155. A. Nuruddin and J. R. Abelson,Thin Solid Films 394, 48 (2001)
156. G. P. Dransfield, Radiat. Prot. Dosim. 91,271 (2000)
157. N. Koshizaki, T. Oyama, Sensors and Actuators B: Chemical, 66, Issues 1–3, (2000) 119-121
158. R. Martins, E. Fortunato, P. Nunes, I. Ferreira, A. Marques, M. Bender, N. Katsarakis, V. Cimalla, and G. Kiriakidis, J. Appl. Phys. 96, 1398 (2004)
159. G. S. T. Rao and D. T. Rao, *Sens. Actuators, B*, vol. 55, pp.166 – 169 (1999)
160. X.-J. Huang and Y.-K. Choi, Sens. Actuators, B 122, 659 (2007)
161. H. T. Ng, J. Han, T. Yamada, P. Nguyen, Y. P. Chen, and M. Meyyappan, Nano Lett. 4, 1247 (2004)
162. M. H. Huang *et al.*, Science 292, 1897 (2001)
163. E. Galoppini, J. Rochford, H. Chen, G. Saraf, Y. Lu, A. Hagfeldt, and G. Boschloo, J. Phys. Chem. B 110, 16159 (2006)
164. W. L. Hughes and Z. L. Wang, Appl. Phys. Lett. 82, 2886 (2003)
165. C.G. Van de Walle, *Phys. Rev. Lett.* 85 (2000) 1012
166. A. Janotti and C.G. Van de Walle, *Phys. Rev.* B **6** (2007) 44
167. Y.R. Park, J. Kim, Y.S. Kim, Appl. Surf. Sci. 255 (2009) 9010
168. P.F. Cai, J.B. You, X.W. Zhang, J.J. Dong, X.L. Yang, Z.G. Yin, N.F. Chen, J. Appl. Phys. 105 (2009) 83713
169. S.Y. Myong, S.I. Park, K.S. Lim, Thin Solid Films 513 (2006) 148
170. S. Eisermann, A. Kronenberger, M. Dietrich, S. Petznick, A. Laufer, A. Polity, B.K. Meyer, Thin Solid Films 518 (2009) 1099
171. J.N. Duenow, T.A. Gessert, D.M. Wood, T.M. Barnes, M. Young, B. To, T.J. Coutts, J. Vac. Sci. Technol. A 25 (2007) 955
172. C.G. Van de Walle and J. Neugebauer, *Annu. Rev. Mater.Res.* 36 (2006) 179
173. S.J. Pearton *et al.*, Superlattices and Microstructures 34 (1-2) (2004) p. 3-32
174. P.W. Tasker, Journal of Physics C: Solid State Physics 12 (1979) 4977
175. H.J. Freund, H. Kuhlenbeck, V. Staemmler, Reports on Progress in Physics 59 (1996) 283–347
176. A. Wander *et al.*, Physical Review Letters 86 (2001) 3811–3814
177. C.B. Duke, A.R. Lubinsky, Surface Science 50 (1975) 605–614
178. N. Jedrecy, S. Gallini, M. Sauvage-Simkin, R. Pinchaux, Surface Science 460 (2000) 136–143
N. Jedrecy, S. Gallini, M. Sauvage-Simkin, R. Pinchaux, Physical Review B 64 (2001) 085424
179. R.W. Nosker, P. Mark, J.D. Levine, Surface Science 19 (1970) 291–317
180. C. Noguera, Journal of Physics-Condensed Matter 12 (2000) R367–R410
181. M. D. McCluskey and S. J. Jokela, JOURNAL OF APPLIED PHYSICS 106, 071101 (2009)
182. J.J. Lander, J. Phys. Chem. Solids (1960) 15324
183. G. Muller, Phys. Status Solidi b (1976) 76525
184. R. Dingle, Phys. Rev. Lett. (1969) 23579
K.C. Mishra *et al.*, Phys. Rev.B (1990) 421423
185. D. C. Look, *et al.*, Physica Status Solidi A: applied research, 201(10) (2004), p. 2203:2212
C. L. Zhang, W. N. Zhou, and Y. Hang, Journal of Crystal Growth, 310(7:9) (2008), p.1819:1822

186. R.Thangavela, M. Rajagopalanb, and J. Kumara, Solid State Comm., 137(9) (2006) 507:511
187. Z.H. Wang *et al.*, Materials Letters, 63 (29) (2009) p. 2533-2535
188. A. Janotti, and C.G. Van de Walle, Applied Physics Letters, 2005. 87 (12): p. 122102-1
S.B. Zhang, S.H. Wei, A. Zunger, Phys. Rev. B - Cond. Matt. and Mater. Phys. 2001. 63 (7)
C. Kilic, A. Zunger, Physical Review Letters 2002. 88 (9): p. 955011-955014
T. Tomita, *et al.*, Applied Physics Letters, 2005. 87 (5): p. 51911-1
189. R.M. Mehra, P. Sagar, and M. Kumar, Thin Solid Films, 2005. 489 (1-2): p. 94-8
S. Eisermann, *et al.*, Thin Solid Films, 2009. 518 (4): p. 1099-1102
G.T. Du, *et al.*, Applied Surface Science, 2007. 253 (6): p. 2999-3003
W. Liu *et al.*, Thin Solid Films, 2007. 515 (5): p. 3057-3060
190. D.C. Reynolds etal., Physical Review B, 1999. 60(4) 2340:2344
191. F. Y. Mao, et al.,Chinese Science Bulletin, 2008. 53(17) 2582:2585
192. T. Becker *et al.*, Surface Science 486 (2001) L502–L506 [Erratum Surface Science 511 (2002) 463]
193. P. Zapol, J.B. Jaffe, A.C. Hess, Surface Science 422 (1999) 1–7
194. M. Kunat *et al.*, Physical Review B 66 (2002) 081402-1–081402-3
195. J.G. Fripiat, A.A. Lucas, J.M. Andre, E.G. Derouane, Chemical Physics 21 (1977) 101–104
196. M. Schiek, K. Al-Shamery, M. Kunat, F. Traeger, C. Woll, Phys. Chem. Chem. Phys. 8 (2006) 1505–1512
197. R.P. Eischens, W.A. Pliskin, M.J.D. Low, Journal of Catalysis 1 (1962) 180–191
G.L. Griffin, J.T. Yates Jr., Journal of Chemical Physics 77 (1982) 3751–3758
198. Kunat, S.G. Girol, U. Burghaus, C. Woll, Journal of Physical Chemistry B 107 (2003) 14350–14356
199. G. Zwicker, K. Jacobi, Surface Science 131 (1983) 179
200. R. Zhang, A. Ludviksson, C.T. Campbell, Surface Science 289 (1993) 1–9
201. A. F. Kohan, G. Ceder, D. Morgan, and C. G. Van de Walle, Phys. Rev. B 61, 15019 (2000)
202. A. Janotti and C. G. Van de Walle, Phys. Rev. B 76, 165202 (2007)
203. L. S. Vlasenko and G. D. Watkins, Phys. Rev. B 72, 035203 (2005)
W. E. Carlos, E. R. Glaser, and D. C. Look,Physica B 308–310, 976 (2001)
204. P. Erhart and K. Albe, Appl. Phys. Lett. 88, 201918 (2006)
205. F. Oba, S. R. Nishitani, S. Isotani, H. Adachi, and I. Tanaka,J. Appl. Phys. 90,824 (2001)
T. R. Paudel and W. R. L. Lambrecht, Phys. Rev. B 77, 205202 (2008)
P. Erhart, A. Klein, and K. Albe, Phys. Rev. B 72 , 085213 (2005)
206. S. Lany and A. Zunger, Phys. Rev. Lett. 98, 045501 (2007)
207. S. F. J. Cox *et al.*, Phys. Rev. Lett. 86, 2601 (2001)
J. M. Gil *et al.*,Phys. Rev. B 64, 075205 (2001)
208. D. M. Hofmann *et al.*, Phys. Rev. Lett. 88, 045504 (2002)
209. M. D. McCluskey *et al.*, Appl. Phys. Lett. 81, 3807 (2002)
S. J. Jokela, M. D. McCluskey, and K. G. Lynn, Physica B340–342,221 (2003)
E. V. Lavrov *et al.*, and R. Helbig, Phys. Rev. B 66, 165205 (2002)
210. S. Limpijumnong and S. B. Zhang, Appl. Phys. Lett. 86, 151910 (2005)
M. G. Wardle, J. P. Goss, and P. R. Briddon, Appl. Phys. Lett. 88, 261906 (2006)
211. S. J. Jokela and M. D. McCluskey, Phys. Rev. B 72, 113201 (2005)
212. K. Shimomura, K. Nishiyama, and R. Kadono, Phys. Rev. Lett. 89, 255505 (2002)
E. V. Lavrov *et al.*, Phys. Rev. B 66, 165205 (2002)
213. G. A. Shi, M. Saboktakin, M. Stavola, and S. J. Pearton, Appl. Phys. Lett. 85, 5601 (2004)
214. E. V. Lavrov, F. Herklotz, and J. Weber,Phys. Rev. Lett. 102, 185502 (2009)
215. S. Zh. Karazhanov and A. G. Ulyashin,Phys. Rev. B78, 085213 (2008)
216. A. Janotti and C. G. Van de Walle, Nature Mater. 6,44 (2007)
217. J. Bang and K. J. Chang, Appl. Phys. Lett. 92, 132109 (2008)

3. Synthesis, methods and materials characterization

Sputtering is relatively cheap and a quick method of thin film production, offering good uniformity over large areas, for example in applications such as transparent conducting layers on large scale solar arrays. An easy control of the parameters is possible using this technique, during the growth or in post-growth treatment.

In this chapter the technique and the basic parameters that have been used for the preparation of intrinsically doped-TiO_2 and ZnO and extrinsically doped-TiO_2 are described. The thin films were deposited using RF reactive sputtering technique, possibly followed by a heat treatment. The techniques used to characterize the structural, electrical, optical and electronic properties of the thin films are briefly described too.

Contents

3.1 Thin films preparation
- 3.1.1 RF reactive sputtering technique – basic principle
- 3.1.2 Experimental set-up

3.2 Thin films characterization
- 3.2.1 Structure and morphology determination
- 3.2.2 Chemical composition
- 3.2.3 Electrical properties
- 3.2.4 Optical properties
- 3.2.5 Work function determination
- 3.2.6 Positron Annihilation Spectroscopy

3.3 Plasma characterization - Optical Emission Spectroscopy (OES)

3.4 References

3.1 Thin films preparation

3.1.1 RF reactive sputtering technique – basic principles

Sputtering is one of the most versatile techniques used for the deposition of transparent conductors when device quality films are required. Sputtering process produces films with higher purity and better controlled composition, provides films with greater adhesion and homogeneity and permits better control of film thickness [1-3].

The principle of this technique is shown in Figure 3.1 *(a)*. Substrates are placed in a vacuum chamber facing the target which is composed of the material to be deposited. The sputtering gas is often an inert gas, generally argon, which is introduced into the chamber to a pressure between 10^{-3} to 10^{-2} mbar. A high negative voltage is applied to the target (cathode), while the substrate holder (anode) is connected to the chamber walls and to the ground or itself held at fixed potential. Under the applied high voltage, the gas is ionized and a plasma is created between the cathode and the anode. Positively charged ions are accelerated toward the cathode and their impact sputters atoms off the target. These atoms travel across the chamber and a fraction of them land on the substrate, resulting in a film that grows in thickness. The deposition rate depends on many parameters, especially on the pressure inside the chamber and on the power applied to the target.

Usually the applied frequency is the RF industrial frequency (13.56 MHz). In a low gas pressure discharge, electrons have a greater velocity than the ions, which are several thousand times heavier. Objects plunged inside the plasma sustain a more important electron bombardment than ion bombardment, and therefore they charge negatively until the ion current and electron current are equal. At the RF powered cathode, the constantly negative potential that appears is called *self-bias*.

Usually, the substrates are electrically connected to the sputter chamber, while the target makes the second electrode. A reactive gas is added to the sputter gas in order to deposit oxides from the target. The chemical composition of the thin films can be varied over a wide range by adjusting the partial pressure of the reactive gas. Sputtering performed in the presence of a reactive gas is called *reactive sputtering*.

3.1.2 Experimental set-up

A sketch of the apparatus used for depositing TiO_2 and ZnO thin films is shown in Figure 3.1 *(b)*. The substrates are placed on a rotating substrate holder in horizontal position. The distance between the substrate and the target can be varied. Infrared lamps can heat the substrates up to 420°*C*. The substrates can be replaced in the deposition chamber without breaking the vacuum inside, thanks to an introduction chamber. The substrates are place in a horizontal position and the distance between substrate and target can be varied.

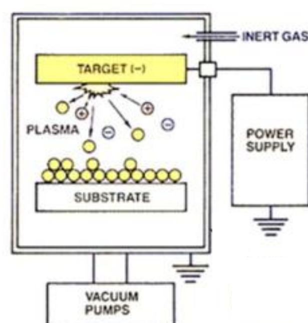

(a) *(b)*

Figure 3.1. *(a)* The principle of RF sputtering; *(b)* Sketch of the apparatus used for depositing TiO_2 and ZnO thin films

Doped-TiO_2 and ZnO thin films were obtained varying more parameters during the deposition. In Table 1 the conditions used for each experiment are listed. The total gas introduced in discharge was kept in all experiments at *30 sccm*. The base pressure in the deposition chamber before the depositions was 3.9×10^{-6} *Pa* and during the depositions was kept at 3.99 *Pa* or 6.66 *Pa*. Post-growth annealing of the films was carried out in a quartz tube at 900°*C* for one hour, with a heating rate of 5°*C/min*, in vacuum (1.5×10^{-4} *Pa*). Cooling was performed under vacuum (1.5×10^{-4} *Pa*) and typically took several hours.

In the case of TiO_2 film deposition a disk target was used (99,998% purity, 10 *cm* diameter). For Nb-containing TiO_2 films deposition, two sputtering arrangements were used: a mosaic target composed of TiO_2 disk onto which Nb wires are placed (occupying 2% Nb of TiO_2 target surface) or two separate TiO_2 and Nb targets (purity 99.99%, 5 *cm* diameter), powered by two different RF power supplies. For ZnO thin films deposition, a ZnO disk target (99,998% purity, 10 *cm* diameter) was used. In order to improve the film homogeneity the substrate holder was rotated during the depositions. Usually smaller substrate pieces of different materials were coated simultaneously. This allowed choosing a suitable substrate for every characterization technique. In an ideal case, all measurements should be made on the same kind of substrate to make sure that good correlations can be established between results, but it is often not possible. Glass, quartz and *n*-type Si (100) were used as substrates in our experiments. The substrates were cleaned in an ultrasonic bath before introducing in the deposition chamber, for 10 minutes in isopropanol.

Table 3.1. Conditions used in each experiment for depositing TiO_2 and ZnO thin films

TiO_2	Target: TiO_2 Gas: Ar, Ar-O_2 (3-33%) and Ar-H_2 (3-33%) Cathode self-bias voltage: from -350 V to -850 V Target-substrate distance: 2.4, 6.9 and 5.9 cm Substrate temperature: RT and 350°C Pressure: 3.99 *Pa* and 6.66 *Pa*
ZnO	Target: ZnO Gas: Ar and Ar-H_2 (3-50%) Cathode self-bias voltage: -550 V Target-substrate distance: 3 cm Substrate temperature: RT Pressure: 6.66 *Pa*
Nb-doped TiO_2	Target: TiO_2 and Nb (mosaic target or two separate targets) Gas: Ar, Ar-O_2 (3-33%) and Ar-H_2 (3-33%) Self-bias voltage to TiO_2 cathode: from -350 V to -850 V Power to Nb target: 1-5 W Target-substrate distance: 2.4, 6.9 and 5.9 cm Substrate temperature: RT, 300°C - 420°C Pressure: 3.99 *Pa* and 6.66 *Pa*

3.2 Thin films characterization

This section gives an overview of the techniques used to characterize the doped-ZnO and TiO_2 thin films. Each sample was characterized, first of all, for its chemical composition and its structure. The electrical and optical properties were investigated for the obtained films. Using X-ray Photoelectron Spectroscopy, the work function for doped-TiO_2 thin films was determined. A study based on a joint use of X-ray Photoelectron Spectroscopy and optical measurements allowed to define the electronic properties of the films (valence band edge, Fermi level position, work function, ionization potential and electron affinity). The defect properties of the films were studied with Positron Spectroscopy. The chemical species present in various plasmas used in deposition process were investigated by Optical Emission Spectroscopy.

3.2.1 Structure and morphology determination

Thin films deposited by sputtering are made of small grains that can be crystalline or amorphous. The size, shape and stacking of the grains are part of the film morphology. For example, the films may show a compact or a columnar structure depending on deposition parameters like reactive gas pressure or substrate temperature [4].

X-ray diffraction (XRD) was used to determine if the film is amorphous or polycrystalline and, in the latter case, the crystallite size. Scanning Electron Microscopy (SEM) images give information about surface morphology of the samples.

Film thickness

Film thickness determination was performed using a Surface Profiler (Tencor Instruments). The profiler scans a tip over the sample surface while recording its vertical position. The tip is pressed on the surface with a constant force (2 *mg*). Measurements paths included sections on the substrate, which were under the mask during the deposition (un-coated), and sections coated by the thin film. The height diference measured be between the two surfaces gives the film thickness. The film thickness is the average over more measurements (more than 5 usually). The film thickness measured by profilometer was used as a starting value in the fitting process during the analysis of the optical measurements.

X-ray Diffraction (XRD)

If the sample is a crystal, x-rays are diffracted only in directions verifying the Bragg condition:

$$2d\sin\theta = n\lambda \tag{3.1}$$

where d is the distance between crystal planes, 2θ the Bragg angle, n an integer, and λ the wavelength of the x-rays. Each crystal has its own signature: the position of the peaks depends on the crystal symmetry and on the size of the elementary cell of the lattice. Crystalline phases present in a sample can be identified by comparison with x-ray diffraction curves compiled in standard databases [5,6].

The shape of each Bragg peak results from a convolution of the crystallite size, of the experimental resolution function, and of internal stress. If we assume that stress is weak and if the resolution of the setup is good enough, the size can be calculated from the full width at half maximum (FWHM) of the peak with Scherrer's equation [7]:

$$Size = \frac{0.9\lambda}{width\ \cos\theta} \tag{3.2}$$

where $width = \sqrt{FWHM^2 - GW^2}$ is in radian, and GW is the diffractometer broadening.

The phase structure of the films was determined by using a Seeman-Bohlin (grazing angle configuration) X-ray diffractometer with $Cu\ K_\alpha$ radiation at an incident angle of 3 in steps of 0.02° (Italstructures APD2000).

Scanning Electron Microscopy (SEM)

The SEM images were acquired with an in-lens detector at the working distance of 4 *mm*, by using the accelerating voltage of 5 *kV* (Field Emission SEM, Ultra 55, Carl Zeiss).

3.2.2 Chemical composition

X-ray Photoelectron Spectroscopy (XPS) was used to investigate the core-levels and the valence band of doped-TiO_2 and ZnO thin films. The oxides stoichiometries were derived from the XPS analysis. Using

Fourier Transform Infrared Spectroscopy - Attenuated Total Reflectance (FTIR-ATR), the hydrogen adsorption or/and incorporation in films was investigated.

X-ray photoelectron spectroscopy (XPS)

Photoelectron Spectroscopy is based on the measurement of the energy of electrons emitted from a surface bombarded by a beam of x-rays [8]. Each atom has its own signature. One of the most important capabilities of XPS is its ability to measure shifts in the binding energy of core electrons resulting from a change in the chemical environment of the emitting atom. In this way the degree(s) of oxidation of each atomic species can be measured. The depth penetration of this chemical analysis is only a few nanometers (typically 25 Å in depth), thus surface contamination and surface oxidation have a great influence on the results and samples must be carefully prepared to obtain valuable information.

The XPS studies were performed on samples using a SCIENTA ESCA 200 spectrometer with a monochromatic Al $K\alpha$ X-ray source (1486.6 eV). The experiments were performed under ultrahigh vacuum ($2x10^{-8}$ Pa) conditions without any additional in situ cleaning procedure. Photoemission spectra showed that carbon and water are the only surface contaminants for all of the investigated films.

The spectra of C *1s*, O *1s* and Ti *2p*, Nb *3d*, Zn *2p* core lines were acquired at 150 *eV* pass energy (resolution of 0.4 *eV*), while the valence band (VB) spectra were acquired at 300 *eV* pass energy. Due to the electrostatic charging of the surfaces, the spectra were corrected for the binding energy shift using as reference the binding energy of C *1s* (285 *eV*). All the binding energies are given with respect to Fermi level. The deconvolution procedure fitting the high-resolution spectra of the core levels was performed with combined Gaussian-Lorentzian functions, after a Shirley-type background subtraction.

The chemical composition of doped-ZnO and TiO_2 films was determined, using the Scienta atomic sensitivity factors of 0.296 for C *1s*, 0.711 for O *1s*, 1.798 for Ti *2p*, 2.517 for Nb *3d* and 3.354 for Zn $2p_{3/2}$. ZnO and TiO_2 oxide stoichiometry were derived.

Fourier Transform Infrared Spectroscopy - Attenuated Total Reflectance (FTIR-ATR)

Infrared spectroscopy is a widely used technique that for many years has been an important tool for investigating chemical processes and structure. The combination of infrared spectroscopy with the theories of reflection has made advances in surface analysis possible. Specific IR reflectance techniques may be divided into the areas of specular reflectance, diffuse reflectance, and internal reflectance. The latter is often termed as attenuated total reflectance. This technique allows qualitative or quantitative analysis of samples with little or no sample preparation which greatly speeds sample analysis.

An attenuated total reflection instrument operates by measuring the changes that occur in a totally internally reflected infrared beam when the beam comes into contact with a sample. An infrared beam is directed onto an optically dense crystal with a high refractive index at a certain angle. This internal reflectance creates an evanescent wave that extends beyond the surface of the crystal into the sample held in contact with the crystal. There must be good contact between the sample and the crystal surface, because the

evanescent wave only extends beyond the crystal 0.5 μ - 5 μ. In regions of the infrared spectrum where the sample absorbs energy, the evanescent wave will be attenuated or altered. The attenuated energy from each evanescent wave is passed back to the IR beam, which then exits the opposite end of the crystal and is passed to the detector in the IR spectrometer. The system then generates an infrared spectrum. The refractive index of the crystal must be significantly greater than that of the sample or else internal reflectance will not occur – the light will be transmitted rather than internally reflected in the crystal. Typically, ATR crystals have refractive index values between 2.38 and 4.01 at 2000 cm^{-1}. It is assumed that the majority of solids and liquids have much lower refractive indices.

ATR-FTIR spectra were acquired for ZnO thin films using an Equinox 55 spectrometer (Bruker Optics) equipped with an ATR Silver Gate (Specac) device. The analyses were carried out in the 350-4000 cm^{-1} range with a resolution of 4 cm^{-1}. The broad absorbance band which appears in the 2600-3800 cm^{-1} interval was studied in particular which includes the C–H stretching bands (~3000 cm^{-1}) overlapped to broad O–H stretching bands (3800÷2600 cm^{-1}).

3.2.3 Electrical properties

Room temperature measurements of the electrical resistivity and Hall mobility were performed using a standard van der Pauw four-point probe technique [9]. In general the electrical connections are either wire bonded, or attached to the film surface by conducting silver glue. In our case, the connections were pressed directly to the film surface.

The resistivities for the obtained films were measured by van der Pauw method and the carrier density and the mobility by Hall effect measurements. The electrical measurements setup is an RH 2030 PhysTech instrument. This setup allows measurements on low as well as high resistive samples. In order to perform Hall effect measurements, the samples can be placed in a permanent magnetic field. In our measurements, this field was kept at 0.88 T. The obtained data provides information concerning carrier type and the carrier concentration according to (for an n-type semiconductor):

$$V_H = \frac{I \times B}{q \cdot n \cdot d} \tag{3.3}$$

If a current I is applied to a sample with thickness d in a perpendicular magnetic field B, the moving charge carriers are deflected by the Lorenz force. A potential difference V_H will build up perpendicular to both the current flow and magnetic field. The accumulation of charge continues until the counteracting electrostatic force cancels the magnetic force on the moving charges. From the polarity of the potential difference V_H it is possible to distinguish between electrons or holes as the majority of charge carriers. If V_H is plotted against B, the carrier type and carrier density can be deduced from the sign and slope of the graph, respectively. Combined with the resistivity data, the carrier mobility can be calculated from (for n-type semiconductor):

$$\sigma = e \cdot n \cdot \mu = \frac{1}{\rho} \tag{3.4}$$

3.2.4 Optical properties

Optical transmission, absorption and reflection data was collected with a double beam spectrophotometer (JASCO V-670), capable of measuring in the wavelength range 190-2700 *nm*. A deuterium lamp is used for 190-350 nm region and a halogen one for 330-2700 nm. The resolution and scan speed can be adjusted. In most experiments the wavelength interval was 0.5 *nm*. From the obtained optical data, the band-gap value can be obtained.

3.2.5 Work function determination

The work function of the films was investigated using X-ray Photoelectron Spectroscopy, by exploiting analyses conditions where the measured energies depend on the work function of the material being analyzed. During XPS of solids, the ejected photoelectrons leave a residual positive charge on the sample. If the sample in contact with the spectrometer is a good electrical conductor, this charge is rapidly neutralized by electrons flowing from the spectrometer (the sample holder) to the sample. On the contrary, if the sample is a poor conductor or insulating, it acquires a *positive* charge, which shifts the energy positions of the spectra towards higher values or even impedes the spectra acquisition. In such cases and in order to neutralize the charge an electron gun (flood gun) is used to bombard the sample surface with additional electrons to compensate the positive surface charging. A zero-charge can then be obtained at equality between the electron current emitted from the surface and the one coming from the flood gun. By further flooding the surface beyond the equilibrium situation, the opposite surface charging occurs and a *negative* potential builds, which corresponds to the potential of the electron beam, Φ_e. Again the energy positions of the spectra are shifted, towards lower values in this case.

In the case of a conducting sample, in good electrical contact with the spectrometer (with no resistance in-between, let’s indicate it as” shorted”), the kinetic energy E_k of the ejected photoelectron is given by the well-known relation:

$$E_k = h\nu - E_B - \Phi_{spec} \tag{3.5}$$

where $h\nu$ is the X-ray photon energy, E_B is the electron binding energy and Φ_{spec} is the work function of spectrometer. E_B is measured relatively to the Fermi level of the sample.

When a fixed non-zero potential, Φ_e, builds on an insulating sample surface, the binding energy is no more measured relatively to the Fermi level of the sample but to the vacuum level, because the kinetic energy of the photoelectron in such case is given by:

$$E_k = h\nu - E_B - \Phi_{sample} + \Phi_e \tag{3.6}$$

where Φ_{sample} is the work function of the sample.

This can be understood by the two energy diagrams in Figure 3.2.

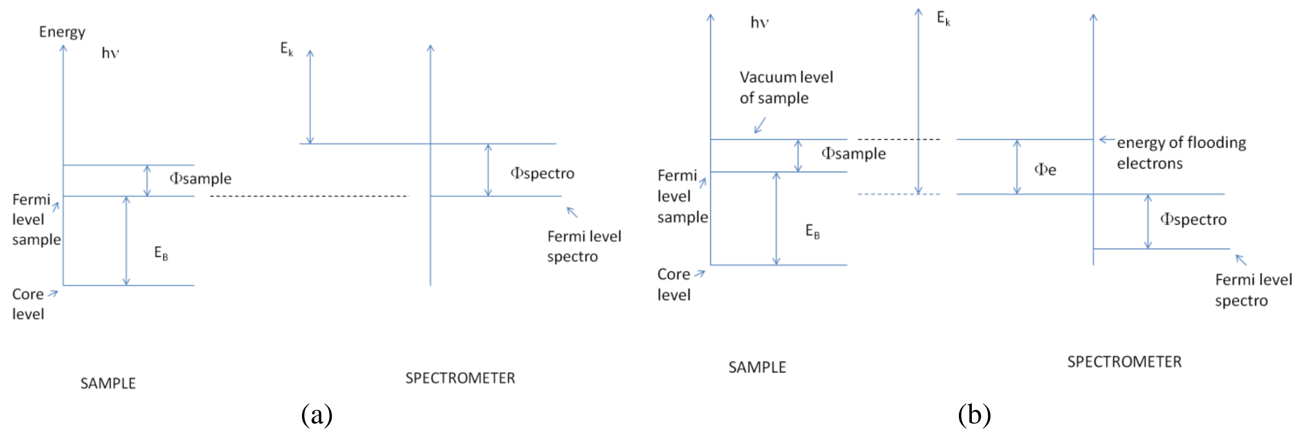

Figure 3.2 Energy level scheme for the case of good electrical contact of the sample with the spectrometer (a) and the case of sample insulated from the spectrometer (b)

This applies to insulating samples, but to any kind of samples too, provided they are electrically insulated from the spectrometer. If a sample is analyzed in both configurations, "shorted " with the spectrometer and insulated from it, the work function of such sample can be derived, as

$$E_k\,(\text{shorted}) - E_k\,(\text{insulated}) = \Phi_{sample} - \Phi_{spec} - \Phi_e \tag{3.7}$$

Φ_{spec} , equal to 4.69, was determined by using a reference material of known work function, in this case gold.

We exploited this method to determine the work function of the samples of this study. Φ_e was varied by varying the potential of the electron flow from the flood gun, beyond the equilibrium value for positive charge compensation which corresponds to a zero-charge surface. The equilibrium potential value is monitored by the C1s BE, coming from contamination, which is used as a reference. Ti2p3/2 spectrum energy, corresponding to a zero-charge surface and to a charged surface with a potential Φ_e was used to determine the work functions of the samples following Eq. (3.7). A zero-charge surface represents the "shorted" case for the oxide samples as it was not easy to have the surface positive charge compensation from a flow of electrons from the spectrometer as in the case of conducting samples as gold. To insulate the gold sample, it was placed on a piece of glass, as shown in Figure 3.3.

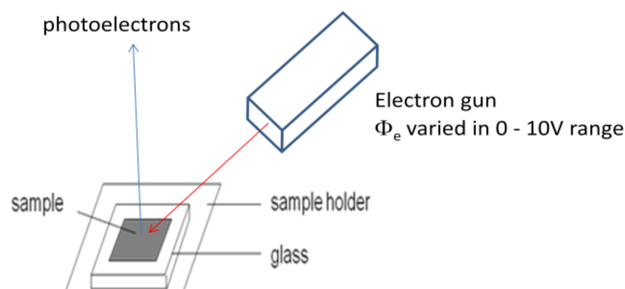

Figure 3.3 Sketch of the insulated case of the sample

3.2.6 Positron Annihilation Spectroscopy (PAS)

Positrons by definition is the antiparticle of the electrons, which has the same mass and magnitude charge as the electrons but positively charged. Positrons spectroscopy techniques have been developed to obtain information on the microscopic properties of the material as well as sensing the atomic and electronic structure of the material. It is particularly useful to detect defects in materials since the positively charged positrons have the tendency in attracting to holes in materials. Today, not only are positrons the most sensitive probe of defects known, but unlike other techniques used to probe for defects, they cause no damage. Some of the positrons spectroscopy techniques are ACAR (Angular Correlation Annihilation Radiation), DBS (Doppler Broadening Spectroscopy), LEPD (Low-energy Positron Diffraction), PAES (Positron-annihilation-induced Auger Electron Spectroscopy, and PALS (Positron Annihilation Lifetime Spectroscopy). In this thesis, Doppler Broadening Spectroscopy and Positron Annihilation Lifetime Spectroscopy were performed for doped-TiO_2 samples.

When positrons are incident onto a material, a few events may happen, schematically shown in Figure 3.4 *(a)*. Positrons may leave the material by backscattering, by inelastic emission before complete thermalization or by reemission (ejected from the material surface due to its positive charge). Positrons may liberate an electron and form a positronium (a short-lived system consists of positron and electron bounded together) in vacuum if a positron leaves from the material. In addition, positrons may be trapped at the surface by forming state positronium or by forming a localized state in the image of potential immediately outside the surface. Even if the positrons do not leave the material, it will annihilate in it eventually. In most cases, positrons lifetime inside a material is less than a fraction of nanosecond, but it is long enough for positron to visit a region of the material and sense the atomic and electronic structure of the environment.

The mean positron implantation depth $\bar{z}$ in nanometres is related to the energy E by the equation:

$$\bar{z} = \frac{40}{\rho} E^{1.6} \tag{3.8}$$

when the material density ρ and energy E are expressed in g/cm^{-3} and *keV*, respectively [10].The diffusion process starts immediately upon the completion of implantation process. For non-metals, this process is difficult to approximate since they don't fully thermalize the positrons. Positrons are very likely to trap in defects during the diffusion process, especially in vacancies and voids. Trap depth depends on the detail of defects and the trapping process depends on the type of materials. Positrons may annihilate during the process of diffusion or trapping. PALS is a useful positron spectroscopy signal to sense the length of time a positron stayed in a material before it annihilate. DBS and ACAR are useful positron spectroscopy signal to sense the energy or angle of the annihilation gamma-ray. Being able to trace the annihilation process in positron spectroscopy allow further microstructure investigations of the materials.

The DB of the 511 *keV* annihilation line was characterized by the shape parameter S(E) and the wing parameter W(E) [10,11]. The S(E) parameter was defined as the ratio of the counts in a central area ($|511–E\gamma| \leq 0.85$ *keV*) to the total area ($|511–E\gamma| \leq 4.25$ *keV*) of the line, while the W(E) as the fraction of counts in the wing region ($1.6 \leq |511–E\gamma| \leq 4$ *keV*) of the line where $E\gamma$ is the energy of the annihilation γ-ray, as depicted in Figure 3.4 *(b)*. S(E) and W(E) represent the positrons annihilating with low and high momentum electrons, respectively.

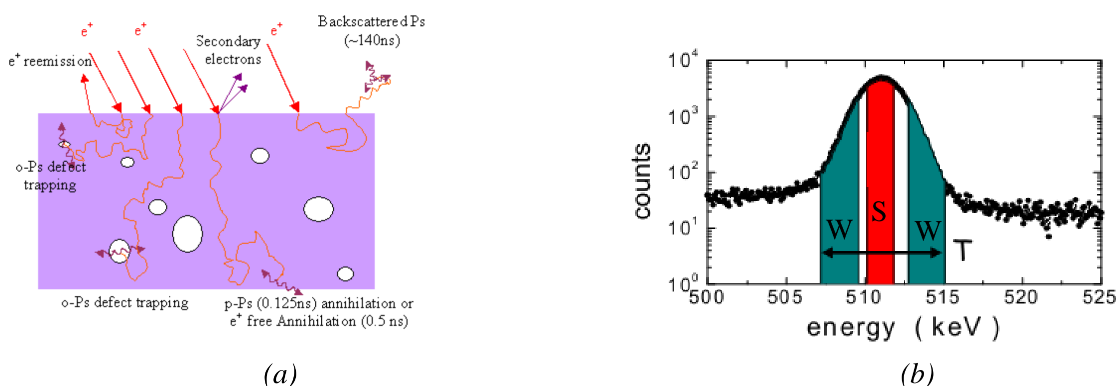

(a) *(b)*

Figure 3.4 *(a)* Brief summary of what happen to positron after it is being implanted into a material; *(b)* S and W parameters in Doppler Broadening Spectroscopy

The measured S(*E*) (and W(*E*)) are linear combinations of the characteristic *S* (and *W*) values multiplied by the fraction *f* of positron annihilating at the surface [S_S; (W_S); f_S], in the *Si* bulk [S_b; (W_b); f_b] and different *i* state [S_i; (W_i); f_i]:

$$S(E) = f_S(E)S_S + \sum_i f_i(E)S_i + f_b(E)S_b \quad (3.9)$$

$$W(E) = f_S(E)W_S + \sum_i f_i(E)W_i + f_b(E)W_b \quad (3.10)$$

$$f_S(E) + \sum_i f_i(E) + f_b(E) = 1 \quad (3.11)$$

The *i* states can be trap sites, interfaces and, as in our case, different sample layers. The VEPFIT program [12] was used to extract the (*S*, *W*) coordinates of each annihilation site and the SWAN program [13] to achieve the annihilation fractions *f* of each site at each energy *E*.

The DB spectra were acquired with a dual parameter multichannel analyzer MPA-3 FAST-COMTEC. The samples were depth profiled by the Doppler Broadening (DB) technique measuring the 511 *keV* positron–electron annihilation line and tuning the positron implantation energy E. The positron–electron annihilation line was acquired with two HPGe detectors in a 180° configuration, 45% efficiency and 1.4 *keV* resolutions. The lifetime measurements were performed with PLEPS (Egger 2010) set up at the FRMII facility at Munich. Lifetime spectra were acquired in the 1–18 *keV* positron implantation energy range and analyzed by POSFIT. The overall (detector plus pulsing system) time resolution was 360 *ps*.

3.3 Plasma characterization

Plasma diagnostics plays an important role in all experiments. Information about fundamental plasma parameters, like electron temperature, electron density etc. is essential in order to evaluate the energy transport into the plasma. There are several diagnostic techniques employed for the determination of these parameters like plasma spectroscopy and Langmuir probe. In the present work, Optical Emission Spectroscopy was used to investigate the plasma created during the depositions.

Optical Emission Spectroscopy (OES)

OES examines the light given by the species in the plasma that have been raised to excited states by impact. Excited species radiates characteristic set of wavelengths that can be used as fingerprints. This unique fingerprint is determined by the fundamental atomic energy levels that are different for each element. OES is an attractive option for plasma process control because it is fast, non-intrusive, monitors multiple elements simultaneously and provides information regarding deposition conditions in the plasma.

The plasma light was collected with an optical fiber through a quartz window of the sputtering chamber and then analyzed by means of a Spectrapro 2300i (Acton Research Corporation) instrument, equipped with an ICCD camera. Emission spectra were recorded in the 200-900 *nm* range with a spectral resolution of 0.2 *nm*.

3.4 References

1. K. Wasa and S. Hayakawa , *Handbook of sputter deposition technology: principles, technology and applications* (1992)
2. M. Ohring, *The materials science of thin* films (1992)
3. S. M. Rossnagel, J.J.Cuomo and W.D. Westwood, *Handbook of plasma processing technology: Fundamentals, etching, deposition, and surface interactions* (1990)
4. R.F. Bunshah, *Deposition technologies for films and coatings: Developments and applications* (1982)
5. PDF-database. JCPDS, International centre for diffraction data (ICDD), 1601 Park Lane, Swarthmore, PA 19081, USA
6. D.K. Smith and R. Jenkins, The Rigaku Journal 6 (1989)
7. P. Scherrer, *Göttinger Nachrichten* (1918)
8. J.B. Lumsden, *X-ray Photoelectron Spectroscopy, materials characterization* (1986)
9. L.J. Van der Pauw, Philips Res. Reports. 13, 1 (1958)
10. P. Asoka-Kumar, K. G. Lynn, and D. O. Welch, J. Appl. Phys. 76, 4935 (1994)
11. H.S. Leipner *et al.*, *Positron Annihilation at Dislocations and Related Point Defects in Semiconductors* (1999)
12. A. van Veen, H. Shut, J. de Vries, R. A. Hakvoort, and M. R. IJpma, in *Proceedings of the Fourth International Workshop on Slow-Positron Beam Techniques for Solids and Surfaces*, (AIP, New York, 1990)
13. A. V. Fedorov, A. van Veen, and H. Schut, Mater. Sci. Forum 363–365, 646 (2001)

4. Deposition of TiO_2 films in different plasmas for intrinsic doping

Titanium dioxide is a nonstoichiometric compound, which has been generally considered as an oxygen-deficient compound, TiO_{2-x}. The most notable point defect of pure TiO_2 called native point defects are the oxygen vacancies and titanium interstitial. The defects responsible for the electronic properties of TiO_{2-x} films is still a subject of discussion in spite of numerous studies devoted to this topic and the varied experimental techniques used to determine it.

Contents

4.1 Introduction
4.2 Deposition in pure-Ar plasma
4.2.1 Effects of cathode self-bias voltage
4.2.1.1 Influence of cathode self-bias voltage variation on the films growth rate
4.2.1.2 Influence of cathode self-bias voltage variation on the films chemical composition
4.2.2 Effects of substrate temperature
4.2.2.1 Influence of substrate temperature on the films chemical composition
4.2.2.2 Influence of substrate temperature on the films structural properties
4.3 Deposition in Ar-O_2 plasma
4.3.1 Influence of O_2 concentration in the gas on the films growth rate
4.3.2 Influence of O_2 concentration in the gas on the films chemical composition
4.3.3 Influence of O_2 concentration in the gas on the films structure and morphology
4.3.4 Influence of O_2 concentration in the gas on the films chemical composition for post-growth annealed in vacuum films
4.3.5. Influence of O_2 concentration in the gas on the films structure and morphology for post-growth annealed in vacuum films
4.4 Deposition in Ar-H_2 plasma
4.4.1 Influence of H_2 concentration in the gas on the films growth rate
4.4.2 Influence of H_2 concentration in the gas on the films chemical composition
4.4.3 Influence of H_2 concentration in the gas on the films structure and morphology
4.4.4 Influence of H_2 concentration in the gas on the films chemical composition for post-growth annealed in vacuum films
4.4.5 Influence of H_2 concentration in the gas on the films structure and morphology for post-growth annealed in vacuum films
4.5 Concluding remarks
4.6 References

4.1 Introduction

In this chapter TiO_2 thin films were deposited by RF sputtering from a ceramic TiO_2 target in Ar, Ar-O_2 and Ar-H_2 atmospheres at room temperature or at 350°C substrate temperature. Post-growth annealing in vacuum at 900°C was performed. The structural and morphological properties of the films were investigated by X-ray Diffraction (XRD) and Scanning Electron Microscopy (SEM). Using X-ray Photoelectron Spectroscopy (XPS) the films chemical composition was investigated, more exactly the stoichiometry and the identification of oxygen vacancies was studied.

4.2 Deposition in pure-Ar plasma

4.2.1 Effects of cathode self-bias voltage

In this section the cathode self-bias voltage was varied from -350 *V* to -750 *V* in order to optimize the preparation process of intrinsically-doped TiO_2.

4.2.1.1 Influence of cathode self-bias voltage variation on the films growth rate

The film thicknesses were measured for TiO_2 thin films prepared in Ar plasma and the growth rate was determined. As seen in Figure 4.1, the growth rate is increasing with the applied self-bias voltage at cathode. The maximum value was obtained when the cathode self-bias voltage was -750 *V* (1.36±0.09 *nm/min*).

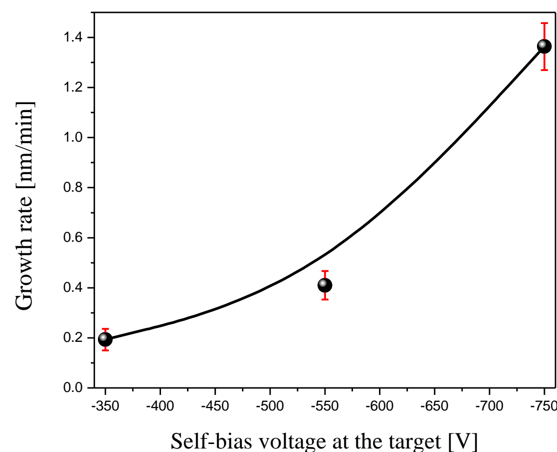

Figure 4.1 Growth rate as a function of cathode self-bias voltage

4.2.1.2 Influence of cathode self-bias voltage variation on the films chemical composition

X-ray Photoelectron Spectroscopy (XPS) measurements were performed for TiO_2 films prepared in Ar plasma, at different cathode self-bias voltages. The C *1s*, O *1s* and Ti *2p* core levels spectra were acquired. Typical C *1s* and O *1s* core-level spectra for TiO_2 films prepared at -550 *V* together with the fit components are shown in Figure 4.2.

C *1s* core level spectra for TiO_2 samples can be well fitted with three components, named C_I, C_{II} and C_{III}, respectively in the Figure 4.2 *(a)*. The first component corresponds to C-H [1], the second one is given by carbon atoms bound as C-O and C-O-C and/or C-OH groups [1], while the third one corresponds to C=O bonds [1].

O *1s* core level spectra can be well fitted with three components, named O_I, O_{II} and O_{III}, respectively in the Figure 4.2 *(b)*. The main peak (O_I) corresponds to oxygen in titanium dioxide [2,3]. The second component (O_{II}) is coming from Ti-OH bonds contribution [1], possible C-O bondings in C-O-C and C-OH groups contribution and from Ti_2O_3 phase contribution [1]. The third component (O_{III}) has been reported to be caused by adsorbed molecular H_2O [4,5] and also C-O bondings like O-C-O or O=C-O [1]. The binding energies of O_I component are listed in Table 4.1.

A typical Ti *2p* core level spectrum together with the fit results is shown in Figure 4.3 *(a)*. The Ti *2p* core level consist of Ti $2p_{3/2}$ and Ti$2p_{1/2}$ contributions. The Ti $2p_{3/2}$ binding energy values are reported in literature as Ti^{4+} states in TiO_2 [6]. The binding energies for Ti^{4+} $2p_{3/2}$ are listed in Table 4.1.

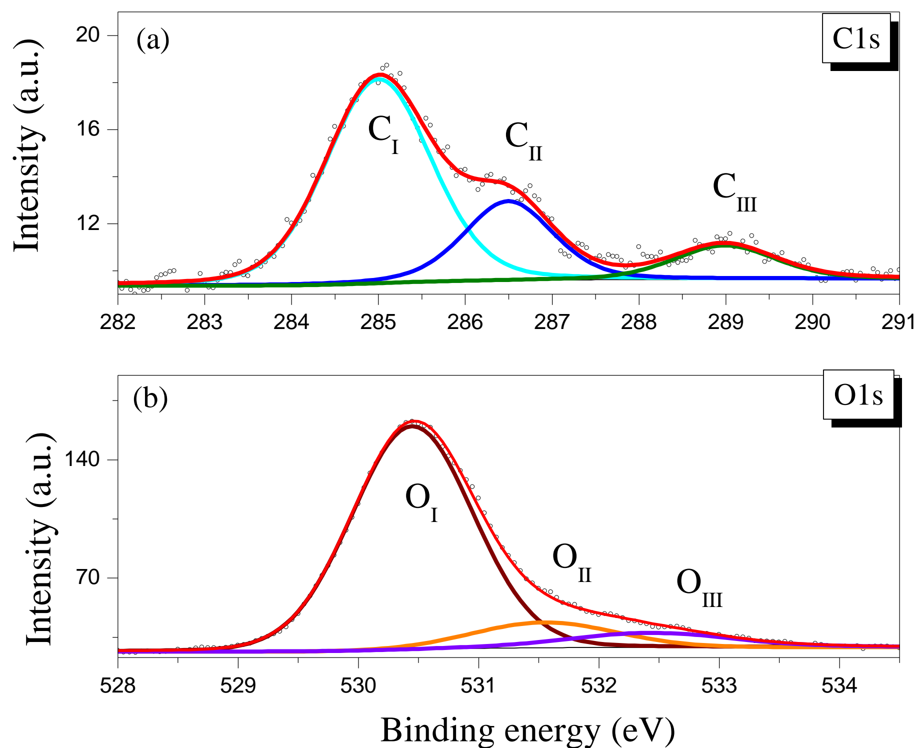

Figure 4.2 Typical C *1s (a)* and O *1s (b)* core-level spectra for TiO_2 prepared at -550 *V*, in Ar plasma

A shift of O *1s* and Ti $2p_{3/2}$ BEs toward higher energies with respect to that of rutile (529.75 *eV* and 458.35 *eV*, not shown) was observed in all the samples [6]. However, the difference between Ti $2p_{3/2}$ and O_I peak BEs remains constant as 71.45±0.03 *eV* and close to that of rutile (71.40 *eV*). This indicates that the chemical states of Ti and O are the same in these films and in rutile. The BE shift observed in the spectra is only related to a variation of E_F with respect to the core lines, due to band bending caused by a non-zero surface potential during the analysis.

The stoichiometry was determined on the basis of the main peak area ratio of O *1s* spectrum (O_I) and the area under the whole Ti *2p* spectrum (Ti $2p_{3/2}$ and Ti $2p_{1/2}$ peaks). The O_I/Ti atomic ratios values are listed in Table 4.1 and plotted as a function of cathode self-bias voltages (Figure 4.3 *(b)*). The TiO_2 films prepared in Ar plasma at various cathode self-bias voltages were under-stoichiometric with respect to the ideal value for TiO_2 ($O_{O\text{-}Ti}$/Ti=2). An increase of O_I/Ti is observed when the cathode self-bias voltage is increased.

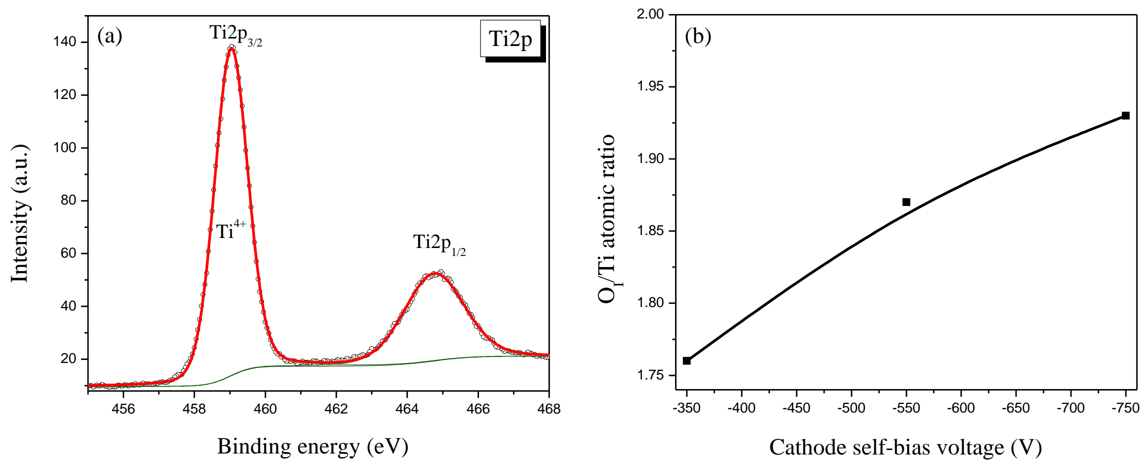

Figure 4.3 *(a)* Ti *2p* core-level spectrum for TiO_2 prepared at -550 *V*, in Ar plasma; *(b)* O_I/Ti atomic ratio as a function of cathode self-bias voltage

The deviation from the ideal stoichiometry TiO_2 (quantified as *x* in TiO_{2-x}) can be due to structural defects as O vacancies, but also to the formation of Ti-OH bonds due to H_2O dissociative adsorption [7]. The Ti-OH bonds are difficult to quantify from the second component of the O *1s* spectrum (O_{II}). From the C *1s* spectrum deconvolution shown in Figure 4.2 *(a)*, the contribution of carbon atoms bound as C-O in C-O-C and/or C-OH groups represented by C_{II} component could be determined.

The O_{II}/Ti and C_{II}/Ti atomic ratios were determined on the basis of the entire Ti *2p* area, the area under the second component of O *1s* (O_{II}) and the area under the second component of C *1s* (C_{II}). The values are listed in Table 4.1 and plotted as a function of cathode self-bias voltage (Figure 4.4 (*a*)). Assuming a maximum value of atomic ratio O/C=1 between O and C atoms contributing to the C-O bonds among C-O, C-O-C and C-OH, the atomic ratio C_{II}/Ti is considered as representing oxygen fraction bound in the different C-O groups. By subtracting C_{II}/Ti ratio values from the O_{II}/Ti ones, in order to represent only the $O_{Ti\text{-}OH}$/Ti atomic

ratio pertaining to hydroxylated Ti, one obtains the plot shown in Figure 4.4 *(b)*, where can be observed that the $O_{Ti\text{-}OH}$/Ti and x in $TiO_{2\text{-}x}$ values are close to each other or even the same. This behavior indicates that the deviation from stoichiometry in TiO_2 films prepared at various cathode self-bias voltages can be due to hydroxylation. The oxygen vacancies in these films cannot be established by this analysis. More insight can be obtained from the valence band states study, as it will be presented later in the following section.

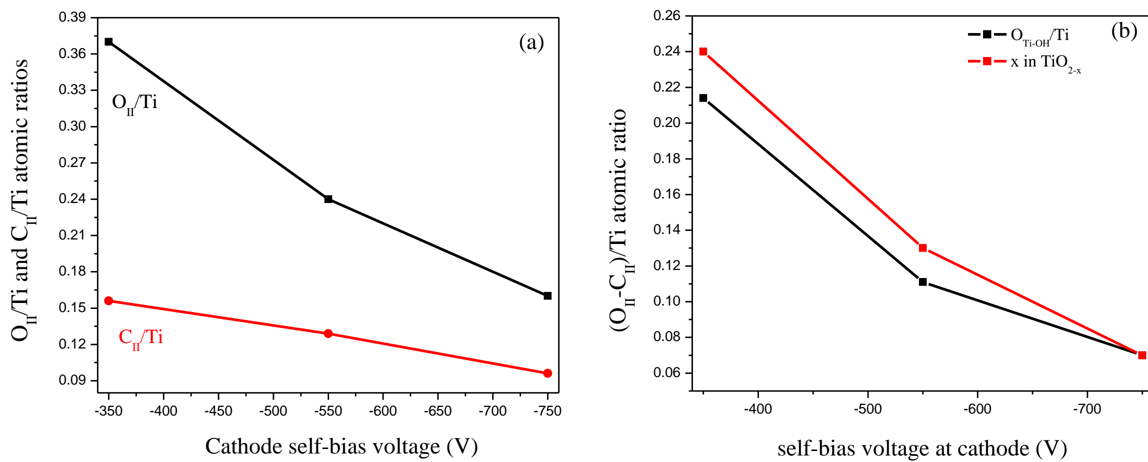

Figure 4.4 *(a)* O_{II}/Ti and C_{II}/Ti atomic ratios as a function of cathode self-bias voltage; *(b)* $O_{Ti\text{-}OH}$/Ti atomic ratio as a function of self-bias voltage at cathode

Table 4.1 O_I, Ti^{4+} *$2p_{3/2}$* binding energies, ΔE (O_I-$Ti^{4+}2p_{3/2}$), O_I/Ti and $O_{Ti\text{-}OH}$/Ti atomic ratios, x in $TiO_{2\text{-}x}$

Cathode self-bias voltage (V)	BE(O_I) (eV)	BE(Ti^{4+} $2p_{3/2}$) (eV)	ΔE (O_I-$Ti^{4+}2p_{3/2}$) (eV)	O_I/Ti	x in $TiO_{2\text{-}x}$	$O_{Ti\text{-}OH}$/Ti
rutile	529.75	458.35	71.40	1.80	0.20	0.43
-350	530.33	458.85	71.48	1.76	0.24	0.22
-550	530.45	459.03	71.42	1.87	0.13	0.12
-750	530.35	458.89	71.46	1.93	0.07	0.07

In the next experiments, TiO_2 films prepared at cathode self-bias voltage of -550 *V* and -750 *V* were used having a higher thickness then the ones prepared at a cathode self-bias voltage of -350 *V*.

4.2.2 Effects of substrate temperature

4.2.2.1 Influence of substrate temperature on the films chemical composition

The substrate temperature was varied during TiO_2 deposition in Ar plasma, at a constant cathode self-bias of -750 *V*. The temperature of the substrate was set at 350°C. The oxidation states and the chemical composition were investigated by XPS analysis.

In Figure 4.5 the O *1s* and Ti *2p* core levels for the sample prepared without intentional heating and for the sample prepared at a substrate temperature of 350°C are shown. C *1s* and O *1s* core-levels can be well fitted with three components, as described in Figure 4.2. For Ti *2p* core-levels of the samples, different numbers of components were necessary for the fit. In the sample without intentional heating, only two components were necessary, as shown in Figure 4.5. For the sample prepared at a substrate temperature of 350°C, in addition to the two components corresponding to Ti^{4+} states in TiO_2, two more components at lower BEs were necessary for a good fit, identified as Ti^{3+} states of Ti. The BEs for these two peaks were attributed in literature to the presence of point defects, like oxygen vacancies in TiO_2 [6,8]. The BE for O_I, Ti^{4+} $2p_{3/2}$ and Ti^{3+} $2p_{3/2}$ are listed in Table 4.2.

The stoichiometric ratio of the samples was determined and is listed in Table 4.2. It was observed the sample prepared at 350°C substrate temperature has a lower stoichiometric ratio.

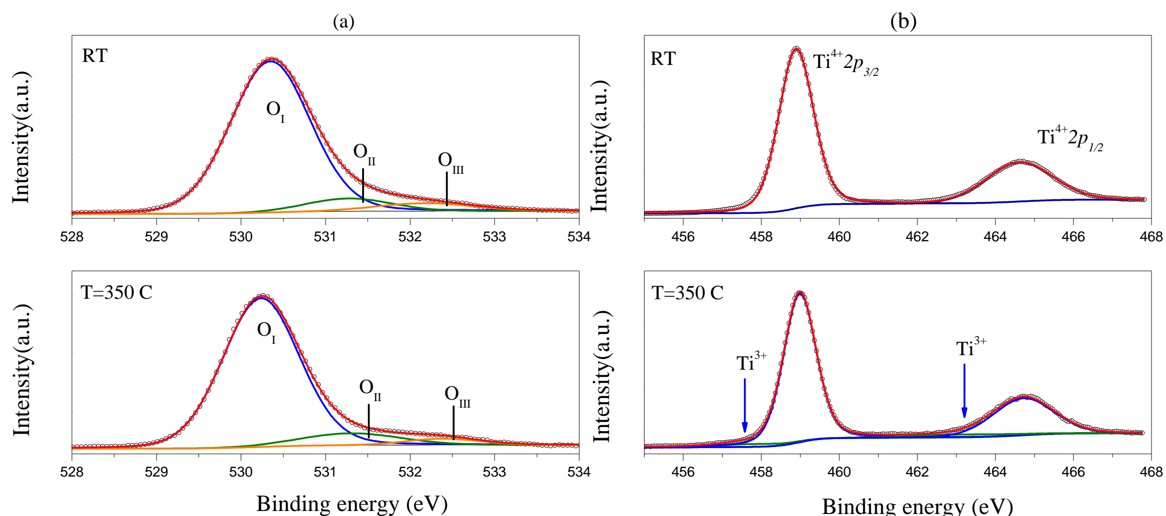

Figure 4.5 O *1s* (a) and Ti *2p* (b) core-levels for TiO_2 prepared at -750 *V*, in Ar plasma, without intentional heating and at a substrate temperature of 350°C

Table 4.2 O_I, Ti^{4+} *$2p_{3/2}$* and Ti^{3+} *$2p_{3/2}$* BEs, ΔE (O_I-Ti^{4+} *$2p_{3/2}$*), O_I/Ti atomic ratio

Substrate temperature	BE(O_I) (eV)	BE(Ti^{4+} $2p_{3/2}$) (eV)	BE(Ti^{3+} $2p_{3/2}$) (eV)	ΔE (O_I-$Ti^{4+}$$2p_{3/2}$) (eV)	$O_I/Ti^{4+,3+}$
RT	530.35	458.89	-	71.46	1.93
350°C	530.24	458.99	457.75	71.25	1.89

4.2. 2.2 Influence of substrate temperature on the films structural properties

The structural properties for TiO_2 films prepared without intentional heating and a temperature to substrate of 350°C, both films prepared in Ar plasma, at -750 *V* were studied. The films without intentional heating were amorphous. For the film prepared at a substrate temperature of 350°C, two diffractions peaks were observed at 2θ=25.49° and 2θ=27.57°, as shown in Figure 4.6. The peak positions were identified to correspond to anatase (101) oriented direction and rutile (110) oriented direction [9], named in Figure 4.6 A(101) and R(110).

The grain size was estimated according to Scherrer equation using A(101) and R(110) peaks and was found to be ~16.7 *nm* and ~12.7 *nm* respectively.

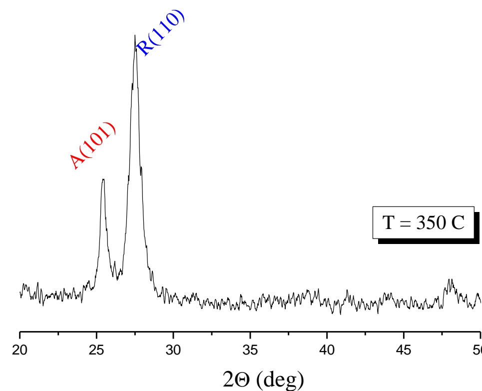

Figure 4.6 XRD pattern for TiO_2 film prepared in Ar, at a substrate temperature of 350°C

4.3. Deposition in Ar-O_2 plasma

4.3.1 Influence of O_2 concentration in the gas on the films growth rate

The addition of oxygen in Ar plasma was investigated, varying the quantity of oxygen in the Ar-O_2 gas mixture from 3 to 20%. The film thicknesses for films prepared at a cathode self-bias voltage of -550 *V* were measured and the growth rate was determined (Figure 4.7). The highest growth rate was found in Ar plasma (0.41±0.02 *nm/min*). When O_2 is introduced in Ar plasma, a decrease of the growth rate is observed until 6%O_2 (0.14±0.02 *nm/min*). A further increase in the oxygen quantity leads to an increase until a value equal to 0.27±0.03 *nm/min* (13%O_2), with no change for higher O_2 concentration. For 20%O_2 added in Ar plasma the growth rate was found to be 0.24±0.02 *nm/min*.

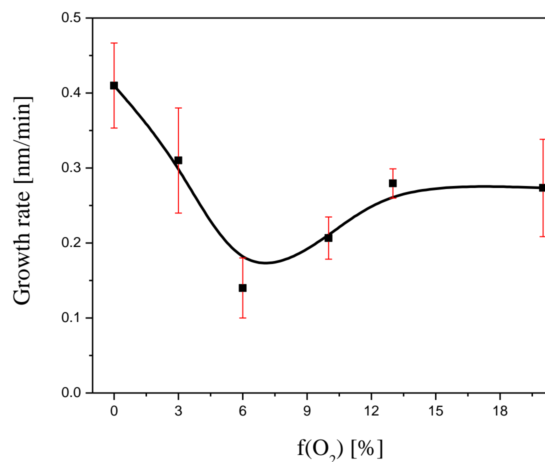

Figure 4.7 Growth rate for TiO_2 films prepared in Ar-O_2 atmosphere, at -550 *V*

4.3.2 Influence of O_2 concentration in the gas on the films chemical composition

X-ray photoelectron spectroscopy measurements were performed for TiO_2 films prepared at –550 *V*, varying the quantity of oxygen introduced in Ar plasma during depositions. The core levels (C *1s*, O *1s*, Ti *2p*) and the valence band (VB) were acquired.

C *1s* and O *1s* core levels spectra for TiO_2 samples deposited in Ar-O_2 atmosphere (3-20% O_2) can be well fitted with three components like for the sample prepared in Ar plasma shown in Figure 4.2 *(a)* and *(b)*, having the same meaning as in the previous section. Ti *2p* core level spectra were fitted with two components (Ti $2p_{3/2}$ and Ti $2p_{1/2}$) corresponding to Ti^{4+} states in TiO_2, similar to the sample deposited in Ar plasma (Figure 4.3 *(a)*). The O_I and Ti^{4+} $2p_{3/2}$ BEs are listed in Table 4.3.

A shift of O *1s* and Ti $2p_{3/2}$ BEs toward higher energies with respect to that of rutile was observed also in this case, with the difference between Ti $2p_{3/2}$ and O_I peak BEs remains constant as 71.28±0.01 *eV*.

Table 4.3 O_I and Ti^{4+} *2p*$_{3/2}$ BEs, O_I/Ti and O_{Ti-OH}/Ti atomic ratios, x in TiO_{2-x} for TiO_2 films in Ar-O_2 (-550 *V*)

[% O_2]	BE(O_I) (eV)	BE(Ti^{4+} 2$p_{3/2}$) (eV)	ΔE (O_I-Ti^{4+} 2$p_{3/2}$) (eV)	O_I/Ti at. ratio	x in TiO_{2-x}	O_{Ti-OH}/Ti
pure-Ar	530.45	459.03	71.42	1.87	0.13	0.12
3%	530.14	458.84	71.30	1.86	0.14	0.07
6%	530.10	458.82	71.28	1.80	0.20	0.08
10%	530.07	458.79	71.28	1.75	0.25	0.23
13%	530.11	458.84	71.27	1.79	0.21	0.14
20%	530.10	458.80	71.30	1.94	0.06	0.03

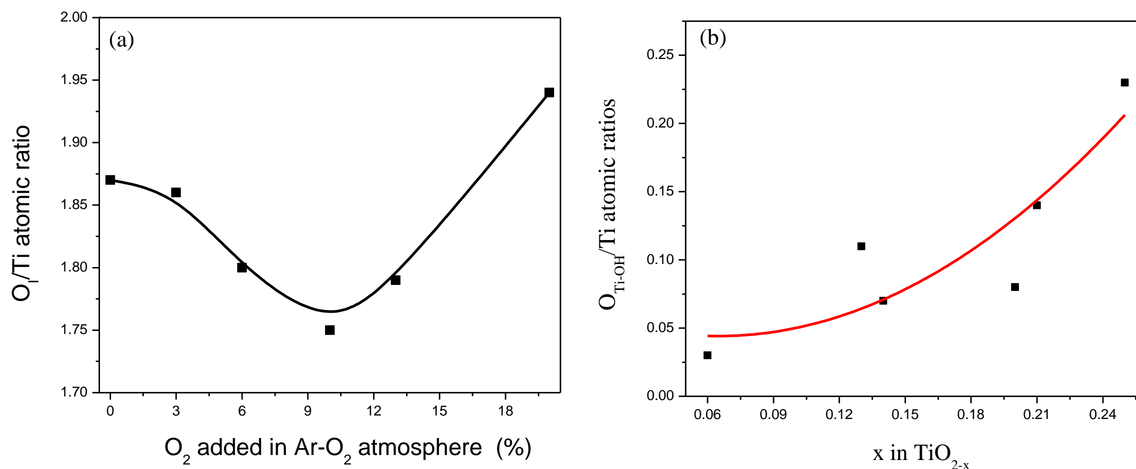

Figure 4.8 *(a)* O_I/Ti atomic ratios for TiO_2 films prepared in Ar-O_2 atmosphere; (b) O_{Ti-OH}/Ti atomic ratios as a function of x in TiO_{2-x} for TiO_2 films prepared in Ar-O_2 atmosphere

O_I/Ti atomic ratios values obtained for TiO_2 films prepared in Ar-O_2 are listed in Table 4.3 and plotted as a function of O_2 concentration added in Ar plasma in Figure 4.8 *(a)*. As can be seen, all the films were under-stoichiometric with respect to the ideal value for TiO_2 (O_{O-Ti}/Ti=2). In Ar plasma a value of 1.87 for O_I/Ti was found. When O_2 is added in Ar plasma a decrease of O_I/Ti until 10%O_2 (O_I/Ti=1.75) followed by an increase after this quantity of oxygen was observed. For 20%O_2 the O_I/Ti ratio was found to be 1.94.

As mentioned in the first section, the deviation from the ideal stoichiometry TiO_2 (quantified as *x* in TiO_{2-x}) can be due to structural defects as O vacancies, but also to the formation of Ti-OH bonds due to H_2O dissociative adsorption [7]. Representing only the O_{Ti-OH}/Ti atomic ratio pertaining to hydroxylated Ti (calculated as in the Section 4.2.1.2), one obtains the plot shown in Figure 4.8 *(b)* as a function of *x* in TiO_{2-x}. From this plot can be concluded that the oxygen vacancies formed during the deposition in Ar-O_2 are partially filled by OH groups forming Ti-OH bonds due to H_2O dissociative absorption.

The influence of oxygen addition in Ar plasma on the valence band states was investigated. Figure 4.9 shows the VB spectra for as-grown TiO_2 films in Ar and Ar-O_2 atmospheres.

Crystal field separates the transition metal *d* states into a triply degenerate state of t_{2g} symmetry and a doubly degenerate state of e_g symmetry. In the octahedral symmetry of titanium dioxide, the e_g states of Ti3d orbitals are σ-bonded with the O *2p* orbitals and the t_{2g} states are π-bonded [10]. The valence band spectrum reflects the density of filled states. The top of TiO_2 valence band is occupied by O *2p* non-bonding states. The e_g states of Ti *3d* orbitals are located at deeper binding energy among the bonding molecular orbitals of the valence band, while the t_{2g} states are situated at lower binding energy than the e_g states. An identification of these states was done for the VB spectra of the films obtained in Ar and Ar-O_2 atmospheres, and are indicated in Figure 4.9.

The VB spectrum for TiO_2 prepared in Ar plasma is well fitted with four Gauss-Lorentz peaks after a Shirley background subtraction, based on the expected contributions from the molecular orbitals [10,11].The results of the fits are given in Table 4.4. As in the case of the core level spectra, all binding energies are given with respect to the Fermi level. The first component located at 4.31 *eV* (peak I in Figure 4.9 *(a)*) is associated with the O *2p* non-bonding states at the top of the valence band. The second and the third components situated at 5.43 *eV* and 7.64 *eV*, respectively (peaks II and III in Figure 4.9 *(a)*) are the result of the *crystal field split* being attributed to O $2p\pi$ and O $2p\sigma$ states. A fourth component (peak IV in Figure 4.9 *(a)*) is located at ~11 *eV*. This peak was observed also for the films prepared in Ar-O_2 atmosphere. The identification of this peak as dissociative or non-dissociative H_2O at TiO_2 surface is difficult due to

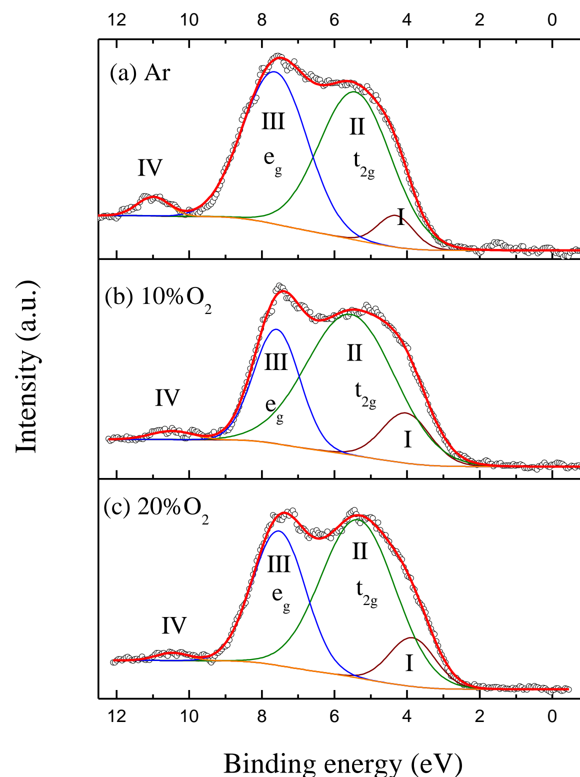

Figure 4.9 VB spectra for TiO_2 films prepared in *(a)* Ar plasma, *(b)* 10%O_2 and (c) 20%O_2 added in Ar plasma

overlapping of different peaks appertaining to hydroxyl groups and molecular water. Hydroxyl groups formed by dissociation of H_2O have two electronic levels of π and σ symmetry. The lower-lying σ level is giving an adsorbed peak reported at a binding energy of 10.8 *eV* overlapping the a_1 level of *molecular* H_2O. The higher-lying π level appertaining to hydroxyl groups overlaps the O *2p* valence band. [10,12-16,17,18]

Table 4.4 Fit results for VB of TiO_2 prepared in Ar and Ar-O_2 plasma and VBM

	VBM [eV]		Peak I	Peak II	Peak III	Peak IV
Ar	3.17	**BE (eV)** **FWHM (eV)**	4.31 1.16	5.43 2.33	7.64 2.07	10.99 1.03
[%O_2]						
3%	2.79	**BE (eV)** **FWHM (eV)**	4.05 1.50	5.54 2.59	7.56 1.66	10.51 1.17
6%	2.62	**BE (eV)** **FWHM (eV)**	4.09 1.57	5.51 2.91	7.58 1.50	10.41 1.29
10%	2.56	**BE (eV)** **FWHM (eV)**	4.03 1.56	5.55 2.86	7.59 1.49	10.48 1.35
13%	2.66	**BE (eV)** **FWHM (eV)**	4.09 1.66	5.52 2.57	7.61 1.65	10.56 1.46
20%	2.64	**BE (eV)** **FWHM (eV)**	3.86 1.49	5.35 2.41	7.53 1.71	10.45 1.06

The VB for TiO_2 prepared with 20%O_2 in Ar-O_2 atmosphere is shown in Figure 4.9 *(c)*. The valence band spectra for all samples prepared in Ar-O_2 can be well fitted with the same number of components like in VB of TiO_2 prepared in pure-Ar. The results of the fits are given in Table 4.4.

The valence band maximum energy (VBM) was determined by extrapolating a linear fit of the final spectrum region to zero intensity, after a Shirley background subtraction. The obtained values for the VBM for both TiO_2 films prepared in Ar and Ar-O_2 atmosphere are reported in Table 4.4. A decrease of VBM is observed when oxygen is added in Ar plasma. A similar trend was observed for the binding energy of O1s

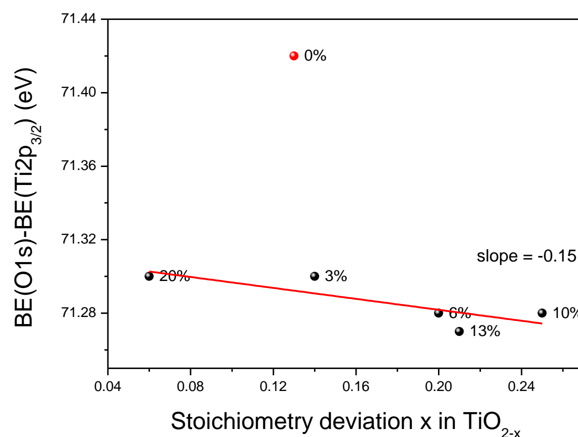

Figure 4.10 BE(O_I)-BE($Ti2p_{3/2}$) in function of x in TiO_{2-x}

core level, involved in Ti^{4+}-O bonds. The results are plotted in Figure 4.10. The higher x, the lower the energy difference between O1s and $Ti2p_{3/2}$ peaks. It can also be seen that the sample made in pure argon deviate from the linear fit of the data points. This kind of relationship can constitute a valuable tool to check the presence of "free" vacancies.

In order to understand if the e_g states corresponding to σ bonds or the t_{2g} states corresponding to π bonds are moving towards higher energies with increasing the stoichiometry, the e_g and t_{2g} BEs referred to Ti $2p_{3/2}$ BE in function of x in TiO_{2-x} are plotted in Figure 4.11. The slopes are given in the figure for each linear dependence. The graphs indicate that both peaks corresponding to the e_g and t_{2g} states are moving towards higher BEs, but the peak corresponding to t_{2g} states is moving more toward higher energies when the substoichiometry is increased (x in TiO_{2-x}).

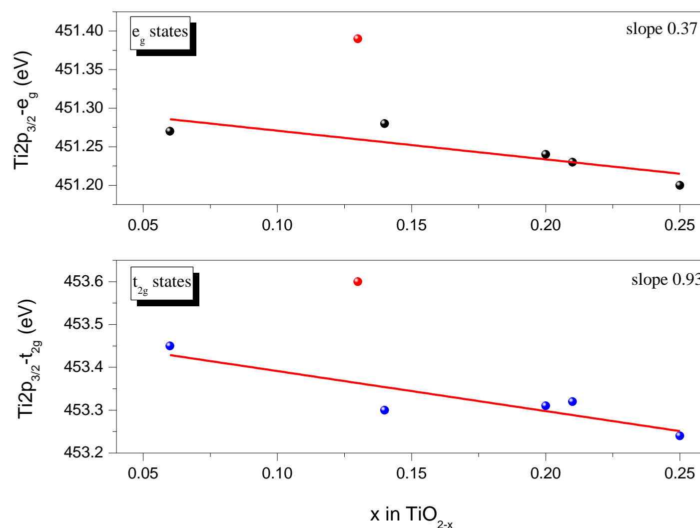

Figure 4.11 Ti $2p_{3/2}$-e_g and $Ti2p_{3/2}$-t_{2g} in function of x in TiO_{2-x}

Information about the OH states (as Ti-OH and/or OH from molecular water) at TiO_2 surface can be extracted also from the VB spectra. From the VB spectra, the area under the peak IV (in Figure 4.9), indicated to be given by the contribution coming from OH groups or H_2O was determined and plotted as a function of O_2 in Ar-O_2 atmosphere (Figure 4.12 (a)). At small quantities of O_2, the OH signal is strongly decreasing. A further increase in O_2 added in Ar plasma leads to a maximum at 10% O_2 for OH signal. In order to understand the relation between the hydroxylation and the oxygen deficiency in TiO_{2-x}, in Figure 4.12 (b) the OH3σ/VB area is plotted in function of x in TiO_{2-x}, where one can observe that the higher x, the higher OH3σ/VB area ratio. The sample obtained in pure argon plasma gives a much higher OH3σ/VB area ratio value than the ones deposited in Ar-O_2 plasmas, even for a same sub-stoichiometry. It is more likely that the oxygen vacancies are only partially hydroxylated in the latter films, vacancies still exist while for the film deposited in pure Ar plasma, the lacking oxygen in oxide bondings are in major part involved in hydroxyl groups.

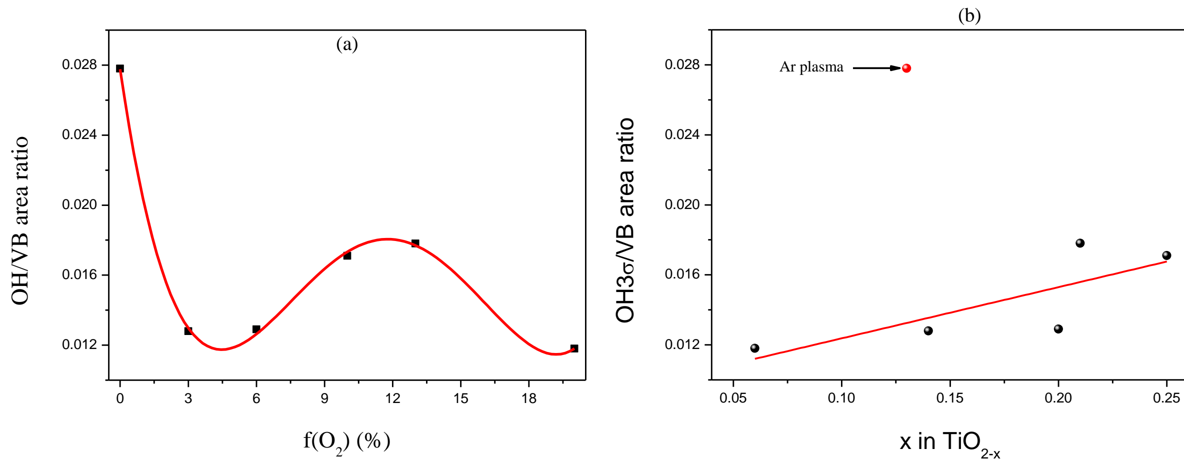

Figure 4.12 OH3σ/VB in function of (a) O_2 added in Ar plasma and (b) of x in TiO_{2-x}

4.3.3 Influence of O_2 concentration in the gas on the films structure and morphology

XRD was performed for TiO_2 films prepared in Ar and Ar-O_2 (20% O_2), at cathode self bias voltage of -750 *V*. The film prepared in Ar plasma was amorphous, while the film prepared in 20% O_2 reveals both anatase and rutile phases of TiO_2, as shown in Figure 4.13. Some authors reported that amorphous TiO_2 can be defined as a material with crystalline domains of a size below the detection limit of XRD (<3-5 nm) [19]. The grain size was estimated according to Scherrer equation using the peaks indicated in the Figure 4.13

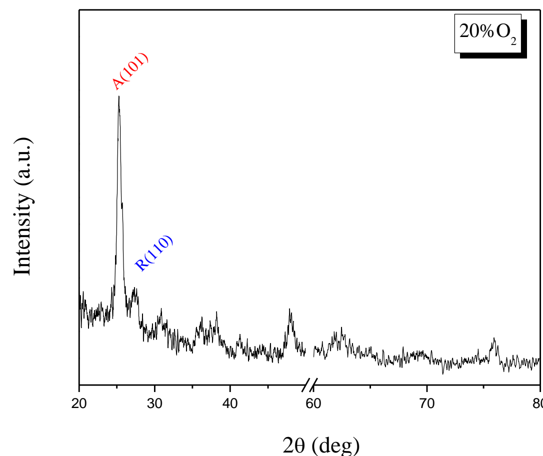

Figure 4.13 XRD spectra for TiO_2 films prepared in Ar-O_2 (20% O_2)

(A(101) and R(110)) and was found to be ~14.8 *nm* and ~4.2 *nm* respectively.

SEM was performed for TiO_2 films prepared in Ar and Ar-O_2 (20%O_2) atmospheres. Figure 4.14 shows the top-view and cross-section images of TiO_2 films deposited on *n*-type Si *(100)* substrates. For both films, the surface morphology shows a dense morphology with agglomerated grains. As seen from cross-section images the films are very compact, homogeneous, adherent to the Si *(100)* substrates, and show a dense columnar growth.

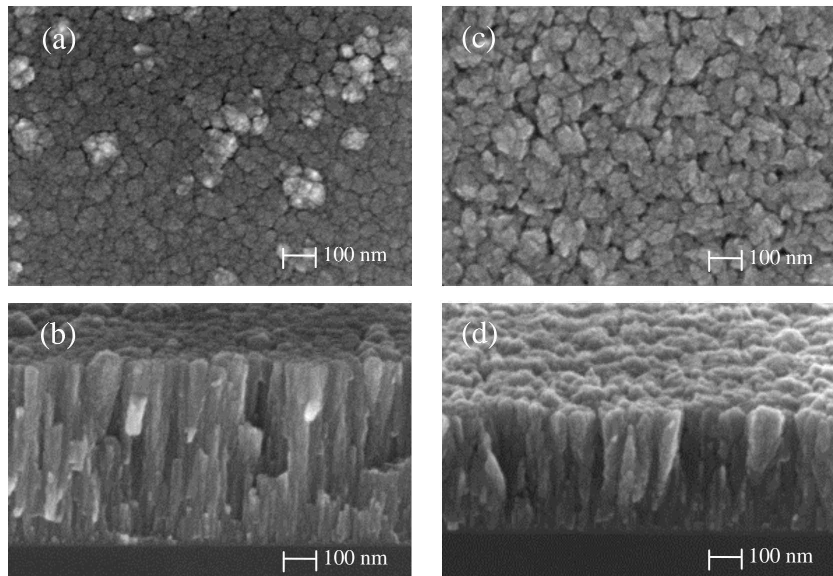

Figure 4.14 Surface and cross-section images for TiO_2 films prepared in (a), (b) Ar; (c), (d) Ar-O_2 plasma

4.3.4 Influence of O_2 concentration in the gas on the films chemical composition for post-growth annealed in vacuum films

Post-growth annealing at 900°C for 1h in vacuum was performed for TiO_2 thin films prepared in Ar and Ar-O_2 (20%O_2), at a self-bias cathode voltage of -750 *V*, in order to improve the structure of the films.

O *1s* and Ti *2p* core levels were acquired using XPS, in order to investigate the oxidation state of the films after post-growth annealing in vacuum. In Figure 4.15 the O *1s* and Ti *2p* core levels for as-grown and annealed TiO_2 films, prepared in Ar and Ar-O_2 plasma are shown. O_I and Ti^{4+} $2p_{3/2}$ BEs are listed in Table 4.5 for both as-grown and annealed TiO_2 films. A shift toward lower BEs for annealed samples is observed for both core-levels. For the sample prepared with 20%O_2 added in Ar plasma, an increase in the O_{II} component of O *1s* peak is observed. Only the Ti^{4+} state was identified in Ti *2p* spectra for both films.

Table 4.5 O_I and Ti^{4+} $2p_{3/2}$ BEs, O_I/Ti, O_{II}/Ti and C_{II}/Ti atomic ratios for as-grown and annealed TiO_2 prepared in Ar and Ar-O_2 plasma

	BE(O_I) (eV)		**BE($Ti^{4+}2p_{3/2}$) (eV)**		**ΔE (eV)**		**O_I/Ti at. ratio**		**O_{II}/Ti at. ratio**		**C_{II}/Ti at. ratio**	
	as-gr	ann	as-gr	ann	as-gr	ann	as-gr	ann	as-gr	ann	as-gr	ann
Ar	530.22	529.73	458.79	458.47	71.43	71.26	1.92	1.79	0.33	0.85	0.26	0.37
20% O_2	530.05	529.68	458.74	458.40	71.31	71.28	1.74	1.85	0.44	0.78	0.29	0.26

The stoichiometry of the samples and the O_{II}/Ti and C_{II}/Ti atomic ratios before and after annealing were compared in Table 4.5. From the values it can be seen that the annealing of sample prepared in Ar plasma is decreasing the stoichiometric ratio and the O_{II} component of O *1s* (indicated to come from Ti-OH bonds, possible C-O bondings in C-O-C and C-OH groups contribution and from Ti_2O_3 phase contribution) is increasing, in the same way as C_{II} component of C *1s* (indicated to come from C-O and C-O-C and/or C-OH groups). Most probably, the oxygen vacancies formed during the annealing are subsequently filled with OH groups. For the sample prepared in Ar-O_2 plasma, the stoichiometric ratio is increasing after annealing and the O_{II} is increasing too. The increase of O_{II} peak after annealing in vacuum is most likely due to Ti-OH bonds increase.

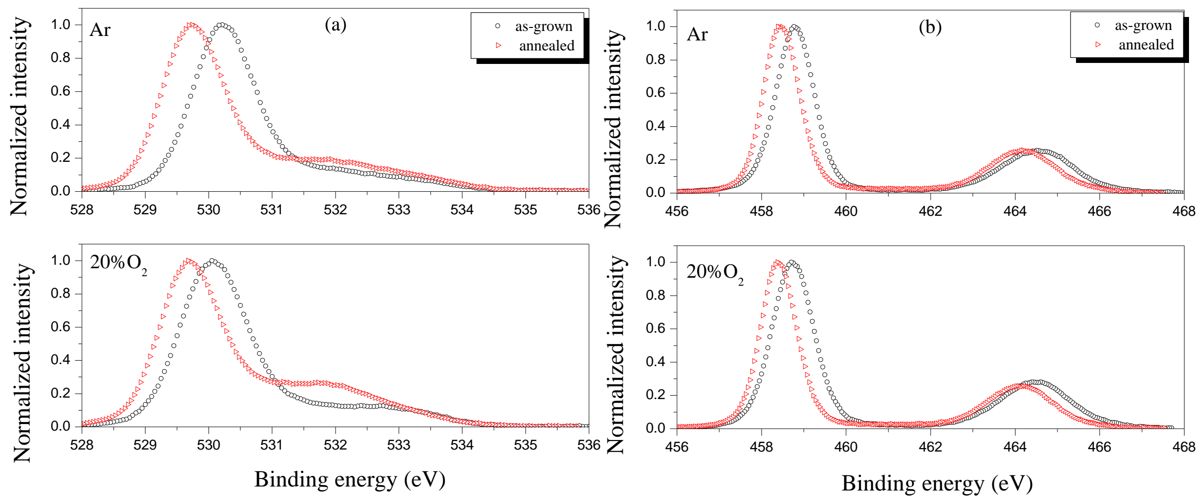

Figure 4.15 O 1s (*a*) and Ti 2p (*b*) core-levels XPS spectra for as-grown and post-growth annealed TiO_2 films prepared in Ar and Ar-O_2

4.3.5 Influence of O_2 concentration in the gas on the films structure and morphology for post-growth annealed in vacuum films

The influence of annealing on the structural properties of TiO_2 films prepared in Ar and Ar-O_2 plasma at -750 *V* was investigated with XRD. As seen in Figure 4.16, in both films anatase and rutile phases of TiO_2 were identified after annealing. The diffraction patterns for anatase and rutile phases of TiO_2 are given in Figure 4.16 for comparison.

The grain size was calculated using to Scherrer equation and are listed in Table 4.6 together with the *A(101)* and *R(110)* peaks positions and FWHMs used for grain size calculations.

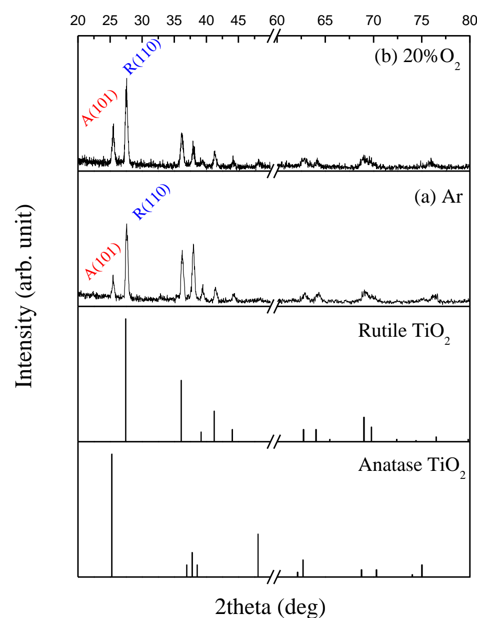

Figure 4.16 XRD spectra for annealed TiO_2 films, prepared in (a) Ar and (b) Ar-O_2 plasma; for comparison, the diffraction patterns of anatase and rutile phases of TiO_2 are shown

Table 4.6 *2θ* Bragg angle, FWHMs of A(101) and R(110) peaks, and grain size values for annealed in vacuum TiO_2 films prepared in Ar and Ar-O_2

Gas	Phase	2θ (deg)	FWHM	Grain size (nm)
Ar	*A (101)*	25.35	0.407	~21.5
	R (110)	27.66	0.375	~19.6
20%O_2	*A (101)*	25.52	0.400	~20.1
	R (110)	27.56	0.364	~22.1

The top-view and cross-section images obtained with SEM for annealed TiO_2 films, prepared in Ar and Ar-O_2 plasmas are shown in Figure 4.17. The surface of the films was damaged due to high temperature of annealing. A complete destruction of the columnar structure is observed, with formation of a porous structure.

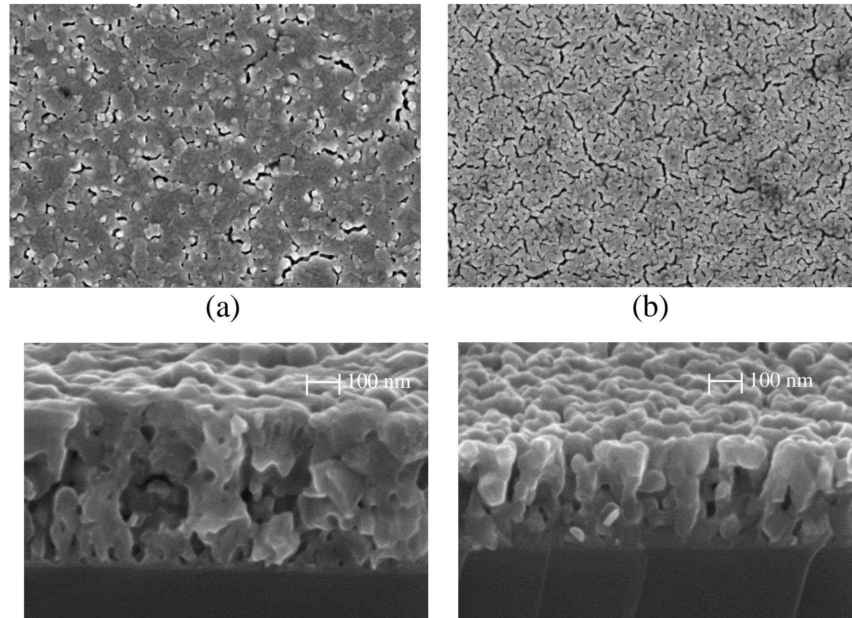

Figure 4.17 Top-view and cross section images for annealed TiO_2 films prepared in (a) Ar; (b) Ar-O_2

4.4. Deposition in Ar-H_2 plasma

4.4.1 Influence of H_2 concentration in the gas on the films growth rate

The addition of hydrogen in Ar plasma was investigated, varying the quantity of hydrogen from 3 to 50%.The film thicknesses were measured for films prepared at a cathode self-bias voltage of -550 *V* and the corresponding growth rate is plotted in Figure 4.18.

A decrease of the growth rate is observed, when a small quantity of hydrogen is added in Ar plasma (3%H_2), but a further increase in H_2 value leads to growth rate values similar to the one obtained in Ar plasma. For 20%H_2 in Ar plasma a value of 0.35 *nm/min* was obtained.

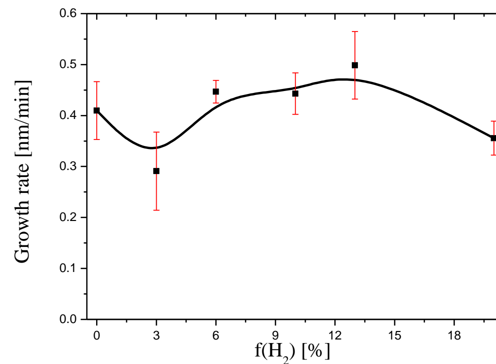

Figure 4.18 Growth rate for TiO_2 films prepared in Ar-H_2 atmosphere

4.4.2 Influence of H_2 concentration in the gas on the films chemical composition

X-ray photoelectron spectroscopy measurements were performed for TiO_2 films prepared at –550 *V*, varying the quantity of hydrogen introduced in Ar plasma during depositions. The core levels (C *1s*, O *1s*, Ti *2p*) and the valence band (VB) were acquired.

Like in samples deposited in Ar and Ar-O_2 plasma, C *1s* and O *1s* core levels spectra for TiO_2 samples deposited in Ar-H_2 atmosphere (3-50% H_2) can be well fitted with three components. For the fit performed on Ti *2p* core level spectra four components were necessary for TiO_2 films prepared in Ar-H_2, as shown in Figure 4.19 *(b)*. For comparison, the Ti *2p* core level spectrum for the film prepared in Ar plasma is shown in Figure 4.19 *(a)*. In addition to the two components corresponding to Ti^{4+} states in TiO_2, two more components at lower BEs were necessary for a good fit, identified as Ti^{3+} states of Ti. The BEs for these two peaks were attributed in literature to the presence of point defects, like oxygen vacancies in TiO_2 [6,8]. At the same binding energy value was reported also Ti_2O_3 phase [20,21]. The BE for O_I, Ti^{4+} $2p_{3/2}$ and Ti^{3+} $2p_{3/2}$ are listed in Table 4.7. A shift of O *1s* and Ti^{4+} $2p_{3/2}$ BEs toward higher energies with respect to that of rutile was observed also in this case. The difference between Ti^{4+} $2p_{3/2}$ and O_I peak BEs remains constant as 71.41±0.03 *eV*.

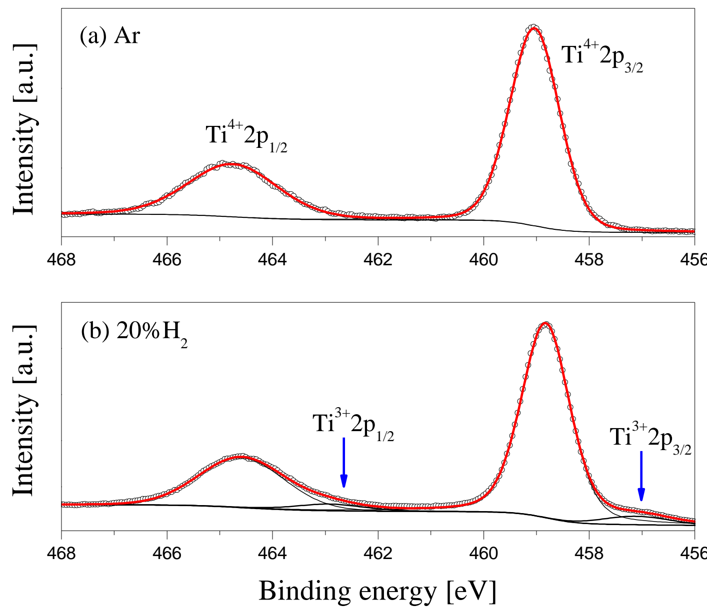

Figure 4.19 Ti *2p* core levels for TiO_2 films prepared in *(a)* Ar plasma and *(b)* Ar-H_2 plasma (20% H_2)

Table 4.7 O_I, Ti^{4+} $2p_{3/2}$ and Ti^{3+} $2p_{3/2}$ BEs, O_I/Ti atomic ratios and x in TiO_{2-x} for TiO_2 prepared in Ar-H_2

[% H_2]	BE(O_I)	BE(Ti^{3+} $2p_{3/2}$) (eV)	BE(Ti^{4+} $2p_{3/2}$) (eV)	ΔE (O_I-Ti^{4+} $2p_{3/2}$) (eV)	O_I/Ti at. ratio	x in TiO_{2-x}
3%	530.35	457.26	458.87	71.38	1.92	0.08
6%	530.31	457.25	458.86	71.45	1.88	0.12
10%	530.35	457.35	458.91	71.44	1.93	0.07
13%	530.33	457.28	458.92	71.41	1.86	0.14
20%	530.27	457.11	458.83	71.44	1.82	0.18
30%	530.47	457.57	459.08	71.39	1.82	0.18
50%	530.61	457.65	459.23	71.38	1.71	0.29

The stoichiometry of TiO_2 films prepared in Ar-H_2 was determined taking into account both Ti^{4+} and Ti^{3+} states of Ti and plotted in Figure 4.20 (a). The values of $O_I/Ti^{4+,3+}$ are listed in Table 4.7. The addition of hydrogen in Ar plasma leads to a decrease of stoichiometry from the ideal value, with increasing the hydrogen quantity in deposition. Plotting the contribution of Ti-OH and Ti_2O_3 at O *1s* peak as a function of x in TiO_{2-x} a dependence like in Figure 4.20 (b) was obtained. The values can be fitted with a linear function, with a slope of 0.34 and a high value of intercept (0.099). For all the TiO_2 films prepared in Ar-H_2 the contribution of oxygen in O_{II} states is higher than x in TiO_{2-x}, which means that beside Ti-OH bonds, there is an additional contribution, most probably Ti_2O_3 phase, indicated also by Ti^{3+} states identified in Ti *2p* XPS spectra.

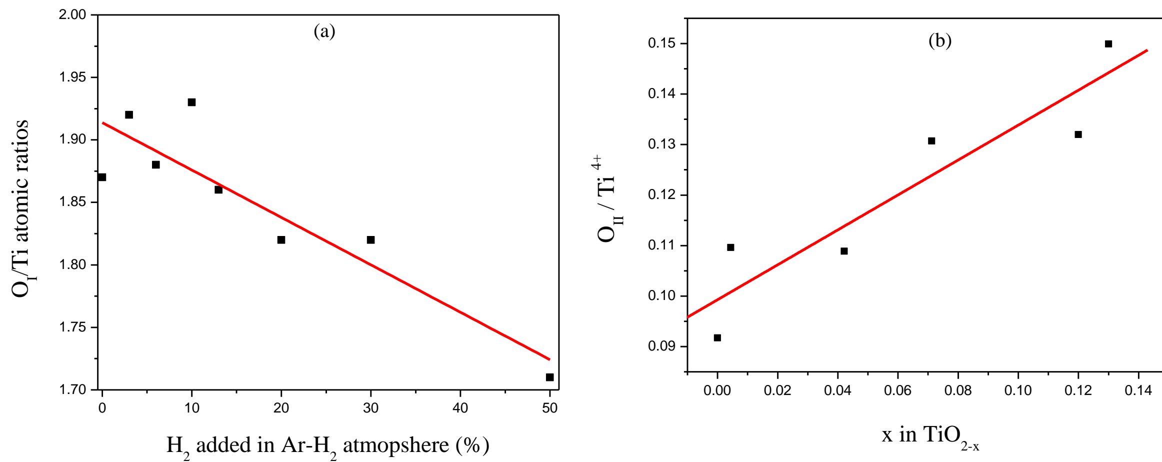

Figure 4.20 (a) O_I/Ti atomic ratios and (b) O_{II}/Ti^{4+} in function of x in TiO_{2-x}

In order to confirm the presence of free oxygen vacancies in the oxide lattice, the energy difference between O_I component of the O1s spectrum and $Ti2p_{3/2}$ (due to Ti^{4+} states) is plotted in function of the deviation from ideal stoichiometry x in TiO_{2-x}, as in the case of the films deposited in Ar-O_2 plasma. The results are displayed in Figure 4.21. The trend observed in the case of the films deposited in Ar-O_2 plasma is less clear here. The stoichiometry deficiency of the oxide is mostly due to the involvement of Ti in other bonds (with OH, H), and free oxygen vacancies are not in majority.

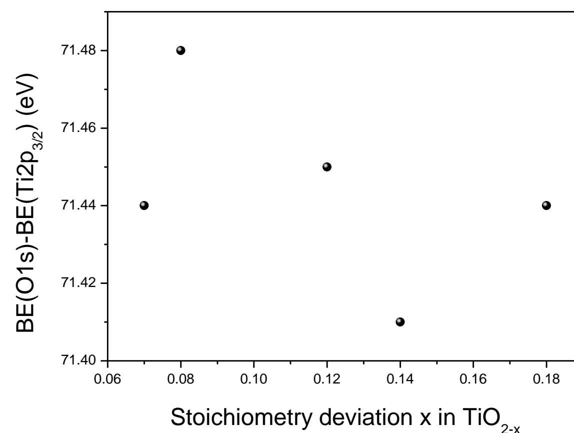

Figure 4.21 Binding energy difference between the $Ti2p_{3/2}$ and O1s (component O_I) core levels in function of x in TiO_{2-x}

Some noticeable changes are observed in the VB of TiO_2 thin films prepared in Ar-H_2 atmosphere. In Figure 4.22 the VB spectra of TiO_2 prepared in 20%H_2 is shown, together with the VB spectrum for TiO_2 prepared in Ar plasma, for comparison. The results for the fits are given in Table 4.8.

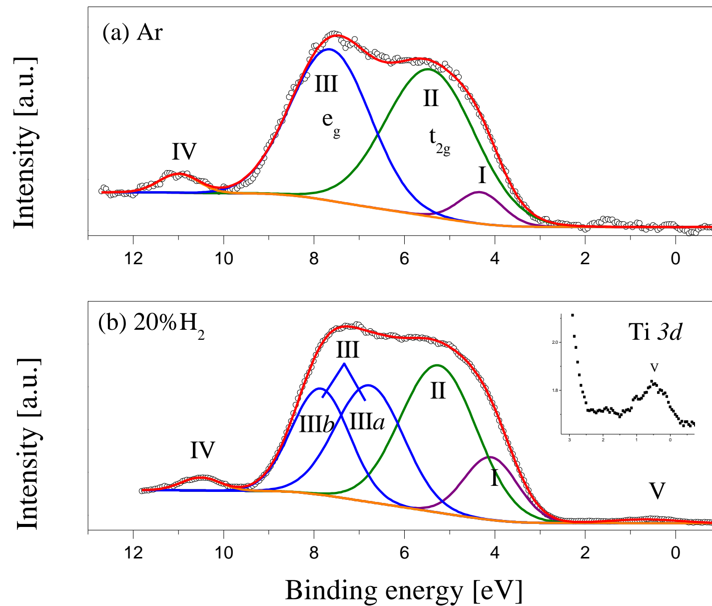

Figure 4.22 VB spectra for TiO_2 films prepared in *(a)* Ar plasma and *(b)* Ar-H_2 plasma (20%H_2)

The VB for TiO_2 samples prepared in Ar-H_2 was best fitted with six components, instead of four as in the case of TiO_2 in Ar plasma. One of the two additional peaks is situated between the valence band maximum and the Fermi level (peak V in Figure 4.22 *(b)*) at 0.66 *eV*. In literature, this peak has been reported for under-stoichiometric TiO_2. It has been assigned to Ti *3d* states being mostly attributed to oxygen vacancies [4-6,11], but also to other defect states like interstitial Ti [22]. The binding energies for this peak are given in Table 4.8. In fact, a similar evolution of both this peak area and that of Ti^{3+} $2p_{3/2}$ peak with the quantity of H_2 introduced in Ar plasma was found. The dependence of Ti *3d*/VB area ratio and Ti^{3+} $2p_{3/2}$/ Ti^{4+} $2p_{3/2}$ atomic ratio on H_2 gas concentration is shown in Figure 4.23. The detected Ti *3d* states can be reasonably attributed to oxygen vacancies.

Table 4.8 VBM, BEs and widths of valence band peaks I through V, A_{IIIa}/A_{IIIb} area ratio

[H₂] in Ar-H₂	VBM (eV)		Peak I	Peak II	Peak III		Peak IV	Peak V	A_{IIIa}/A_{IIIb}
					IIIa	IIIb			
3%	3.02	**BE (eV)**	4.02	5.02	6.45	7.74	10.58	1.32	0.76
		FWHM (eV)	1.05	2.04	1.63	1.62	1.17	2.47	
6%	2.99	**BE (eV)**	3.96	4.99	6.49	7.74	10.53	0.93	0.98
		FWHM (eV)	1.10	1.96	1.76	1.57	1.28	2.17	
10%	3.06	**BE (eV)**	4.12	5.12	6.61	7.84	10.57	0.86	1.09
		FWHM (eV)	1.25	1.99	1.82	1.56	1.22	1.98	
13%	3.14	**BE (eV)**	4.21	5.41	6.89	7.91	10.62	0.70	0.89
		FWHM (eV)	1.29	2.07	1.60	1.49	1.18	1.68	
20%	2.95	**BE (eV)**	4.09	5.25	6.77	7.85	10.50	0.66	1.30
		FWHM (eV)	1.39	1.99	1.77	1.50	1.02	1.82	

The other additional peak was necessary to fit the VB spectra in the e_g states region. Instead of one peak III, such peak is split into peak III*a* and III*b*, located at 6.77 *eV* and 7.85 *eV*, respectively. Such a split in the e_g states region has been reported also by other authors in their work [11,23-26] for TiO_2 particles with dimensions of 10-20 nm [24] and for annealed nanocrystalline TiO_2 films which have larger crystallite sizes being correlated with a conversion upon annealing to the *anatase* phase with a larger, more complex unit cell [11]. The existence of this split in nanocrystalline anatase phase of TiO_2 is also confirmed by Choi et al. [27] for grain sizes of 12-30 nm.

Different physical mechanisms have previously been proposed to explain the splitting of the e_g band. An explanation is that the splitting may be due to slight distortions of the TiO_6 octahedron in rutile and anatase structures that results from the configurationally deformation predicted by the Jahn-Teller theorem [25,28]. The splitting is also attributed by some authors to effects of long-range orders, and in particular to the influence of the interactions of Ti with the second-neighbour shell [23,24,29].

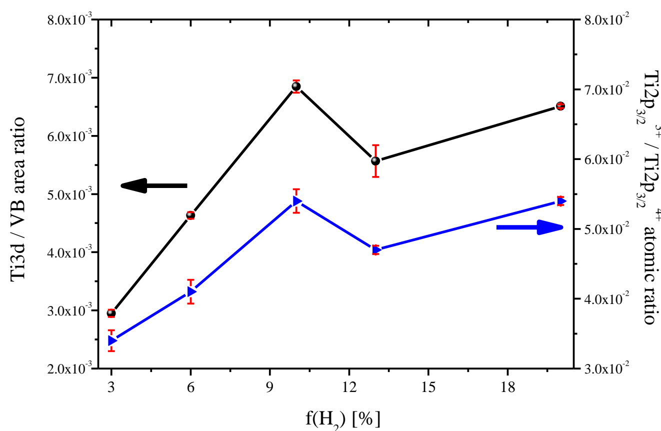

Figure 4.23 Ti3d/VB area ratio and Ti^{3+}/ Ti^{4+} atomic ratio dependence on the %H_2

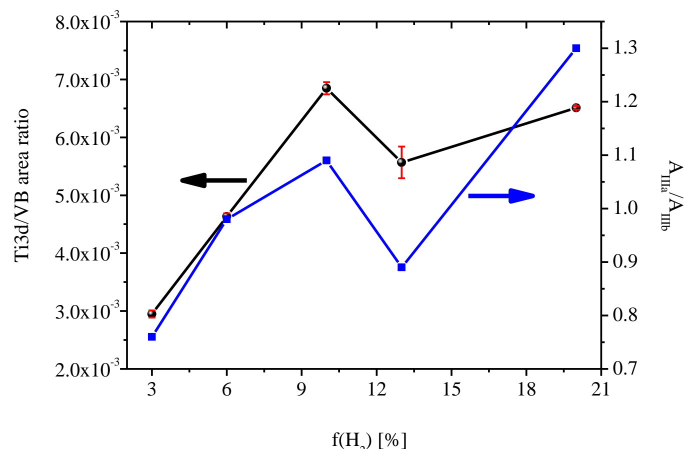

Figure 4.24 Ti3d/VB area ratio and A_{IIIb}/A_{IIIa} dependence on the %H_2

In order to understand better the behaviour of this split, the area ratio A_{IIIa}/A_{IIIb} calculated on the basis of both III*a* and III*b* peaks area ratio was determined and listed in Table 4.8. A correlation was found the oxygen vacancies represented by Ti *3d* peak (peak V) and the area ratio A_{IIIa}/A_{IIIb} (Figure 4.24). According to this plot the split of e_g states is following the oxygen vacancies behaviour.

The values of VBM for TiO_2 samples prepared in Ar-H_2 are listed in Table 4.8. No clear trend was observed.

In order to follow the OH states present at the surface when H_2 is added in Ar plasma, the OH3σ/VB area ratio together with Ti *3d* area ratio and Ti *3d* BEs is plotted as a function of H_2 added in Ar plasma in Figure 4.25. A direct correlation was found between OH3σ peak area ratio to VB and oxygen vacancies, represented by Ti *3d*/VB area ratio. OH3σ peak area ratio to VB is decreasing when the oxygen vacancies are increasing. This behavior leads to the conclusion that the water is dissociated at oxygen vacancies, forming OH groups. In the same time, the BE of peak Ti *3d* correlated with the oxygen vacancies in TiO_2, is decreasing together with the OH groups.

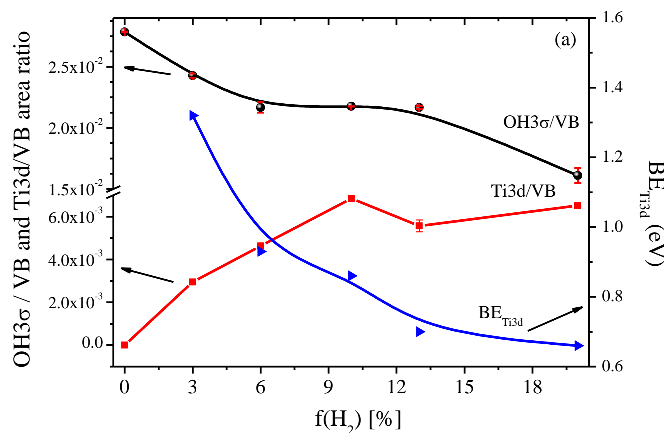

Figure 4.25 OH3σ/VB and Ti *3d* area ratio and Ti *3d* BEs in function of H_2 in Ar-H_2 plasma

4.4.3 Influence of H_2 concentration in the gas on the films structure and morphology

XRD pattern reveals an amorphous structure for TiO_2 samples prepared in Ar-H_2 (20%H_2), at a cathode self-bias of -750 *V*.

SEM images with the top-view and the cross-section for TiO_2 in Ar-H_2 (20%H_2) are shown in Figure 4.26 The surface morphology shows a dense morphology with agglomerated grains. The films are very compact, homogeneous, adherent to the Si *(100)* substrates, and show a dense columnar growth.

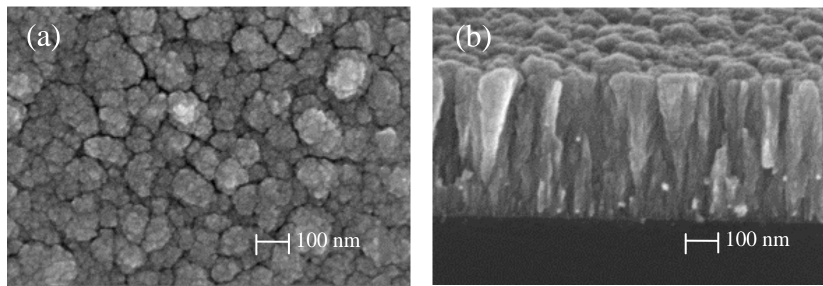

Figure 4.26 Top-view (a) and cross-section (b) images for TiO_2 prepared Ar-H_2 plasma (20% H_2)

4.4.4 Influence of H_2 concentration in the gas on the films chemical composition for post-growth annealed in vacuum films

Post-growth annealing at 900°C for 1h in vacuum was performed for TiO_2 thin films Ar-H_2 (20% H_2), at a self-bias cathode voltage of -750 *V*, in order to change the amorphous structure of the films.

Like in the case of TiO_2 films prepared in Ar and Ar-O_2, the oxidation states and the stoichiometry were investigated before and after annealing. In Figure 4.27 the O *1s* and Ti *2p* core levels for as-grown and annealed TiO_2 film prepared in Ar-H_2 plasma are shown. For comparison, the core-levels recorded for TiO_2 prepared in Ar plasma are shown in the same figure. O_I and Ti^{4+} $2p_{3/2}$ BEs are listed in Table 4.9. In contrast to the samples prepared in Ar and Ar-O_2, the shift toward higher BE of O *1s* and Ti *2p* was observed for TiO_2 prepared in Ar-H_2. The Ti^{3+} states observed in the sample prepared in Ar-H_2 atmosphere are not anymore detected after annealing.

O_I/Ti, O_{II}/Ti and C_{II}/Ti atomic ratios were determined and listed in Table 4.9. The annealing treatment induces a decrease in the stoichiometry of TiO_2 films prepared in Ar-H_2. O_{II} component of O *1s* spectrum is increasing but together with C_{II} component of C *1s* spectrum, which means that most of O_{II} component is due to C-O bonds.

Table 4.9 O_I and Ti^{4+} $2p_{3/2}$ BEs, O_I/Ti, O_{II}/Ti and C_{II}/Ti atomic ratios for as-grown (as-gr) and annealed (ann) TiO_2 prepared in Ar and Ar-H_2 plasma

	BE(O_I) (eV)		**BE($Ti^{4+}2p_{3/2}$) (eV)**		**BE($Ti^{3+}2p_{3/2}$) (eV)**		**ΔE (eV)**		**O_I/Ti at. ratio**		**O_{II}/Ti at. ratio**		**C_{II}/Ti at. ratio**	
	as-gr	ann	as-gr	ann	as-gr	ann	as-gr	ann	as-gr	ann	as-gr	ann	as-gr	ann
Ar	530.22	529.73	458.79	458.47	-	-	71.43	71.26	1.92	1.79	0.33	0.85	0.26	0.37
20%H_2	530.22	530.50	458.83	459.30	457.19	-	71.39	71.20	1.73	1.69	0.36	1.16	0.15	1.96

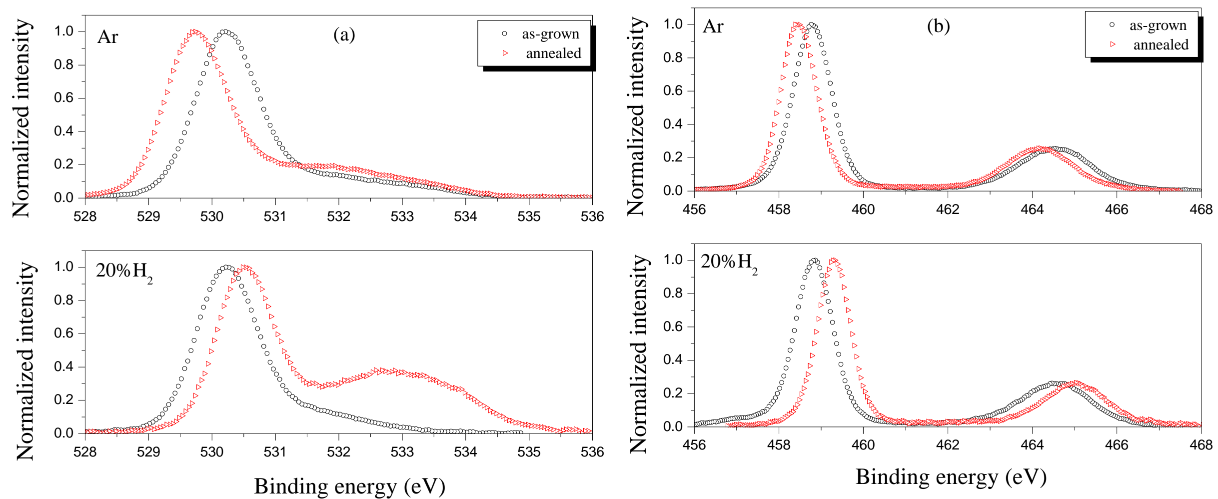

Figure 4.27 O 1s (*a*) and Ti 2p (*b*) core-levels XPS spectra for as-grown and post-growth annealed TiO_2 films prepared in Ar and Ar-H_2

4.4.5 Influence of H_2 concentration in the gas on the films structure and morphology for post-growth annealed in vacuum films

The structure of annealed TiO_2 film prepared in Ar-H_2 plasma at -750 *V* was investigated with XRD (Figure 4.28). After annealing, the film reveals the rutile TiO_2 phase growth from an amorphous structure with grain size of ~15 *nm*.

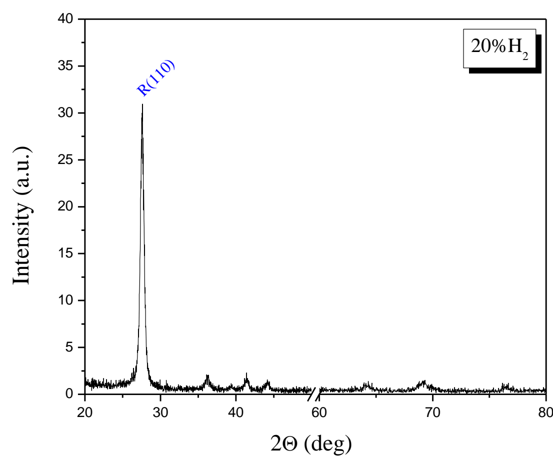

Figure 4.28 XRD for annealed TiO_2 film, prepared in Ar-H_2 plasma

In Figure 4.29 the top-view and cross-section images for the annealed TiO_2 film prepared in Ar-H_2 are shown. The columnar structure from the as-grown film is preserved after annealing, with less porosity.

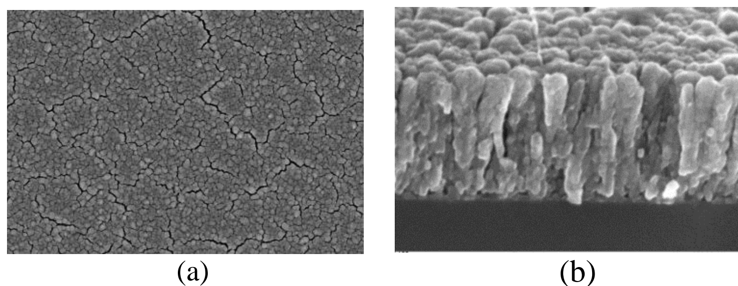

Figure 4.29 Top-view (a) and cross-section (b) images for annealed TiO_2 film prepared in Ar-H_2 plasma

4.5 Concluding remarks

The influence of cathode self-bias voltage variation on the TiO_2 films chemical composition deposited in Ar plasma at room temperature was investigated. The results showed that the deviation from stoichiometry in these films is due to hydroxylated Ti, and not to oxygen vacancies. Films with an amorphous structure were obtained in Ar plasma at room temperature. SEM images reveal a dense surface morphology with agglomerated grains and very compact, homogeneous columnar growth. The post-growth annealing in vacuum at 900°C of TiO_2 films prepared in Ar plasma improved the crystalline structure of the films, but no additional oxygen vacancies were observed. Most probably, the oxygen vacancies formed during the annealing are subsequently filled with OH groups.

If the substrate temperature is increased during the deposition at 350°C, two peaks with low intensities can be detected in Ti *2p* XPS core level spectrum, attributed to Ti^{3+} states of Ti. The BEs of these peaks are identified as oxygen vacancies in TiO_2. The obtained film is polycrystalline, with anatase (101) and rutile (110) oriented direction.

The investigation of the TiO_2 films chemical composition deposited in Ar-O_2 atmosphere at room temperature reveals that the oxygen vacancies formed during the deposition in Ar-O_2 are partially filled by OH groups forming Ti-OH bonds due to H_2O dissociative absorption. No Ti^{3+} states indicating the presence of oxygen vacancies were detected in the Ti *2p* XPS core level spectrum. But an effect of oxygen concentration in the gas mixture (and the number of formed oxygen vacancies) on the VBM was observed: the higher x in TiO_{2-x}, the larger the VBM recession towards higher energies. Films with both anatase and rutile phases of TiO_2 were obtained in Ar-O_2 atmosphere. SEM images reveal a dense surface morphology with agglomerated grains and very compact, homogeneous columnar growth. Similar to the films prepared in Ar plasma, the post-growth annealing in vacuum at 900°C of TiO_2 films prepared in Ar-O_2 atmosphere improved the crystalline structure, but the oxygen vacancies formed during annealing in vacuum are subsequently filled with OH groups.

The TiO_2 films chemical analysis deposited in Ar-H_2 atmosphere at room temperature reveals the Ti^{3+} states indicating the presence of oxygen vacancies in the Ti *2p* XPS core level spectrum. The VB investigation allowed the identification of two additional features, comparing with VB corresponding to TiO_2 films prepared in Ar-O_2: one peak (Ti 3d) situated between the VBM and the Fermi level attributed to under-stoichiometric TiO_2 and the other additional peak was necessary to fit the VB spectra in the e_g states region. Such a split in the e_g states region has been reported for TiO_2 particles with reduced dimensions and for annealed nanocrystalline TiO_2 films which have larger crystallite sizes being correlated with a conversion upon annealing to the anatase phase with a larger, more complex unit cell. The XRD patterns for these films reveal an amorphous structure. SEM images show a dense surface morphology with agglomerated grains and very compact, homogeneous columnar growth. The post-growth annealing in vacuum at 900°C of TiO_2 films prepared in Ar-H_2 atmosphere improved the crystalline structure of the films, the rutile phase of TiO_2 being obtained. A different behaviour of the films structure as compared with the films prepared in Ar and Ar-O_2

plasma was observed in the SEM images for the films prepared in Ar-H_2 plasma. The columnar structure from the as-grown film is preserved after annealing in vacuum, with less porosity.

4.6 References

1. Beamson G and Briggs D (1992) *High resolution XPS of organic polymers*, The Scienta ESCA300 Database (West Sussex: Wiley)
2. Jun J, Shin J H and Dhayal M (2006) Appl. Surf. Sci. 252 3871
3. Moulder J F, Stickle W F, Sobol P E and Bomber K D (1995) *Handbook of X-ray Photoelectron Spectroscopy* ed J Chastaing and R C King Jr, Physical Electronics (Eden Prairie, MN: Electronics, Inc)
4. Yang W P, Costa D and Marcus P (1994) J. Electrochem. Soc. 141 2669
5. Marques H P, Canario A R and Moutinho A M C (2009) Appl. Surf. Sci. 255 7389
6. Diebold U (2003) Surf. Sci. Reports 48 53
7. Liu L M, Crawford P and Hu P (2009) Prog. Surf. Science 84 155.
8. Göpel W, Anderson J A, Frankel D, Jaehing M, Phillips K, Schäfer J A and Rocker G (1984) Surf. Sci. 139 333
9. PDF-database. JCPDS, International centre for diffraction data (ICDD), 1601 Park Lane, Swarthmore, PA 19081, USA
10. Cox P A (1992) *Transition metal oxides: An introduction to their electronic structure and properties* (Clarendon press, Oxford).
11. Huravlev J F, Kuznetsov M V and Gubanov V A (1992) Journal of Electron Spectroscopy and Related Phenomena 38 169-176.
12. Eriksen S, Naylor P D and Egdell R G (1987) Spectrochimica Acta 43A 1535.
13. Muryn C A, Tirvengadum G, Crouch J J, Warburton D R, Raiker G N, Thornton G and Law D S L (1989) J. Phys.: Condens. Matter 1 SB127.
14. Muryn C A, Hardman P J, Crouch J J, Raiker G N, Thornton G and Law D S L (1991) Surface Science 251-252 747.
15. Kurtz R L, Bauer R S, Msdey T E, Román E and De Segovia J (1989) Surf. Sci. 218 178.
16. Hugenschmidt M B, Gamble L and Campbell C T (1994) Surf. Sci. 302 329.
17. Stefanovich E V and Truong T N 1999 Chem. Phys. Lett. 299 623.
18. Henderson M A 2002 Surf. Sci. Rep. 46 1.
19. Eufinger K, Poelman D, Poelman H, De Gryse R and Marin G B 2008 Thin Solid Films: Process Appl.189
20. Werfel F and Brümmer O 1983 Physica Scrupta 28 92-96.
21. Chan C M, Trigwell S and Duering T 1990 Surface and Interface Analysis 15 349-354
22. Laidani N, Cheyssac P, Perrière J, Bartali R, Gottardi G, Luciu I and Micheli V 2010 J. of Phys. D, Appl. Phys. 43 485402.
23. Fleming L, Fulton C C, Lucovsky G, Rowe J E, Ulrich M D and Lüning J 2007 J. Appl. Phys. 102 033707.
24. Di Valentin C, Pacchioni G and Selloni A 2006 Phys. Rev. Lett. 97 166803.
25. Thompson T L and Yates J T 2006 Chem. Rev. 106 4428.
26. Wendt S et al. 2008 Science 320 1755.
27. Choi H C, Ahn H J, Jung Y M, Lee M K, Shin H J, Kim S B and Sung Y E 2004 Applied Spectroscopy 58 598.
28. Brydson R, Sauer H, Engel W, Thomas J M, Zeitler E, Kosugi N and Kuroda H 1989 J. Phys. Condens. Matter. 1 797.
29. Cotton F A 1990 Chemical applications of group theory, 3rd ed (Wiley-Interscience).

5. Extrinsic doping of TiO_2 films

One potential candidate for TCOs whithout indium is Nb-doped titanium dioxide, therefore understanding the doping mechanisms and limits when Nb is introduced in the TiO_2 lattice is of great importance. The Nb effect on the structural and morphological properties of the films was also investigated.

Contents

5.1 Introduction
5.2 Sputtering from TiO_2-Nb mosaic target
5.2.1 Effects of cathode self-bias voltage
5.2.1.1 Influence of cathode self-bias voltage variation on the film growth rate
5.2.1.2 Influence of cathode self-bias voltage variation on the film chemical composition
5.2.2 Structure and morphology of as-grown films at room temperature
5.2.3 Influence of post-growth annealing in vacuum on the film chemical composition
5.2.4 Influence of post-growth annealing in vacuum on the film structure and morphology
5.2.5 Effects of substrate temperature during the films deposition
5.2.5.1 Influence of substrate temperature on the film chemical composition
5.2.5.2 Influence of substrate temperature on the film structure
5.3 Co-sputtering from separate TiO_2 and Nb targets
5.3.1 Film growth rate
5.3.2 Film chemical composition
5.3.3 Film structural properties
5.3.4 Influence of post-growth annealing in vacuum on the film chemical composition
5.3.5 Influence of post-growth annealing in vacuum on the film structure
5.3.6 Effects of substrate temperature during the films deposition
5.3.6.1 Influence of substrate temperature on the film chemical composition
5.3.6.2 Influence of substrate temperature on the film structure
5.4 Concluding remarks
5.5 References

5.1 Introduction

In this chapter Nb-TiO_2 thin films were prepared by RF sputtering, in Ar atmosphere, at room temperature or at various substrate temperatures. Two different target arrangements were used in these experiments: a mosaic target, in which Nb wires were placed on the TiO_2 target, and co-sputtering from separately TiO_2 and Nb targets for a better control over the Nb concentration. In the later arrangement, low concentrations (< 2.3%) of Nb in the films were obtained. Post-growth annealing in vacuum at 900°C was performed. The structural and morphological properties of the films were investigated by X-ray Diffraction (XRD) and Scanning Electron Microscopy (SEM). Using X-ray Photoelectron Spectroscopy (XPS) the films chemical composition was investigated.

5.2 Sputtering from TiO_2-Nb mosaic target

5.2.1 Effects of cathode self-bias voltage

The cathode self-bias voltage was varied from -350 *V* to -750 *V* in order to optimize the preparation process of extrinsically-doped TiO_2.

5.2.1.1 Influence of cathode self-bias voltage variation on the films growth rate

The film thicknesses were measured for Nb-doped TiO_2 thin films prepared in Ar plasma and the growth rate was determined. From Figure 5.1 can be seen that the growth rate is increasing with the applied self-bias voltage at cathode. The maximum value was obtained for a cathode self-bias voltage of -750 V (2.96±0.12 *nm/min*).

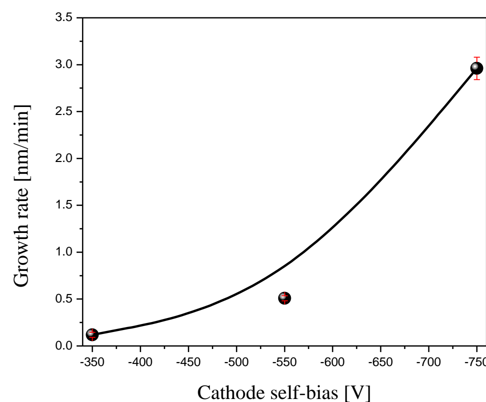

Figure 5.1 Growth rate as a function of cathode self-bias voltage

5.2.1.2 Influence on chemical composition

XPS measurements were performed for Nb-doped TiO_2 films prepared in Ar plasma, at different cathode self-bias voltages. The C *1s*, O *1s*, Ti *2p* and Nb *3d* core levels spectra were acquired. Three components were necessary for fitting C *1s* and O *1s* core-levels spectra for Nb-doped TiO_2 films, described in Chapter 4.

For Ti *2p* core-level of Nb-doped TiO_2 prepared in Ar plasma, three components were necessary for the fit, like in Figure 5.2 (a). Ti^{4+} and Ti^{3+} states were detected in the XPS spectra for Ti *2p*. The component corresponding to Ti^{3+} states in Ti $2p_{1/2}$ peak was too small to be detected. Nb *3d* core level spectrum with the fit results for Nb-doped TiO_2 film prepared in Ar plasma at -550 *V* is shown in Figure 5.2 (b). The Nb *3d* core level spectrum consists of Nb $3d_{5/2}$ and Nb $3d_{3/2}$ contributions. The Nb $3d_{5/2}$ BE value is attributed in literature to Nb^{5+} states in Nb_2O_5 [1].

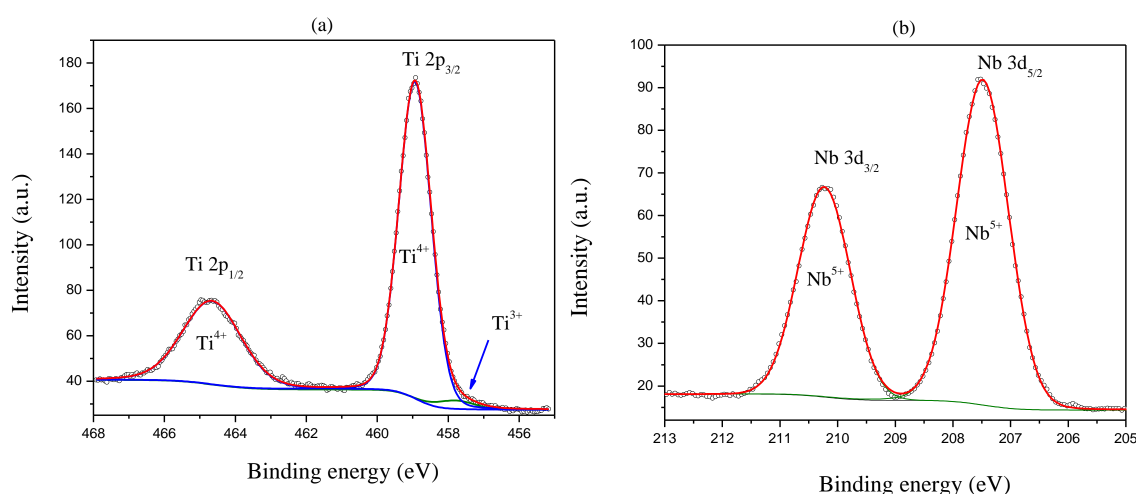

Figure 5.2 (a) Ti 2p and (b) Nb 3d core levels for Nb-doped TiO_2 film, prepared in Ar plasma (-550 *V*)

The BEs of O_I, Ti^{4+} $2p_{3/2}$, Ti^{3+} $2p_{3/2}$ and Nb^{5+} $3d_{5/2}$ components are listed in Table 5.1. A shift of O *1s* and Ti^{4+} $2p_{3/2}$ BEs toward higher energies with respect to that of rutile was observed in all the samples [2],with a difference between Ti^{4+} $2p_{3/2}$ and O_I peak BEs of 71.52±0.02 *eV*.

The concentration of Nb was determined for each sample and the values are given in Table 5.1. The concentration of Nb in the films prepared in Ar plasma is decreasing when the cathode self-bias voltage is increasing. This decrease of Nb concentration in the films can be explained by an increased cross-contamination process of the two components of the TiO_2-Nb mosaic target leading to Nb wires oxidation and/or TiO_2-coated Nb wires.

The chemical formulas were determined, described as $Ti_{1-x}Nb_yO_2$, using the main component of O *1s* core-level (designated as O_I) corresponding to oxygen bonded to titanium in TiO_2, the entire Ti *2p* and Nb *3d* spectra.

The chemical composition in Nb-TiO_2 films were obtained and are shown in Table 5.1. Similar values of x and y in $Ti_{1-x}Nb_yO_2$ films prepared at -350 V and -550 V can be observed, indicating a substitution of Ti by Nb in the film structure. For the film prepared at -750 V, more Nb is obtained according to the chemical composition, more probably due to the formation of Nb oxide. The values of x in $Ti_{1-x}Nb_yO_2$ films are decreasing with increasing the cathode self-bias voltage indicating an increase in the oxygen vacancies.

Table 5.1 O_I, Ti^{4+} *$2p_{3/}2$*, Ti^{3+} *$2p_{3/2}$* and Nb^{5+} *$3d_{5/2}$* BEs, Nb atomic concentration in the films and the chemical formula

Cathode self-bias voltage (V)	BE(O_I) (eV)	BE(Ti^{4+} $2p_{3/2}$) (eV)	BE(Ti^{3+} $2p_{3/2}$) (eV)	BE(Nb^{5+} $3d_{5/2}$) (eV)	ΔE (eV)	Nb(at%)	Chemical composition
rutile	529.75	458.35	-	-	71.40	-	-
-350	530.51	458.98	457.73	207.53	71.53	12.16	$Ti_{1-0.33}Nb_{0.37}O_2$
-550	530.47	458.93	457.79	207.48	71.54	9.47	$Ti_{1-0.32}Nb_{0.28}O_2$
-750	530.27	458.77	457.51	207.35	71.50	5.22	$Ti_{1-0.11}Nb_{0.16}O_2$

The VB spectrum for Nb-doped TiO_2 film prepared at a cathode self-bias voltage of -550 *V* is shown in Figure 5.3 (b) together with the VB for TiO_2 film prepared in the same conditions, for comparison. The same components were identified as for the TiO_2 film prepared in Ar plasma, described in detail in Chapter 4.

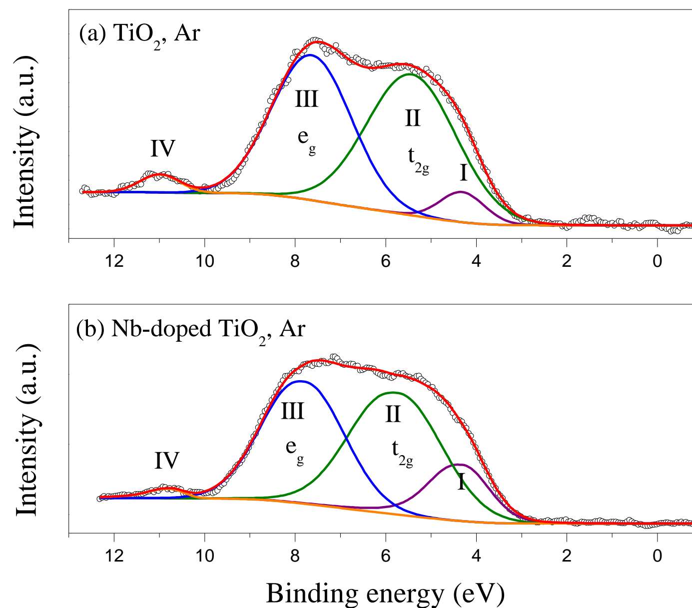

Figure 5.3 VB spectra for (a) TiO_2 and (b) Nb-doped TiO_2 prepared in Ar plasma, at -550 *V*

In the next experiments, Nb-doped TiO_2 films prepared at cathode self-bias voltages of -550 *V* and -750 *V* were used, having a higher thickness then the ones prepared at a cathode self-bias voltage of -350 *V*.

5.2.2 Structure and morphology of as-grown films at room temperature

The structure of Nb-doped TiO_2 films prepared in Ar plasma, at -750 *V* was investigated with XRD. The as-grown films reveal an amorphous structure. The top-view and cross-section images (Figure 5.4) of Nb-doped TiO_2 show a dense morphology with agglomerated grains and a dense columnar structure, adherent to the Si *(100)* substrates.

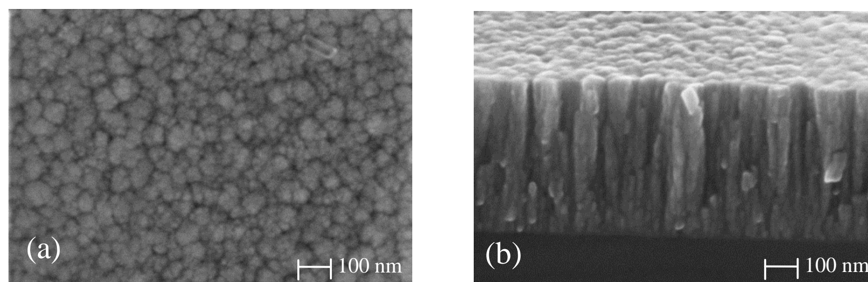

Figure 5.4 (a) Surface and (b) cross-section images for as-grown Nb-TiO_2 film prepared in Ar plasma

5.2.3 Influence of post-growth annealing in vacuum on the film chemical composition

Post-growth annealing at 900°C for 1h in vacuum was performed for Nb-doped TiO_2 films prepared in Ar plasma, at a self-bias cathode voltage of -750 *V*, in order to improve the structure of the films.

C *1s*, O *1s*, Ti *2p* and Nb *3d* core levels were acquired using XPS, in order to investigate the oxidation state of the films after post-growth annealing and are shown in Figure 5.5. For comparison, the XPS spectra for as-grown Nb-doped TiO_2 are shown. O_I, Ti^{4+} $2p_{3/2}$, Nb^{5+} $3d_{5/2}$ BEs for as-grown and annealed Nb-doped TiO_2 prepared in Ar plasma are listed in Table 5.2. A slight shift toward lower BEs was observed in the annealed samples. The oxidation states of Ti and Nb does not change after annealing.

From the chemical composition of Nb-TiO_2 film before and after annealing in vacuum it is observed that after annealing x in $Ti_{1-x}Nb_yO_2$ does not change considerably.

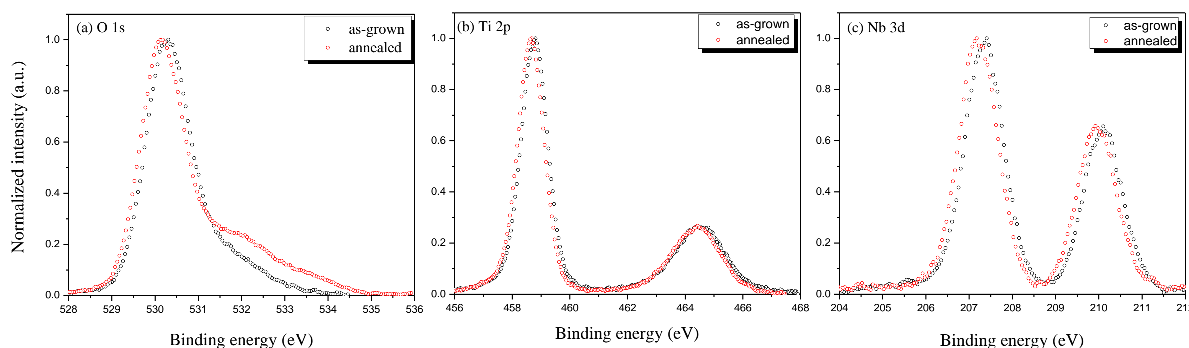

Figure 5.5 O 1s (*a*), Ti 2p (*b*) and (*c*) Nb 3d core-levels XPS spectra for as-grown and post-growth annealed Nb-doped TiO_2 film prepared in Ar

Table 5.2 O_I, Ti^{4+} *$2p_{3/2}$*, Nb^{5+} *$3d_{5/2}$* BEs for as-grown and annealed Nb-doped TiO_2 prepared in Ar plasma

BE(O_I) (eV)		**BE(Ti^{4+} $2p_{3/2}$) (eV)**		**BE(Nb^{5+} $3d_{5/2}$) (eV)**		**Chemical composition**	
as-gr	ann	as-gr	ann	as-gr	ann	as-gr	ann
530.27	530.14	458.77	458.66	207.34	207.21	$Ti_{1-0.11}Nb_{0.16}O_2$	$Ti_{1-0.10}Nb_{0.16}O_2$

5.2.4 Influence of post-growth annealing in vacuum on the film structure and morphology

The structure of annealed in vacuum Nb-TiO_2 film prepared in Ar plasma at -750 *V* was investigated and is shown in Figure 5.6. Both anatase and rutile phases of TiO_2 were identified with weak intensities. The grain size was calculated using to Scherrer equation using A(101) and R(110) peaks and values of ~22 *nm* and ~6.3 *nm* were calculated.

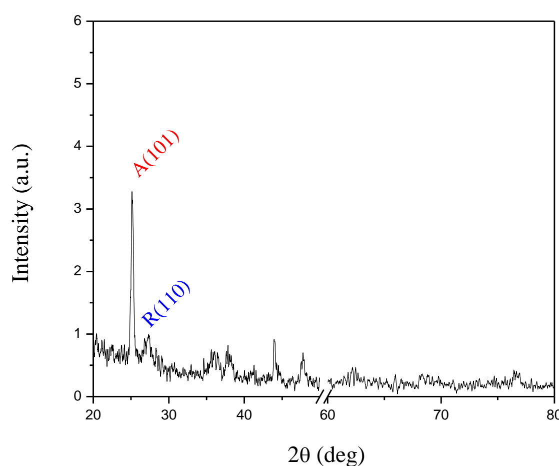

Figure 5.6 XRD pattern for annealed in vacuum Nb-TiO_2 film, prepared in Ar plasma

The morphology of annealed Nb-doped TiO_2 film prepared in Ar plasma is dense and the columnar structure is preserved, like in Figure 5.7. The surface is not damaged after annealing, like in TiO_2 films prepared in the same conditions.

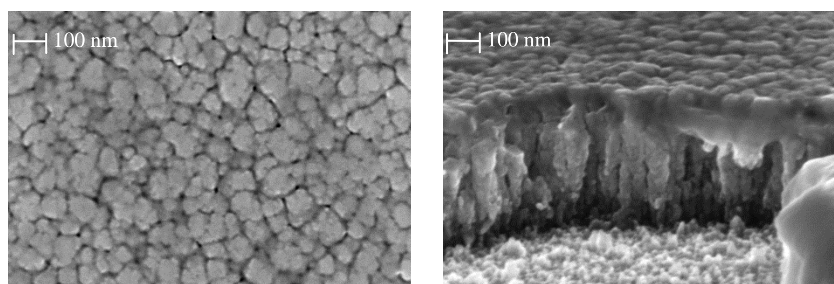

Figure 5.7 Top-view and cross-section images for annealed Nb-doped TiO_2 film prepared in Ar plasma

5.2.5 Effects of substrate temperature during the films deposition

5.2.5.1 Influence of substrate temperature on the film chemical composition

The substrate temperature was increased at 350°C during Nb-TiO_2 films deposition at a cathode self–bias voltage -750 *V* and the chemical states of Ti *2p* and Nb *3d* were studied with XPS. The C *1s*, O *1s*, Ti *2p* and Nb *3d* core-levels for the sample described before were acquired (not shown).

The C *1s* and O *1s* core-levels can be well fitted with three components, with the same meaning as in the previous sections. The Ti *2p* core-level is fitted with three components, two corresponding to Ti^{4+} states in TiO_2 and the other one component corresponding to Ti^{3+} states. In the case of Nb *3d* core-level two components were necessary corresponding to Nb^{5+} states in Nb_2O_5, while Nb-TiO_2 film deposited without intentional heating, one more component was necessary for a good fit of Nb *3d* core level, corresponding to Nb^{4+} states in NbO_2. The BEs for O_I, Ti^{4+} $2p_{3/2}$, Ti^{3+} $2p_{3/2}$, Nb^{5+} $3d_{5/2}$, Nb^{4+} $3d_{5/2}$ are listed in Table 5.3.

From the chemical formulas for the sample prepared at room temperature and the one deposited at 350°C substrate temperature (see Table 5.3) one can conclude that the deposition of Nb-TiO_2 at 350°C substrate temperature resulted in a better substitution of Ti by Nb than the one made at room temperature due to the close values of x and y in $Ti_{1-x}Nb_yO_2$. The increase of x value for the sample prepared at 350°C substrate temperature indicate a decrease in the oxygen vacancies as compared to the sample prepared at RT.

Table 5.3 O_I, Ti^{4+} $2p_{3/2}$, Ti^{3+} $2p_{3/2}$, Nb^{5+} $3d_{5/2}$ and Nb^{4+} $3d_{5/2}$ Bes and the chemical composition of NB-TiO2 films prepared in Ar plasma, at various substrate temperatures during the deposition

Substrate temperature	BE(O_I) (eV)	BE(Ti^{4+} $2p_{3/2}$) (eV)	BE(Ti^{3+} $2p_{3/2}$) (eV)	BE(Nb^{5+} $3d_{5/2}$) (eV)	BE(Nb^{4+} $3d_{5/2}$) (eV)	ΔE (O_I-Ti2$p_{3/2}$) (eV)	Chemical composition
RT	530.27	458.77	457.51	207.35	205.85	71.50	$Ti_{1-0.11}Nb_{0.16}O_2$
350°C	530.55	459.07	457.76	207.60	-	71.48	$Ti_{1-0.14}Nb_{0.16}O_2$

5.2.5.2 Influence of substrate temperature on the film structure

XRD patterns reveal an amorphous structure for Nb-TiO_2 films deposited at room temperature and the one deposited at 350°C substrate temperature. Even at high substrate temperature (350°C) the extrinsically-doped TiO_2 was amorphous.

5.3 Co-sputtering from separate TiO_2 and Nb targets

For a better control over the concentration of Nb in Nb-doped TiO_2 thin films, another configuration was adopted: co-sputtering from separate TiO_2 and Nb targets. The depositions were performed at a constant self-bias voltage of -850 *V* on the TiO_2 target. Powers in the range 1-5 *W* were used for Nb sputtering. The carrier gas was argon. Low concentrations of Nb (<3%) were obtained using co-sputtering from TiO_2 and Nb targets.

5.3.1 Film growth rate

The growth rates were determined for Nb-doped TiO_2 films deposited in Ar plasma. The variation of the growth rate as a function of the applied power to Nb target is shown in Figure 5.8. As can be observed in the figure, the growth rate slightly increases with the power applied to Nb target. The maximum growth rate (2.19±0.23 *nm/min*) was found when the power applied to Nb target was 5 *W*. The increase in growth rate can be explained by the fact that the powered Nb cathode contributed in increasing the ion density of the discharge.

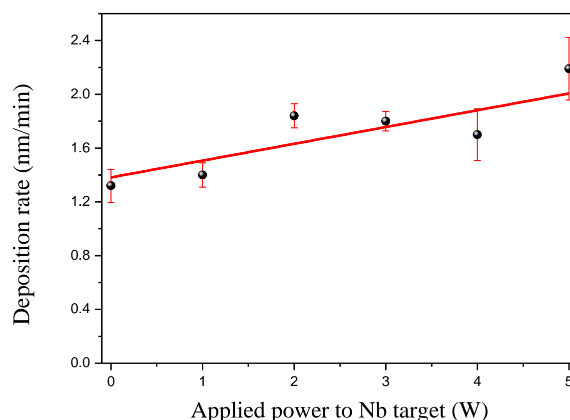

Figure 5.8 Growth rate for Nb-TiO_2 films prepared in Ar plasma, at -850 *V* on TiO_2

5.3.2 Chemical composition

The C *1s*, O *1s*, Ti *2p* and Nb *3d* core levels spectra were acquired with XPS for Nb-doped TiO_2 films prepared in Ar plasma, varying the power applied to Nb target. Three components were necessary for fitting C *1s* and O *1s* core-levels spectra. For Ti *2p* core-level of Nb-doped TiO_2 prepared in Ar plasma, three components were necessary for the fit. Ti^{4+} and Ti^{3+} states were detected in the XPS spectra for Ti *2p*. For Nb *3d* core level spectrum only two components were necessary. Only the Nb^{+5} states were detected in these films.

The BEs of O_I, Ti^{4+} $2p_{3/2}$, Ti^{3+} $2p_{3/2}$ and Nb^{5+} $3d_{5/2}$ components are listed in Table 5.4. A shift of O *1s* and Ti^{4+} $2p_{3/2}$ BEs toward higher energies with respect to that of rutile was observed in all the samples [2],with a difference between Ti^{4+} $2p_{3/2}$ and O_I peak BEs of 71.45±0.01 *eV*.

Table 5.4 O_I, Ti^{4+} $2p_3/2$, Ti^{3+} $2p_{3/2}$ and Nb^{5+} $3d_{5/2}$ BEs

Voltage (V)	Applied power to Nb (W)	BE(O_I) (eV)	BE(Ti^{4+} $2p_{3/2}$) (eV)	BE(Ti^{3+} $2p_{3/2}$) (eV)	BE(Nb^{5+} $3d_{5/2}$) (eV)	ΔE (O_I-$Ti^{4+}2p_{3/2}$) (eV)
0	0 (TiO_2)	530.25	458.82	-	-	71.43
19	1	530.28	458.82	457.63	207.45	71.46
37	2	530.27	458.83	457.76	207.50	71.44
46	3	530.28	458.83	457.64	207.40	71.45
55	4	530.27	458.82	457.66	208.64	71.45
66	5	530.40	458.94	457.73	207.44	71.46
-	rutile	529.75	458.35	-	-	71.40

The concentration of Nb was determined in Nb-doped TiO_2 thin films prepared in Ar plasma, at different powers applied to the Nb target. The obtained values are given in Table 5.5 and are plotted in Figure 5.9 as a function of the power applied to Nb target. For 1 and 2 *W*, it was not possible to determine the exact value of

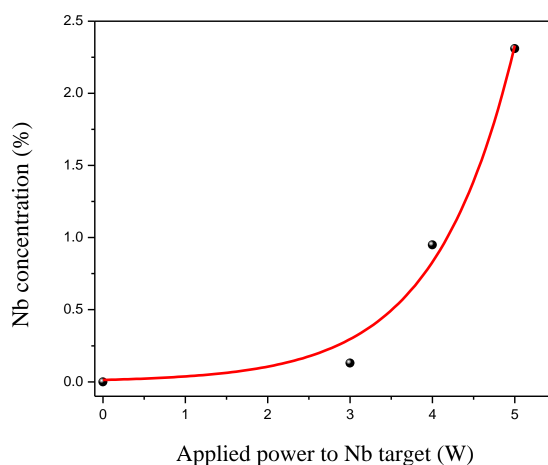

Figure 5.9 Nb concentration as a function of the power applied at Nb target; the curve is an exponential fit of the plot

the Nb concentration from the XPS spectra, due to very low intensity of Nb 3d peaks. The interpolated Nb concentrations for 1 W and 2 W were derived from Figure 5.9.

The chemical compositions were obtained and are listed in Table 5.5. An explanation for the decreased value of x in $Ti_{1-x}Nb_yO_2$ for the films prepared from two separate TiO_2 and Nb targets can be attributed to the formation of oxygen vacancies in the films. For the film prepared at 4 W the chemical composition indicates a better substitution of Ti by Nb atoms.

Table 5.5 %Nb and the chemical formulas in extrinsically-doped TiO_2

Applied power to Nb (W)	%Nb	Chemical composition
1	0.04	$Ti_{1+0.04}Nb_{0.0001}O_2$
2	0.11	$Ti_{1+0.04}Nb_{0.0003}O_2$
3	0.13	$Ti_{1+0.09}Nb_{0.0004}O_2$
4	0.95	$Ti_{1+0.04}Nb_{0.03}O_2$
5	2.31	$Ti_{1+0.03}Nb_{0.06}O_2$

5.3.3 Structure of as-grown films at room temperature

X-ray Diffraction patterns reveal an amorphous structure for all Nb-doped TiO_2 films prepared in Ar plasma, by co-sputtering fromTiO_2 and Nb targets.

5.3.4 Influence of post-growth annealing in vacuum on the film chemical composition

Like in the others experiments, in order to obtain a polycrystalline structure of the films, post-growth annealing at a temperature of 900°C for 1h in vacuum was performed for extrinsically-doped TiO_2 films, prepared in Ar plasma. Only two samples were analyzed by XPS: the sample prepared at an applied power to Nb target of 1 W and the sample prepared at 4 W, being of interest due to the excellent electrical properties, described in detail later, in Section 7.3.2.

The O *1s*, C *1s*, Ti *2p* and Nb *3d* core-levels were acquired for both samples. In Figure 5.10 only the O *1s* and Ti *2p* XPS spectra are shown for the annealed samples, for which niobium was sputtered with 1 *W* and 4 *W*. The O *1s* and C *1s* for both films are well fitted with three components. For fitting the Ti *2p* core-level spectra, the sample prepared at 1 *W* needs to be fit with two components only (Ti^{4+}), while in the sample prepared with higher power applied to Nb the Ti^{3+} states were detected.

The BEs for O_I, Ti^{4+} $2p_{3/2}$ and Ti^{3+} $2p_{3/2}$ are listed in Table 5.6, together with the as-grown Nb-doped TiO_2 films, for comparison.

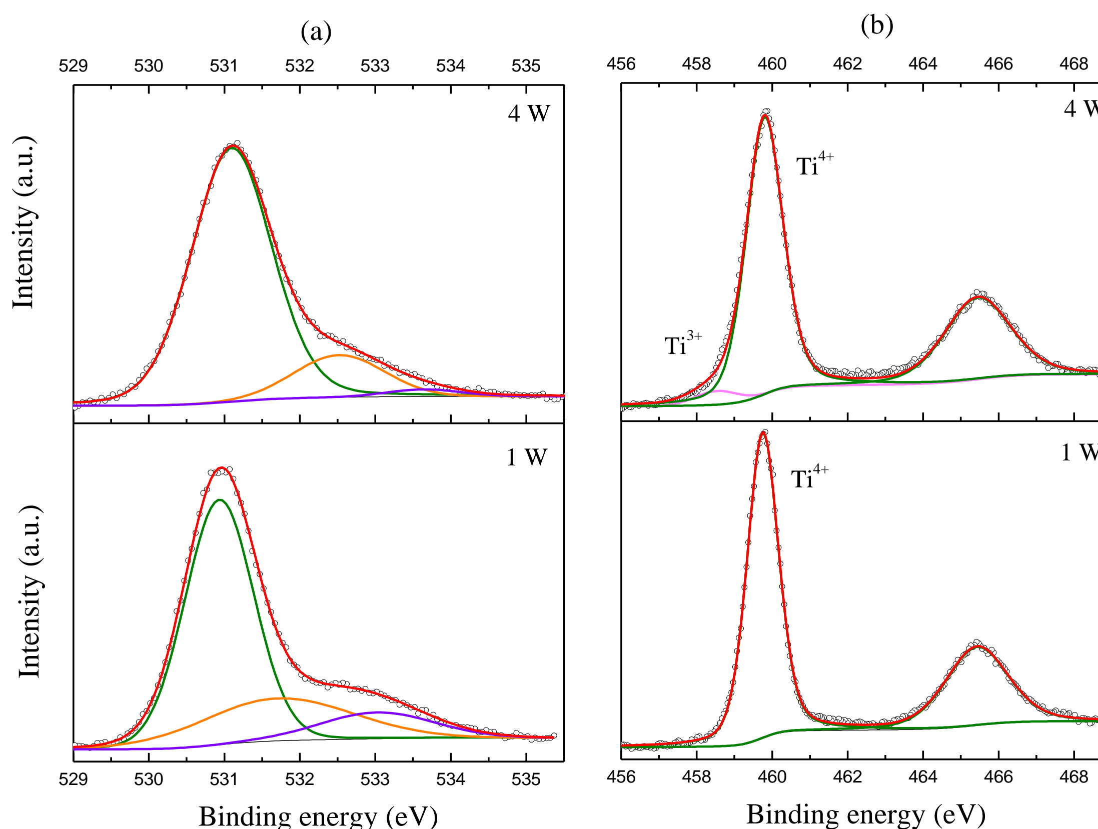

Figure 5.10 (a) O *1s* and (b) Ti *2p* XPS spectra for Nb-doped TiO_2 thin films, with the applied power to Nb target of 1 *W* (bottom) and 4 *W* (top)

The Nb *3d* core-level XPS spectrum for the sample in which Nb was sputtered with 4 *W* is shown in Figure 5.11. For the sample prepared with the power of 1 *W*, the concentration of Nb was too small to be acquired with high resolution of the peaks with XPS. Nb^{5+} and Nb^{4+} oxidation states were detected in the Nb *3d* XPS spectrum. In Table 5.6 the BEs of Nb^{5+} $3d_{5/2}$ and Nb^{4+} $3d_{5/2}$ are listed for both as-grown and post-growth annealed samples.

The chemical composition for the annealed samples was determined and compared with the ones for the as-grown samples. For the sample prepared at 1 *W* the chemical composition for the as-grown film was $Ti_{1+0.04}Nb_{0.0001}O_2$ and for the film annealed in vacuum was found to be $Ti_{1+0.24}Nb_{0.11}O_2$. A decrease for x in $Ti_{1-x}Nb_yO_2$ was observed indicating the formation of more oxygen vacancies after annealing in vacuum. For the sample prepared at 4 W the chemical composition for the as-grown film was $Ti_{1+0.04}Nb_{0.03}O_2$ and for the film annealed in vacuum was found to be $Ti_{1-0.16}O_2Nb_{0.10}$. In this case, x in $Ti_{1-x}Nb_yO_2$ is increased indicating less oxygen vacancies formed during the annealing in vacuum. For the annealed sample prepared at 4 W, the chemical composition indicates a better substitution of Ti by Nb atoms.

Table 5.6 O_I, Ti^{4+} $2p_{3/}2$, Ti^{3+} $2p_{3/2}$, Nb^{5+} $3d_{5/2}$ and Nb^{4+} $3d_{5/2}$ BEs

Applied power to Nb (W)	BE(O_I) (eV)		BE(Ti^{4+} $2p_{3/2}$) (eV)		BE(Ti^{3+} $2p_{3/2}$) (eV)		ΔE (eV)		BE(Nb^{5+} $3d_{5/2}$) (eV)		BE(Nb^{4+} $3d_{5/2}$) (eV)	
	as-gr	ann	as-gr	ann	as-gr	ann	as-gr	ann	as-gr	ann	as-gr	ann
1	530.28	530.93	458.82	459.75	457.63	-	71.46	71.18	207.45	207.78	-	-
4	530.27	531.10	458.82	459.80	457.66	458.54	71.45	71.30	208.64	208.38	-	207.44

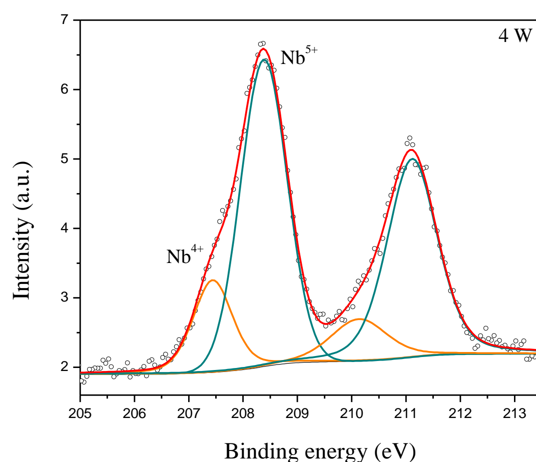

Figure 5.11 Nb *3d* XPS spectrum for Nb-doped TiO_2 film with the applied power to Nb target of 4 *W*

5.3.5 Influence of post-growth annealing in vacuum on the film structure

The structure of post-growth annealed Nb-doped TiO_2 films with different concentrations of Nb were investigated with XRD. The A(101) and R(110) peaks position and FWHM corresponding to anatase (101) oriented direction and rutile (110) oriented direction are listed in Table 5.7. For comparison, TiO_2 film prepared in the same conditions is given.

The annealed in vacuum TiO_2 film shows only the anatase phase with ~16.5 nm grain size. For annealed in vacuum Nb-TiO_2 films deposited by co-sputtering from two separate targets at low powers applied to the Nb target (1-3 *W*) only the anatase (101) peak was observed, with a decrease in the grains dimension. At 4 *W* the rutile peak was detected, while at 5 *W* both anatase and rutile phases were identified. An explanation for the rutile peak observed in the XRD pattern for the sample prepared at 4 W can be the segregation of Nb as Nb oxide amorphous.

Table 5.7 The positions and the FWHMs of the detected XRD peaks for post-growth annealed Nb-TiO_2

Applied Power to Nb (W)	Phase	2θ(deg)	FWHM	Grain size (nm)
0 (TiO_2)	A(101)	25.21	0.480	16.5
1	A(101)	25.26	0.535	14.8
2	A(101)	25.26	0.390	20.6
3	A(101)	25.29	0.590	13.3
4	R(110)	27.21	0.790	9.9
5	A(101)	25.21	0.530	14.9
	R(110)	27.26	0.840	9.3

5.3.6 Effects of substrate temperature during the films deposition

5.3.6.1 Influence of substrate temperature on the film chemical composition

The substrate temperature during Nb-TiO_2 films deposition was varied, from 300°C to 420°C, for films prepared in Ar plasma, with co-sputtering from TiO_2 and Nb targets. The applied power to the Nb target was set to 4 *W*.

The chemical states of the core-levels were studied with XPS. The C *1s*, O *1s*, Ti *2p* and Nb *3d* core-levels were acquired. In Table 5.8 the BEs of O_I, Ti^{4+} $2p_{3/}2$, Ti^{3+} $2p_{3/2}$, Nb^{5+} $3d_{5/2}$ and Nb^{4+} $3d_{5/2}$ for the samples deposited at different substrate temperatures together with the sample prepared at room temperature are given. As can be seen, when the film is deposited heating the substrate up to 300°C or more, only Ti^{4+} states were detected in the XPS spectra of Ti *2p* core-level. Nb^{4+} states were identified in the Nb *3d* core-level spectra for substrate temperatures below 350°C. The atomic ratio Nb^{4+}/Nb^{5+} was calculated and is given in Table 5.8.

The chemical composition of the samples was investigated. It was observed that x in $Ti_{1-x}Nb_yO_2$ is decreasing until 350°C substrate temperature indicating the formation of more oxygen vacancies in these films. For higher substrate temperatures x is decreasing indicating less oxygen vacancies in the respective films. A good substitution of Ti by Nb atoms is observed only in the sample prepared at RT and the one prepared at 420°C substrate temperature.

Table 5.8 O_I, Ti^{4+} $2p_{3/}2$, Ti^{3+} $2p_{3/2}$, Nb^{5+} $3d_{5/2}$ and Nb^{4+} $3d_{5/2}$ Bes, Nb^{4+}/Nb^{5+} atomic ratio and the chemical composition for Nb-TiO_2 films deposited at various substrate temperatures

T	BE(O_I) (eV)	BE (Ti^{4+} $2p_{3/2}$) (eV)	BE (Ti^{3+} $2p_{3/2}$) (eV)	ΔE (O_I-$Ti^{4+}2p_{3/2}$) (eV)	BE (Nb^{5+} $3d_{5/2}$) (eV)	BE (Nb^{4+} $3d_{5/2}$) (eV)	Nb^{4+}/Nb^{5+} at. ratio	Chemical composition
RT	530.27	458.82	457.66	71.45	208.64	-	-	$Ti_{1+0.04}Nb_{0.03}O_2$
300°C	529.88	458.67	-	71.21	207.19	-	-	$Ti_{1+0.10}Nb_{0.02}O_2$
350°C	529.84	458.58	-	71.26	207.08	206.24	0.021	$Ti_{1+0.16}Nb_{0.03}O_2$
400°C	529.88	458.63	-	71.25	207.15	206.31	0.016	$Ti_{1-0.05}Nb_{0.02}O_2$
420°C	530.02	458.79	-	71.23	207.32	206.51	0.039	$Ti_{1+0.03}Nb_{0.02}O_2$

5.3.6.2 Influence of substrate temperature on the film structure

The structure and the morphology of the Nb-TiO_2 samples deposited at various substrate temperatures were investigated. XRD spectra for the films are shown in Figure 5.12. The sample deposited without intentional heating shows an amorphous structure. At low substrate temperature (300°C) the anatase phase was detected. Increasing the temperature, the anatase-to-rutile transformation occurs. Usually, this transformation occurs at a temperature of ~450°C.

In Table 5.9 the A(101) and R(110) peaks positions and the FWHMs of the peaks are given. As can be seen, there is no significant variation in the grains dimension with an increase in the substrate temperature. The grain size for the films prepared at various substrate temperatures and the one prepared at room temperature is ~10 nm.

Table 5.9 The positions and the FWHMs of the detected XRD peaks for Nb-TiO_2 prepared at various substrate temperatures

Substrate temperature	Phase	2θ(deg)	FWHM	Grain size (nm)
RT	R(110)	27.21	0.790	9.9
300°C	A(101)	25.26	0.752	10.4
350°C	R(110)	27.46	0.784	9.9
400°C	R(110)	27.42	0.773	10.1
420°C	R(110)	27.40	0.719	10.8

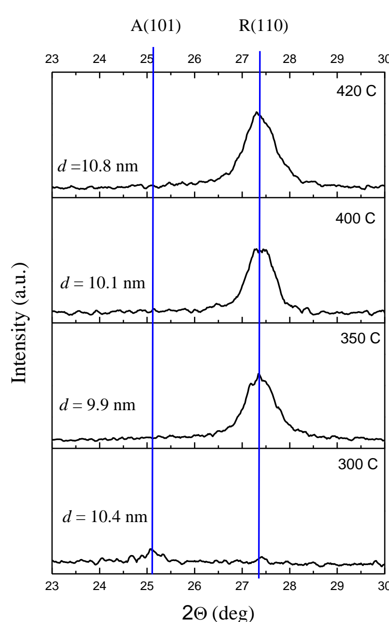

Figure 5.12 XRD patterns for Nb-TiO_2 films (-850 V for TiO_2 target and 4 W for Nb target) prepared in Ar plasma at various substrate temperatures

The top-view and cross-section images for the sample deposited at 350°C substrate temperature (Figure 5.13) shows a dense morphology with agglomerated grains and a dense columnar structure.

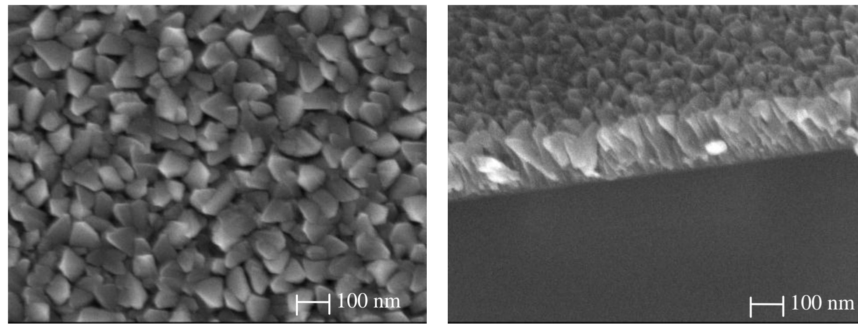

Figure 5.13 The top-view and cross-section images for Nb-TiO_2 film deposited at 350°C substrate temperature (-850 V for TiO_2 target and 4 W for Nb target)

5.4 Concluding remarks

Nb-TiO_2 films were deposited in Ar plasma, using two different target arrangements: a mosaic target, in which Nb wires were placed on the TiO_2 target, and co-sputtering from separately TiO_2 and Nb targets for a better control over the Nb concentration.

The chemical composition of Nb-TiO_2 films sputtered from a TiO_2-Nb mosaic target in Ar plasma (RT) at various cathode self-bias voltages was investigated. In this configuration high values for Nb concentration in the films were obtained (5-12%). A decrease of Nb concentration in the films with increasing the cathode self-bias voltage was observed explained by an increased cross-contamination process of the two components of the TiO_2-Nb mosaic target leading to Nb wires oxidation and/or TiO_2-coated Nb wires. According to the chemical composition a better substitution of Ti by Nb was observed at low cathode self-bias voltages (-350 V and -550 V), while at higher cathode self-bias voltage (-750 V) Nb-oxide is formed. An increase in the number of oxygen vacancies was observed with increasing the cathode self-bias voltage. The as-grown Nb-TiO_2 films were having an amorphous structure and a dense morphology with agglomerated grains. The post-growth annealing in vacuum at 900°C of the films improved the crystalline structure of the films, both anatase and rutile phases being detected, and an increase in the number of oxygen vacancies in the chemical composition was observed. The columnar structure from the as-grown film is preserved after annealing in vacuum. The deposition of Nb-TiO_2 at 350°C substrate temperature resulted in a better substitution of Ti by Nb than the one made at room temperature, with less oxygen vacancies in the film, but with an amorphous structure.

In the second configuration, when Nb-TiO_2 films were co-sputtered from two separate TiO_2 and Nb targets in Ar plasma (RT), low Nb concentrations were measured in the films ($< 2.3\%$). The chemical composition of these films indicates the formation of oxygen vacancies during the deposition, but a higher number than in the films sputtered from a TiO_2-Nb mosaic target. For the film prepared at 4 W applied to Nb target (0.95% Nb) the chemical composition indicates a better substitution of Ti by Nb atoms. Also these films, deposited at RT, show an amorphous structure. The post-growth annealing in vacuum at 900°C of the films improved the crystalline structure of the films, with anatase phase detected at low powers applied to Nb target ($< 0.13\%$Nb) and anatase - rutile mixture at 5 W (2.3%Nb). The sample prepared at 4 W shows the rutile phase and from the chemical composition after annealing in vacuum a better substitution of Ti by Nb was observed. The deposition of Nb-TiO_2 films at various substrate temperatures during the deposition (300°C - 420°C) resulted in a better substitution of Ti by Nb at high substrate temperature (420°C), and the rutile phase was detected. The formation of more oxygen vacancies as compared to the sample prepared at RT was confirmed by the chemical composition of the films prepared at 300°C and 350°C. For higher substrate temperatures (400°C and 420°C), less oxygen vacancies were observed.

5.5 References

1. Beamson G and Briggs D (1992) *High resolution XPS of organic polymers*, The Scienta ESCA300 Database (West Sussex: Wiley)
2. Diebold U (2003) Surf. Sci. Reports 48 53

6. TiO_2 film deposition and characterization for intrinsic-extrinsic co-doping

In this chapter a mixed intrinsic-extrinsic doping of TiO_2 films, obtained by Nb incorporation and the creation of internal defects is investigated, using O_2 and H_2 as reactive gases for intrinsic doping and Nb as extrinsic dopant. The structural, morphological and the chemical composition of these films were studied.

Contents

6.1 Introduction
6.2 Film deposition in Ar-O_2 plasma
6.2.1 Sputtering of Nb-TiO_2 films from a mosaic target
6.2.1.1 Film growth rate
6.2.1.2 Film chemical composition
6.2.1.3 Film structure and morphology
6.2.1.4 Influence of post-growth annealing on the film chemical composition
6.2.1.5 Influence of post-growth annealing on the film structure and morphology
6.2.2 Deposition of Nb-TiO_2 films by co-sputtering from two separate targets
6.2.2.1 Film growth rate
6.2.2.2 Film chemical composition
6.2.2.3 Film structure
6.2.2.4 Influence of post-growth annealing on the film chemical composition
6.2.2.5 Influence of post-growth annealing on the film structure
6.3 Film deposition in Ar-H_2 plasma
6.3.1 Sputtering of Nb-TiO_2 films from a mosaic target
6.3.1.1 Film growth rate
6.3.1.2 Film chemical composition
6.3.1.3 Film structure and morphology
6.3.1.4 Influence of post-growth annealing on the film chemical composition
6.3.1.5 Influence of post-growth annealing on the film structure and morphology
6.3.1.6 Influence of substrate temperature on the film chemical and structural properties
6.3.2 Deposition of Nb-TiO_2 films by co-sputtering from two separate targets
6.3.2.1 Film growth rate
6.3.2.2 Film chemical composition and structure
6.3.2.3 Influence of post-growth annealing on the film chemical composition
6.3.2.4 Influence of post-growth annealing on the film structural properties
6.4 Concluding remarks
6.5 References

6.1 Introduction

In this chapter co-doped Nb-TiO_2 films were deposited by RF sputtering, using O_2 and H_2 as reactive gases for intrinsic doping and Nb as extrinsic dopant. Two different target arrangements were used in these experiments: a mosaic target, in which Nb wires were placed on the TiO_2 target, and co-sputtering from separately TiO_2 and Nb targets. Their structural and morphological properties were investigated by X-ray Diffraction (XRD) and Scanning Electron Microscopy (SEM). The changes in the chemical composition were studied using X-ray Photoelectron Spectroscopy (XPS).

6.2 Film deposition in Ar-O_2 plasma

6.2.1 Sputtering of Nb-TiO_2 films from a mosaic target

The Nb-TiO_2 thin films presented in this section were sputtered from a mosaic target, described in the experimental section. Oxygen concentration introduced in Ar plasma was varied from 3 to 20%. The cathode self-bias voltages were fixed at -550 *V* and -750 *V*.

6.2.1.1 Film growth rate

The growth rates for Nb-TiO_2 films deposited in Ar-O_2 atmospheres were determined for films deposited at -550 *V* and are plotted as a function of the oxygen introduced in Ar discharge in Figure 6.1. The highest growth rate was obtained for the film prepared in Ar plasma (0.51±0.02 *nm/min*). This value is higher compared to the TiO_2 film deposited in Ar, where the film growth rate was 0.41±0.02 *nm/min*.

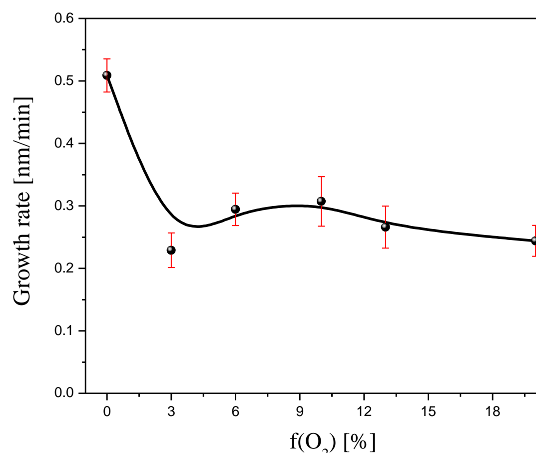

Figure 6.1 Film growth rate for Nb-TiO_2 prepared in Ar-O_2 atmosphere, at -550 V self-bias voltage on mosaic Nb-TiO_2 cathode

When a small amount of oxygen is added in discharge, a decrease of the Nb-TiO_2 films growth rate is observed until a value of 0.22±0.02 *nm/min*, followed by a region with approximately constant values for the growth rate, when higher concentrations of oxygen are added in discharge. This behavior is similar to the TiO_2 films growth rate. A decrease was observed when O_2 was added in Ar plasma with a minimum at 6%O_2 (0.14±0.02 *nm/min*). For 20%O_2 added in Ar plasma the Nb-TiO_2 and TiO_2 films growth rate was found to be the same (0.24±0.02 *nm/min*).

6.2.1.2 Film chemical composition

The C *1s*, O *1s*, Ti *2p* and Nb *3d* core-levels and the VB were acquired with XPS in order to analyze the chemical composition of Nb-doped TiO_2 films deposited in Ar-O_2 atmosphere, at -550 *V*.

C *1s* and O *1s* core-levels spectra for Nb-TiO_2 films deposited in Ar-O_2 atmosphere can be well fitted with three components. For Ti *2p* and Nb *3d* core-levels, two components were used for a good fit, corresponding to Ti^{4+} and Nb^{5+} states. The O_I, Ti^{4+} $2p_{3/2}$ and Nb^{5+} $3d_{5/2}$ BEs are listed in Table 6.1. The difference between Ti^{4+} $2p_{3/2}$ and O_I peak BEs are also reported in the Table.

Table 6.1 O_I, Ti^{4+} $2p_{3/2}$ and Nb^{5+} $3d_{5/2}$ BEs for Nb-doped TiO_2 films prepared in Ar-O_2 atmosphere

%O_2	**O_I (*eV*)**	**Ti^{4+} $2p_{3/2}$(eV)**	**ΔE (eV)**	**Nb^{5+} $3d_{5/2}$ (*eV*)**	**Nb(%)**	**Chemical formula**
pure-Ar	530.47	458.92	71.55	207.48	9.47	$Ti_{1-0.32}Nb_{0.28}O_2$
3%	530.33	458.78	71.55	207.24	6.21	$Ti_{1-0.22}Nb_{0.19}O_2$
6%	530.31	458.79	71.60	207.32	5.82	$Ti_{1-0.15}Nb_{0.18}O_2$
10%	530.29	458.77	71.52	207.34	5.51	$Ti_{1-0.17}Nb_{0.17}O_2$
13%	530.19	458.67	71.52	207.22	5.40	$Ti_{1-0.19}Nb_{0.16}O_2$
20%	530.21	458.68	71.53	207.26	5.58	$Ti_{1-0.19}Nb_{0.17}O_2$

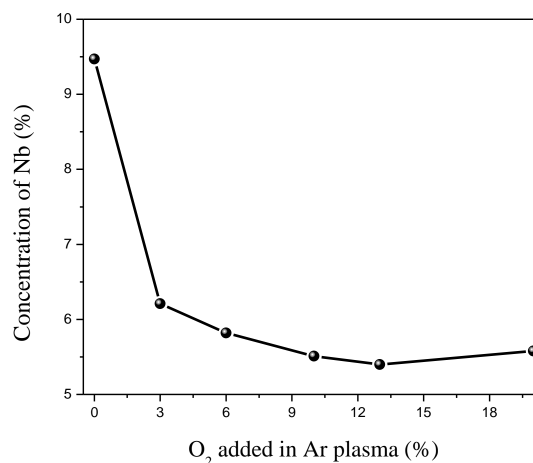

Figure 6.2 Nb concentration variation as a function of O_2 added in Ar plasma

The concentration of Nb in the Nb-TiO_2 films was determined from the XPS measurements and is listed in Table 6.1. As can be seen in Figure 6.2 a strong decrease is observed for a small quantity of oxygen (3%) added in Ar plasma. After 3% O_2, the Nb concentration in the films with increasing the oxygen quantity in Ar plasma remains in the range 5-6%. The chemical compositions were determined for Nb-TiO_2 films deposited in Ar-O_2 and are given in Table 6.1. Similar to the TiO_2 films prepared in Ar-O_2 in the same conditions as Nb-TiO_2 films, a decrease of x in $Ti_{1-x}Nb_yO_2$ is observed, with a minimum at 6% O_2 added in Ar plasma, after this oxygen concentration x in $Ti_{1-x}Nb_yO_2$ increasing again. The variation of x in $Ti_{1-x}Nb_yO_2$ with the O_2 concentration added in the gas mixture can be attributed to the formation of oxygen vacancies during the deposition at room temperature. According to the chemical compositions of Nb-TiO_2 films seems that Ti is not substituted by Nb in these films, and only oxygen vacancies are formed.

The VB of Nb-doped TiO_2 films prepared at various oxygen concentrations added in Ar plasma was investigated. The VBs for Nb-doped TiO_2 films prepared in Ar-O_2 atmosphere, with 3% and 20% O_2 added in discharge are shown in Figure 6.3 (b) and (c). For comparison, the VB of the sample prepared in pure-Ar is shown in Figure 6.3 (a). Four components were necessary for fitting the VB spectra, as described in Chapter 4. The VBM of the films prepared in Ar-O_2 atmosphere were determined and are listed in Table 6.2.

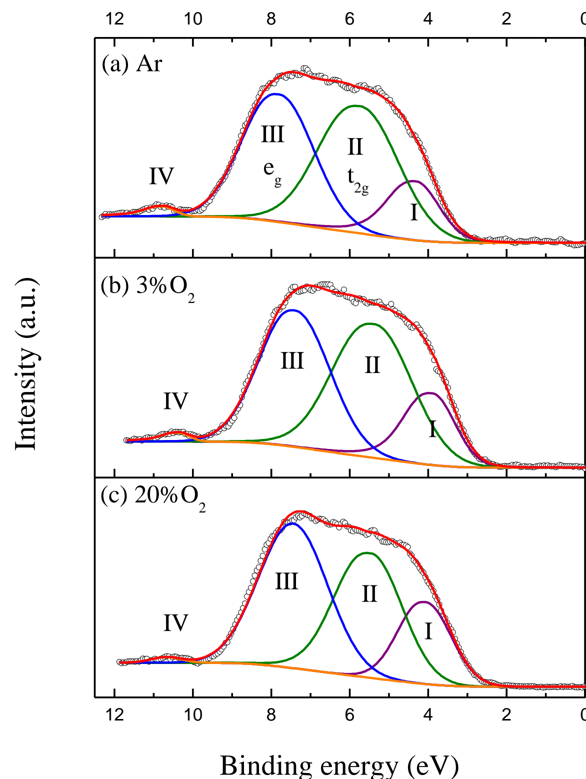

Figure 6.3 VB spectra for Nb-doped TiO_2 films prepared in (a) Ar plasma, (b) 3% O_2 and (c) 20% O_2 added in Ar-O_2 atmosphere (-550 *V*)

Table 6.2 Fit results for VB of Nb-TiO_2 prepared in Ar-O_2 atmosphere

[%O_2]	VBM [eV]		Peak I	Peak II	Peak III	Peak IV
pure-Ar	3.14	**BE (eV)** **FWHM (eV)**	4.30 1.38	5.73 2.26	7.80 2.07	10.78 0.74
3%	2.71	**BE (eV)** **FWHM (eV)**	3.89 1.35	5.36 2.23	7.39 2.07	10.37 0.67
6%	2.82	**BE (eV)** **FWHM (eV)**	4.15 1.56	5.51 1.84	7.31 2.00	10.84 0.30
10%	2.90	**BE (eV)** **FWHM (eV)**	4.01 1.37	5.40 2.38	7.56 2.07	10.68 0.85
13%	2.62	**BE (eV)** **FWHM (eV)**	3.74 1.12	5.20 2.56	7.47 2.07	10.61 0.84
20%	2.71	**BE (eV)** **FWHM (eV)**	4.07 1.54	5.46 1.87	7.44 2.07	10.67 0.91

From the VB spectra, the area under the peak IV in Figure 6.3, indicated to be given by the contribution coming from OH groups as a consequence of H_2O dissociation was determined and plotted as OH3σ/VB in function of O_2 in Ar-O_2 atmosphere in Figure 6.4. As can be seen, the OH3σ/VB is decreasing when O_2 concentration in discharge is increased. Comparing with TiO_2 films prepared in Ar-O_2 atmosphere, the values for OH3σ/VB in Nb-TiO_2 films were much lower and decreasing with increasing the oxygen concentration in the gas mixture. For the sample prepared in pure-Ar OH3σ/VB value obtained for TiO_2 film was 0.028, while for Nb-TiO_2 film was 0.014. An increase for OH3σ/VB value was observed for TiO_2 films with increasing x in TiO_{2-x}.

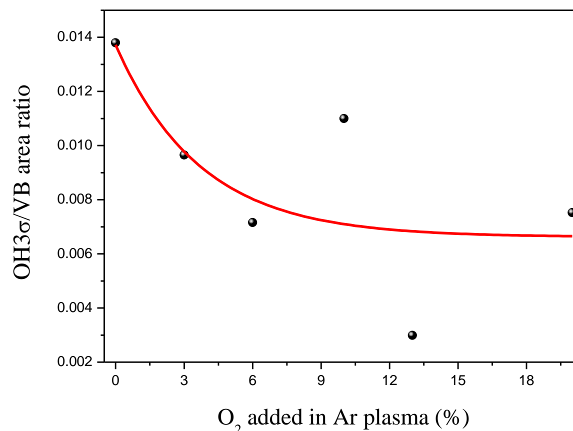

Figure 6.4 OH3σ/VB as a function of O_2 added in Ar plasma (-550 V)

6.2.1.3 Film structure and morphology

The Nb-TiO_2 films structure was analyzed by XRD. All the samples were having an amorphous structure.

The top-view and cross-section SEM images for Nb-TiO_2 film deposited in Ar-O_2 atmosphere, with 20%O_2 added in Ar plasma, at -750 *V* are shown in Figure 6.5. The film shows a dense morphology with agglomerated grains and a dense columnar structure.

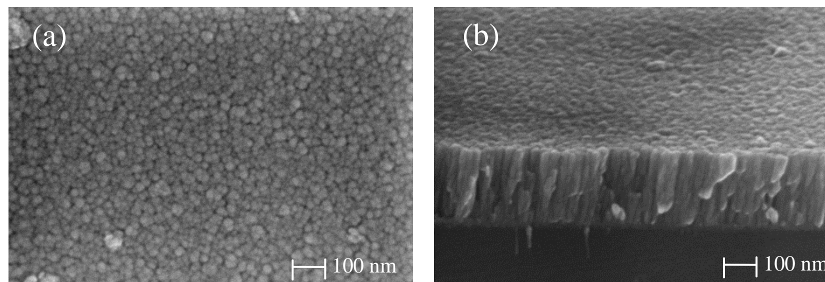

Figure 6.5 (a) Top-view and (b) cross-section images for Nb-TiO_2 film prepared in Ar-O_2 (20%O_2)

6.2.1.4 Influence of post-growth annealing on the film chemical composition

Post-growth annealing at 900°C for 1h in vacuum of Nb-TiO_2 films deposited at -750 *V* in Ar-O_2 gas mixture (20%O_2) was performed. The changes in core-levels were investigated with XPS. In Figure 6.6 are shown the O *1s*, Ti *2p* and Nb *3d* XPS spectra, for as-grown and post-growth annealed Nb-TiO_2 films. In O *1s*, an increase in the second component after annealing is observed. Ti^{3+} states were detected after annealing in the Ti *2p* core-level. Also in Nb *3d* core-level additional states were detected after annealing, the Nb^{4+} states. The BEs of O_I, Ti^{4+} $2p_{3/2}$, Ti^{3+} $2p_{3/2}$, Nb^{5+} $3d_{5/2}$ and Nb^{4+} $3d_{5/2}$ for as-grown and post-growth annealed Nb-TiO_2 films prepared in 20%O_2 in Ar-O_2 atmosphere are listed in Table 6.3.

The chemical composition was determined for both as-grown and annealed in vacuum films and is given in Table 6.4. No considerable change is observed in the x value in $Ti_{1-x}Nb_yO_2$ after annealing in vacuum.

Table 6.3 O_I, Ti^{4+} $2p_{3/2}$, Ti^{3+} $2p_{3/2}$, Nb^{5+} $3d_{5/2}$ and Nb^{4+} $3d_{5/2}$ BEs for as-grown and post-growth annealed Nb-TiO_2 prepared in Ar-O_2

	BE(O_I) (eV)		**BE(Ti^{4+} $2p_{3/2}$) (eV)**		**BE(Ti^{3+} $2p_{3/2}$) (eV)**		**ΔE (O_I-Ti$2p_{3/2}$) (eV)**		**BE($Nb^{5+}$$3d_{5/2}$) (eV)**		**BE($Nb^{4+}$$3d_{5/2}$) (eV)**	
	as-gr	ann	as-gr	ann	as-gr	ann	as-gr	ann	as-gr	ann	as-gr	ann
20%O_2	530.11	530.15	458.62	458.97	-	456.91	71.49	71.18	207.15	207.31	-	205.92

Table 6.4 Nb concentrations, Nb^{4+}/Nb^{5+} and the chemical compositon for as-grown and post-growth annealed Nb-TiO_2 prepared in Ar-O_2

	%Nb		Nb^{4+}/Nb^{5+}		Chemical composition	
	as-gr	ann	as-gr	ann	as-gr	ann
20%O_2	4.57	6.92	-	0.0052	$Ti_{1-0.10}Nb_{0.14}O_2$	$Ti_{1-0.11}Nb_{0.21}O_2$

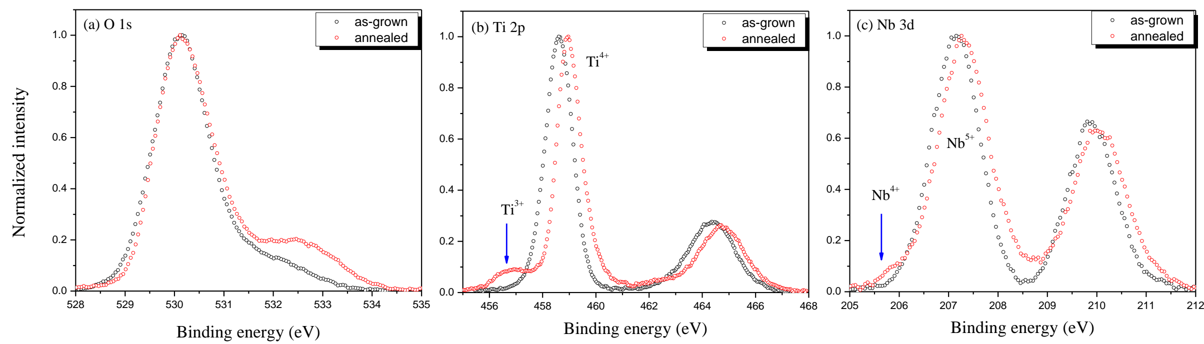

Figure 6.6 O *1s*, Ti *2p* and Nb *3d* XPS spectra for as-grown and post-growth annealed in vacuum Nb-TiO_2 films prepared in Ar-O_2 atmosphere (20%O_2), at -750 V

6.2.1.5 Influence of post-growth annealing on the film structure

After the post-growth annealing of in vacuum of Nb-TiO_2 film prepared in Ar-O_2 gas mixture, the XRD pattern reveals only the anatase phase, as shown in Figure 6.7, while for the Nb-TiO_2 and TiO_2 films prepared in Ar plasma and annealed in vacuum both anasate and rutile phases were detected. The calculated grain size for post-growth annealed in vacuum Nb-TiO_2 film prepared in Ar-O_2 gas mixture using the Scherrer equation was ~18.4 *nm*, similar to the values obatined for the Nb-TiO_2 and TiO_2 films prepared in Ar plasma and annealed in vacuum (~22 *nm* and ~21 *nm* respectively).

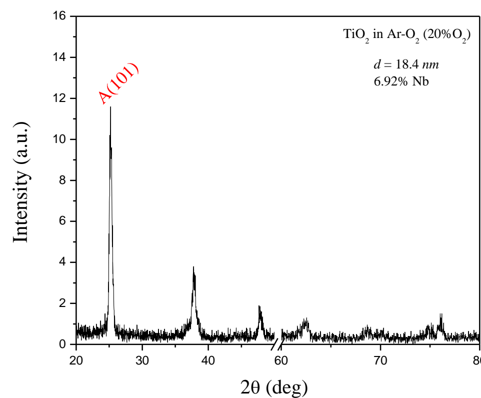

Figure 6.7 XRD pattern for post-growth annealed in vacuum Nb-TiO_2 film prepared in Ar-O_2, with 20%O_2

Even after post-growth annealing at high temperature (900°C), the morphology of Nb-TiO_2 film prepared with 20% O_2 remains dense with agglomerated grains and a dense columnar structure (Figure 6.8).

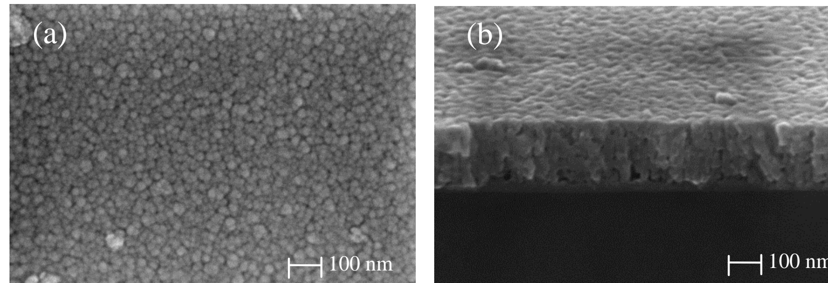

Figure 6.8 Top-view and cross-section images for post-growth annealed Nb-TiO_2 film prepared in Ar-O_2 (20% O_2)

6.2.2 Deposition of Nb-TiO_2 films by co-sputtering from two separate targets

The Nb-TiO_2 thin films presented in this section were obtained by co-sputtering from two separate targets of TiO_2 and Nb, for a better control over the Nb concentration. Oxygen concentration introduced in Ar plasma was set at 10% during all the experiments and the applied power to Nb target was varied, in order to have a wide range of Nb concentrations in the deposited films. The cathode self-bias voltage was fixed at -850 *V*.

6.2.2.1 Film growth rate

The growth rate for Nb-TiO_2 films deposited at -850 V, in 10% O_2 added in Ar plasma, at various powers applied to Nb target is shown in Figure 6.9. When Nb is sputtered, the growth rate is decreasing significantly, from 0.86±0.06 *nm/min* when no Nb was sputtered, to 0.23±0.02 *nm/min* when 3 *W* was

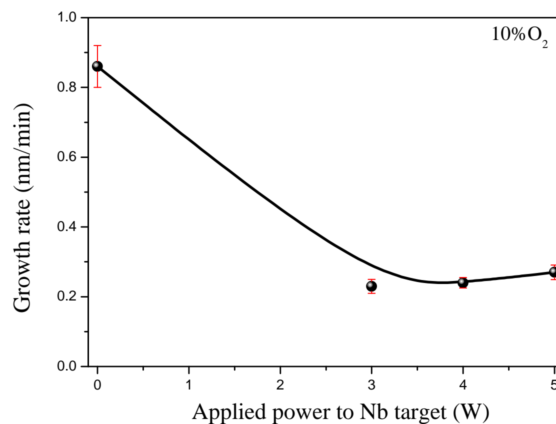

Figure 6.9 Film growth rates for co-sputtered at RT Nb-TiO_2 deposited at 10% O_2 as a function of applied power to Nb target

applied to Nb target. The decrease in film growth rate value is more likely due to the oxidation of the Nb target in the Ar-O_2 plasma. Increasing the power, no major changes are observed in the growth rate.

6.2.2.2 Film chemical composition

The core-levels of Nb-TiO_2 films prepared with 10% O_2, at various applied powers to Nb target were investigated with XPS. For O *1s* and C *1s* core-levels three components were necessary. In Ti *2p* core-level spectra, Ti^{3+} states were detected only for 4 *W* and 5 *W* powers applied to Nb target. Niobium was detected in all the films only as Nb^{5+}. In Table 6.5 the BEs of O_I, Ti^{4+} $2p_{3/}2$, Ti^{3+} $2p_{3/2}$ and Nb^{5+} $3d_{5/2}$ are given.

The Nb concentration in Nb-TiO_2 films prepared at 10% O_2 is plotted as a function of applied power to Nb target in Figure 6.10 and the values are given in Table 6.6. In all the films, the Nb concentration was less the 1%. An experimental fit of the plot could be performed. Interpolated Nb concentration values could be derived for the films grown at 1 W and 2 W.

The chemical composition of the films was determined and is given in Table 6.6. From the chemical composition it is observed that x in $Ti_{1-x}Nb_yO_2$ is increasing for the films prepared at 4 W and 5 W as compared to the sample prepared at 3 W, indicating a reduction in the number of oxygen vacancies in these films.

Table 6.5 O_I, Ti^{4+} $2p_{3/}2$, Ti^{3+} $2p_{3/2}$ and Nb^{5+} $3d_{5/2}$ BEs for Nb-TiO_2 films prepared in 10% O_2 and various applied powers to Nb target

Applied power to Nb (W)	BE(O_I) (eV)	BE(Ti^{4+} $2p_{3/2}$) (eV)	BE(Ti^{3+} $2p_{3/2}$) (eV)	ΔE (O_I-Ti$2p_{3/2}$) (eV)	BE(Nb^{5+} $3d_{5/2}$) (eV)
3	529.88	458.56	-	71.32	206.97
4	530.39	459.17	457.97	71.22	210.68
5	529.59	458.44	457.30	71.15	209.13

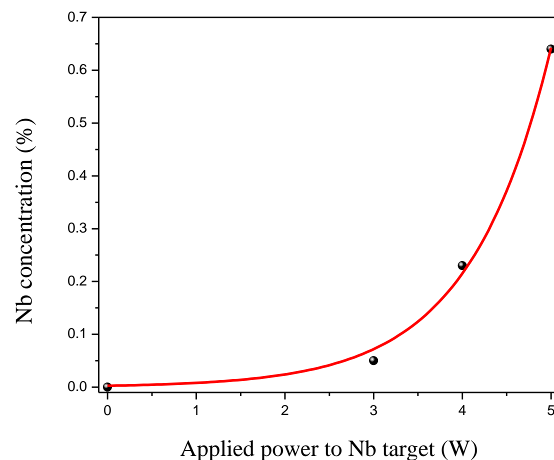

Figure 6.10 Nb concentration determined in co-sputtered at RT Nb-TiO_2 films prepared with 10% O_2, at different applied powers to Nb target

Table 6.6 Nb concentrations and the chemical composition for Nb-TiO_2 films prepared in 10%O_2 and various applied powers to Nb target

Applied power to Nb (W)	%Nb	Chemical formula
1	0.009	-
2	0.02	-
3	0.05	$Ti_{1+0.19}O_2Nb_{0.001}$
4	0.23	$Ti_{1+0.03}O_2Nb_{0.01}$
5	0.64	$Ti_{1+0.09}O_2Nb_{0.01}$

6.2.2.3 Film structure

The crystalline structure of co-sputtered Nb-TiO_2 films prepared in 10%O_2 added in Ar plasma, at various applied powers to Nb target were investigated by XRD. The films were found to be amorphous.

6.2.2.4 Influence of post-growth annealing on the film chemical composition

Post-growth annealing was performed for all Nb-TiO_2 samples prepared in 10%O_2 at various powers applied to Nb target. The chemical composition of the samples deposited with 3 *W* and 4 *W* applied power to Nb target were analyzed with XPS. No Ti^{3+} and Nb^{4+} states were detected in the Ti *2p* and Nb *3d* core-levels for post-growth annealed samples. In Table 6.7 the BEs of O_I, Ti^{4+} $2p_3/2$, Ti^{3+} $2p_{3/2}$ and Nb^{5+} $3d_{5/2}$ are given.

The chemical composition in the as-grown and annealed in vacuum Nb-TiO_2 films prepared in 10%O_2 added in Ar plasma are given. A decrease of x in $Ti_{1-x}Nb_yO_2$ after annealing is observed, indicating an increase in the number of oxygen vacancies.

Table 6.7 O_I, Ti^{4+} $2p_3/2$, Ti^{3+} $2p_{3/2}$ and Nb^{5+} $3d_{5/2}$ BEs

Applied power to Nb (W)	BE(O_I) (eV)		BE(Ti^{4+} $2p_{3/2}$) (eV)		BE(Ti^{3+} $2p_{3/2}$) (eV)		ΔE (O_I-Ti2$p_{3/2}$) (eV)		BE(Nb^{5+} $3d_{5/2}$) (eV)		Chemical formula	
	as-gr	ann	as-gr	ann	as-gr	ann	as-gr	ann	as-gr	ann	as-gr	ann
3	529.88	530.86	458.56	459.63	-	-	71.32	71.23	206.97	208.28	$Ti_{1+0.19}Nb_{0.001}O_2$	$Ti_{1+0.22}Nb_{0.001}O_2$
4	530.39	530.80	459.17	459.58	457.97	-	71.22	71.22	210.68	208.14	$Ti_{1+0.03}Nb_{0.01}O_2$	$Ti_{1+0.09}Nb_{0.01}O_2$

6.2.2.5 Influence of post-growth annealing on the film structure

After post-growth annealing in vacuum, the structure of Nb-TiO_2 films prepared in 10%O_2 with different concentrations of Nb become polycrystalline. Both anatase and rutile phases of TiO_2 were detected in the XRD patterns, as shown in Figure 6.11, with broad peaks. At the highest concentration of Nb in these films, corresponding to 5 W the applied power to Nb target, the anatase peak A(101) is very intense.

In Table 6.8 the positions and the FWHMs of the A(101) and R(110) XRD peaks are given, together with the calculated grain sizes. The grain size appears to decrease for a higher value of Nb concentration in the films (equivalent with a higher power applied to Nb target).

Table 6.8 The positions and the FWHMs of the detected A(101) and R(110) XRD peaks for post-growth annealed Nb-TiO_2 prepared in 10% O_2, at various powers applied to Nb target

Applied Power to Nb (W)	Phase	2θ(deg)	FWHM (deg)	Grain size (nm)
3	A(101)	25.33	0.567	~13.9
	R(110)	27.59	0.736	~10.6
4	A(101)	25.32	0.624	~12.6
	R(110)	27.48	0.670	~11.7
5	A(101)	25.35	0.680	~11.5
	R(110)	27.47	0.890	~11.0

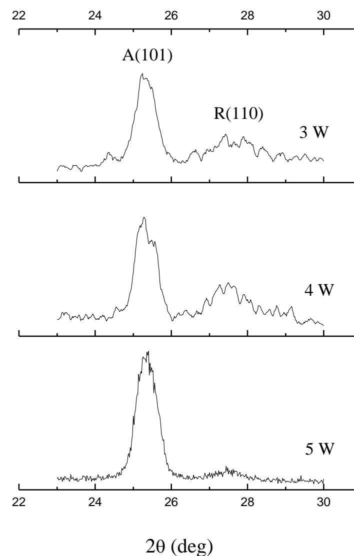

Figure 6.11 XRD patterns for co-sputtered Nb-TiO_2 films prepared at RT in 10% O_2 at various applied powers to Nb target

6.3 Film deposition in Ar-H_2 plasma

6.3.1 Sputtering of Nb-TiO_2 films from a mosaic target

The Nb-TiO_2 thin films presented in this section were sputtered from a mosaic target, described in the experimental section. Hydrogen concentration introduced in Ar plasma was varied from 3 to 20%. The cathode self-bias voltages were fixed at -550 *V* and -750 *V*.

6.3.1.1 Film growth rate

The growth rates for Nb-TiO_2 films deposited at -550 *V* on TiO_2 cathode, at various concentrations of hydrogen added in Ar plasma were determined and are plotted in Figure 6.12. The addition of small amount of H_2 in Ar plasma leads to a slight increase in the growth rate, from 0.51±0.02 *nm/min* when no H_2 was introduced in Ar plasma to 0.61±0.03 *nm/min* when 3%H_2 was added in discharge. At high hydrogen concentration in discharge (20%H_2) the growth rate drops to low values (0.27±0.04 *nm/min*).

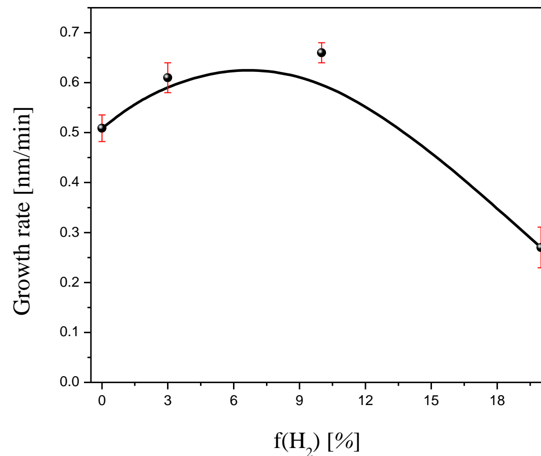

Figure 6.12 Growth rate for Nb-TiO_2 films prepared at RT in Ar-H_2 atmosphere, at -550 *V*

6.3.1.2 Film chemical composition

The chemical composition of Nb-TiO_2 films deposited as -550 *V* on TiO_2 cathode, in various concentrations of H_2 added in Ar plasma was studied with XPS. The C *1s*, O *1s*, Ti *2p* and Nb *3d* core levels were acquired for each sample.

Similar to the case of intrinsic doping of TiO_2 when hydrogen was used as reactive gas in discharge, in Ti *2p* core-level spectra, Ti^{3+} states were detected in all Nb-TiO_2 films prepared in Ar-H_2 atmosphere. Only Nb^{5+} states were detected in Nb *3d* core-level spectra. In Table 6.9 the BEs of O_I, Ti^{4+} $2p_{3/2}$, Ti^{3+} $2p_{3/2}$ and Nb^{5+} $3d_{5/2}$ are given.

The chemical formulas were determined and are given in Table 6.9. x in $Ti_{1-x}Nb_yO_2$ is decreasing when hydrogen is added in Ar plasma, indicating an increase in the number of oxygen vacancies. The decrease is more pronounced when 3%H_2 is added in the gas mixture attributed to a higher number of formed oxygen vacancies. Increasing the H_2 concentration in the gas mixture, less oxygen vacancies were observed, most probably filled by Ti-OH from H_2O dissociation or Ti-H bonds coming from the interaction of the film with the Ar-H_2 plasma..

Table 6.9 O_I, Ti^{4+} *$2p_{3/2}$*, Ti^{3+} *$2p_{3/2}$* and Nb^{5+} *$3d_{5/2}$* BEs, Nb concentration and chemical formulas for Nb-TiO_2 films prepared in Ar-H_2 (-550 *V* on TiO_2 target)

	BE(O_I)	**BE(Ti^{4+}) (eV)**	**BE(Ti^{3+}) (eV)**	**ΔE O_I-Ti2$p_{3/2}$ (eV)**	**BE(Nb^{5+})**	**Nb(at.%)**	**Chemical formula**
pure-Ar	530.47	458.92	-	71.55	207.48	9.47	$Ti_{1-0.32}O_2Nb_{0.28}$
[%H_2]							
3%	530.56	459.04	457.93	71.52	207.57	3.87	$Ti_{1-0.19}O_2Nb_{0.11}$
10%	530.63	459.11	457.52	71.52	207.66	9.38	$Ti_{1-0.23}O_2Nb_{0.29}$
20%	530.44	458.94	457.85	71.50	207.45	10.82	$Ti_{1-0.24}O_2Nb_{0.33}$

The Nb concentration in Nb-TiO_2 films prepared in Ar-H_2 atmosphere is plotted in Figure 6.13. When a small amount of hydrogen is added in discharge, the Nb concentration is decreasing from 9.47 when the films were deposited in Ar plasma to 3.87 when 3%H_2 was added in discharge. Increasing the hydrogen amount in discharge, the Nb concentration in the films was found to be similar to the value found in the film deposited in Ar plasma. A further increase of H_2 concentration in discharge leads to an increase in the Nb concentration. The increase in Nb concentration with the hydrogen quantity added in the gas mixture can be explained by the formation of ArH^+ ion, easily formed in Ar-H_2 plasmas [1]. The ArH^+ ion is able to increase the metal sputtering.

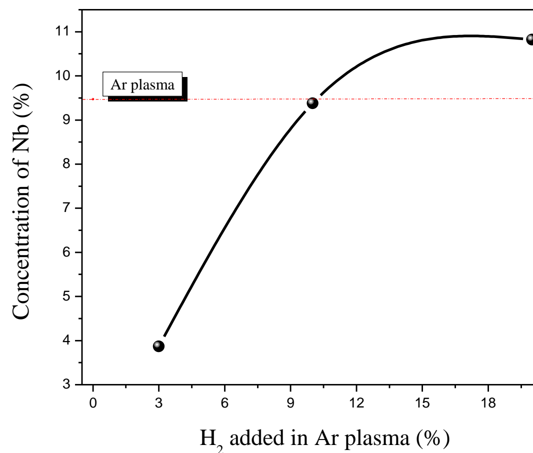

Figure 6.13 Nb concentration variation as a function of H_2 added in Ar plasma for Nb-TiO_2 films prepared at RT (-550 V on TiO_2 cathode)

The VB of Nb-TiO_2 film prepared at 20%H_2 added in discharge, at -550 *V* is shown in Figure 6.14. The VB was best fitted with five components. As in the case of intrinsically-doped TiO_2 films prepared in Ar-H_2 atmosphere, in the e_g states region two components were necessary, denoted in Figure 6.14 as III*a* and III*b*. Also the Ti *3d* peak corresponding to oxygen vacancies was detected, denoted in the figure as peak V. The BEs and FWHMs of all components are given in Table 6.10.

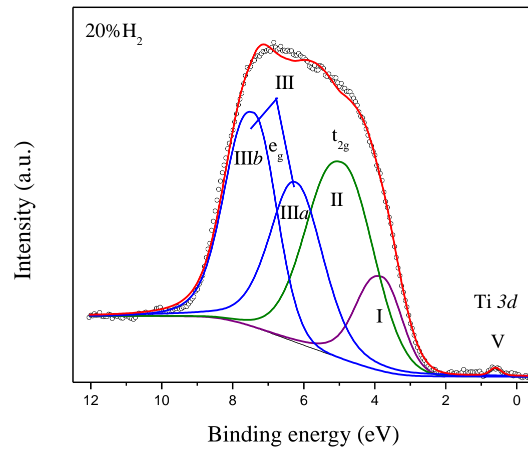

Figure 6.14 VB for Nb-doped TiO_2 film prepared in Ar-H_2 atmosphere (20%H_2), at RT and -550 *V* on TiO_2 cathode

Table 6.10 VB fit results for Nb-TiO_2 film prepared at RT in Ar-H_2 atmosphere (-550 *V* on TiO_2 cathode)

[%H_2]		Peak I	Peak II	Peak III*a*	Peak III*b*	Peak V
20%	**BE (eV)**	3.80	4.91	6.21	7.42	0.59
	FWHM (eV)	1.32	2.05	1.77	1.50	0.37

6.3.1.3 Film structure and morphology

The films structure was investigated with XRD. All the as-grown Nb-TiO_2 films prepared in Ar-H_2 atmosphere were amorphous.

The top-view and cross-section images for one sample prepared with 20%H_2 introduced in discharge, at -750 *V* is shown in Figure 6.15. The film has a dense morphology and a columnar structure.

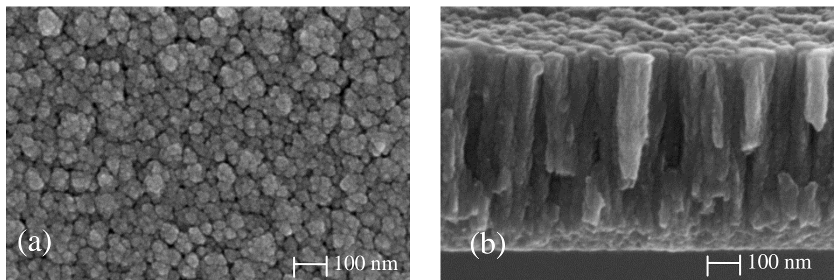

Figure 6.15 Top-view and cross-section images for Nb-TiO_2 film prepared in Ar-H_2 (20%H_2)

6.3.1.4 Influence of post-growth annealing on the film chemical composition

After post-growth annealing in vacuum of Nb-TiO_2 samples prepared in Ar-H_2 atmosphere at -750 *V*, the chemical composition was investigated with XPS. The Nb concentration in this film was 10%.

In Figure 6.16 the O *1s*, Ti *2p* and Nb *3d* core-levels XPS spectra for as-grown and post-growth annealed Nb-TiO_2 films prepared with 20%H_2 added in Ar plasma are shown. Strong shifts in all spectra for the post-growth annealed samples can be observed. In Table 6.11 the BEs of O_I, Ti^{4+} $2p_{3/2}$, Ti^{3+} $2p_{3/2}$, and Nb^{5+} $3d_{5/2}$ for as-grown and annealed samples are given. Ti^{3+} states were detected in both as-grown and annealed samples. No Nb^{4+} states were detected in the Nb *3d* core-level spectra.

The chemical composition for the as-grown and annealed in vacuum sample was obtained: $Ti_{1-0.21}Nb_{0.33}O_2$ for the as-grown sample and $Ti_{1-0.38}Nb_{0.42}O_2$ for the annealed one. An increase of x value in $Ti_{1-x}Nb_yO_2$ is observed after annealing in vacuum, correlated with a reducing in the number of oxygen vacancies, but the presence of Ti^{3+} states indicates the contrary.

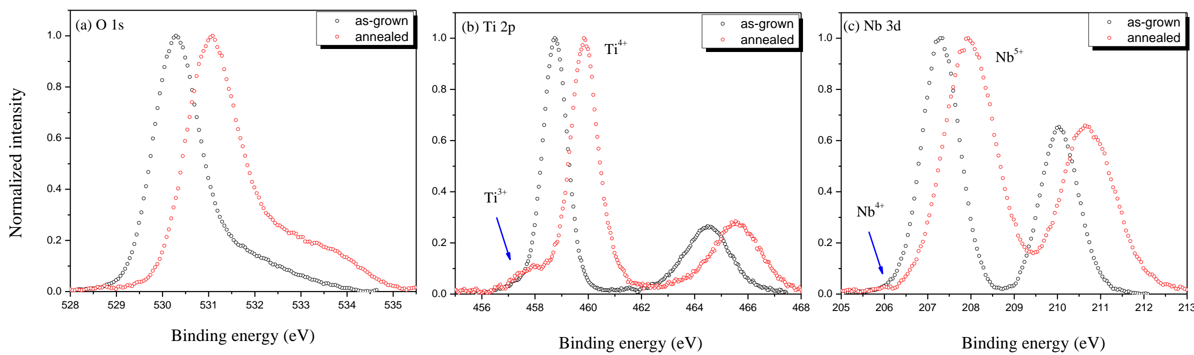

Figure 6.16 (a) O *1s*, (b) Ti *2p* and (c) Nb *3d* XPS spectra for as-grown and post-growth annealed Nb-TiO_2 films prepared in Ar-H_2 atmosphere, ar RT, -750 V on TiO_2 cathode

Table 6.11 O_I, Ti^{4+} $2p_{3/2}$, Ti^{3+} $2p_{3/2}$, and Nb^{5+} $3d_{5/2}$ BEs for as-grown and post-growth annealed Nb-TiO_2 prepared in Ar-H_2, at RT (-750 V on TiO_2 cathode)

	BE(O_I) (eV)		**BE($Ti^{4+}2p_{3/2}$) (eV)**		**BE($Ti^{3+}2p_{3/2}$) (eV)**		**ΔE(O_I-Ti$2p_{3/2}$) (eV)**		**BE($Nb^{5+}3d_{5/2}$) (eV)**	
	as-gr	ann	as-gr	ann	as-gr	ann	as-gr	ann	as-gr	ann
20%H_2	530.27	531.03	458.76	459.85	457.39	457.87	71.51	71.18	207.30	207.97

6.3.1.5 Influence of post-growth annealing on the film structure and morphology

The structure of post-growth annealed Nb-TiO_2 films prepared with 20% H_2 in discharge at -750 *V* was investigated with XRD. After annealing, the amorphous structure transforms predominantly in anatase phase, as can be seen in the XRD pattern in Figure 6.17, similar to the annealed in vacuum Nb-TiO_2 film prepared in the same conditions in Ar-O_2 atmosphere, while for the one prepared in Ar plasma both anatase and rutile phases were detected. The grains size was found to be ~14.4 *nm*, smaller than in the case of annealed in vacuum Nb-TiO_2 films prepared in Ar and Ar-O_2 atmosphere, where the grains size was ~20 *nm*.

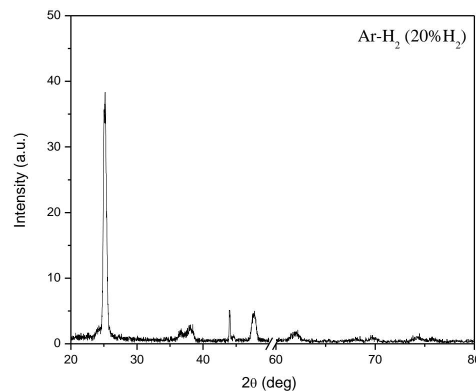

Figure 6.17 XRD pattern for post-growth annealed Nb-TiO_2 film prepared in Ar-H_2, with 20% H_2

In the SEM images shown in Figure 6.18 can be observed that the dense morphology is preserved after post-growth annealing. The structure of annealed Nb-TiO_2 film is very compact.

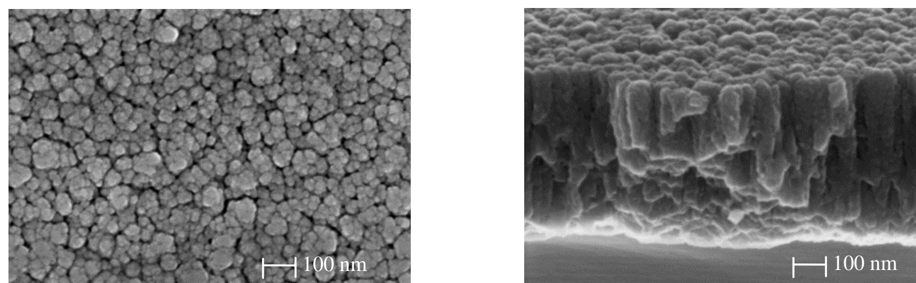

Figure 6.18 Top-view and cross-section images for post-growth annealed in vacuum Nb-TiO_2 film prepared in Ar-H_2 (20% H_2) at RT (-750 V on TiO_2 cathode)

6.3.1.6 Influence of substrate temperature on the film chemical and structural properties

Nb-TiO_2 film deposited with 3%H_2 added in Ar plasma, at a substrate temperature of 350°C, at -750 *V* cathode self-bias voltage, was characterized from the structural and chemical point of view.

In Figure 6.19 the O *1s*, Ti *2p* and Nb *3d* core-levels XPS spectra are shown. Ti^{3+} states were detected in the Ti *2p* core level XPS spectrum for this sample. In the Nb *3d* core-level XPS spectrum beside Nb^{5+} and Nb^{4+} states, another peak was detected identified as Nb^{2+} states in NbO compound. In Table 6.12 the O_I, Ti^{4+} $2p_{3/2}$, Ti^{3+} $2p_{3/2}$, Nb^{5+} $3d_{5/2}$, Nb^{4+} $3d_{5/2}$ and Nb^{2+} $3d_{5/2}$ BEs are listed. The Nb concentration in this film was 10.39%. The atomic ratios Nb^{4+}/Nb^{5+}, Nb^{2+}/Nb^{5+}, Ti^{3+}/Ti^{4+} were determined and are given in Table 6.13. According to the chemical composition of this film no oxygen vacancies were formed during the deposition.

The structure of this sample investigated with XRD was amorphous.

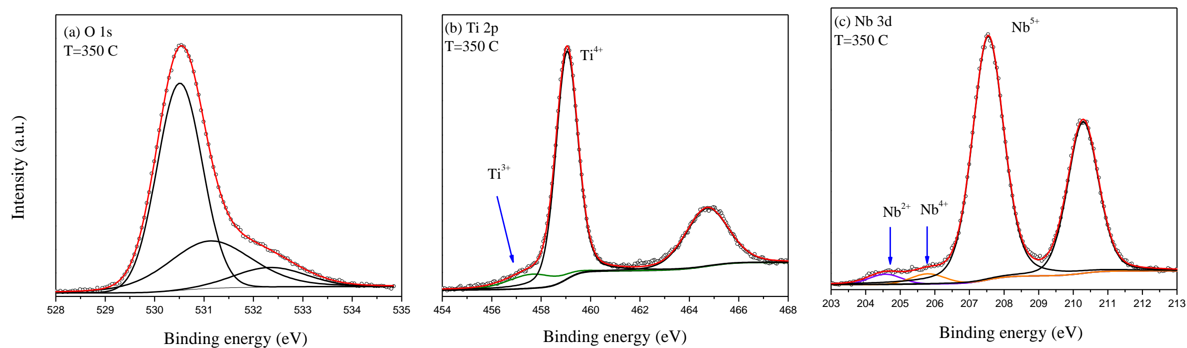

Figure 6.19 (a) O *1s*, (b) Ti *2p* and (c) Nb *3d* core-levels XPS spectra for Nb-TiO_2 sample prepared with 3%H_2 introduced in Ar plasma at -750 *V* cathode self-bias voltage and 350°*C* substrate temperature

Table 6.12 O_I, Ti^{4+} $2p_{3/2}$, Ti^{3+} $2p_{3/2}$, Nb^{5+} $3d_{5/2}$, Nb^{4+} $3d_{5/2}$ and Nb^{2+} $3d_{5/2}$ BEs for Nb-TiO_2 prepared in Ar-H_2 (3%H_2) at 350°C substrate temperature

BE(O_I) (eV)	BE(Ti^{4+} $2p_{3/2}$) (eV)	BE($Ti^{3+}$$2p_{3/2}$) (eV)	ΔE (O_I-Ti$2p_{3/2}$) (eV)	BE(Nb^{5+} $3d_{5/2}$) (eV)	BE(Nb^{4+} $3d_{5/2}$) (eV)	BE(Nb^{2+} $3d_{5/2}$) (eV)
530.51	459.05	457.63	71.46	207.54	205.80	204.56

Table 6.13 Nb concentration, Nb^{4+}/Nb^{5+}, Nb^{2+}/Nb^{5+}, Ti^{3+}/Ti^{4+} atomic ratios and the chemical formula for Nb-TiO_2 prepared in Ar-H_2 at 350°C substrate temperature

%Nb	Nb^{4+}/Nb^{5+}	$Nb2^{+}/Nb^{5+}$	Ti^{3+}/Ti^{4+}	Chemical composition
10.39	0.025	0.024	0.09	$Ti_{1+0.01}Nb_{0.33}O_2$

6.3.2 Deposition of Nb-TiO_2 films by co-sputtering from two separate targets

The Nb-TiO_2 films described in this section were obtained by co-sputtering from two separate targets of TiO_2 and Nb. Hydrogen concentration added in Ar plasma was set at 10% and the applied power to Nb target was varied. The cathode self-bias voltage was fixed at -850 *V*.

6.3.2.1 Film growth rate

The growth rates were determined for Nb-TiO_2 films deposited in Ar-H_2 atmosphere (10%H_2) at -850 *V* and are plotted in Figure 6.20 as a function of applied powers to Nb targets. A slight increase is observed with increasing the power to Nb target due to the contribution of Nb cathode to the discharge power.

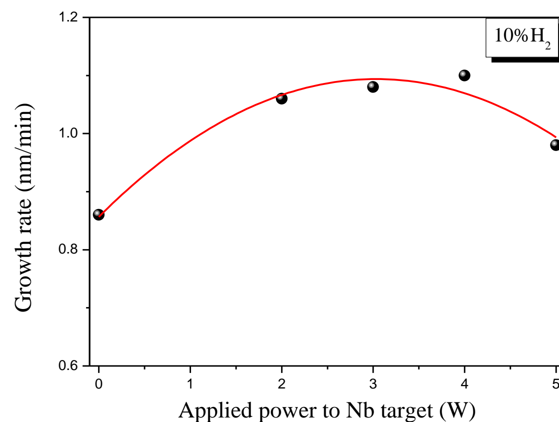

Figure 6.20 Growth rate for Nb-TiO_2 films deposited at 10%H_2 as a function of applied power to Nb target

6.3.2.2 Film chemical composition and structure

The chemical composition of the obtained films was investigated with XPS. In all the Ti *2p* core-levels XPS spectra, Ti^{3+} and Nb^{5+} states were detected. The BEs of O_I, Ti^{4+} $2p_{3/}2$, Ti^{3+} $2p_{3/2}$, Nb^{5+} $3d_{5/2}$ from XPS measurements are listed in Table 6.14.

The Nb concentration is plotted in Figure 6.21 as a function of the applied powers to Nb target. An increase is observed when the power applied to Nb target is increased. The Nb concentrations for each power applied to Nb target is given in Table 6.14. An experimental fit of the plot could be performed. Interpolated Nb concentration value could be derived for the film grown at 3 W.

According to the chemical composition for these films, given in Table 6.14, in $Ti_{1-x}Nb_yO_2$ is increasing with the applied power to Nb target indicating a decrease in the number of oxygen vacancies with increasing the power to Nb target.

Table 6.14 O_I, Ti^{4+} *2p*$_{3/}$2, Ti^{3+} $2p_{3/2}$, Nb^{5+} $3d_{5/2}$ and Nb^{4+} $3d_{5/2}$ BEs for Nb-TiO_2 films prepared in 10% H_2 and various applied powers to Nb target

Applied power to Nb (W)	BE(O_I) (eV)	BE(Ti^{4+} $2p_{3/2}$) (eV)	BE(Ti^{3+} $2p_{3/2}$) (eV)	ΔE (eV)	BE(Nb^{5+} $3d_{5/2}$) (eV)	%Nb	Chemical formula
3	530.31	458.90	457.30	71.41	207.39	0.07	$Ti_{1+0.30}Nb_{0.0023}O_2$
4	530.34	458.90	457.39	71.44	209.02	0.38	$Ti_{1+0.09}Nb_{0.01}O_2$
5	529.94	458.65	457.19	71.29	209.20	2.03	$Ti_{1+0.13}Nb_{0.06}O_2$

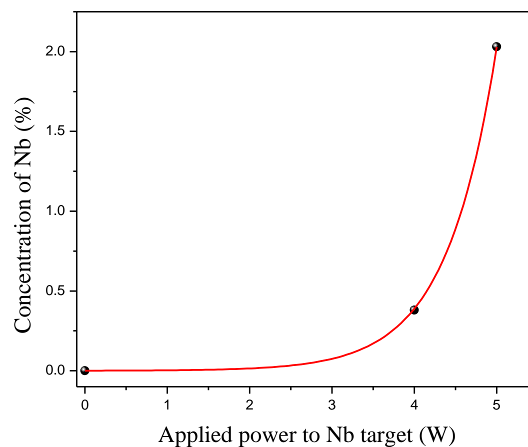

Figure 6.21 Nb concentration in Nb-TiO_2 films prepared in 10% H_2 at various powers applied to Nb target (-850 V on TiO_2

The structural properties of the films were investigated with XRD. The XRD patterns reveal an amorphous structure.

6.3.2.3 Influence of post-growth annealing on the film chemical composition

After post-growth annealing in vacuum at 900°C of Nb-TiO_2 samples prepared with 10% H_2 added in Ar plasma, at various powers applied to Nb target (co-sputtering configuration from separate targets), the chemical composition was investigated with XPS. The samples prepared at 2 *W* and 5 *W* were analyzed. In the as-grown films Ti^{4+}, Ti^{3+} and Nb^{5+} states were detected. After annealing Nb^{4+} states were detected for the annealed film prepared at 5 W, while for the sample prepared at 2 W the Nb 3d signal was too small to identify the oxidation states of Nb. The BEs of the peaks are given in Table 6.15.

The chemical compositions for the annealed samples were determined and are given in Table 6.16. According to the formulas, a decrease in the number of oxygen vacancies after annealing in vacuum is observed, represented by the increase of x in $Ti_{1-x}Nb_yO_2$.

Table 6.15 O_I, Ti^{4+} *2p*$_{3/2}$, Ti^{3+} *2p*$_{3/2}$,Nb^{5+} *3d*$_{5/2}$ and Nb^{4+} *3d*$_{5/2}$ BEs for annealed in vacuum Nb-TiO_2 films prepared in 10% H_2 added in Ar plasma at 2 and 5 W powers to Nb target

Applied power to Nb (W)	**BE(O_I) (eV)**		**BE(Ti^{4+} *2p*$_{3/2}$) (eV)**		**BE(Ti^{3+} *2p*$_{3/2}$) (eV)**		**ΔE (O_I-Ti2$p_{3/2}$) (eV)**		**BE(Nb^{5+} *3d*$_{5/2}$) (eV)**		**BE(Nb^{4+} *3d*$_{5/2}$) (eV)**	
	as-gr	ann	as-gr	ann	as-gr	ann	as-gr	ann	as-gr	ann	as-gr	ann
2	-	530.83	-	459.54	-	-	-	71.29	-	…	-	…
5	529.94	530.70	458.65	459.40	457.19	-	71.29	71.30	209.20	208.13	-	207.14

Table 6.16 Nb^{4+}/Nb^{5+} atomic ratio and the chemical composition for annealed in vacuum Nb-TiO_2 films prepared in 10% H_2 added in Ar plasma at 2 and 5 W powers to Nb target

Applied power to Nb (W)	**Nb^{4+}/Nb^{5+}**		**Chemical composition**	
	as-gr	ann	as-gr	ann
2	-	-	-	$Ti_{1+0.09}Nb_{0.00031}O_2$
5	-	0.15	$Ti_{1+0.13}Nb_{0.06}O_2$	$Ti_{1+0.07}Nb_{0.03}O_2$

6.3.2.4 Influence of post-growth annealing on the film structural properties

The structure of the post-growth annealed in vacuum Nb-TiO_2 films co- sputtered from TiO_2 and Nb targets in 10% H_2 added in the gas mixture was investigated with XRD. For all the films deposited in Ar-H_2 at various powers applied to Nb target a very broad peak was detected.

Examples of the obtained XRD spectra for pure-TiO_2 and Nb-TiO_2 film prepared at 2 W and 4 W together with the fit results are shown in Figure 6.22. Beside anatase and rutile peaks, the other peaks were identified to correspond to $Ti_{10}O_{19}$, a compound from the Magnéli series [2,3]. At 5 W power to Nb target, only the rutile phase was detected.

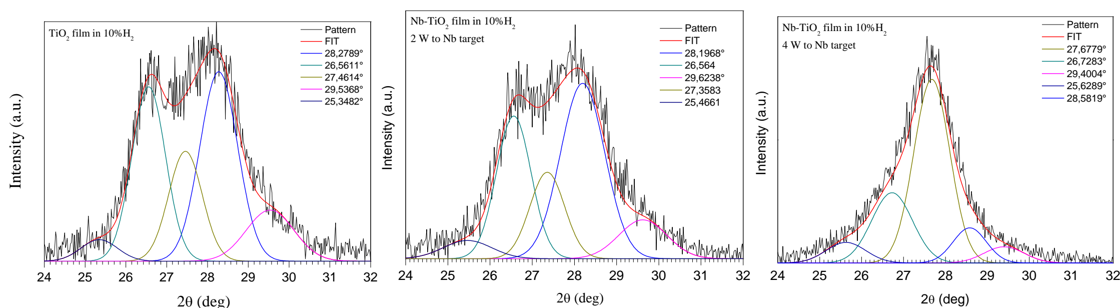

Figure 6.22 XRD spectra for annealed in vacuum TiO_2 and Nb-TiO_2 film prepared in 10% H_2 added in Ar plasma (-850 V to TiO_2 cathode)

6.4 Concluding remarks

Nb-TiO_2 films were deposited in Ar-O_2 and Ar-H_2 plasmas, using two different target arrangements: a mosaic target, in which Nb wires were placed on the TiO_2 target, and co-sputtering from separately TiO_2 and Nb targets for a better control over the Nb concentration.

The Nb concentrations in Nb-TiO_2 films sputtered from a TiO_2-Nb mosaic target in Ar-O_2 plasma (RT) are decreasing with increasing the O_2 concentration in the gas mixture (5-9%). Oxygen vacancies are formed in Nb-TiO_2 films during the deposition in Ar-O_2 atmosphere. The as-grown Nb-TiO_2 films were having an amorphous structure and a dense morphology with agglomerated grains. The post-growth annealing in vacuum at 900°C of the films improved the crystalline structure of the film prepared in Ar-O_2. The anatase phase was detected with XRD. The columnar structure from the as-grown film is preserved after annealing in vacuum.

When Nb-TiO_2 films were co-sputtered from two separate TiO_2 and Nb targets in Ar-O_2 plasma with 10%O_2 added in the gas mixture (RT), low Nb concentrations were measured in the films ($< 0.64\%$). A reduction in the number of oxygen vacancies is observed with increasing the applied power to Nb. XRD spectra reveals an amorphous structure for the as-grown films. After the post-growth annealing in vacuum at 900°C of the films, both anatase and rutile phases were observed. An increase in the number of oxygen vacancies is observed for the annealed in vacuum films.

High values of Nb concentration were obtained for Nb-TiO_2 films sputtered from a TiO_2-Nb mosaic target in Ar-H_2 plasma deposited at RT (4-11%). For these samples an increase in the Nb concentration with increasing the H_2 concentration in the gas mixture was observed, explained by the formation of ArH^+ ion, able to increase the metal sputtering. It was observed that oxygen vacancies are formed in Nb-TiO_2 films during the deposition in Ar-H_2 atmosphere, a higher number for small concentrations of H_2 in the gas mixture. Increasing the H_2 concentration in the gas mixture, less oxygen vacancies are observed, most probably filled by Ti-OH or Ti-H bonds. The as-grown Nb-TiO_2 films are having an amorphous structure and a dense morphology with agglomerated grains. The post-growth annealing in vacuum at 900°C of the films changed the amorphous structure in predominantly anatase phase. The columnar structure from the as-grown film is preserved after annealing in vacuum.

For Nb-TiO_2 films co-sputtered from two separate TiO_2 and Nb targets in Ar-H_2 plasma with 10%H_2 added in the gas mixture (RT), the Nb concentrations were $< 2\%$. The structure of the as-grown films was amorphous, as detected with XRD. A decrease in the number of oxygen vacancies with increasing the power to Nb target was observed. The post-growth annealing in vacuum at 900°C of the films changed the amorphous structure in a mixture of anatase, rutile and possible $Ti_{10}O_{19}$ phases.

6.5 References

1. N. Laidani, R. Bartali, P. Tosi and M. Anderle, *J. Phys. D: Appl. Phys.* **37** (2004) 2593

2. L. Kihlborg and I. Olovsson, Acta Cryst. A 53 (1997), 103

3. H.K. Ardakani, Thin Solid Films 248 (1994), 234

7. Electrical, optical and electronic properties of doped-TiO_2 films

High optical transparency and electrical conductivity are fundamental criteria for having a good quality transparent conductive oxide material. All electronic scattering contributions present in the material influence the mobility, and determine the upper limit of conductivity. Therefore, understanding the electronic properties variations with these intrinsic or extrinsic impurities can help to improve the transparency and the electrical conductivity in the TCO materials.

Contents

7.1 Introduction
7.2 Intrinsically doped-TiO_2 films
- 7.2.1 Electrical properties of as-grown films
- 7.2.2 Influence of post-growth annealing on film electrical properties
- 7.2.3 Influence of substrate temperature on film electrical properties
- 7.2.4 Optical properties of as-grown films
- 7.2.5 Influence of post-growth annealing on film optical properties
- 7.2.6 Influence of substrate temperature on film optical properties
- 7.2.7 Figure of merit of intrinsically-doped TiO_2 films
- 7.2.8 Electronic properties of as-grown films
- 7.2.9 Influence of post-growth annealing on film electronic properties

7.3 Extrinsically doped-TiO_2 films
- 7.3.1 Electrical properties of as-grown films
- 7.3.2 Influence of post-growth annealing on film electrical properties
- 7.3.3 Influence of substrate temperature on film electrical properties
- 7.3.4 Optical properties of as-grown films
- 7.3.5 Influence of post-growth annealing on film optical properties
- 7.3.6 Influence of substrate temperature on film optical properties
- 7.3.7 Figure of merit of extrinsically-doped TiO_2 films
- 7.3.8 Electronic properties of as-grown films
- 7.3.9 Influence of post-growth annealing on film electronic properties

7.4 Intrinsically-extrinsically co-doped TiO_2 films
- 7.4.1 Electrical properties of as-grown films
- 7.4.2 Influence of post-growth annealing on film electrical properties
- 7.4.3 Influence of substrate temperature on film electrical properties
- 7.4.4 Optical properties of as-grown films
- 7.4.5 Influence of post-growth annealing on film optical properties
- 7.4.6 Influence of substrate temperature on film optical properties
- 7.4.7 Figure of merit of intrinsically-extrinsically co-doped TiO_2 films
- 7.4.8 Electronic properties of as-grown films
- 7.4.9 Influence of post-growth annealing on film electronic properties

7.5 Concluding remarks
7.6 References

7.1 Introduction

In this chapter the electrical, optical and electronic properties of intrinsically, extrinsically and intrinsically-extrinsically co-doped TiO_2 films were investigated. The conductivity, carrier density and mobility values of the films were obtained from van der Pauw and Hall effect measurements. The optical properties were investigated with a double beam spectrophotometer. The work function with respect to the vacuum level was determined using X-ray photoelectron Spectroscopy. The obtained valence band edge, Fermi level position, work function, ionization potential and electron affinity with respect to vacuum level allowed the representation of a schematic band scheme for the investigated films.

7.2 Intrinsically-doped TiO_2 films

7.2.1 Electrical properties of as-grown films

The conductivity of the as-grown TiO_2 films prepared in pure-Ar, Ar-O_2 and Ar-H_2 atmospheres, at -550 *V*, -750 *V* and -850 *V* cathode self-bias voltages were measured. For all the films, the conductivity values are in the order 10^{-2}-10^{-3} $\Omega^{-1}cm^{-1}$.

7.2.2 Influence of post-growth annealing on film electrical properties

In order to obtained high values of conductivity, a necessary criterion for a transparent conductive material, the as-grown TiO_2 films, prepared in pure-Ar, 20%O_2 and 20%H_2 added in Ar plasma, at -750 *V* were post-growth annealed at a temperature of 900°C, for 1h, in vacuum.

In Figure 7.1 the conductivity values of as-grown and post-growth annealed films prepared in various

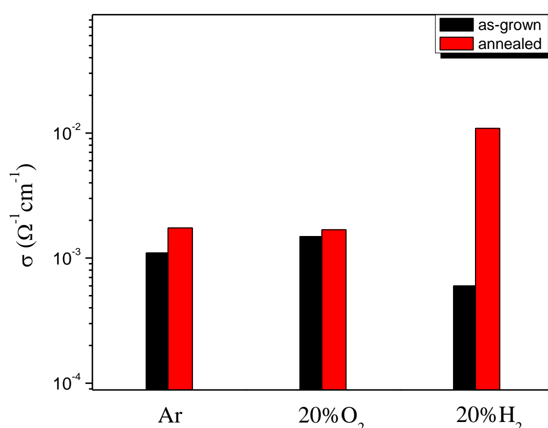

Figure 7.1 Conductivity values for post-growth annealed TiO_2 films deposited in Ar, Ar-O_2 (20%O_2) and 20%H_2 (20%H_2)

atmospheres are plotted. As can be seen, in Ar and Ar-O_2 atmospheres, no changes in the conductivity values are observed. When hydrogen is added in Ar atmosphere, an increase from 6.02x10^{-3} $\Omega^{-1}cm^{-1}$ to 1.9 x10^{-2} $\Omega^{-1}cm^{-1}$ is observed in the conductivity value.

The TiO_2 films prepared at -850 *V* were post-growth annealed at the same temperature and in the same conditions, like the samples prepared at -750 *V*. For these samples, beside the conductivity values, the carrier concentration and mobility values were measureable. The measured values for TiO_2 films prepared in Ar-O_2 and Ar-H_2 atmospheres with different concentrations of O_2 and H_2 are given in Table 7.1.

Table 7.1 Conductivity, carrier concentration and mobility values for post-growth annealed TiO_2 films prepared in various Ar-O_2 and Ar-H_2 atmospheres

	Conductivity ($\Omega^{-1}cm^{-1}$)	**Carrier density n_e (cm^{-3})**	**Mobility ($cm^2V^{-1}s^{-1}$)**
pure-Ar	10^{-3}	-	-
f(O_2)			
3%	3.52x10^2	2.95x10^{19}	74
10%	2.99x10^2	4.59x10^{18}	406
20%	2.92x10^2	3.56x10^{18}	512
33%	1.13x10^2	7.22x10^{18}	97
f(H_2)			
3%	2.17x10^1	2.35x10^{18}	53
10%	3.37x10^1	1.89x10^{18}	111
20%	3.47x10^1	2.96x10^{18}	73
33%	1.20x10^2	1.44x10^{18}	519

In Figure 7.2 (a) the conductivity, carrier concentration and mobility values for post-growth annealed TiO_2 films prepared in various Ar-O_2 gas mixtures are shown. For comparison, the conductivity (4.24x10^3 $\Omega^{-1}cm^{-1}$), carrier concentration (1.03x10^{21} cm^{-3}) and mobility (25.7 $cm^2V^{-1}s^{-1}$) values for an ITO sample deposited on glass substrate were measured and are shown in the same plot.

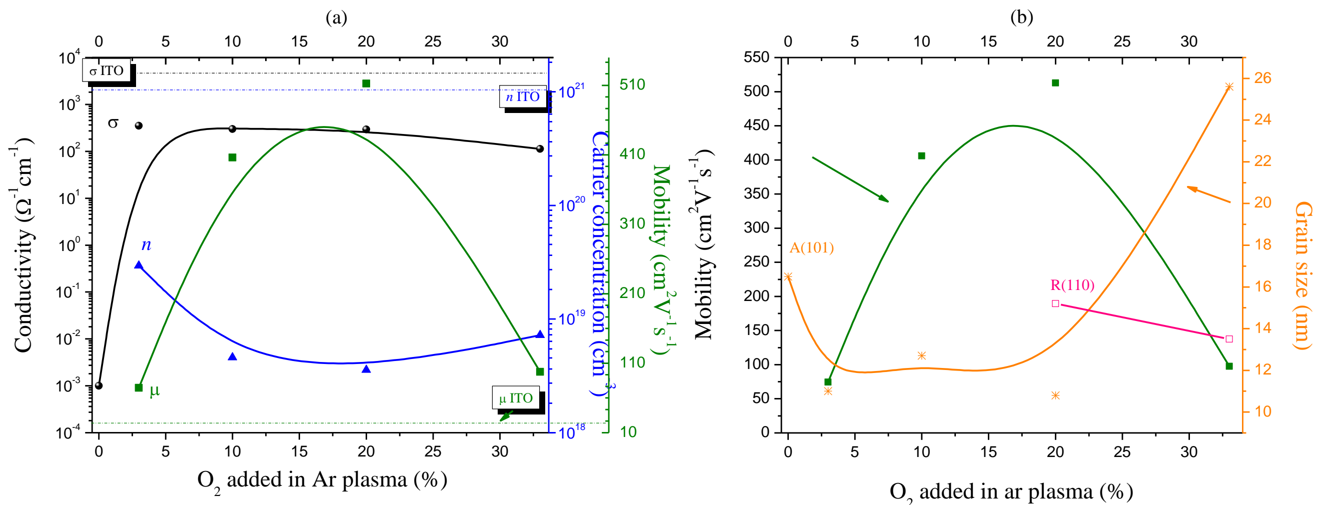

Figure 7.2 (a) Conductivity, carrier concentration and mobility values and (b) mobility and grain sizes for post-growth annealed TiO_2 films prepared in Ar-O_2 atmosphere, at -850 *V*

The addition of oxygen in Ar plasma leads to an increase in the conductivity value, from 10^{-3} $\Omega^{-1}cm^{-1}$ to $3.52x10^{2}$ $\Omega^{-1}cm^{-1}$ when 3%O_2 is added in discharge, with a corresponding carrier density (n_e) of 2.95 x10^{19} cm^{-3} and 74 $cm^2V^{-1}s^{-1}$ mobility. For a further increase in the oxygen content in discharge the conductivity values remains in the same order. The carrier density is decreasing when the O_2 concentration is increased. High mobility values were measured for these films. An increase in the mobility with increasing the O_2 quantity in Ar plasma is observed, reaching a maximum at 20%O_2 added in discharge and after decreasing. No correlation was found between the mobility values and the dimension of the grains measured for these films, as shown in Figure 7.2 (b). An increase in the grains dimension should lead to an increase also in the mobility values, as the grain boundaries number decrease but in this case the opposite is observed. A possible explanation for the increase in mobility values can be attributed to the number of intrinsic defects in the films [1]. By minimizing the intrinsic defects in the material, a high mobility can be achieved.

Similar to O_2 addition in Ar plasma, the addition of hydrogen in Ar plasma leads to an increase in the conductivity value, from 10^{-3} $\Omega^{-1}cm^{-1}$ to $2.17x10^{1}$ $\Omega^{-1}cm^{-1}$ when 3%H_2 is added in discharge, with a corresponding carrier density (n_e) of 2.53x10^{18} cm^{-3} and mobility of 53 $cm^2V^{-1}s^{-1}$, as shown in Figure 7.3 (a). The measured conductivity, carrier density and mobility values for the films prepared in various Ar-H_2 atmospheres are listed in Table 7.1. A further increase in the hydrogen content in discharge leads to an increase in the conductivity values. When 33%H_2 is added in discharge, the measured conductivity value was found to be $1.20x10^{2}$ $\Omega^{-1}cm^{-1}$, with a corresponding carrier density (n_e) of 1.44x10^{18} cm^{-3}. The n_e values are not considerably changing with the hydrogen content in Ar plasma. High values for mobility were obtained also in these samples, but a different evolution with the H_2 content, comparing with the mobility evolution for the films prepared in Ar-O_2 atmosphere. For H_2 concentrations in the range 3-20% the mobility values were in the range 50-111 $cm^2V^{-1}s^{-1}$. For 33%H_2 in discharge, an increase for the mobility value is observed (519 $cm^2V^{-1}s^{-1}$). Like in the case of TiO_2 films prepared in Ar-O_2 atmosphere, also in these films no correlation was found between the grains dimension and the mobility (Figure 7.3 (b)) and a possible

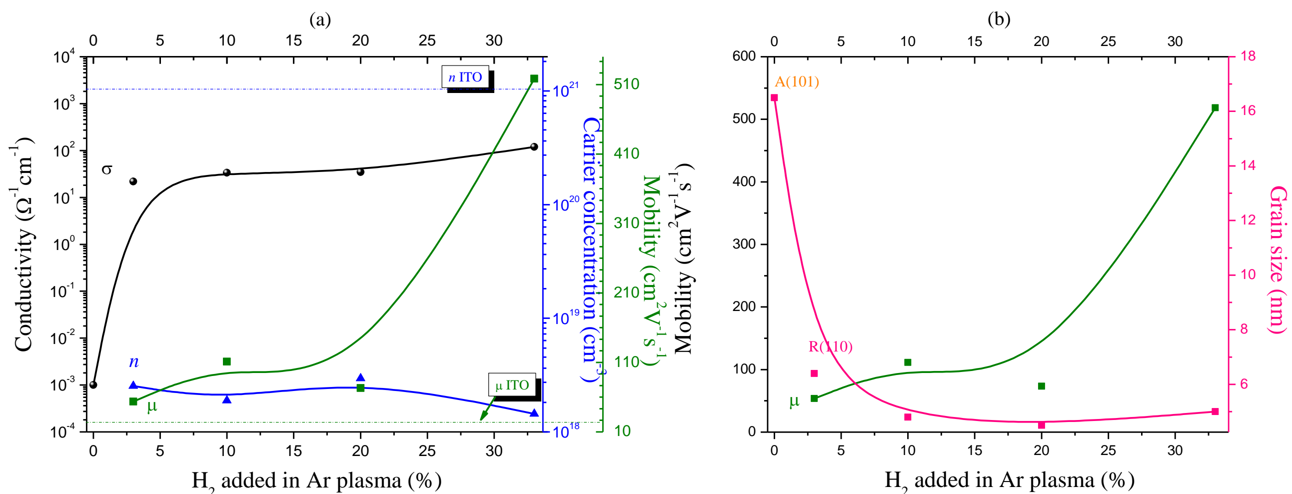

Figure 7.3 (a) Conductivity, carrier concentration and mobility values and (b) mobility and grain sizes for post-growth annealed TiO_2 films prepared in Ar-H_2 atmosphere, at -850 *V*

explanation for the high mobility can be a small number of intrinsic defects in the films. It was suggested that hydrogen passivates the structural defects in TCO materials [1].

7.2.3 Influence of substrate temperature on film electrical properties

The electrical properties for TiO_2 film prepared in Ar plasma, at a substrate temperature of 350°C and a cathode self-bias voltage of -750 *V* were measured. High value of conductivity was found for this film (2.7x10^2 $\Omega^{-1}cm^{-1}$). The measured carrier density value was 1.31x10^{18} cm^{-3}.

7.2.4 Optical properties of as-grown films

The optical properties for as-grown TiO_2 films on glass substrate prepared in pure-Ar, Ar-O_2 and Ar-H_2 atmospheres, at a cathode self-bias voltage of -750 *V* were investigated. In Figure 7.4 the transmittance and the absorption coefficient spectra for as-grown TiO_2 films deposited in various atmospheres are shown. In the visible region (400-800 *nm*), the average transmittance is 75% for TiO_2 film prepared in pure-Ar, 80% when 20% O_2 is added in Ar plasma and 65% when 20% H_2 is added in discharge.

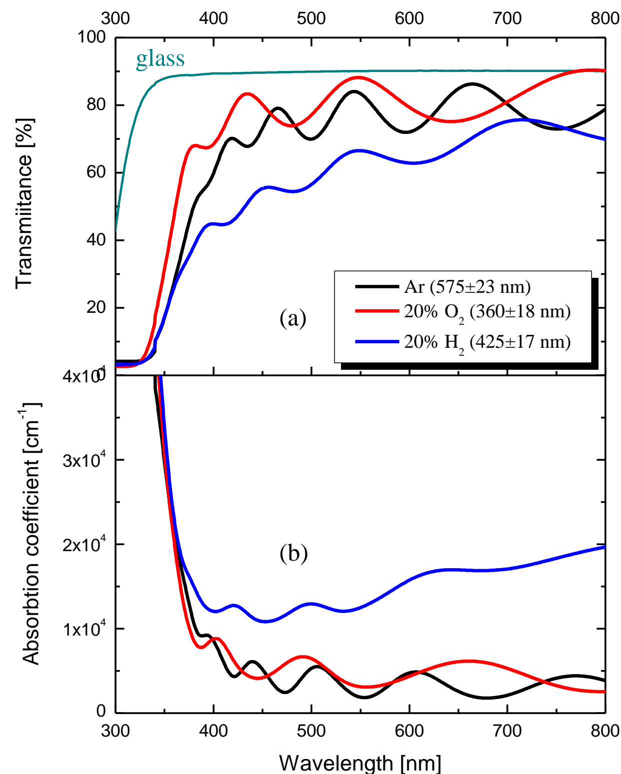

Figure 7.4 Transmittance (a) and absorption coefficient (b) for as-grown TiO_2 films in Ar, Ar-O_2 and Ar-H_2 atmospheres, at -750 *V*

The estimated direct optical band gap values are determined from the Tauc plot, and values are 3.29 *eV* for the sample prepared in pure-Ar, 3.36 *eV* when 20% O_2 is added in discharge and 3.46 *eV* for 20% H_2 in Ar-H_2 atmosphere.

7.2.5 Influence of post-growth annealing on film optical properties

Post-growth annealing at 900°C in vacuum was performed for TiO_2 films deposited on quartz substrate, at various oxygen and hydrogen concentrations added in Ar plasma, at -850 *V*. The measured transmittance spectra in the visible region are shown in Figure 7.5. When oxygen is added in Ar plasma, the annealed TiO_2 films are having a much higher transparency (~60%) then the film prepared in Ar plasma (~35%). Less transparent TiO_2 films are obtained when hydrogen is added in discharge (~45%).

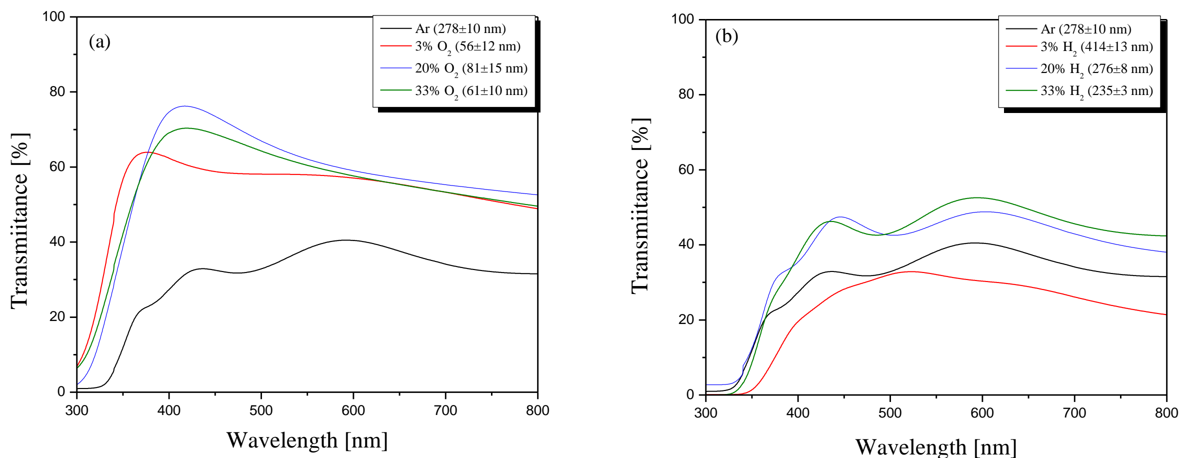

Figure 7.5 Transmittance spectra for post-growth annealed TiO_2 films prepared in various (a) Ar-O_2 and (b) Ar-H_2 atmospheres, at -850 *V*

The absorption coefficient in the visible region is plotted in Figure 7.6. The average value in the visible region was determined for each sample and the values for as-grown and post-growth annealed TiO_2 films are listed in Table 7.2. All the obtained values are in the order of 10^4 cm^{-1}. An increase in α values is observed after annealing for both type of TiO_2 films prepared in Ar-O_2 and Ar-H_2 atmospheres, attributed to the formation of oxygen vacancies after annealing. The increase is higher in the case of the samples prepared in Ar-O_2 atmosphere, explained by the higher number of vacancies formed in Ar-O_2 atmosphere.

The optical direct band gap values were determined and the values for as-grown and post-growth annealed films are listed in Table7.2. A decrease in band gap is observed for the sample prepared in pure-Ar. The addition of O_2 in Ar plasma leads to an increase in band gap, while H_2 is decreasing the optical band gap.

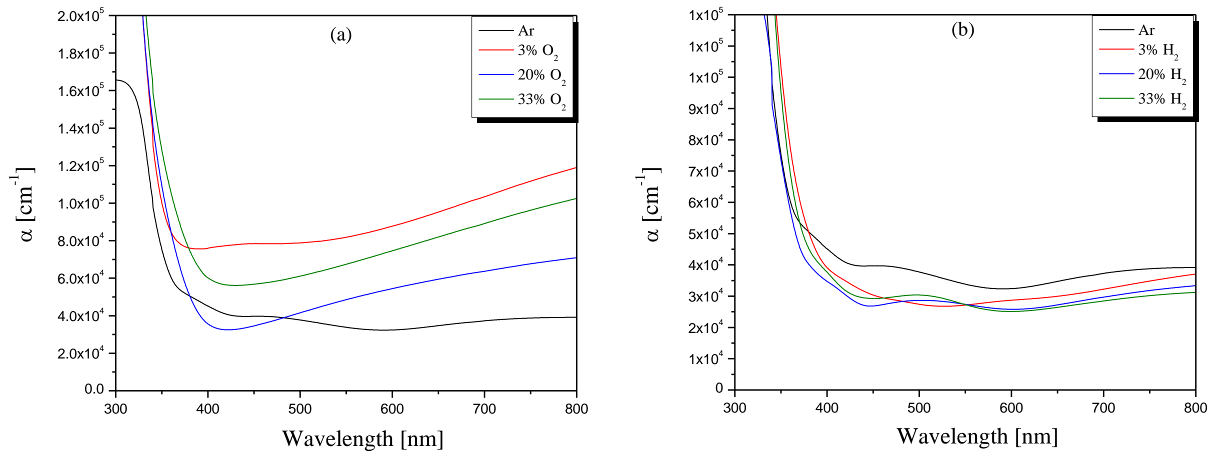

Figure 7.6 Absorption coefficient spectra in the visible region for post-growth annealed TiO_2 films prepared in various (a) Ar-O_2 and (b) Ar-H_2 atmospheres, at -850 *V*

Table 7.2 Absorption coefficient in the visible region (300-800 nm) and the optical band gap values for as-grown and post-growth annealed TiO_2 films prepared in various Ar-O_2 and Ar-H_2 atmospheres

	α (cm^{-1})		E_g (*eV*)	
	as-gr	**ann**	**as-gr**	**ann**
pure-Ar	$5.55x10^3$	$3.57x10^4$	3.35	3.20
f(O_2)				
3%	$3.04x10^4$	$8.54x10^4$	3.08	3.36
10%	$1.70x10^4$	$6.28x10^4$	3.28	3.27
20%	$3.09x10^4$	$5.75x10^4$	3.22	3.32
33%	$4.25x10^4$	$8.50x10^4$	3.17	3.26
f(H_2)				
3%	$2.60x10^4$	$3.12x10^4$	3.50	3.13
10%	$2.60x10^4$	$2.84x10^4$	3.54	3.27
20%	$2.20x10^4$	$2.98x10^4$	3.33	3.13
33%	$2.40x10^4$	$2.68x10^4$	3.40	3.21

7.2.6 Influence of substrate temperature on film optical properties

In Figure 7.7 the transmittance and the absorption coefficient spectra in the visible region for TiO_2 films prepared at different substrate temperatures: one sample prepared without intentional heating (RT) and the other one prepared at 350°C substrate temperature are shown. Both samples were deposited in Ar atmosphere, at a cathode self-bias voltage of -750 *V*. The transmittance of the sample prepared at 350°C substrate temperature is slightly decreasing. The optical band gap values were determined: 3.40 *eV* for the

sample prepared without intentional heating and 3.33 *eV* for the sample prepared at 350°C substrate temperature. An increase in the absorption coefficient value was observed for the sample prepared at a substrate temperature T=350°C, explained by the formation of oxygen vacancies as seen from the XPS analysis.

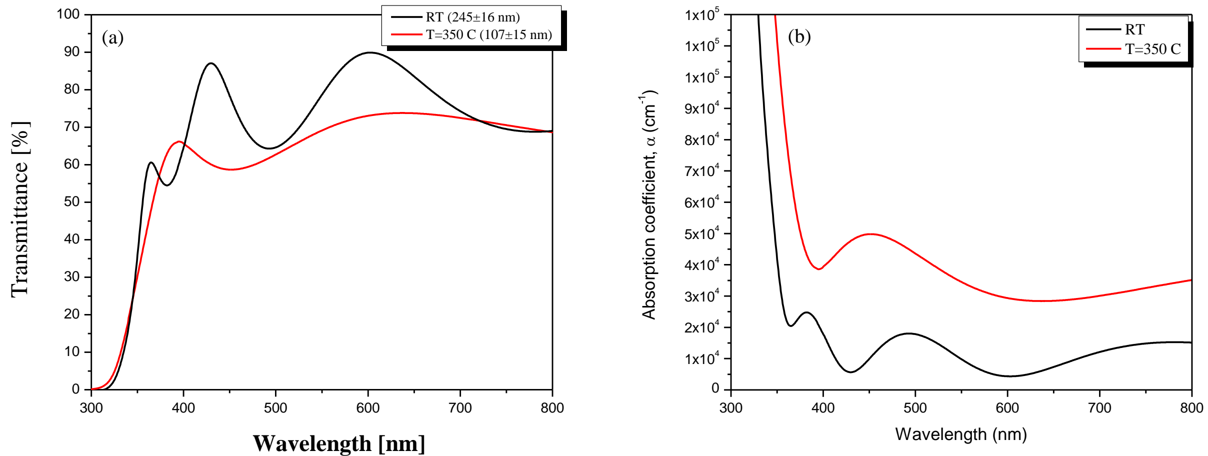

Figure 7.7(a) Transmittance and (b) α for TiO_2 films prepared at different substrate temperatures during deposition, in Ar atmosphere, at -750 *V*: without intentional heating and at T=350°C

7.2.7 Figure of merit of intrinsically-doped TiO_2 films

As described in Chapter 2, the figure of merit (FOM) is an important parameter for comparing the properties of different TCOs films. Because the obtained films were having different thicknesses, the figure of merit was calculated using the relation developed by Iles and Soclof [2] defined as:

$$F = \frac{\alpha}{\sigma}$$

In Figure 7.8 the figure of merit values for post-growth annealed TiO_2 films prepared in various Ar-O_2 and Ar-H_2 atmospheres, at -850 V are plotted together with the corresponding figure of merit value for ITO. The FOM values for TiO_2 films prepared in Ar-O_2 atmosphere are closer to the one corresponding to ITO film, while H_2 addition does not improve the quality of the films as TCO material, except the sample where 33% H_2 was added in Ar plasma.

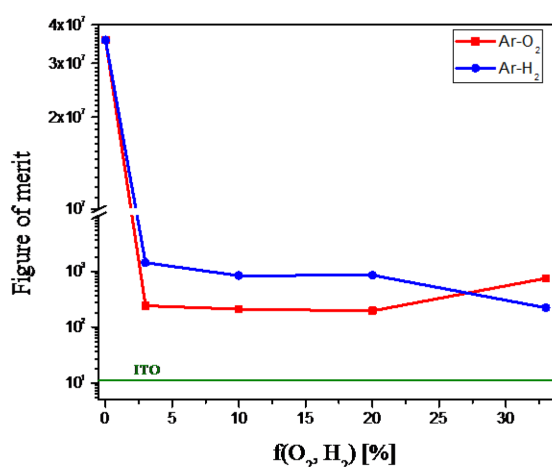

Figure 7.8 Figure of merit values for intrinsically-doped TiO_2 films, prepared in Ar-O_2 and Ar-H_2 atmospheres, at -850 *V*

7.2.8 Electronic properties of as-grown films

The joint use of XPS and optical measurements allowed defining the electronic properties of the films: valence band edge, Fermi level position, work function, ionization potential and electron affinity with respect to vacuum level. From XPS measurements the work function (WF) and the valence band maximum (VBM) with respect to vacuum level were determined. The determined VBM value was corrected removing the band bending effect, due to the surface charging during XPS analysis. Details about the determination of such value are given in Chapter 3. The resulting value is denoted as VBM(q=0) in Table 7.3. The direct band gap E_g was determined from the optical measurements performed on the samples. The ionization potential I_p and the electron affinity χ with respect to vacuum level were calculated using I_p=WF+VBM(q=0) and χ= I_p-E_g. A band scheme of TiO_2 films prepared in different atmospheres was drawn. It should be stressed that the work function is not a materials constant, but rather can be modified (1) trough carrier–doping, which raises the Fermi level, thereby lowering the work function (for a fixed ionization potential) and (2) by the presence of the surface dipole, which can increase the ionization potential and therefore the work function (for a fixed Fermi level), or a combination of these two phenomena.

In Figure 7.9 (a) the band scheme for as-grown TiO_2 films prepared in various atmospheres at -750 *V* is shown. The values of work function, electron affinity, optical band gap and ionization potential are given in the figure. The sample prepared in Ar has a work function of 4.13 *eV*. When 20%O_2 is added in Ar plasma, an increase in the work function value is observed, until 4.65 *eV*, while when 20%H_2 is added in Ar plasma, the work function value is decreasing (3.48 *eV*).

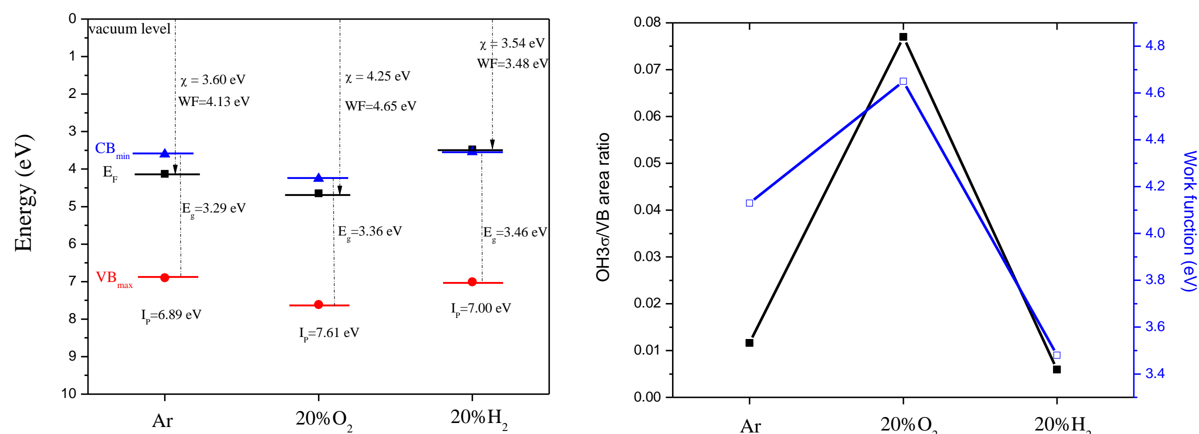

Figure 7.9 (a) Band scheme for as-grown TiO_2 films prepared in Ar-O_2 and Ar-H_2 atmosphere, at -750 *V* showing the VB maximum energy, the work function, the electron affinity and the direct band gap and (b) the OH3σ/VB area ratio and work function as obtained by XPS (the lines serve only to guide the eye).

In order to investigate the change of WF with the surface chemistry modification, the OH3s/VB area ratio from the XPS measurements in the VB region was plotted together with the WF values in Figure 7.9 (b). A good correlation between the two parameters is observed, the higher the OH groups number, the higher the WF.

For a better understanding of the effect of oxygen and hydrogen plasmas on the work function, similar measurements were done for as-grown TiO_2 films prepared at -850 *V*, in different oxygen and hydrogen concentrations introduced in Ar plasma. The obtained values for work function, valence band edge, optical band gap, ionization potential and electron affinity are listed in Table 7.3. Also for these samples, the band schemes were drawn and are shown in Figure 7.10. Similar effects when oxygen or hydrogen was added in Ar plasma were observed. An increase in the work function was observed with increasing the O_2 concentration reaching values of 6.19±0.19 *eV* and a decrease with increasing the H_2 concentration.

Table 7.3 Work function, valence band edge, optical band gap, ionization potential and electron affinity values for as-grown TiO_2 films in Ar-O_2 and Ar-H_2 atmospheres, at -850 *V*

	WF (*eV*)	**VBM (q=0) (*eV*)**	**E_g (*eV*)**	**I_p (*eV*)**	**χ (*eV*)**
TiO_2 bulk	5.97	-	3.30	-	-
pure-Ar	4.57±0.10	2.12	3.35	6.69	3.34
f(O_2)					
3%	4.51±0.12	1.60	3.08	6.11	3.03
10%	5.06±0.12	1.97	3.28	7.03	3.75
20%	5.81±0.15	1.83	3.22	7.64	4.42
33%	6.19±0.19	1.56	3.17	7.75	4.58
f(H_2)					
3%	3.36±0.10	2.85	3.50	6.21	2.71
10%	3.96±0.04	3.33	3.54	7.29	3.75
20%	4.02±0.05	2.49	3.33	6.51	3.18
33%	4.00±0.05	2.48	3.40	6.48	3.08

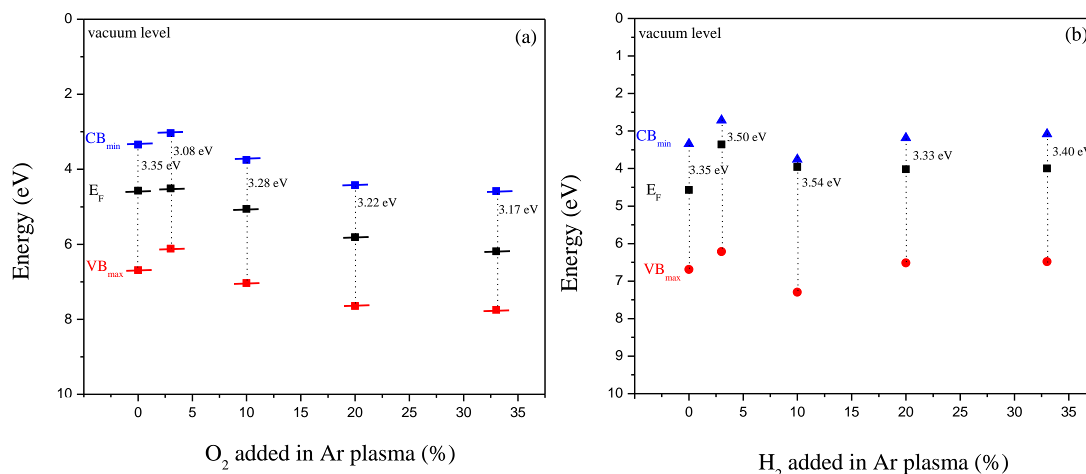

Figure 7.10 Band schemes for as-grown TiO_2 films prepared in (a) Ar-O_2 and (b) Ar-H_2 atmospheres, at -850 *V*; the direct E_g values are given in the Figure;

In Figure 7.11 the OH3σ/VB area ratios were plotted together with the WF values for as-grown TiO_2 films prepared in Ar-O_2 and Ar-H_2 gas mixtures (-850 *V* to TiO_2 cathode). For the films prepared in Ar-O_2 atmosphere a good correlation was observed between the two parameters, both are increasing with increasing the oxygen concentration in Ar plasma. For the samples prepared in Ar-H_2 plasma also a good correlation of these two parameters was observed, but until 20%H_2 in Ar plasma. It is more likely a hydrogen terminated surface which gives (i) low WF and (ii) the lack of correlation for high H_2 contents in Ar plasma. A possible explanation can be due to a competitive effect of OH groups and H on the surface.

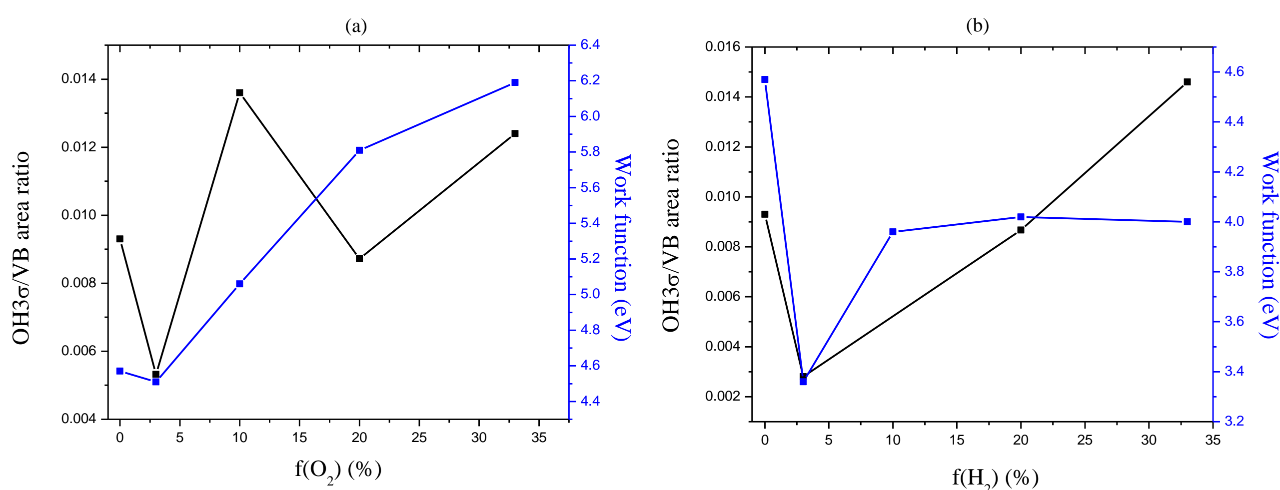

Figure 7.11 OH3σ/VB area ratio and work function as obtained by XPS in function of (a) %O_2 and (b) %H_2 added in Ar plasma, for as-grown TiO_2 films at -850 *V* to TiO_2 cathode

7.2.9 Influence of post-growth annealing on film electronic properties

The electronic properties were determined also for post-growth annealed TiO_2 samples, prepared at self-bias cathode voltage of -750 *V*, in various atmospheres. The annealing temperature was set at 900°C, for one hour, in vacuum.

In Figure 7.12 (a) the band schemes obtained for post-growth annealed TiO_2 films prepared in various atmospheres are shown. No significant changes after annealing in the work function values were observed for the samples prepared in Ar and Ar-O_2 atmosphere, for 20% O_2. When hydrogen was used as reactive gas in Ar plasma, the work function value decreased after annealing, from 3.48 *eV* for as-grown film to 2.55 *eV* for the annealed one.

The work function variation was found to be in good correlation with the conductivity values measured for post-growth annealed TiO_2 films prepared in various atmospheres, as shown in Figure 7.12 (b).

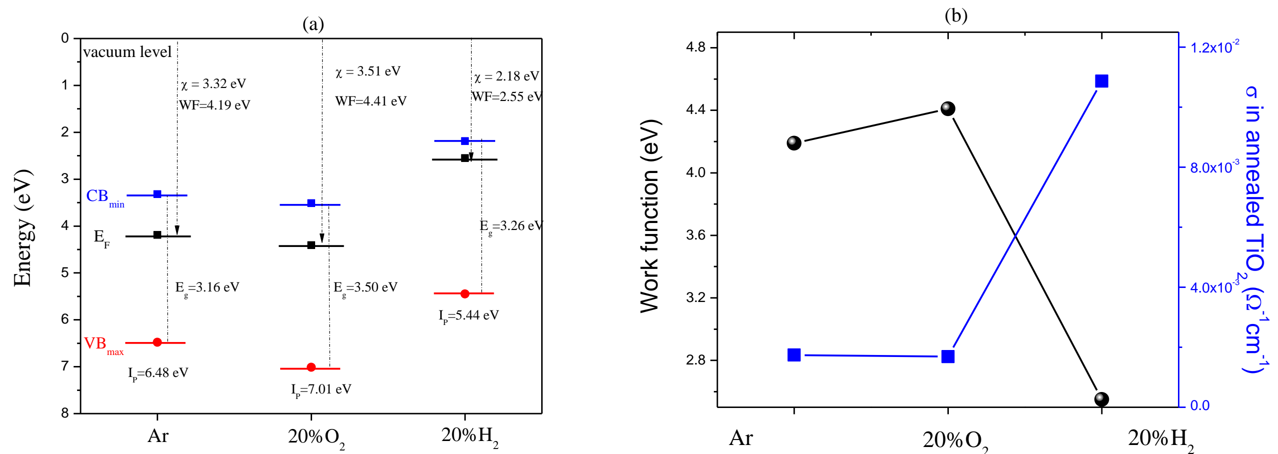

Figure 7.12 (a) Band scheme and (b) WF and conductivity values for post-growth annealed TiO_2 films prepared in Ar-O_2 and Ar-H_2 atmosphere, at -750 *V* (the lines serve only to guide the eye)

7.3 Extrinsically-doped TiO_2 films

7.3.1 Electrical properties of as-grown films

The conductivity of the as-grown Nb-TiO_2 films prepared in pure-Ar plasma, at -550 *V*, -750 *V* and -850 *V* cathode self-bias voltages were measured. For all the films, the conductivity values are in the order of 10^{-2}-10^{-3} $\Omega^{-1}cm^{-1}$, similar to the values obtained for as-grown TiO_2 films.

7.3.2 Influence of post-growth annealing on film electrical properties

Post-growth annealing in vacuum was performed for Nb-TiO_2 film prepared in Ar plasma, at -750 *V*. The annealing temperature was set at 900°C, for one hour, in vacuum. The conductivity value measured for the annealed Nb-TiO_2 film containing ~5% Nb in the film was $1.78 \times 10^2\ \Omega^{-1}cm^{-1}$.

For obtaining lower concentrations of Nb in the films, a better control over the sputtering process is necessary. Nb concentrations less than 2.3% were measured in the Nb-TiO_2 films prepared by co-sputtering from two different targets of TiO_2 and Nb. The films were post-growth annealed in vacuum at the same temperature and in the same conditions like the ones prepared from the mosaic target at -750 *V*. In Table 7.4 the measured conductivity, carrier density and mobility values are listed and plotted in Figure 7.13 (a). The highest conductivity value was obtained when 4 *W* was used as applied power to Nb target (corresponding to 0.95% Nb in the film) with $1.05 \times 10^{22}\ cm^{-3}$ carrier density and a mobility value of 3.54 $cm^2V^{-1}s^{-1}$.

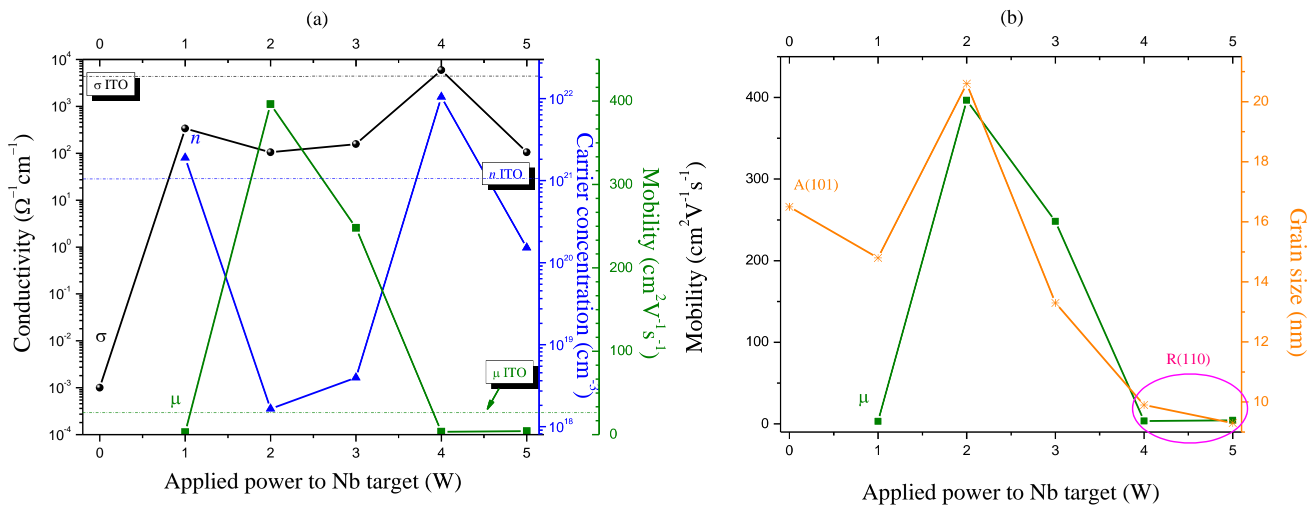

Figure 7.13 (a) Conductivity, carrier concentration and mobility values and (b) mobility and grain size values for post-growth annealed Nb-TiO_2 films prepared at various powers applied to Nb target, in Ar atmosphere, at -850 *V*

The carrier density and the mobility values are in good correlation (Figure 7.13 (a)), an increase in n leads to a decrease in μ and the vice-versa. The increase or decrease in mobility values is also correlated with the grains dimension, as shown in Figure 7.13 (b). For low powers (1 W - 3 W) applied to Nb target the anatase phase was identified in the XRD analysis. When 4 W the anatase-to-rutile transformation was observed, and low grain size was obtained for rutile, affecting the mobility.

Table 7.4 Conductivity, carrier concentration and mobility values for post-growth annealed Nb-TiO_2 films prepared in Ar plasma, at various applied powers to Nb target

[Nb] (%)	Power to Nb target (W)	Conductivity ($\Omega^{-1}cm^{-1}$)	Carrier density n_e (cm^{-3})	Mobility ($cm^2V^{-1}s^{-1}$)
0.04	1	$3.37x10^2$	$1.90x10^{21}$	1.11
0.11	2	$1.05x10^2$	$1.65x10^{18}$	487
0.13	3	$1.57x10^2$	$3.95x10^{18}$	248
0.95	4	$5.95x10^3$	$1.05x10^{22}$	3.54
2.31	5	$1.05x10^2$	$1.52x10^{20}$	4.3

7.3.3 Influence of substrate temperature on film electrical properties

The substrate temperature was varied from 300 to 420°C during the deposition of Nb-TiO_2 films in Ar plasma. All the films were deposited at 4W power applied to Nb target, corresponding to Nb concentrations of ~0.95%. No post-growth annealing in vacuum was performed for these films. The conductivity values measured for these films are plotted in Figure 7.14 as a function of the substrate temperature. An increase is observed with increasing the substrate temperature.

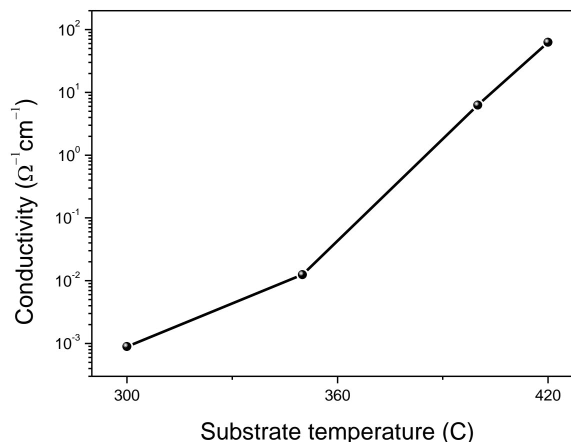

Figure 7.14 σ values for as-grown Nb-TiO_2 films deposited in Ar plasma at various substrate temperatures

7.3.4 Optical properties of as-grown films

The transmittance and the absorption coefficient spectra in the visible range for as-grown Nb-TiO_2 film (thickness 450±20 *nm*) prepared in Ar plasma, at -750 *V* are shown in Figure 7.15. The Nb concentration in the film was found to be ~5%. For this film, the TiO_2-Nb mosaic target was used. The average transmittance

in the visible range is ~65% and the average absorption coefficient $7x10^3$ cm^{-1}. The optical direct band gap was estimated from the Tauc plot and is $E_g = 3.40 \pm 0.01$ eV.

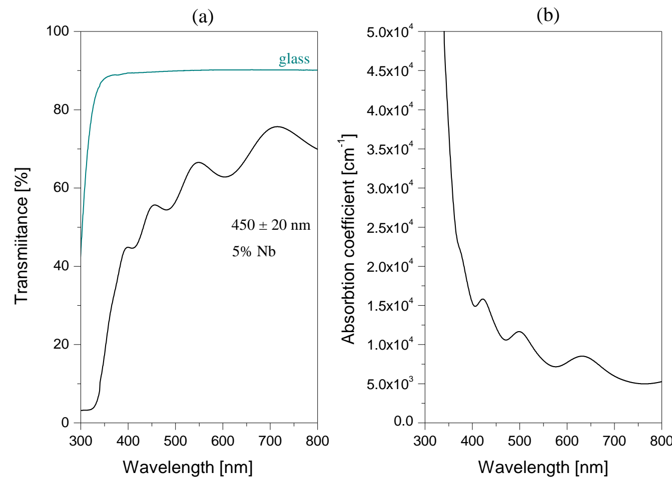

Figure 7.15 Transmittance (a) and absorption coefficient (b) for as-grown Nb-TiO_2 film prepared in Ar atmosphere, at -750 V

Films with lower concentrations of Nb were deposited, using the co-sputtering arrangement, where two separate TiO_2 and Nb targets were sputtered in Ar plasma. The transmittance and the absorption coefficient spectra, together with the Nb concentrations in the films determined with XPS are shown in Figure 7.16. High transmittance values were obtained in the visible range for low concentrations of Nb. For the samples prepared at a power in the range 1-4 W, the average transmittance in the visible range is ~75-80%. The average absorption coefficient values in the visible domain are in the range $3.50x10^3$ - $8.30x10^3$ cm^{-1}.

The optical direct band gap values were determined for each sample prepared at different power values applied to Nb target and the values are 3.26 eV, 3.38 eV, 3.30 eV, 3.30 eV and 3.22 eV respectively.

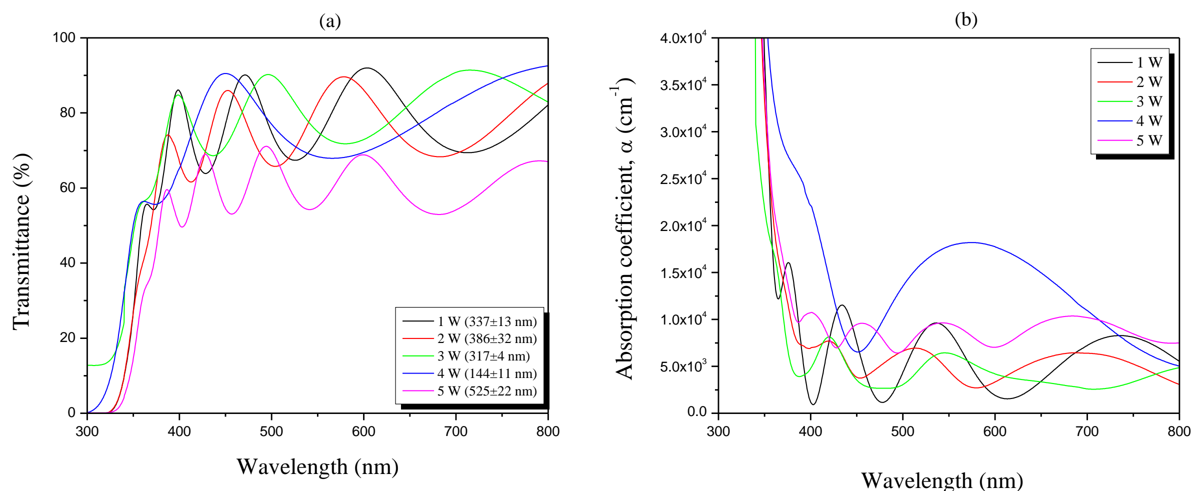

Figure 7.16 (a) Transmittance and (b) absorption coefficient for Nb-TiO_2 films prepared in Ar plasma, at different powers applied to Nb target

7.3.5 Influence of post-growth annealing on film optical properties

The optical properties of post-growth annealed co-sputtered Nb-TiO_2 films prepared in Ar plasma, at various powers applied to Nb target (-850 *V*) were investigated. In Figure 7.17 the transmittance and absorption coefficient spectra in the visible range are shown. The average transmittance of the films in the visible range was low (~30%), except the samples prepared at 3 *W* and 4 *W* applied to Nb target with the average transmittance of 40% and 50% respectively. The absorption coefficient values for the samples increase with one order of magnitude after post-growth annealing.

The optical direct band gap values after post-growth annealing of the samples prepared at different applied powers to Nb target remains approximately constant: 3.15 *eV*, 3.11 *eV*, 3.11 *eV*, 3.14 *eV* and 3.28 *eV* respectively.

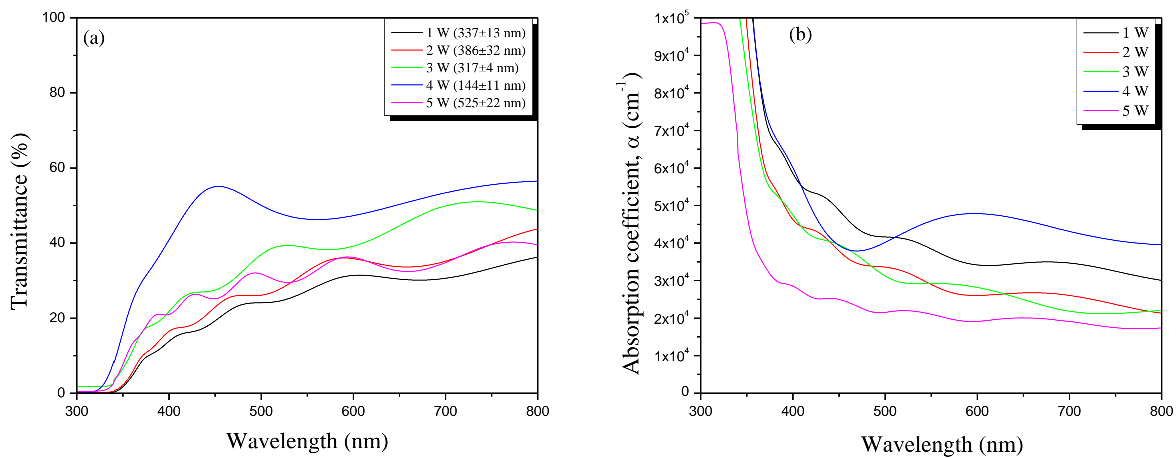

Figure 7.17 (a) Transmittance and (b) absorption coefficient for post-growth annealed Nb-TiO_2 films prepared in Ar plasma, at different powers applied to Nb target

7.3.6 Influence of substrate temperature on film optical properties

Substrate temperatures ranging from 300°C to 420°C were used during the deposition of Nb-TiO_2 films in pure-Ar plasma. The power applied to Nb target in the co-sputtering configuration was set at 4 *W* (corresponding to 0.95% Nb concentration in the films) and the cathode self-bias voltage was set at -850 *V*.

The transmittance and optical absorption coefficient spectra in the visible range for the Nb-TiO_2 film prepared without intentional heating and the films deposited at various substrate temperatures are shown in Figure 7.18. As can be seen, the average transmittance is decreasing with increasing the substrate temperature and the absorption coefficient values are increasing.

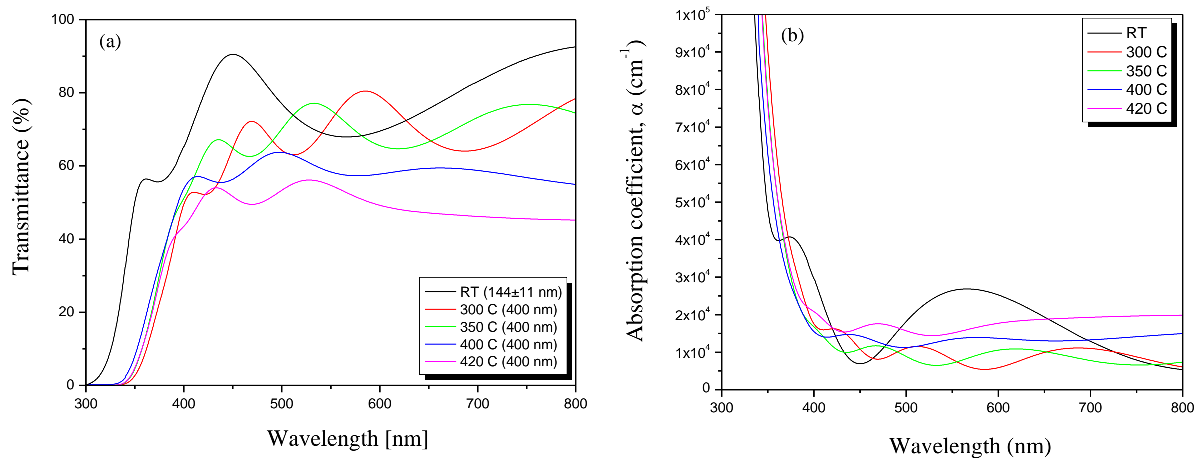

Figure 7.18 (a) Transmittance and (b) absorption coefficient for Nb-TiO_2 films prepared in Ar plasma, at various substrate temperatures, when the power applied to Nb target was set at 4 *W*

The optical direct band gap values are lower than the optical band gap for the sample prepared without intentional heating. For 300°C, 350°C, 400°C and 420°C substrate temperatures the optical band gaps were 3.14 *eV*, 3.22 *eV*, 3.23 *eV* and 3.26 *eV* respectively, while for the sample prepared without intentional heating the band gap value was 3.30 *eV*, with an amorphous structure as indicated in XRD pattern.

7.3.7 Figure of merit of extrinsically-doped TiO_2 films

In order to evaluate the quality of post-growth annealed Nb-TiO_2 films co-sputtered from two separate targets in Ar plasma the figure of merit was determined using the ratio $\frac{\alpha}{\sigma}$. The obtained values are plotted in Figure 7.19 as a function of various powers applied to Nb target. The figure of merit values for the obtained

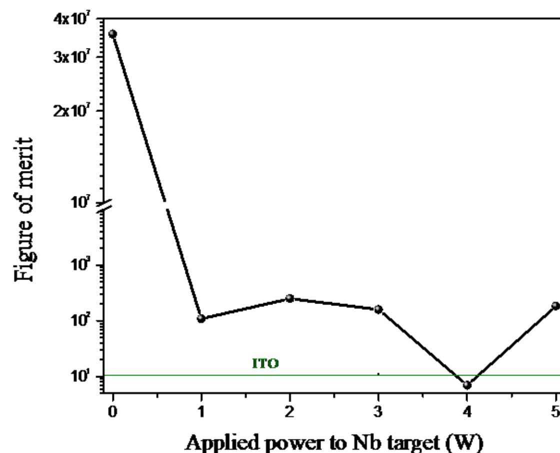

Figure 7.19 Figure of merit values for extrinsically-doped TiO_2 films with Nb, prepared in Ar atmosphere, at -850 *V*

films are one order higher than the value corresponding to ITO film, except the sample prepared at 4 *W* applied to Nb target. The FOM of this sample is lower than the one corresponding to ITO.

7.3.8 Electronic properties of as-grown films

The band scheme for Nb-TiO_2 film prepared in Ar plasma at -750 *V* cathode self-bias voltage, when a mosaic target was used for sputtering is shown in Figure 7.20 (a). The obtained values of work function, electron affinity, optical band gap and ionization potential are given in the figure. The work function value (4.03 *eV*) is slightly decreased comparing with the work function value obtained for TiO2 sample deposited in Ar plasma (4.13 *eV*).

For lower concentrations of Nb (co-sputtering configuration from two separate TiO_2 and Nb targets), the obtained work function values for all the films were higher than the work function corresponding to TiO_2 film deposited in pure-Ar plasma. The values for work function, valence band edge, optical band gap, ionization potential and electron affinity with respect to the vacuum level for Nb-TiO_2 films prepared in Ar plasma at various powers applied to Nb target are listed in Table 7.5 and the band schemes for these samples are drawn in Figure 7.20 (b). The value indicated as VBM(q=0) in the Table 7.5 corresponds to the VBM corrected from band bending effect.

According to the band schemes, for none of the sample the Fermi level is not into the conduction band or very close to the conduction band minimum edge, as expected from the low resistivity values and high carrier concentrations for these films.

A good correlation was found between the OH3σ signal and the WF values, as shown in Figure 7.21.

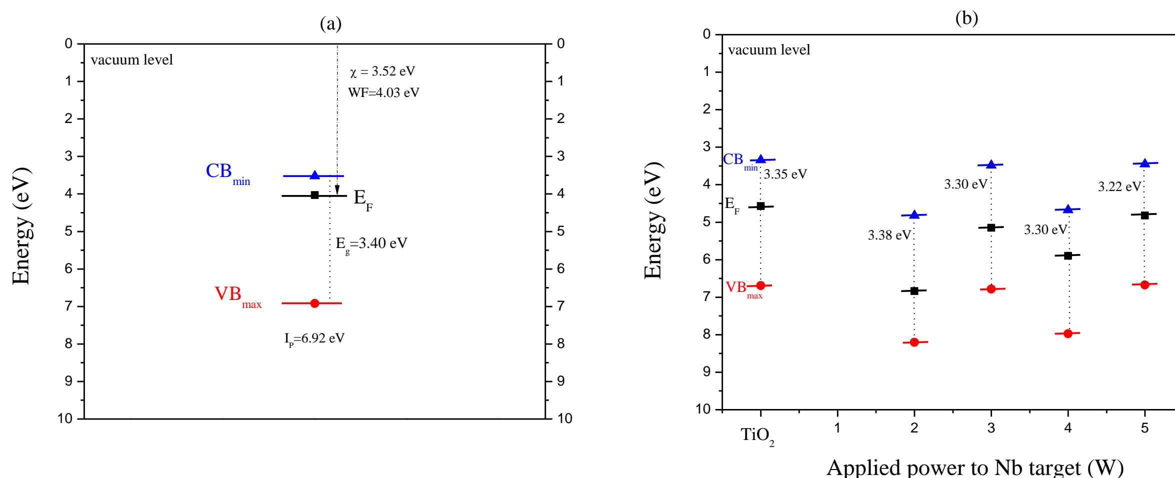

Figure 7.20 Band schemes for (a) as-grown Nb-TiO_2 film prepared in Ar atmosphere, at -750 *V* and (b) as-grown TiO_2 films prepared in Ar atmosphere varying the powers applied to Nb target, at -850 *V*, the values indicated in the figure corresponds to E_g

Table 7.5 Work function, valence band edge, optical band gap, ionization potential and electron affinity values for as-grown Nb-TiO_2 films prepared at various powers applied to Nb target, at -850 *V*, in Ar plasma

Power (W)	WF (*eV*)	VBM (q=0) (*eV*)	E_g (*eV*)	I_p (*eV*)	χ (*eV*)
0 (TiO_2)	4.57±0.10	2.12	3.35	6.99	3.34
2	6.84±0.55	1.36	3.38	8.20	4.82
3	5.15±0.19	1.63	3.30	6.78	3.48
4	5.90±0.49	2.07	3.30	7.97	4.67
5	4.82±0.19	1.85	3.22	6.67	3.45

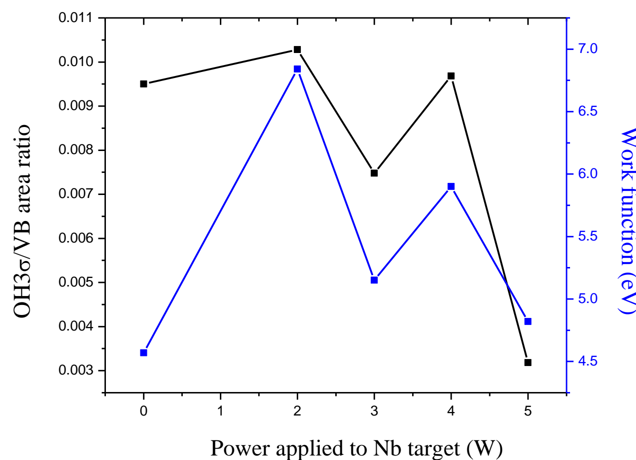

Figure 7.21 OH3σ/VB area ratio and work function as obtained by XPS in function of the power applied to Nb target, for as-grown Nb-TiO_2 films (-850 *V* to TiO_2 cathode), in Ar plasma

7.3.9 Influence of post-growth annealing on film electronic properties

The work function for post-growth annealed Nb-TiO_2 film (5%Nb) prepared in Ar plasma at -750 *V* (mosaic target configuration) is slightly increasing comparing with the as-grown film prepared in the same conditions, as can be seen from Figure 7.22 (a).

For the sample prepared at -850 V, in Ar, with the highest conductivity value obtained for 4 W, WF value was determined (WF=2.39 eV). The band scheme obtained for this sample is shown in Figure 7.22 (b) together with the WF, χ, E_g and I_p values with respect to vacuum level, where can be seen that the Fermi level position is situated above the CB_{min}. However a discrepancy can be observed between the optical gap and the position of the Fermi level. In degenerated semi-conductors, the optical gap undergoes a shift towards higher energy, due to Burstein-Moss effect [3], which is not the case here. The measured band gap is

thought however not to pertain to the intrinsic band structure of the film, but to describe rather an optical absorption by band-like defect states and energetically close to the conduction band minimum, within the gap. Such a behavior has been evidenced in a study of the optical properties of the defects in TiO_2 [Ref. 22 in Chapter 4]. On the other hand, the low value found for the WF of this sample can be explained by the presence of a surface dipole, whose positive polarity is directed towards vacuum and the negative one

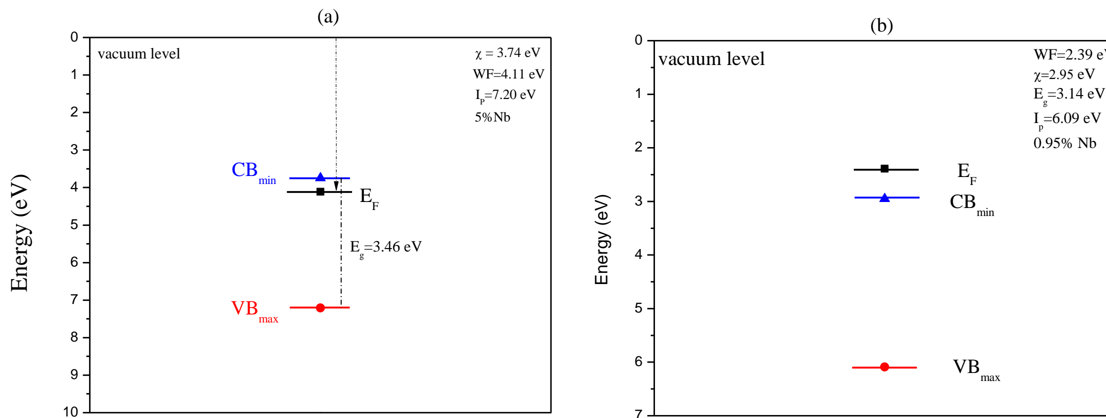

Figure 7.22 Band schemes for Nb-TiO_2 films prepared at (a) -750 V and (b) -850 V on TiO_2 cathode and 4 W on Nb cathode, both films being post-growth annealed in vacuum and deposited in Ar

towards the surface. In such case, even if band bending due to the analysis itself is avoided here, the one due to a surface dipole is un-avoidable and a downward band bending may bring the CB_{min} at a lower level and increase the energy distance between the Fermi level and CB_{min}.

7.4 Intrinsically-extrinsically co-doped TiO_2 films

7.4.1 Electrical properties of as-grown films

The measured conductivity values of the as-grown Nb-TiO_2 films prepared in Ar-O_2 and Ar-H_2 plasmas, at -550 *V*, -750 *V* and -850 *V* cathode self-bias voltages were in the order 10^{-2}-10^{-3} $\Omega^{-1}cm^{-1}$.

7.4.2 Influence of post-growth annealing on film electrical properties

Post-growth annealing at 900°C, for one hour, in vacuum was performed for Nb-TiO_2 films prepared in Ar-O_2 (20%H_2) and Ar-H_2 (20%H_2) atmospheres, at -750 *V*, sputtered from a mosaic target. The Nb concentration in these films, according to XPS measurements were ~4.5% and ~10% respectively. The

conductivity values measured after annealing are 1.36x10^1 $\Omega^{-1}cm^{-1}$ for the film prepared with 20%O_2 added in Ar plasma and 2.89x10^1 $\Omega^{-1}cm^{-1}$ for the one prepared with 20%H_2 added in Ar plasma.

Nb-TiO_2 films prepared by co-sputtering from two different targets of TiO_2 and Nb with 10%O_2 and 10%H_2 added in Ar plasma (-850 *V*) were post-growth annealed at the same temperature and in the same conditions like the ones prepared from the mosaic target at -750 *V*. The Nb concentration in these films was less than 2%. The measured conductivity, carrier density and mobility values are listed in Table 7.6.

Table 7.6 Conductivity, carrier concentration and mobility values for post-growth annealed Nb-TiO_2 films prepared with 10%O_2 and 10%H_2 added in Ar plasma, at various applied powers to Nb target

	Power to Nb target (W)	**Conductivity ($\Omega^{-1}cm^{-1}$)**	**Carrier density n_e (cm^{-3})**	**Mobility ($cm^2V^{-1}s^{-1}$)**
pure-Ar	-	10^3	-	-
10%O_2	3	4.98x10^1	6.79x10^{18}	45.7
	4	1.45x10^1	2.50x10^{19}	3.63
	5	3.05x10^1	8.16x10^{19}	2.34
10%H_2	2	3.88x10^1	1.56x10^{18}	156
	3	3.64x10^1	1.33x10^{18}	171
	4	2.94x10^1	1.09x10^{18}	168
	5	1.62x10^1	8.70x10^{17}	116

In Figure 7.23 (a) the conductivity, carrier density and mobility values for Nb-TiO_2 films prepared in Ar-O_2 atmosphere are plotted. Lower values of conductivity were obtained when oxygen was added in Ar plasma comparing these results with the ones for the films obtained in Ar plasma, at different powers applied to Nb target. The carrier densities for these films are in the order 10^{18}-10^{19} cm^{-3}, smaller than the carrier densities of Nb-TiO_2 films prepared in Ar plasma and are increasing with the power applied to Nb target.

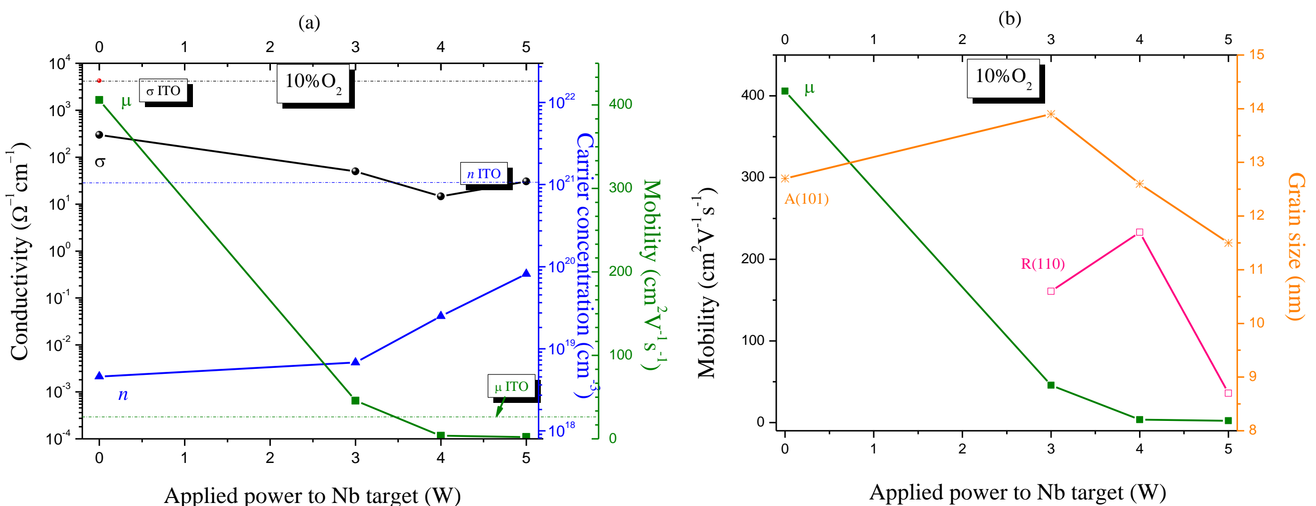

Figure 7.23 (a) Conductivity, carrier concentration and mobility values and (b) mobility and grains dimensions for post-growth annealed Nb-TiO_2 films prepared at various powers applied to Nb target, in 10%O_2 added in Ar plasma, at -850 *V*

The mobility values are decreasing with increasing the power applied to Nb target, as can be seen in Figure 7.23 (a). No clear correlation is observed between the grain size and the mobility values, as shown in Figure 7.23 (b).

When hydrogen is added in Ar plasma, the conductivity values are smaller than the conductivity values for Nb-TiO_2 films prepared in pure-Ar plasma and are slightly decreasing with increasing the power applied to Nb target, and the carrier density is decreasing (Figure 7.24 (a)). The measured mobility values for these films are in the range 100-170 $cm^2V^{-1}s^{-1}$. Also in these films, no clear correlation can be found between the mobility values and the grain size (Figure 7.24 (b)). It is also known that Ti-H bonds passivates the defects like vacancies and enhance the carrier mobility.

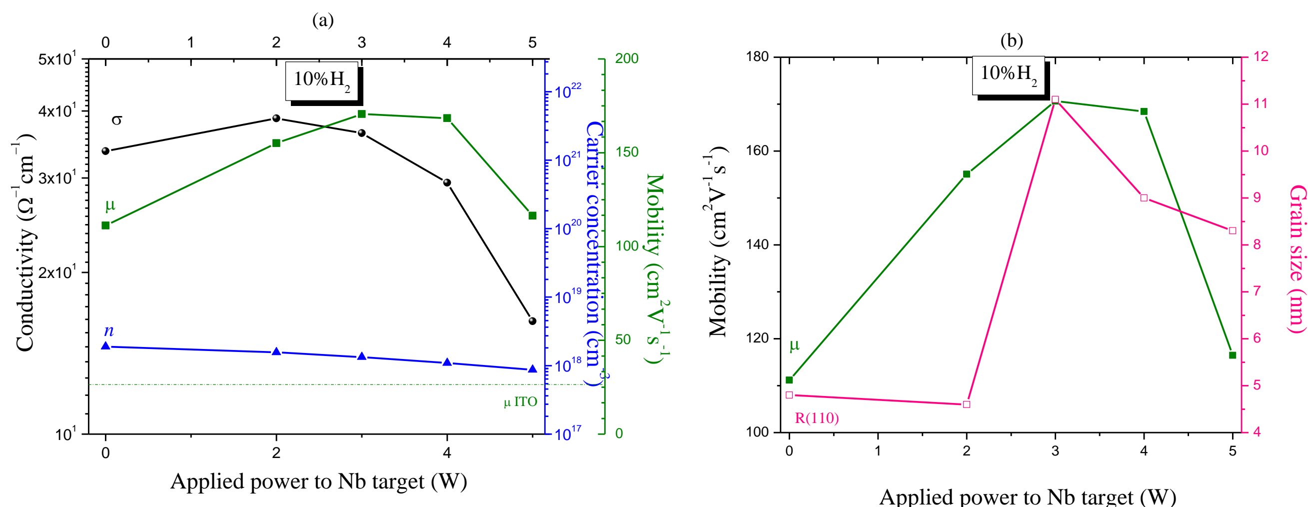

Figure 7.24 (a) Conductivity, carrier concentration and mobility values and (b) mobility and grains dimensions for post-growth annealed Nb-TiO_2 films prepared at various powers applied to Nb target, in 10% H_2 added in Ar plasma, at -850 *V*

In order to understand the correlation between high mobility values and low electron density or the opposite case, the dependence of the carrier density on the electron mobility for the annealed in vacuum intrinsically, extrinsically and intrinsically-extrinsically co-doped TiO_2 samples is plotted in Figure 7.25, indicating the power applied to the Nb target and the O_2 and H_2 concentration added in the gas mixture.

It is well known that the low electron mobility values are a result of scattering by grain boundaries and/or point defects. Post deposition heat treatment reduces point and/or dislocation defects in the amorphous or poorly crystalised films by increasing the grain size and improving the overall crystal structure enhancing the electron mobility, but this is not our case, because the grain size values for the samples with high μ and low *n* were not much higher than the grain size corresponding to the samples with low μ and higher *n*.

Another possible explanation for the high μ values can be the formation of anatase phase in these films, reported to give a higher μ value than the rutile one. But also this explanation does not fit in our case, because the films with high μ and low *n* were having anatase, rutile or anatase-rutile structures.

It has been suggested that hydrogen passivates the structural defects in TCO materials in the same way as is well known for thin film silicon, enhancing the electron mobility. But this can explain only the properties

of the samples prepared in $Ar-H_2$ gas mixture, not the ones prepared in Ar and $Ar-O_2$ gas mixture with high values of μ.

A possible explanation for the increase in mobility values can be attributed to the number of intrinsic defects in the films [1]. By minimizing the intrinsic defects in the material, a high mobility can be achieved.

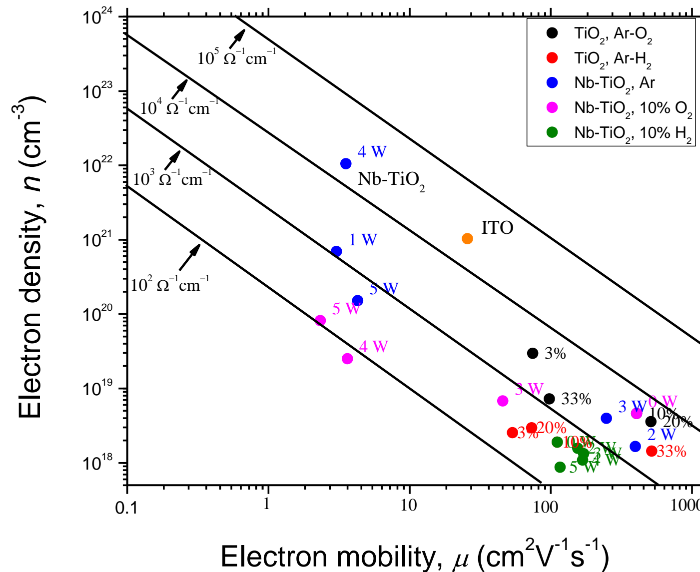

Figure 7.25 Carrier concentration vs. electron mobility for intrinsically, extrinsically and intrinsically-extrinsically co-doped annealed in vacuum TiO_2 films (-850 V on TiO_2 cathode)

7.4.3 Influence of substrate temperature on film electrical properties

$Nb-TiO_2$ films were prepared at a substrate temperature of 350°C during the sputtering from mosaic (-750 *V*) target or the co-sputtering configuration (-850 *V*). Both depositions were performed with 3% H_2 added in Ar plasma. The measured conductivity values were 6.25×10^2 $\Omega^{-1}cm^{-1}$ when the film was deposited from a mosaic target and 4.72×10^1 $\Omega^{-1}cm^{-1}$ when co-sputtering from two separate TiO_2 and Nb targets was used.

7.4.4 Optical properties of as-grown films

The transmittance and the absorption coefficient spectra in the visible range for as-grown Nb-TiO_2 films prepared in Ar-O_2 (20%O_2) and Ar-H_2 (20%H_2) atmospheres at -750 *V* from a mosaic target are shown in Figure 7.26. The corresponding thickness values and the Nb concentrations measured with XPS for both films are given in the figure. The average absorption coefficient in the visible range for both films is ~$7x10^3$ cm^{-1}. The optical direct band gap values are similar in values: 3.57±0.01 *eV* for Nb-TiO_2 film prepared in Ar-O_2 and 3.55±0.03 *eV* for for the film prepared in Ar-H_2.

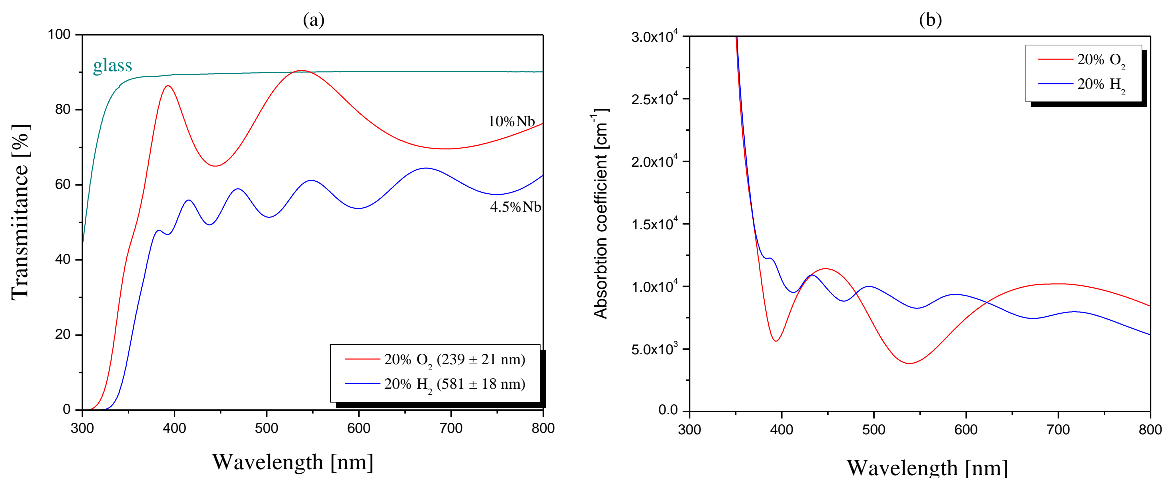

Figure 7.26 (a) Transmittance and (b) absorption coefficient for as-grown Nb-TiO_2 films prepared in Ar-O_2 (20%O_2) and Ar-H_2 (20%H_2) atmospheres, at -750 *V*

The optical properties for co-sputtered Nb-TiO_2 films obtained with 10%O_2 and 10%H_2 added in Ar plasma were investigated. In Figure 7.27 the transmittance and the absorption coefficient spectra for Nb-TiO_2 films prepared in Ar-O_2 at various powers applied to Nb target are shown and in Figure 7.28 the transmittance and the absorption coefficient corresponding to the samples prepared with 10%H_2.

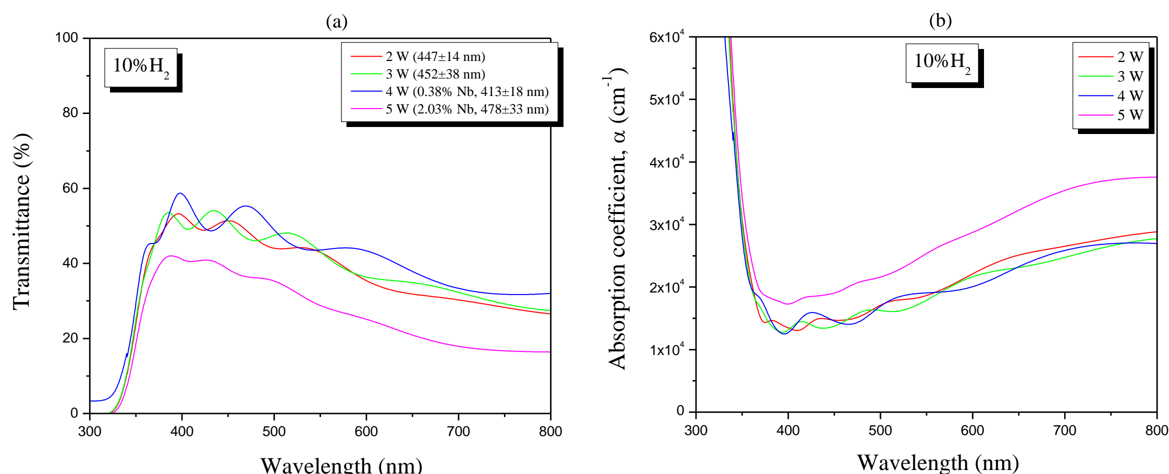

Figure 7.27 (a) Transmittance and (b) absorption coefficient for Nb-TiO_2 films prepared in Ar-H_2 plasma, at different powers applied to Nb target

No changes in the optical direct band gap values of the films were observed: 3.33 *eV*, 3.32 *eV* and 3.31 *eV* for 3 *W*, 4 *W* and 5 *W* powers applied to Nb target when 10% O_2 was added in Ar plasma and 3.37 *eV*, 3.33 *eV* and 3.34 *eV* for 3 *W*, 4 *W* and 5 *W* powers applied to Nb target when H_2 was used as reactive gas in the depositions.

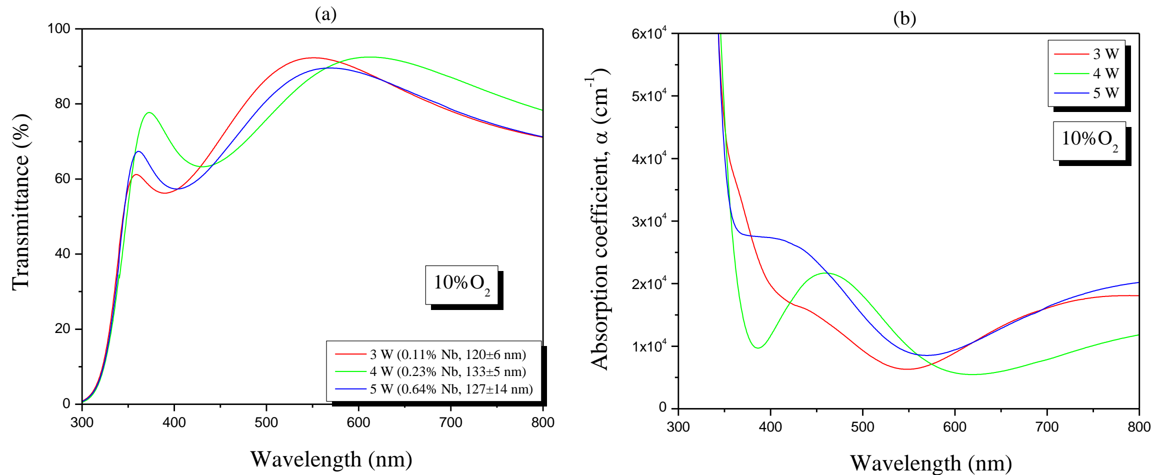

Figure 7.28(a) Transmittance and (b) absorption coefficient for Nb-TiO_2 films prepared in Ar-O_2 plasma, at different powers applied to Nb target

7.4.5 Influence of post-growth annealing on film optical properties

The Nb-TiO_2 films prepared by co-sputtering from two separate targets, in Ar-O_2 (10% O_2) and Ar-H_2 (10% H_2) gas mixtures were post-growth annealed in vacuum at 900°C. The transmittance and absorption coefficient spectra in the visible range are shown in Figure 7.29 for the samples prepared in Ar-O_2 at various powers applied to Nb and in Figure 7.30 for the ones prepared in Ar-H_2 at different powers. After annealing in vacuum the transmittance is decreasing for both types of films, most probably due to the formation of new

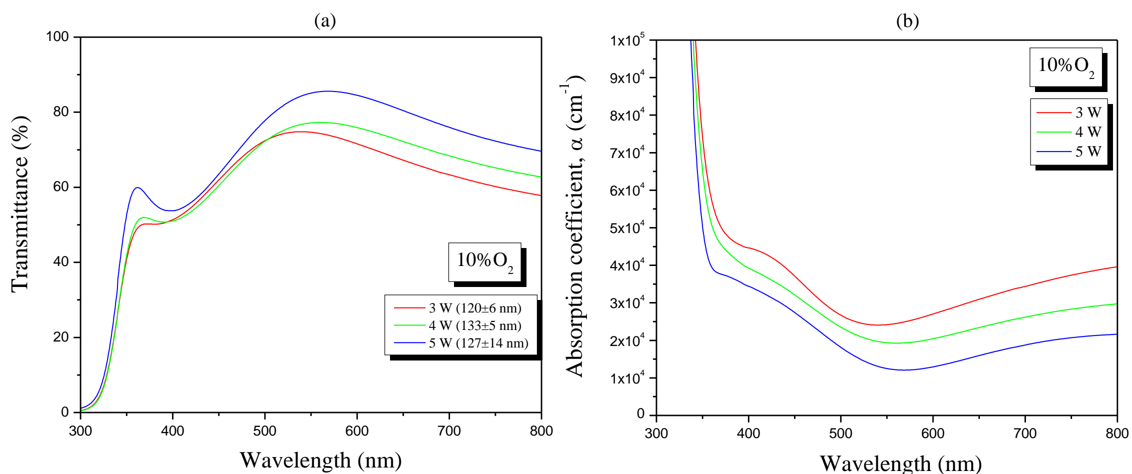

Figure 7.29 (a) Transmittance and (b) absorption coefficient for post-growth annealed in vacuum Nb-TiO_2 films prepared in Ar-O_2 plasma, at different powers applied to Nb target

oxygen vacancies after the post-growth annealing in vacuum.

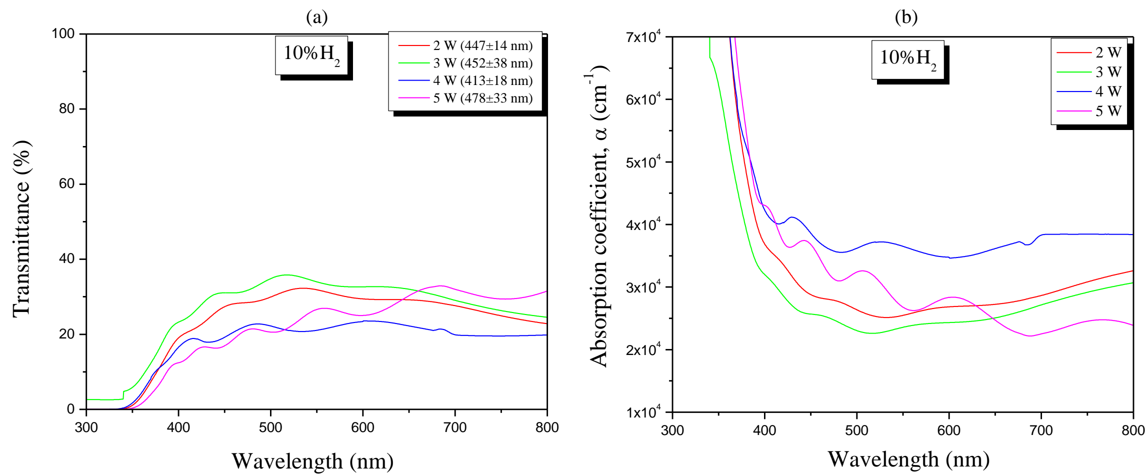

Figure 7.30 (a) Transmittance and (b) absorption coefficient for post-growth annealed in vacuum Nb-TiO_2 films prepared in Ar-H_2 plasma, at different powers applied to Nb target

7.4.6 Influence of substrate temperature on film optical properties

Low transmittance (~30%) was observed for the Nb-TiO_2 film prepared in Ar-H_2 plasma (3%H_2 added in discharge) when the substrate temperature during deposition was set at 350°C. The film was deposited from a mosaic target, at -750 *V*.

7.4.7 Figure of merit of intrinsically-extrinsically co-doped TiO_2 films

The quality of Nb-TiO_2 films co-sputtered from two targets in Ar-O_2 and Ar-H_2 atmospheres was evaluated, using the ratio $\frac{\alpha}{\sigma}$. The obtained values are plotted in Figure 7.31 (a) as a function of the power applied to Nb target. The FOM values for the obtained films are two orders higher than the value corresponding to ITO film.

A similarity was observed between the FOM values for these samples and the FOM values for un-doped TiO_2 films prepared in various atmospheres (Ar-O_2 and Ar-H_2), shown in Figure 7.31 (b). The plots for intrinsically-doped TiO_2 resemble those of intrinsic-extrinsic doped TiO_2. Nb introduction has no effect in improving the films performance as TCO.

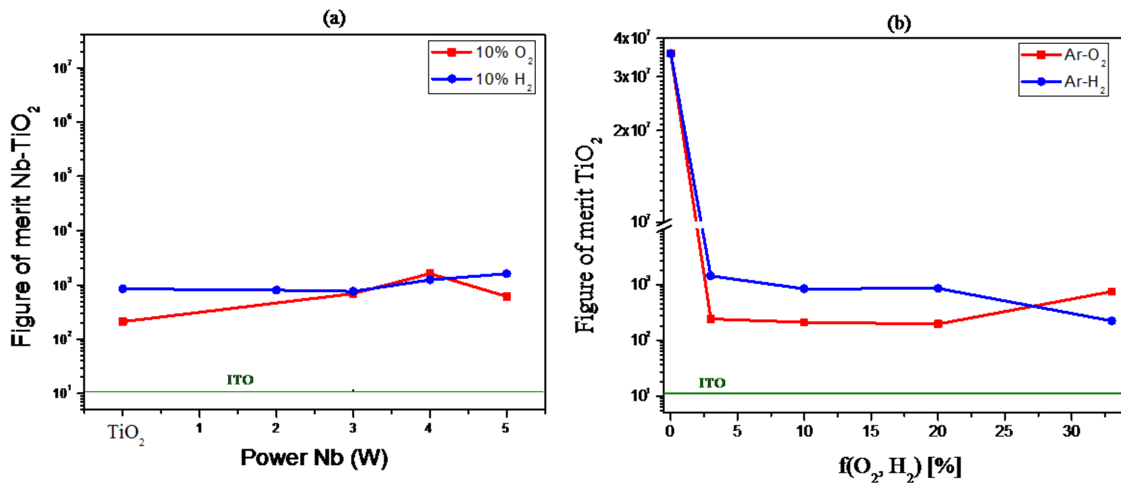

Figure 7.31 Figure of merit values for (a) intrinsically-extrinsically co-doped Nb-TiO_2 and (b) intrinsically-doped TiO_2 films, prepared in Ar-O_2 and Ar-H_2 atmospheres, at -850 *V*

7.4.8 Electronic properties of as-grown films

In Figure 7.32 (a) the band scheme for as-grown Nb-TiO_2 films sputtered from a mosaic target in Ar-O_2 (20%O_2) and Ar-H_2 (20%H_2) atmospheres at -750 *V* is shown. Similar to TiO_2 films prepared in Ar-O_2 plasma, the work function value for Nb-TiO_2 film prepared in Ar-O_2 plasma is increasing until a value of 6.70 *eV* and when the film is deposited using Ar-H_2 plasma the work function value is decreasing (3.08 *eV*), comparing with the sample prepared in pure-Ar plasma, with a work function equal to 4. 03 *eV*. The OH3s/VB area ratio and the WF values dependence is shown in Figure 7.32 (b).

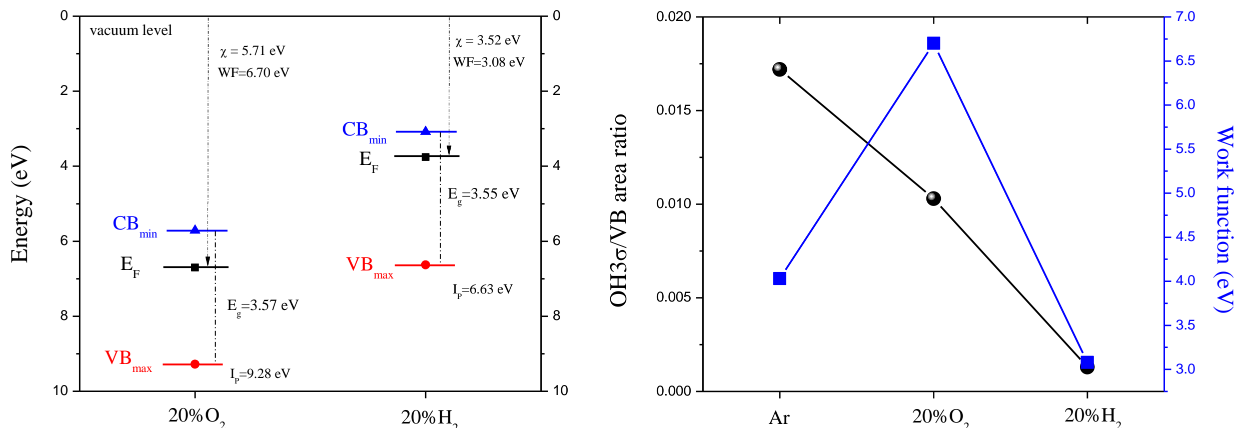

Figure 7.32 (a) Band scheme and (b) OH3σ/VB area ratio with WF for as-grown Nb-TiO_2 films prepared in Ar-O_2 (20%O_2) and Ar-H_2 (20%H_2) atmosphere, at -750 *V* (the lines serve only to guide the eye)

For Nb-TiO_2 samples prepared by co-sputtering from two separate targets the work function, valence band edge, optical band gap, ionization potential and electron affinity values with respect to the vacuum level are listed in Table 7.7 (where VBM(q=0) is the VBM value corrected for the band bending effect during the XPS analysis) and the obtained band schemes are shown in Figure 7.33. High values of WF were obtained for the samples deposited in Ar-O_2 gas mixture and low WF values when H_2 was added in discharge.

The role of OH groups in determining the work function value can be understood from Figure 7.34 where this parameter is plotted together with the OH3σ/VB area ratio from XPS analysis. A somewhat good correlation can be found between these two parameters for samples deposited in Ar-O_2 plasma, but not in the case of Ar-H_2 plasma. The surface of these two kinds of samples is clearly different, besides the OH3σ /VB area ratio is much lower in the case of Ar-H_2 plasma, which corresponds to much lower values of the work function. The surface is more likely H-terminated.

Table 7.7 WF, VB_{max}, E_g, I_p and χ values for as-grown Nb-TiO_2 films deposited in Ar-O_2 (10%O_2) and Ar-H_2 (10%H_2) atmospheres at various powers applied to Nb target, at -850 *V*

	Power (W)	**WF (*eV*)**	**VBM (q=0) (*eV*)**	**E_g (*eV*)**	**I_p (*eV*)**	**χ (*eV*)**
10%O_2	0 (TiO_2)	5.06±0.12	1.97	3.28	7.03	3.75
	3	6.57±0.66	1.78	3.33	8.35	5.02
	4	7.30±0.79	2.08	3.32	9.38	6.06
	5	4.96±0.17	1.81	3.31	6.77	3.46
10%H_2	0 (TiO_2)	3.96±0.04	3.33	3.54	7.29	3.78
	3	3.74±0.15	2.16	3.37	5.90	2.53
	4	3.86±0.09	2.05	3.33	5.91	2.58
	5	3.56±0.08	2.42	3.34	5.98	2.64

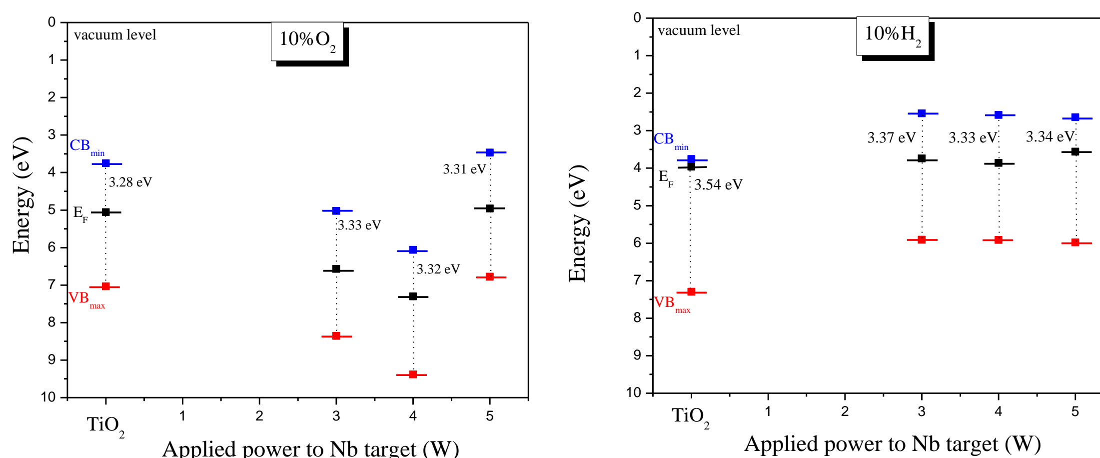

Figure 7.33 Band schemes for as-grown Nb-TiO_2 films prepared in (a) Ar-O_2 (10%O_2) and (b) Ar-H_2 (10%H_2) atmospheres varying the powers applied to Nb target, at -850 *V*

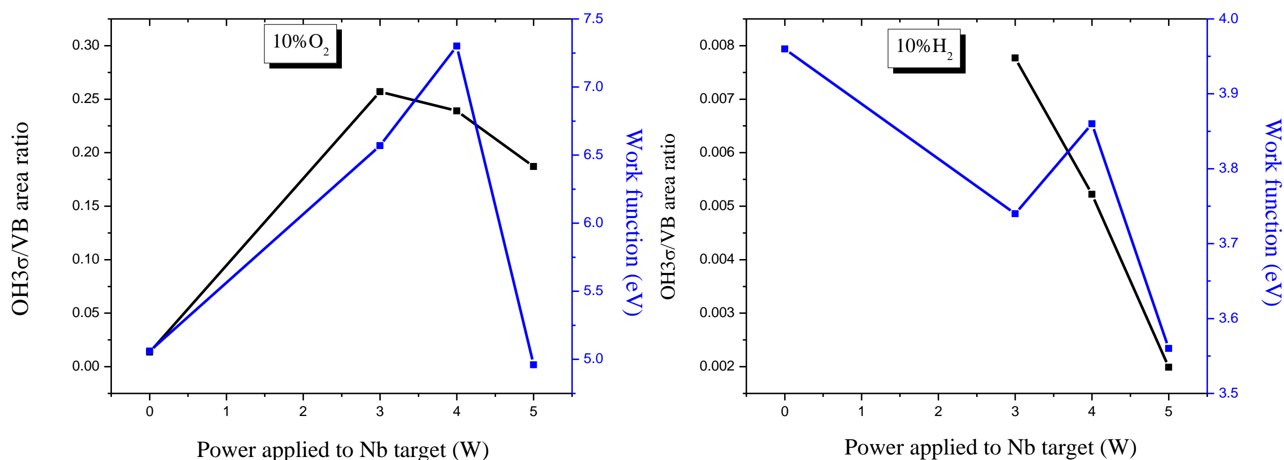

Figure 7.34 OH3σ/VB area ratio and WF as obtained by XPS in function of the power applied to Nb target for as-grown TiO_2 films at -850 *V* to TiO_2 cathode for (a) 10%O_2 and (b) 10%H_2 added in Ar plasma

7.4.9 Influence of post-growth annealing on film electronic properties

The work function for post-growth annealed in vacuum Nb-TiO_2 films sputtered from a mosaic target in Ar-O_2 and Ar-H_2 plasmas at -750 *V* was determined and the band schemes for these samples are shown in Figure 7.35 (a).

No correlation was found between the OH3s/VB area ratio and the WF values for the annealed in vacuum films prepared in various gas mixtures, as can be seen in Figure 7.35 (b).

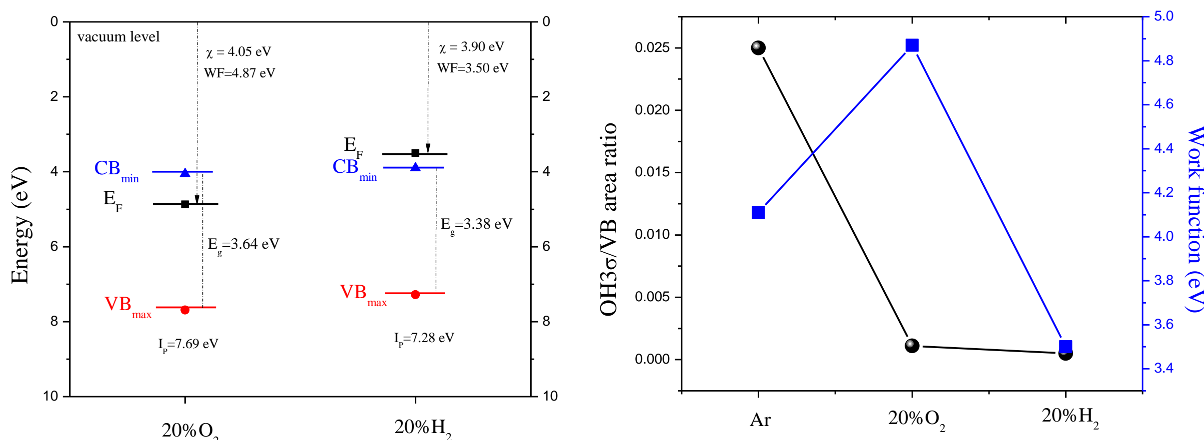

Figure 7.35 (a) Band scheme and (b) OH3s/VB area ratio with the WF values for post-growth annealed Nb-TiO_2 films prepared in Ar-O_2 (20%O_2) and Ar-H_2 (20%H_2) atmosphere (-750 *V* on TiO_2 cathode), the lines serve only to guide the eye

7.5 Concluding remarks

The electrical, optical and electronic properties of intrinsically, extrinsically and intrinsically-extrinsically co-doped TiO_2 were studied.

The conductivity values for as-grown intrinsically, extrinsically and intrinsically-extrinsically co-doped TiO_2 films prepared in Ar, Ar-O_2 and Ar-H_2 gas mixtures were low (10^{-2}-10^{-3} $\Omega^{-1}cm^{-1}$). The films were transparent in the visible region (400-800 *nm*). The hydrogen addition in the gas mixture in high concentrations decreased the transmittance of the films. Also the Nb addition in the sputtering process in too high concentrations is decreasing the transmittance of the films.

The annealing in vacuum at 900°C improved the electrical properties of the intrinsically-doped TiO_2 films. High conductivity values were obtained. For the TiO_2 films prepared in Ar-O_2 the measured σ was in the range $1.13x10^2$ - $3.52x10^2$ $\Omega^{-1}cm^{-1}$ and n_e is decreasing with increasing the O_2 concentration in the gas mixture ($2.95x10^{19}$ cm^{-3} for 3%O_2 to $7.22x10^{18}$ cm^{-3} for 33%O_2). High mobility values were measured for these samples (74-512 $cm^2V^{-1}s^{-1}$), attributed to a small number of intrinsic defects in the films. The transparency of the films decreased after annealing in vacuum and an increase in the absorption coefficient value was observed, due to an increase in the number of oxygen vacancies during the annealing in vacuum. The direct band gap is increasing after annealing.

For the annealed samples prepared in Ar-H_2 values the measured σ values were in the range $2.17x10^1$ – $1.2x10^2$ $\Omega^{-1}cm^{-1}$. No great variation is observed for n_e values ($1.44x10^{18}$ cm^{-3} - $2.96x10^{18}$ cm^{-3}). The mobility values are increasing with increasing the H_2 concentration in the gas mixture (53-519 $cm^2V^{-1}s^{-1}$), attributed to a small number of intrinsic defects in the films and the presence of hydrogen in the discharge, known to passivate the structural defects in TCO materials. The transparency of the films decreased after annealing in vacuum and an increase in the absorption coefficient value was observed, but less than in the case of the samples prepared in Ar-O_2 gas mixture, indicating an increase in the number of oxygen vacancies during the annealing in vacuum. The direct band gap is decreasing after annealing.

High value of conductivity was found for the TiO_2 film prepared at 350°C substrate temperature during the deposition in Ar plasma ($2.7x10^2$ $\Omega^{-1}cm^{-1}$), but with low carrier density value was $1.31x10^{18}$ cm^{-3}. An increase in the absorption coefficient value as compared to the sample prepared at RT in the same conditions was observed, indicating the formation of oxygen vacancies during annealing in vacuum.

The annealing in vacuum at 900°C improved the electrical properties of extrinsically-doped TiO_2 films. High conductivity values ($1.05x10^2$ - $5.95x10^3$ $\Omega^{-1}cm^{-1}$) were obtained for low concentration of Nb (<2.3%) in the films (co-sputtered from two separate TiO_2 and Nb targets). The highest conductivity value was obtained when 4 W was used as applied power to Nb target (corresponding to 0.95% Nb in the film) with $1.05x10^{22}$ cm^{-3} carrier density and μ=3.54 $cm^2V^{-1}s^{-1}$. The carrier density values are in good correlation with the mobility values in these films. An increase in n_e leads to a decrease in μ and the vice-versa. The increase or decrease in mobility values is also correlated with the grains dimension. The transparency of the films decreased after annealing in vacuum and an increase in the absorption coefficient value was observed, due to

an increase in the number of oxygen vacancies during the annealing in vacuum. The direct band gap is decreasing after annealing.

An increase in the conductivity values was observed for Nb-TiO_2 films prepared at various substrate temperatures (300-420°C) during the deposition in Ar plasma (from 10^{-3} $\Omega^{-1}cm^{-1}$ to 10^{2} $\Omega^{-1}cm^{-1}$). The transmittance of the films was decreasing with increasing the substrate temperature and the absorption coefficient values were increasing.

The annealing in vacuum at 900°C improved the electrical properties of intrinsically-extrinsically co-doped TiO_2 films, prepared by co-sputtering from two separate TiO_2 and Nb targets, with 10% O_2 and 10% H_2 added in Ar plasma. Conductivity values in the range $1.45x10^{1}$ – $4.98x10^{1}$ $\Omega^{-1}cm^{-1}$ were measured for co-sputtered Nb-TiO_2 films (<2%Nb) at various applied powers to Nb target (-850 V on TiO_2 cathode), lower values comparing with the Nb-TiO_2 films prepared in Ar plasma. n_e values for the films prepared with 10% O_2 added in the gas mixture are in the order 10^{18}-10^{19} cm^{-3}, smaller than the n_e values for Nb-TiO_2 films prepared in Ar plasma and are increasing with the power applied to Nb target. The mobility values are decreasing with increasing the power applied to Nb target. No clear correlation is observed between the grain size and μ values. n_e values for the films prepared with 10% H_2 added in the gas mixture are in the order 10^{17}-10^{18} cm^{-3}, smaller than the n_e values for Nb-TiO_2 films prepared in Ar plasma and are decreasing with the power applied to Nb target. Also for these samples, no clear correlation is observed between the grain size and μ values. The transparency of the films decreased after annealing in vacuum and an increase in the absorption coefficient value was observed, indicating an increase in the number of oxygen vacancies during the annealing in vacuum. The direct band gap is decreasing after annealing.

High value of conductivity was found for the Nb-TiO_2 film prepared at 350°C substrate temperature during the deposition in Ar-H_2 plasma with 3% H_2 (10^{1} – 10^{2} $\Omega^{-1}cm^{-1}$), but with low transmittance of the films.

The figure of merit was determined for all the films. The extrinsically-doped TiO_2 films prepared by co-sputtering from two separate TiO_2 and Nb targets in Ar plasma were having the best optical and electrical properties, while the intrinsically and intrinsically-extrinsically co-doped TiO_2 films were having similar values, higher than the extrinsically-doped TiO_2.

Doping with intrinsic defects of TiO_2 films gave high values of conductivity, but not enough to allow the use of these films as replacement of ITO as a transparent conductor. The best intrinsically-doped films in terms of optical and electrical properties were TiO_2 films deposited in Ar-O_2 gas mixture. Higher conductivity values were obtained for extrinsic-doped TiO_2 films in comparison with the un-doped TiO_2 films prepared in Ar-O_2 gas mixture. The best performance in terms of optical transparency and conductivity, which raised the films at ITO level, was obtained for a narrow concentration range of Nb. All Nb concentrations above 2.3 at.% were ineffective in doping. It was understood that well-doped films (high n) means also an anatase-to-rutile transformation "inhibited". When the anatase-to-rutile transformation occurs, it was accompanied by reduced crystallite size, which leads also to a reduction of electron mobility in these films. No effective Nb-doping effect on the electrical properties of the films prepared with such processes was found. Even if the conductivity values were high, they keep far from the ITO value. The doping

efficiency loss in TiO_2-Nb films grown in Ar-O_2 and Ar-H_2 plasmas are attributed to the conductivity loss regarded primarily the carrier density (only a very limited increase was obtained with Nb incorporation in the case of Ar-O_2 gas mixtures and no effect at all was obtained in the case of Ar-H_2 gas mixture, while in the films prepared in Ar plasma, nearly four orders of magnitude improvement brought about by Nb was observed) and the structure distortion introduced by the presence of defects like oxygen vacancies or Ti-OH and/or Ti-H bonds expected to modify the solubility of Nb in the TiO_2 structure.

The valence band edge, Fermi level position, work function, ionization potential and electron affinity with respect to vacuum level were determined for all the samples. An increase in the WF value was observed with increasing the O_2 concentration in the gas mixture and a decrease with increasing the H_2 concentration. A correlation was found between the OH groups number and the WF values for the samples prepared in Ar-O_2 gas mixture. In the case of the samples prepared in Ar-H_2 gas mixture, also a good correlation of these two parameters was observed, but until 20%H_2 in Ar plasma, most probably due to a hydrogen terminated surface, therefore a competitive effect of OH groups and H on the surface.

7.6 References

1. S. Calnan, A. N. Tiwari, Thin Solid Films 518 (2101) 1839-1849
2. P.A. Iles and S.I. Soclof, Proceedings of the 12th IEEE Photovoltaic Conference, November (1976) (unpublished), p. 978
3. E. Burstein, Phys. Rev. Lett. 93, 632 (1954)

8. Investigation of structural vacancies in doped-TiO_2 by positron annihilation spectroscopy

Studies of positron annihilation in metals, semi-conductors, nanocrystals, amorphous materials, and ceramics revealed that positrons can be trapped by vacancies both in the metallic and nonmetallic sublattices, in vacancy clusters, at grain boundaries, by dislocations, etc.

In this chapter the local atomic environment of vacancies in intrinsically, extrinsically and intrinsically-extrinsically co-doped TiO_2 was studied by electron–positron annihilation, a promising and universally recognized experimental approach to investigation of solids with point, linear, extended, and bulk defects.

Contents

8.1 Introduction
8.2 Intrinsically-doped TiO_2
- 8.2.1 Structural vacancies in as-grown films
- 8.2.2 Structural vacancies in post-growth annealed films

8.3 Extrinsically doped-TiO_2
- 8.3.1 Structural vacancies in as-grown films
- 8.3.2 Structural vacancies in post-growth annealed films

8.4 Intrinsically-extrinsically co-doped TiO_2
- 8.4.1 Structural vacancies in as-grown films
- 8.4.2 Structural vacancies in post-growth annealed films

8.5 S-W plot
8.6 Concluding remarks
8.7 References

8.1. Introduction

The structural vacancies were investigated in the intrinsically, extrinsically and intrinsically-extrinsically co-doped TiO_2 films, prepared in various gas mixtures (Ar, Ar-O_2 and Ar-H_2) by Doppler broadening measurements and positron lifetime measurements. The influence of the post-growth annealing in vacuum at 900°C on the structural properties of the films was also investigated.

8.2 Intrinsically-doped TiO_2

8.2.1 Structural vacancies in as-grown films

Doppler broadening measurements for as-grown TiO_2 films prepared in Ar, Ar-O_2 (20%O_2) and Ar-H_2 (20%H_2) atmospheres on Si (100) substrates at a self-bias cathode voltage of -750 *V* were performed at room temperature (RT). The mentioned films are having an amorphous structure, except the film prepared in Ar-O_2 atmosphere, characterized by X-ray Diffraction measurements.

The Doppler broadening spectra were analyzed and the *S* and *W* line shape parameters were defined. The characteristic valence-electron annihilation parameter *S* identifies the extent of positron annihilation with valence electrons. The core-electron annihilation parameter *W* is a characteristic of the annihilation of positrons with core electrons.

The open volume depth profile of the studied samples can be described by the analysis of the dependence of *S* parameter on positron energy implantation *E* curves, shown in Figure 8.1 (a). The line through the experimental points was obtained by a fitting procedure (VEPFIT program) based on the solution of the stationary positron diffusion equation. In all investigated samples, the experimental data were satisfactorily fitted assuming a structure of three layers each of them ascribed to a different positron annihilation sites: the

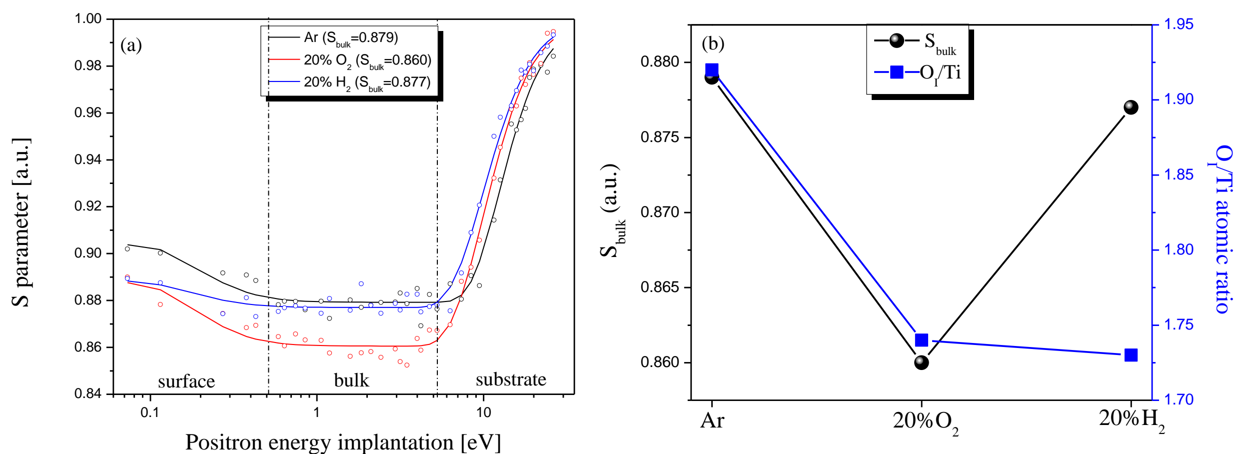

Figure 8.1 (a) *S-E* curves for as-grown TiO_2 films in Ar, Ar-O_2 (20%O_2) and Ar-H_2 (20%H_2) atmospheres, the solid lines represent a fit by VEPFIT; (b) S_{bulk} and O_I/Ti atomic ratios in various atmospheres (the lines are used only to guide the eye)

deposited film, an intermediate layer (bulk) and a semi infinite Si bulk layer. The *S* parameter value characteristic for each layer can be extracted. The *S* values for the bulk region for the studied films are plotted in Figure 8.1 (a).

For TiO_2 film prepared in Ar plasma the S value is S_{bulk}=0.879. When oxygen is introduced in Ar plasma, S_{bulk} is decreasing reaching a value equal to 0.860. The decrease of S-parameter was indicated to correspond to less open volumes in the film. The O_I/Ti atomic ratio value is also decreasing for the sample prepared in Ar-O_2 atmosphere, as shown in Figure 8.1 (b) [1].

Adding hydrogen in Ar plasma, S_{bulk} value is slightly decreasing (S_{buk}=0.877) indicating less open volumes. The O_I/Ti atomic ratio was similar to the one corresponding to the sample prepared in Ar-O_2 atmosphere, most probably due to the formation of Ti-OH coming from the H_2O dissociation.

For a better understanding of the dynamic variation of defects, positrons lifetime measurements (PAL) were performed for as-grown TiO_2 film prepared in pure-Ar plasma. After injecting of the positron in the material it diffuses and is drawn by defects where it can be trapped and thereafter annihilates. The lifetime of the positron depends on how quickly it encounters an electron since the positron and electron annihilate each other and release γ-rays that escape the system without any interaction. If the electron density is lower at trapping sites than the bulk density, then the positron lifetime will increase relative to the life-time in a defect-free bulk. Thus, positron lifetime analysis can provide information on the character, size and concentration of the trapping sites.

The PAL spectra were recorded at room temperature (RT). The best computer fits of the PAL spectra were achieved using two lifetime components in the substrate region and three components in the surface and bulk region, with corresponding intensity values. Titanium and TiO_2 rutile reference samples were also measured.

The probability that the positron survives in the sample after a time t is given as:

$$n(t) = I_1 \exp\left(-\frac{t}{\tau_1}\right) + I_2 \exp\left(-\frac{t}{\tau_2}\right)$$

if τ_1 and τ_2 correspond to two different kinds of defects. In the case of the present samples, three components of positron lifetime were evidenced.

The positron lifetime components τ_1, τ_2 and τ_3 and their related intensities I_1, I_2 and I_3 as a function of the positron implantation energy for the film prepared in Ar plasma were measured, as can be seen in Figure 8.2. The obtained lifetime values correspond to typical lifetime values for amorphous TiO_2: τ_1 is attributed to free positrons in material (vacancies) being the shortest component, τ_2 is arisen from positron trapping in microvoids inside or at the interfaces/grain boundaries, which are supposed to have larger free volume and τ_3 is attributed to the orto-positronium annihilation in a free space [2]. The third component will not be taken into account due to the corresponding small intensity in all the samples.

In Table 8.1 the positron lifetime values reported in the literature for Ti and TiO_2 are listed. These values were used for the identification of the measured lifetimes for our films.

Table 8.1 Positron lifetimes in TiO_2

Amorphous TiO_2 [2]	τ_1~210-246 ps; τ_2~450-455 ps; τ_3~1400-1500 ps
Bulk Ti	~143–152 ps [3]
Monovacancies Ti	~222 ps [3]
Dislocations of Ti	~168-195 ps [3]
Vacancy clusters of Ti (N=10)	~500 ps [3]
Bulk TiO_2	~148 ps [4]
Oxygen vacancy	~170 ps [4]
Ti vacancy	~190 ps [4]
Microvoids at interfaces	~400-580 ps [4]

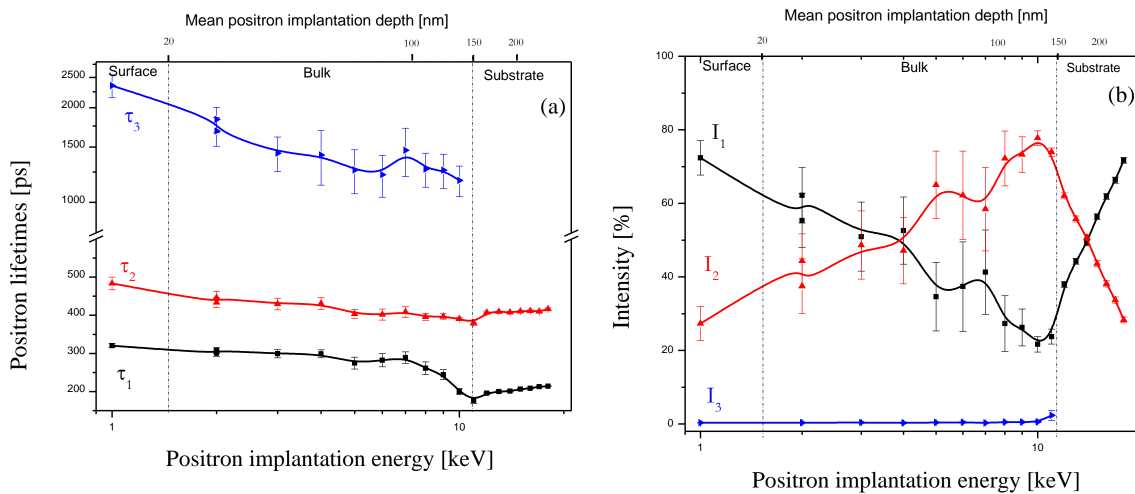

Figure 8.2 (a) The positron lifetime components τ_1, τ_2 and τ_3 and (b) their related intensities I_1, I_2 and I_3 as a function of the positron implantation energy for as-grown TiO_2 film obtained in Ar

The positron lifetime components τ_1, τ_2 and τ_3 (related to the electron density at the defect) and their related intensities I_1, I_2 and I_3 (related to the number of defects) were measured for a given positron implantation energy corresponding to the bulk region (2-4 *keV*), determined from *S* curves. The obtained

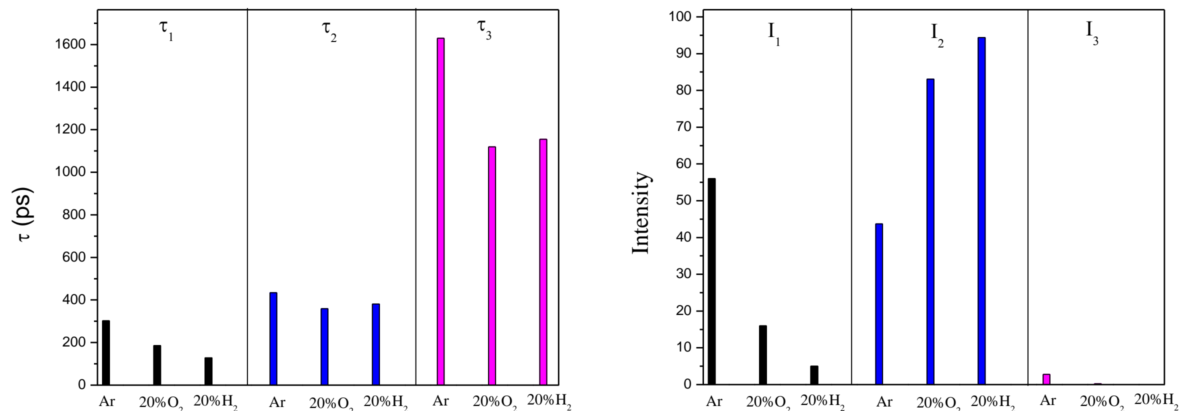

Figure 8.3 (a) The positron lifetime values τ_1, τ_2 and τ_3 and (b) their related intensities I_1, I_2 and I_3 for as-grown TiO_2 films obtained in Ar, Ar-O_2 and Ar-H_2 plasmas

values are given in Table 8.2 and are plotted in Figure 8.3.

For the as-grown samples prepared in Ar-O_2 and Ar-H_2 atmospheres, the positron lifetime τ_1 is decreasing compared to τ_1 in the film prepared in Ar plasma (from 302 *ps* in Ar plasma to 185 *ps* in Ar-O_2 plasma and 128 *ps* in Ar-H_2 plasma). I_1 is also decreasing when O_2 or H_2 is used in Ar plasma, from 56% in Ar plasma to 16% in Ar-O_2 and for 20%H_2 introduced in discharge reaches a value equal to 5%.

τ_1 value for the sample prepared in Ar plasma (302 *ps*) is much higher for what reported for O or Ti vacancies in TiO_2. For the samples prepared in Ar-O_2 and Ar-H_2 gas mixtures, τ_1 values are much closer to the reported values for O or Ti vacancies and can be attributed to positrons annihilation in vacancies, more likely in oxygen vacancies as it came out from the XPS analysis results. The high value of τ_1 for the sample prepared in Ar plasma could be due to decorated-vacancy clusters (possibly V-O_2).

An opposite trend was found between the intensity I_1 and O_I/Ti atomic ratio from the XPS analysis, shown in Figure 8.4. A decrease in I_1 intensity should be correlate with an increase in the stoichiometric ratio. This could indicate that the vacancies in the films prepared in Ar-O_2 and Ar-H_2 gas mixtures are more passivated than in the film prepared in pure-Ar plasma.

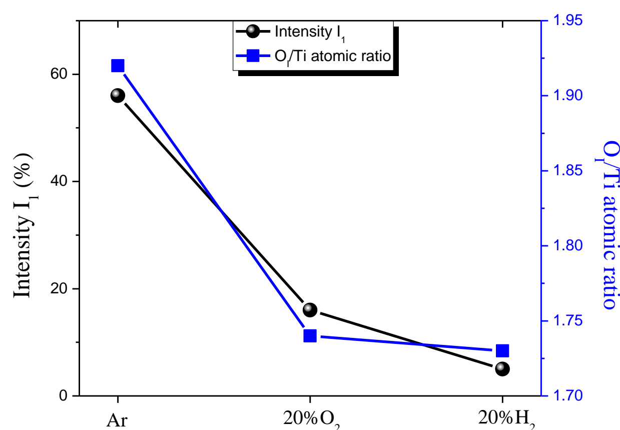

Figure 8.4 O_I/Ti atomic ratios from XPS analysis and Intensity I_1 corresponding to lifetime τ_2 for as-grown TiO_2 films prepared in various atmospheres (the lines are used only to guide the eye)

The second lifetime τ_2 associated with the positron trapping in microvoids inside or at the interfaces/grain boundaries is decreasing compared to τ_2 in the film prepared in Ar plasma (from 434 *ps* in Ar plasma to 359 *ps* in Ar-O_2 plasma and 381 *ps* in Ar-H_2 plasma). The decrease in τ_2 value indicates larger grain size and a lower density of interface/grain boundary. The sample prepared in Ar-O_2 was not amorphous when analyzed with XRD as the sample prepared in Ar plasma, but nanocrystalline anatase and rutile phases were observed, a possible explanation for the decrease in τ_2 value. The decrease of τ_2 value for the sample prepared in Ar-H_2 can be explained with the XPS results presented in Chapter 4, where it was observed the existence of Jahn-Teller effect when hydrogen is introduced in Ar plasma. This mechanism was reported for nanocrystalline

TiO_2 films. I_2 is increasing when O_2 or H_2 is used in Ar plasma, from 43% in Ar plasma to 83% in Ar-O_2 and 94% in Ar-H_2.

τ_3 value, characteristic of microvoids defects with much lower electron density such as pores, in which positronium can form, is highest for the sample prepared in pure-Ar plasma, with the highest value of I_3.

Table 8.2 The lifetime values and the corresponding intensities for as-grown and annealed TiO_2 and Nb-TiO_2 samples

		Ar	**Ar-O_2 (20%O_2)**	**Ar-H_2 (20%H_2)**			**Ar**	**Ar-O_2 (20%O_2)**	**Ar-H_2 (20%H_2)**
as-grown TiO_2	τ_1 (ps)	302.6±4.5	185.5±8.7	128±10	**as-grown Nb-TiO_2**	τ_1 (ps)	273.5±11.9	63.5±2.5	330.1±8.3
	I_1 (%)	56.0±4.1	16.1±1.6	5.0±0.4		I_1 (%)	33.0±7.2	9.5±0.2	49.2±6.2
	τ_2 (ps)	434.6±7.5	359.0±2.5	381±1		τ_2 (ps)	394.7±8.8	357.2±0.5	474.7±10.6
	I_2 (%)	43.7±4.1	83.1±1.6	94.4±0.3		I_2 (%)	66.8±7.0	90.2±0.2	50.6±6.1
	τ_3 (ps)	1630±95	1120±62	1155±75		τ_3 (ps)	1054±185	1627±100	1820±317
	I_3 (%)	0.3±0.04	0.8±0.1	0.6±0.1		I_3 (%)	0.2±0.1	0.3±0.03	0.2±0.06
annealed TiO2	τ_1 (ps)	79.8±2.2	266±10	340.7±2.2	**annealed Nb-TiO2**	τ_1 (ps)	298±3	322.4±2.1	300.6±1.2
	I_1 (%)	13.3±0.2	27.7±4.8	82.4±2.2		I_1 (%)	78.8±3.4	87.3±2.1	84.9±1.0
	τ_2 (ps)	349.9±1.2	395±5	490.8±9.4		τ_2 (ps)	451.9±14.8	519±20	493.6±6.5
	I_2 (%)	83.9±0.3	72.1±4.8	17.6±2.2		I_2 (%)	21.1±3.3	12.5±2.0	15.1±1.0
	τ_3 (ps)	681±20	1633±140			τ_3 (ps)	1788±319	2145±277	
	I_3 (%)	2.8±0.4	0.2±0.04			I_3 (%)	0.1±0.04	0.2±0.04	

8.2.2 Structural vacancies in post-growth annealed films

The structural vacancies of the post-growth annealed in vacuum at 900°C TiO_2 films were investigated. The dependence of *S* parameter on the positron energy implantation *E* for the annealed samples is shown in Figure 8.5 (a). The S_{bulk} values are given in the figure.

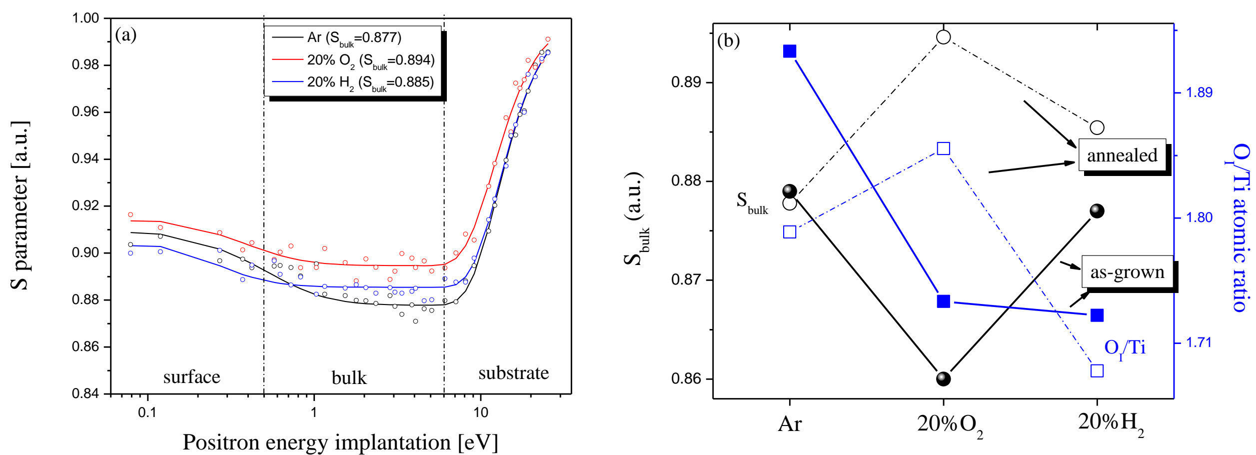

Figure 8.5 (a) *S-E* curves for annealed TiO_2 films prepared in Ar, Ar-O_2 (20%O_2) and Ar-H_2 (20%H_2) atmospheres, the solid lines represent a fit by VEPFIT; (b) S_{bulk} and O_I/Ti atomic ratios in various atmospheres (the lines are used only to guide the eye)

After annealing, the S_{bulk} value for the film prepared in Ar plasma does not considerably change (0.877), for the sample prepared in Ar-O_2 gas mixture is increasing (from 0.860 to 0.894) indicating more open volumes and for the sample prepared in Ar-H_2 gas mixture is also increasing (from 0.877 to 0.885). A good correlation was found between the S_{bulk} values and O_I/Ti atomic ratios from XPS analysis for as-grown and annealed samples as shown in Figure 8.5 (b).

The positron lifetime values τ_1, τ_2 and τ_3 and their related intensities I_1, I_2 and I_3 measured for a given positron implantation energy corresponding to the bulk region (2-4 *keV*), determined from *S* curves for the post-growth annealed in vacuum samples prepared in Ar, Ar-O_2 and Ar-H_2 atmospheres are given in Table 8.2 and plotted in Figure 8.6.

The positron lifetime τ_1 is decreasing after annealing in vacuum for the film prepared in Ar plasma (from 302 *ps* in as-grown film to 79 *ps* in annealed film) and is increasing for the annealed samples prepared in Ar-O_2 and Ar-H_2 plasmas (from 185 ps to 266 ps in Ar-O_2 and from 128 ps to 340 ps in Ar-H_2). τ_1 is strongly decreasing after annealing for the sample prepared in Ar plasma, most probably due to the desorption of O_2 in the V-impurity complex (decomposition of the complex). For the samples prepared in Ar-O_2 and Ar-H_2 gas mixtures τ_1 is increasing after annealing, most probably due to the formation of divacancies.

I_1 is also decreasing after annealing for the film prepared in Ar plasma (from 56% in as-grown film to 13% in annealed film) and is increasing for the annealed samples prepared in Ar-O_2 and Ar-H_2 plasmas (from 16% to 27% in Ar-O_2 and from 5% to 82% in Ar-H_2). If the O_I/Ti atomic ratios are plotted together with I_1 values (Figure 8.7 (a)) in Ar and Ar-O_2 atmospheres, the same behavior is observed, but not in the case of Ar-H_2.

The second lifetime τ_2 associated with the positron trapping in microvoids inside or at the interfaces/grain boundaries is decreasing after annealing in the film prepared in Ar plasma (from 434 *ps* in Ar plasma to 349 *ps*), explained by the formation of anatase and rutile phases after annealing in vacuum. For the samples

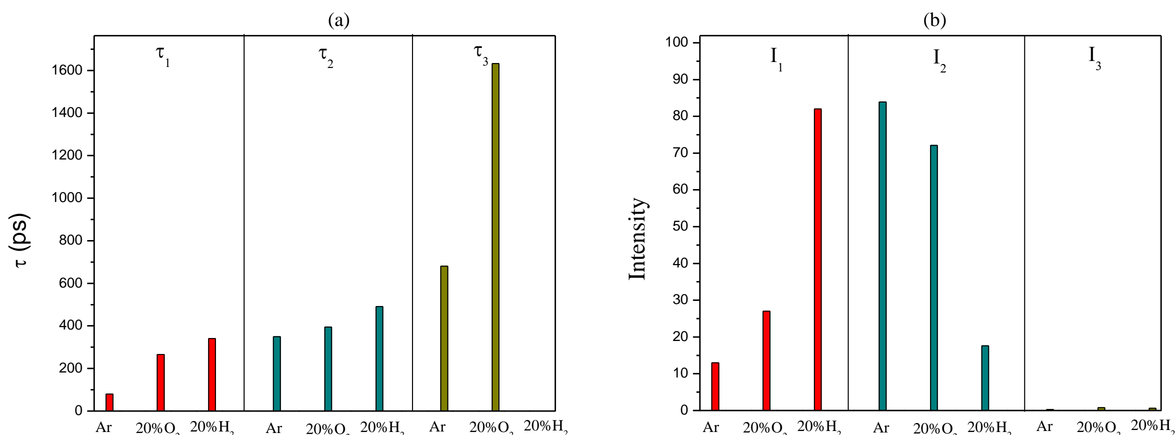

Figure 8.6 (a) The positron lifetime values τ_1, τ_2 and τ_3 and (b) their related intensities I_1, I_2 and I_3 for post-growth annealed TiO_2 films obtained in Ar, Ar-O_2 and Ar-H_2 plasmas

prepared in Ar-O_2 and Ar-H_2 plasmas an increase of τ_2 is observed after annealing in vacuum (from 359 *ps* to 395 *ps* in Ar-O_2 plasma and from 381 *ps* to 490 *ps* in Ar-H_2 plasma). After annealing in vacuum, both TiO_2 films prepared in Ar-O_2 and Ar-H_2 plasmas were not amorphous anymore, but anatase-rutile and rutile phases were detected. I_2 is increasing after annealing for the film prepared in Ar plasma (from 43% in as-grown film to 83% in annealed film) explained by the formation of a porous structure after annealing and is decreasing for the annealed samples prepared in Ar-O_2 and Ar-H_2 plasmas (from 83% to 72% in Ar-O_2 and from 94% to 17% in Ar-H_2) where less porous structure (in Ar-O_2 plasma) or preserved columnar structure (in Ar-H_2 plasma) after annealing was observed. In Figure 8.7 (b) the grain dimensions are plotted together with the intensity I_2.

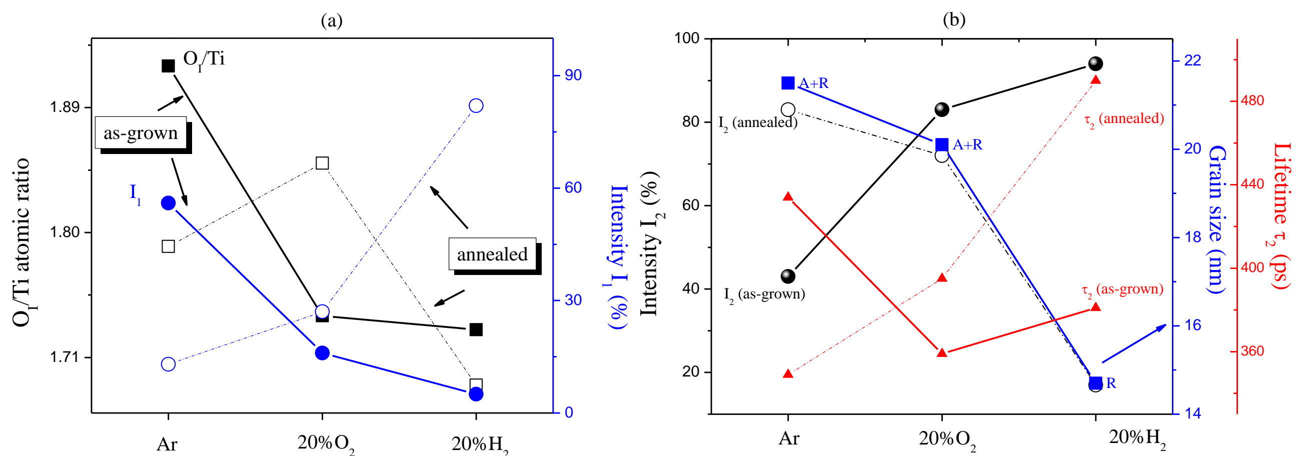

Figure 8.7 (a) O_I/Ti atomic ratios and intensity I_1 corresponding to lifetime τ_1 and (b) Intensity I_2 corresponding to lifetime τ_2 and grains dimension for as-grown and post-growth annealed in vacuum TiO_2 films prepared in various atmospheres (the lines are used only to guide the eye)

8.3 Extrinsically-doped TiO_2

8.3.1 Structural vacancies in as-grown films

The dependence of *S* parameter on positron energy implantation *E* for Nb-TiO_2 film prepared in Ar plasma is shown in Figure 8.8. The concentration of Nb in this film was 5 at.%, measured with XPS. The S_{bulk} value determined for this film (S_{bulk}=0.887) is higher than the S_{bulk} value in TiO_2 film, prepared in Ar plasma (S_{bulk}=0.879), indicating more open volumes after the Nb introduction in the lattice. The chemical formula obtained for this sample was $Ti_{1-0.11}Nb_{0.16}O_2$ and for as-grown TiO_2 sample prepared in the same conditions the stoichiometric ratio O_I/Ti was 1.93.

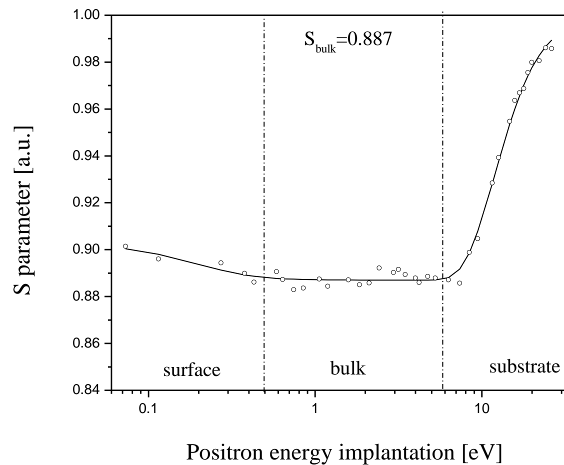

Figure 8.8 *S-E* curve for as-grown Nb-TiO_2 film prepared in Ar plasma, the solid lines represent a fit by VEPFIT;

The positron lifetime components τ_1, τ_2 and τ_3 and their related intensities I_1, I_2 and I_3 as a function of the positron implantation energy for the Nb-TiO_2 film prepared in Ar plasma was measured, shown in Figure 8.9. The obtained lifetime values correspond to typical lifetime values for amorphous TiO_2 [2].

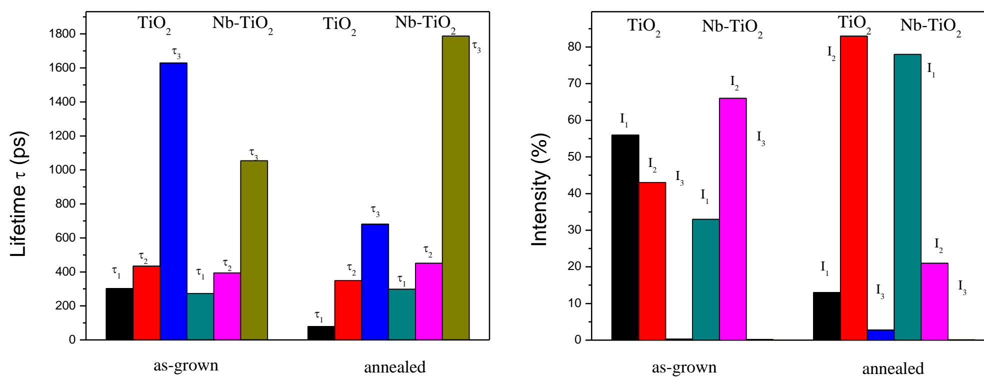

Figure 8.9 Lifetime and intensity values for as-grown and annealed TiO_2 and Nb-TiO_2 films prepared in Ar plasma

The obtained values for the bulk region are: τ_1=273 ps with I_1=33%, τ_2=394 ps with I_2=66%, τ_3=1054 ps with I_3=0.2% and are plotted in Figure 8.9. A decrease in I_1 value is observed after the introduction of Nb in TiO_2 lattice (from 56% in TiO_2 film to 33% in Nb-TiO_2 film), indicated to correspond to a decrease in the oxygen vacancies relative number.

τ_2 value is decreasing in Nb-TiO_2 film (from 434 ps in TiO_2 film to 394 ps in Nb-TiO_2 film) indicating a lower density of interface/grain boundary in Nb-TiO_2 film. The corresponding intensity I_2 is increasing when

Nb is introduced in TiO_2 structure (from 43% in TiO_2 film to 66% in Nb-TiO_2 film). A lower value for τ_3 lifetime component is observed for Nb-TiO_2 film prepared in Ar plasma, comparing with τ_3 lifetime value corresponding to pure-TiO_2 film prepared in Ar plasma (τ_3=1630 ps for TiO_2 film and τ_3=1054 ps for Nb-TiO_2 film).

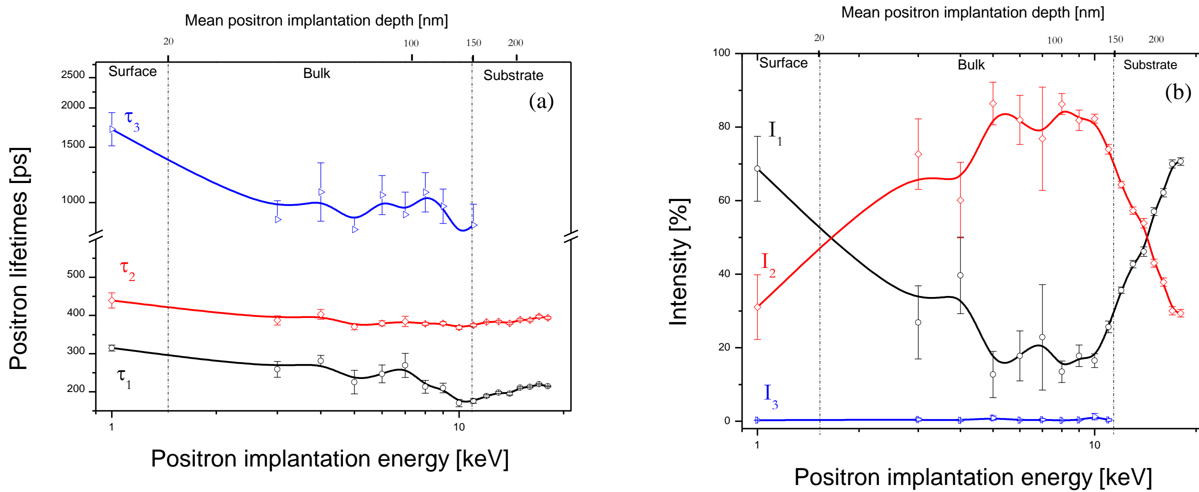

Figure 8.10 (a) The mean positron lifetime profiles and (b) intensities for as-grown Nb-TiO_2 sample obtained in Ar plasma

8.3.2 Structural vacancies in post-growth annealed films

The dependence of *S* parameter on positron energy implantation *E* for post-growth annealed in vacuum Nb-TiO_2 film prepared in Ar plasma is shown in Figure 8.11. After annealing S_{bulk}=0.881, remaining approximately the same like in the as-grown film. For annealed TiO_2 film, S_{bulk} is smaller (S_{bulk}=0.877),

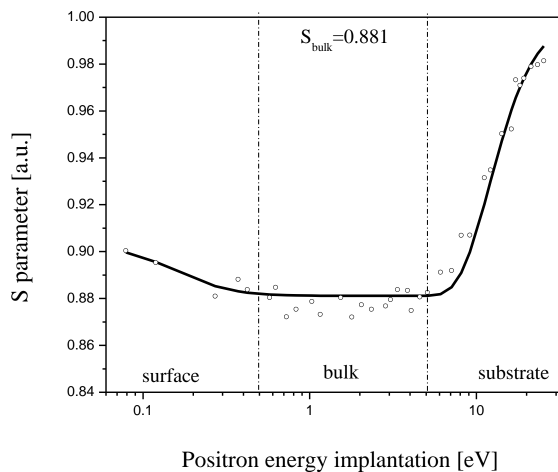

Figure 8.11 *S-E* curve for post-growth annealed Nb-TiO_2 film prepared in Ar plasma, the solid lines represent a fit by VEPFIT;

indicating less open volumes.

The positron lifetime values τ_1, τ_2 and τ_3 and their related intensities I_1, I_2 and I_3 were measured for a given positron implantation energy corresponding to the bulk region (2-4 *keV*), determined from *S* curves. The obtained values are given in Table 8.2 (τ_1=298 ps with I_1=78%, τ_2=451 ps with I_2=21%, τ_3=1788 ps with I_3=0.1%) and plotted in Figure 8.12 together with the positron lifetime values τ_1, τ_2 and τ_3 and their related intensities I_1, I_2 and I_3 for as-grown Nb-TiO_2 film deposited in Ar plasma.

After annealing, I_1 value associated with the vacancies in material is increasing (from 33% for as-grown to 78% for annealed). τ_2 value is increasing in annealed Nb-TiO_2 film (from 394 ps in as-grown film to 451 ps in annealed film) and the corresponding I_2 value is decreasing after annealing (from 66% in as-grown film to 21% annealed film) indicating a lower density of interface/grain boundary. The result is confirmed by XRD measurements, where it was observed that the amorphous as-grown Nb-TiO_2 film became polycrystalline (anatase+rutile) after annealing in vacuum, with grain dimensions of ~22 nm.

In conclusion, the Nb addition in TiO_2 films indicates more open volumes, an increase in the relative number of oxygen vacancies and a lower density of interface/grain boundary. After annealing in vacuum, no considerable changes in the open volume nature are observed and the number of oxygen vacancies is increasing, while the density of interface/grain boundary is decreasing.

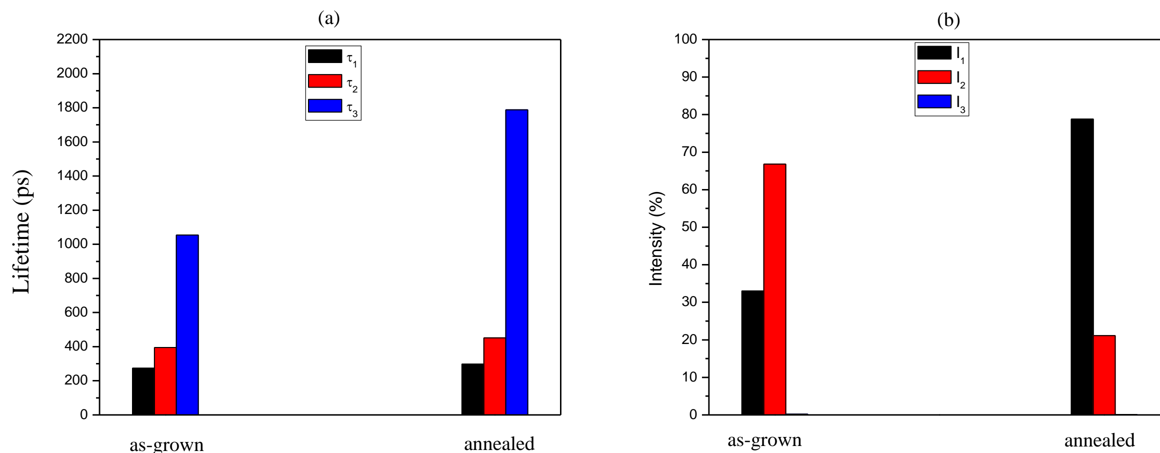

Figure 8.12 (a) The positron lifetime values τ_1, τ_2 and τ_3 and (b) their related intensities I_1, I_2 and I_3 for post-growth annealed Nb-TiO_2 film obtained in Ar plasma

8.4 Intrinsically-extrinsically co-doped TiO_2

8.4.1 Structural vacancies in as-grown films

The dependence of *S* parameter on positron energy implantation *E* for as-grown Nb-TiO_2 films prepared in Ar-O_2 (20%O_2) and Ar-H_2 (20%H_2) atmospheres are shown in Figure 8.13 together with the film prepared in

Ar plasma. The concentration of Nb in the film prepared in Ar-O_2 atmosphere was ~4.5 at.% and for the film prepared in Ar-H_2 was ~10.5 at.%, measured with XPS.

A decrease in S_{bulk} value as compared to the film prepared in Ar plasma is observed for the sample prepared in Ar-O_2 plasma, indicating less open volumes in the film and an increase in the case of the sample prepared in Ar-H_2 gas mixture, indicating more open volumes.

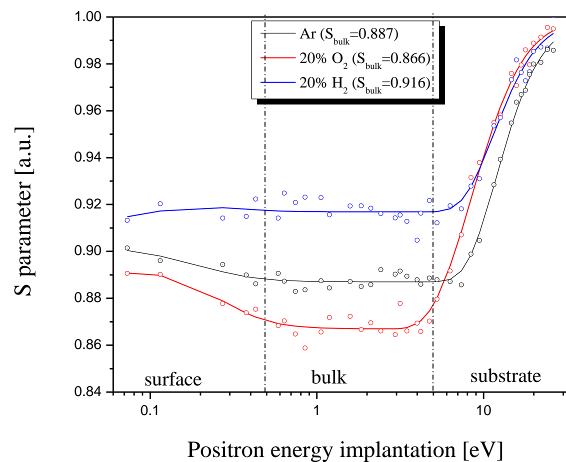

Figure 8.13 *S-E* curves for as-grown Nb-TiO_2 films in Ar, Ar-O_2 (20%O_2) and Ar-H_2 (20%H_2) atmospheres, the solid lines represent a fit by VEPFIT

The positron lifetime values τ_1, τ_2 and τ_3 and their related intensities I_1, I_2 and I_3 were measured for a given positron implantation energy corresponding to the bulk region (2-4 *keV*) in as-grown Nb-TiO_2 films prepared in Ar-O_2 and Ar-H_2 atmospheres. The obtained values are plotted in Figure 8.15.

When O_2 is used in Ar plasma while depositing Nb-TiO_2 films, τ_1 value is decreasing (from 273 ps in Ar plasma to 63 ps in Ar-O_2 plasma) and the corresponding intensity I_1 is decreasing (from 33% in Ar plasma to

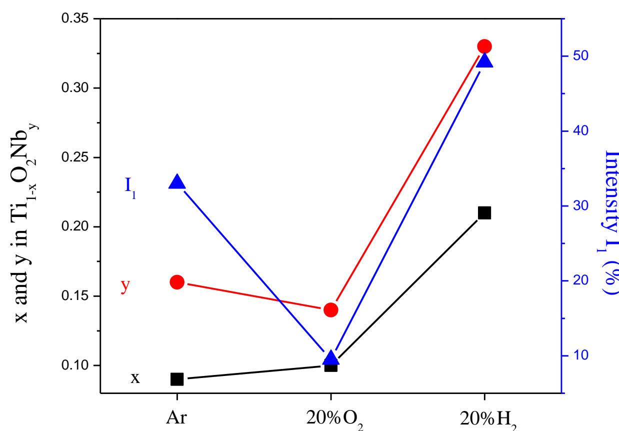

Figure 8.14 x and y in $Ti_{1-x}O_2Nb_y$ and intensity I_1 corresponding to lifetime τ_1 for as-grown Nb-TiO_2 films prepared in various atmospheres (the lines are only to guide the eye)

9.5% in Ar-O_2 plasma), indicating a decrease in the number of vacancies in material (Figure 8.14). τ_2 value is decreasing (from 394 ps in Ar plasma to 357 ps in Ar-O_2 plasma) and the corresponding intensity I_2 is increasing (from 60% in Ar plasma to 90% in Ar-O_2 plasma). Both films show an amorphous structure in the XRD patterns.

For H_2 added in Ar plasma while depositing Nb-TiO_2 films τ_1 value is increasing (from 273 ps in Ar plasma to 330 ps in Ar-H_2 plasma) and the corresponding intensity I_1 is increasing (from 33% in Ar plasma to 49% in Ar-H_2 plasma), indicating an increase in the number of vacancies, in agreement with the chemical formula for this film (Figure 8.14). τ_2 value is increasing (from 394 ps in Ar plasma to 474 ps in Ar-H_2 plasma) and the corresponding intensity I_2 is decreasing (from 66% in Ar plasma to 50% in Ar-H_2 plasma) indicating a lower density of interface/grain boundary. Both films show an amorphous structure in the XRD patterns.

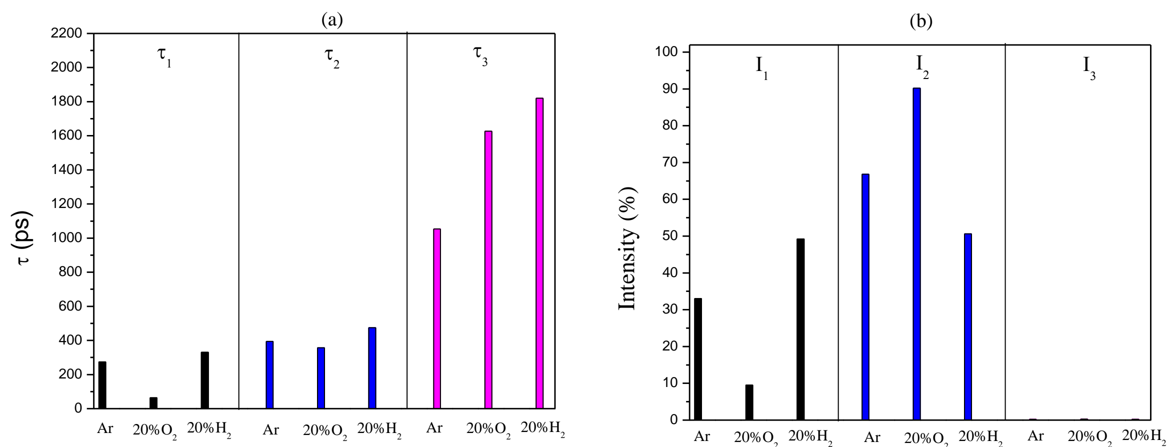

Figure 8.15 (a) The positron lifetime values τ_1, τ_2 and τ_3 and (b) their related intensities I_1, I_2 and I_3 for as-grown Nb-TiO_2 films obtained in Ar, Ar-O_2 and Ar-H_2 plasmas

8.4.2 Structural vacancies in post-growth annealed films

After post-growth annealing in vacuum performed for Nb-TiO_2 films prepared in Ar-O_2 and Ar-H_2 atmospheres, the S- and W-parameter curves were measured. The dependence of *S* parameter on positron energy implantation *E* for both type of films are shown in Figure 8.16.

After annealing in vacuum, the S_{bulk} values for the samples prepared in Ar-O_2 and Ar-H_2 atmospheres are S_{bulk}=0.882 for Ar-O_2 plasma and S_{bulk}=0.874 for Ar-H_2 plasma. The lower value for the sample prepared in Ar-H_2 plasma indicates a lower number of open volumes in this film as compared to the film prepared in Ar-O_2.

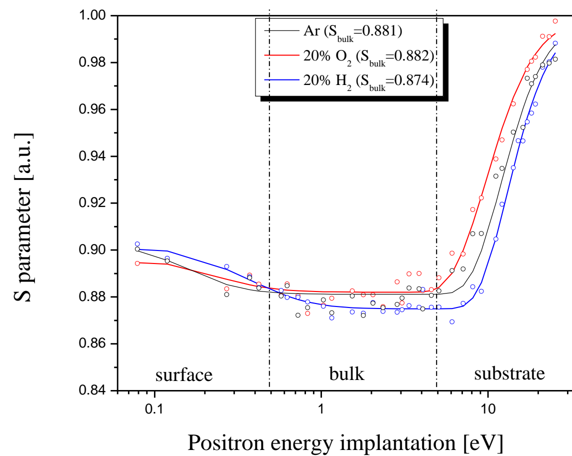

Figure 8.16 *S-E* curves for annealed Nb-TiO_2 films prepared in Ar, Ar-O_2 (20%O_2) and Ar-H_2 (20%H_2) atmospheres, the solid lines represent a fit by VEPFIT

For the sample prepared with oxygen added in Ar plasma the S_{bulk} value is increasing after annealing in vacuum, indicating more open volumes in the film. When hydrogen is used in Ar plasma during the deposition of Nb-TiO_2, after post-growth annealing in vacuum the S_{bulk} value is decreasing, indicating less open volumes in the film after annealing in vacuum.

The positron lifetime values τ_1, τ_2 and τ_3 and their related intensities I_1, I_2 and I_3 were measured for a given positron implantation energy corresponding to the bulk region (2-4 *keV*) in the post-growth annealed in vacuum Nb-TiO_2 films. The obtained values are plotted in Figure 8.17.

Similar values for τ_1 lifetime were obtained after annealing in vacuum of Nb-TiO_2 films (298 ps in Ar plasma, 322 ps in Ar-O_2 plasma and 300 ps in Ar-H_2 plasma), indicating the same nature of the defects in all

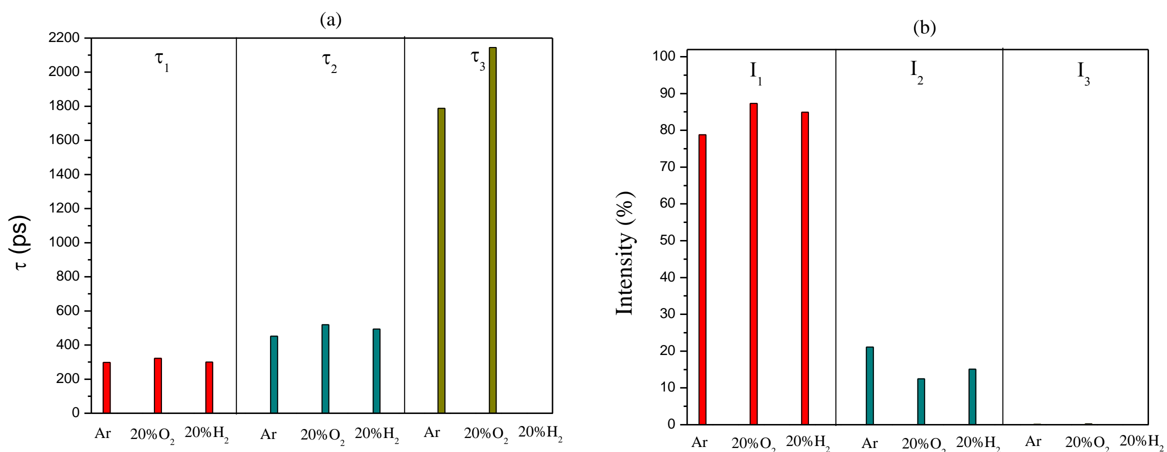

Figure 8.17 (a) The positron lifetime values τ_1, τ_2 and τ_3 and (b) their related intensities I_1, I_2 and I_3 for post-growth annealed in vacuum Nb-TiO_2 films obtained in Ar, Ar-O_2 and Ar-H_2 plasmas

the films. The corresponding intensity I_1 is increasing after annealing for both Nb-TiO_2 films prepared in Ar-O_2 and Ar-H_2 plasma (78% in Ar plasma, 87% in Ar-O_2 plasma and 84% in Ar-H_2 plasma), indicating an increase in the number of oxygen vacancies (Figure 8.18 (a)), in agreement with the chemical formula determined for these films ($Ti_{1-0.11}Nb_{0.21}O_2$ for the film prepared in Ar-O_2 plasma and $Ti_{1-0.38}Nb_{0.42}O_2$ for the film prepared in Ar-H_2 plasma).

τ_2 lifetime value is increasing after annealing in vacuum for Nb-TiO_2 film prepared in Ar-O_2 (451 ps in Ar plasma and 519 ps in Ar-O_2 plasma) and the corresponding intensity I_2 is decreasing (from 21% in Ar plasma to 12.5% in Ar-O_2 plasma). After annealing in vacuum, the XRD patterns reveal the mixed anatase-rutile phases for the film prepared in Ar plasma and only the anatase phase for the film prepared in Ar-O_2 plasma. When H_2 is added in Ar plasma, τ_2 lifetime value is slightly increasing after annealing in vacuum for Nb-TiO_2 film prepared in Ar-O_2 (451 ps in Ar plasma and 493 ps in Ar-H_2 plasma) and the corresponding intensity I_2 is also decreasing (from 21% in Ar plasma to 15% in Ar-H_2 plasma). XRD measurements reveal the anatase phase for this film. The decrease of I_2 is not correlated with the decrease in grain size (Figure 8.18 (b)).

In conclusion, after annealing in vacuum, both films prepared in Ar-O_2 and Ar-H_2 gas mixtures indicates the same nature of defects in the films and an increased number of oxygen vacancies. More open volumes were observed in the annealed Nb-TiO_2 film prepared in Ar-O_2 gas mixture, while in the film prepared in Ar-H_2 gas mixture less open volumes were observed.

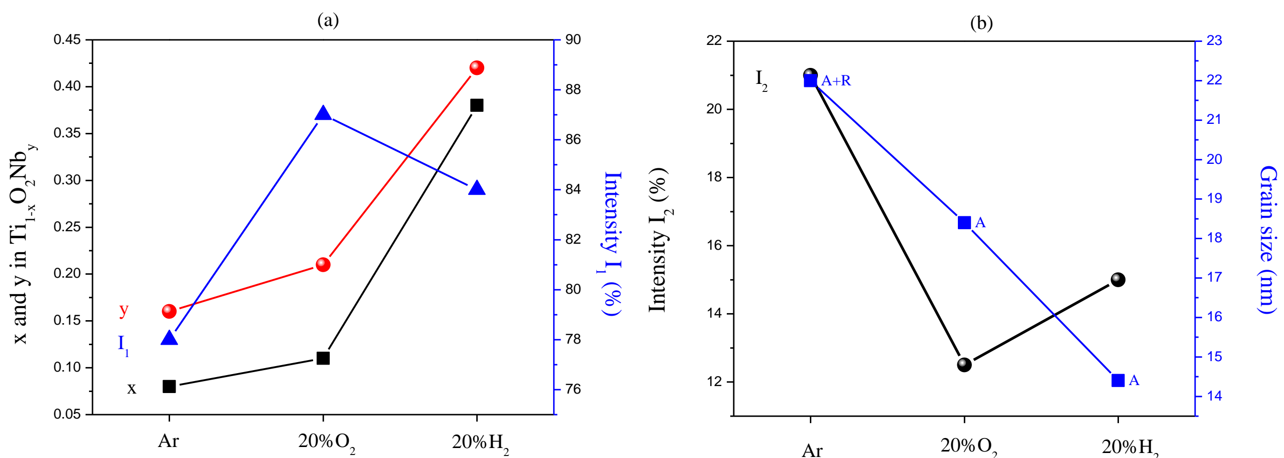

Figure 8.18 (a) x and y in $Ti_{1-x}O_2Nb_y$ and intensity I_1 corresponding to lifetime τ_1 and (b) Intensity I_2 corresponding to lifetime τ_2 and grain dimensions for post-growth annealed in vacuum Nb-TiO_2 films prepared in various atmospheres (the lines are only to guide the eyes)

8.5 S-W plot

To identify the different positron trapping sites, the correlation between S- and W-parameters for the samples was also investigated. This plot can provide complementary information on the defects, and is usually used to verify the change of defect species or the chemical surrounding of the defects. The S-parameter versus W-parameter graph is shown in Figure 8.19.

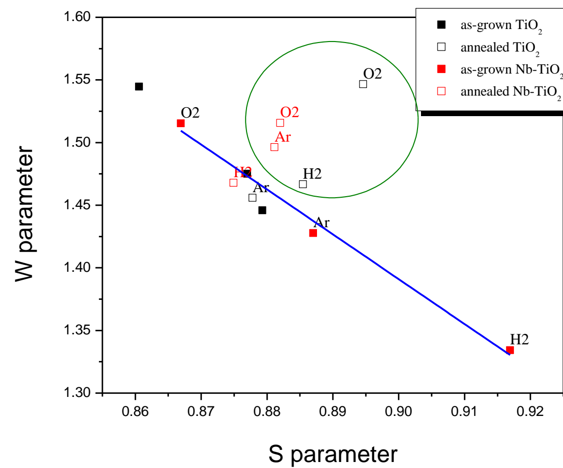

Figure 8.19 S-W plot for as-grown in various atmospheres and annealed TiO_2 and Nb-TiO_2 films

All the data points for as-grown TiO_2 and Nb-TiO_2 films were concentrated on a straight line, together with the annealed TiO_2 film prepared in Ar plasma and Nb-TiO_2 prepared in Ar-H_2 gas mixture. It can be concluded that these films contain positron trapping defects of the same type. The same conclusion cannot hold for the defects in TiO_2 and Nb-TiO_2 films grown in Ar-O_2 and Ar-H_2 plasma. Practically all the data points for the films deposited in Ar-O_2 and Ar-H_2 and annealed deviate from the linear fit, while all the as-grown films, whatever is the gas mixture used to create the plasma during deposition and the presence or absence of Nb incorporated, are well aligned to the linear fit. As annealing is expected to free the originally passivated vacancies from OH and H groups chemically bound or H_2O and O_2 physisorbed molecules, this could generate a variation of the electronic environment of these vacancies, as the plot indicates.

8.6 Concluding remarks

The structural vacancies in TiO_2 films deposited in Ar, Ar-O_2 and Ar-H_2 gas mixtures were investigated. When the film is deposited in Ar-O_2 gas mixture, less open volumes were detected as compared to the film prepared in Ar plasma. In the case of the film deposited in Ar-H_2 gas mixture, also a decrease in the open volume density was observed, but less than in the case of the film prepared in Ar-O_2, most probably due to the formation of Ti-OH bonds. After annealing in vacuum at 900°C, more open volumes were detected for both films prepared in Ar-O_2 and Ar-H_2. The lifetime values observed in the films prepared in Ar-O_2 and Ar-H_2 gas mixtures were attributed to oxygen vacancies, while for the film prepared in Ar plasma were attributed to vacancy-impurity complex. A passivation of the oxygen vacancies in the films prepared in Ar-O_2 and Ar-H_2 was observed. After annealing in vacuum at 900°C, the lifetime values variation indicates the desorption of O_2 in the V-impurity complex for the film prepared in Ar and the formation of divacancies in the films prepared in Ar-O_2 and Ar-H_2.

For the Nb-TiO_2 film deposited in Ar plasma, a higher open volume density, an increase in the relative number of oxygen vacancies and a lower density of interface/grain boundary were observed comparing with the TiO_2 film prepared in Ar plasma. After annealing in vacuum, no considerable changes in the open volume density is observed and the number of oxygen vacancies is increasing, while the density of interface/grain boundary is decreasing.

The structural analysis of the as-grown Nb-TiO_2 films prepared in Ar-O_2 gas mixture indicates less open volumes and a smaller relative number of oxygen vacancies as compared to the as-grown Nb-TiO_2 film prepared in Ar plasma, while the one prepared in Ar-H_2 plasma indicates more open volumes and a higher number of oxygen vacancies. After annealing in vacuum, both films prepared in Ar-O_2 and Ar-H_2 gas mixtures indicates the same nature of defects in the films and an increased number of oxygen vacancies. More open volumes were observed in the annealed Nb-TiO_2 film prepared in Ar-O_2 gas mixture, while in the film prepared in Ar-H_2 gas mixture less open volumes were observed.

8.7 References

1. P.G. Coleman, N.B. Chilton, J.A. Baker, J. Phys.: Condens. Matter 2 (1990) 9355
2. H. Murakami, N. Onizuka, J. Sasaki, N. Thonghai, Journal of Materials Science 33 (1998) 5811 – 5814
3. Misheva et al., Thin Solid Films 283 (1996) 26
4. E. M. Hassan et al., Defect and Diffusion Forum Vols. 319-320 (2011) pp 151-159

9. Doping of ZnO films deposited in Ar-H_2 plasma by intrinsic defects

The structural and physical properties of intrinsically-doped ZnO thin films deposited by RF sputtering were studied. Pure-Ar and Ar-H_2 at various concentrations were used to grow the films on *n*-type Si (100) wafers and glass without external heating. The plasma chemical species were followed by optical emission spectroscopy (OES). X-ray photoelectron spectroscopy (XPS) and ATR-FTIR (Attenuated Total Reflection Fourier-Transformed Infrared) spectroscopy were used to study the bulk and surface chemical composition of the films, X-ray Diffraction (XRD) analysis allowed lattice structure and grain size determination while samples morphology was checked with a scanning electron microscope (SEM). The films were also characterized for their electrical and optical properties.

Contents

9.1 Introduction
9.2 Film growth rate in Ar-H_2 plasma
9.3 H_2 effect on the film chemical composition
9.4 H_2 effect on the film structural properties
9.5 H_2 effect on the plasma composition
9.6 H_2 effect on the film electrical properties
9.7 H_2 effect on the film optical properties
9.8 Concluding remarks
9.9 References

9.1 Introduction

Unintentional levels of *n*-type conductivity in ZnO, historically attributed to native point defects like interstitial zinc (Zn_i), Zn-on-O antisite (Zn_O) and oxygen vacancies (V_O) [1], has recently been attributed to extrinsic impurities, H in particular [2,3]. The realization that hydrogen can act as an electrically active impurity in ZnO has significant consequences for device development. Understanding hydrogen incorporation role in the determination of ZnO thin films properties becomes a crucial step for its application as transparent conductive oxide (TCO).

Zinc oxide thin films were deposited by RF sputtering in Ar-H_2 plasma at different H_2 concentrations (0-50%) from a pure ZnO target, without external heating. The influence of hydrogen addition in Ar plasma on the oxide growth process and on its electrical properties was investigated.

9.2 Film growth rate in Ar-H_2 plasma

The growth rates were determined for ZnO films prepared in different Ar-H_2 atmospheres and are shown in Figure 9.1. As can be observed, when H_2 is added in discharge, the growth rate is decreasing. The highest value of growth rate was obtained in pure-Ar plasma (4.27±0.32 *nm/min*).

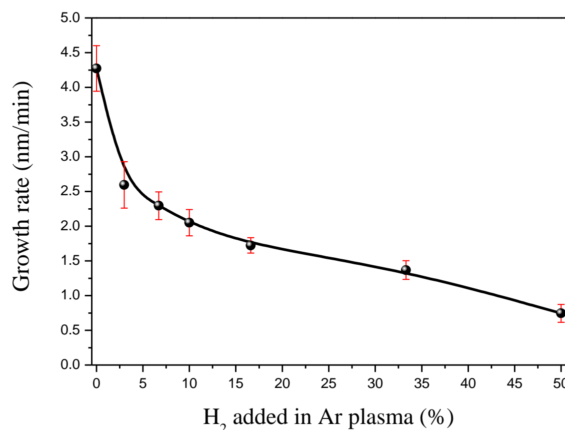

Figure 9.1 Growth rates for ZnO films deposited in Ar-H_2 atmospheres, at different concentrations of H_2 in Ar plasma

9.3 Hydrogen effect on the film chemical composition

XPS measurements were performed for ZnO thin films prepared in Ar-H_2 atmosphere. A closer examination of the Zn $2p_{3/2}$ and O *1s* photoemission lines revealed that a contamination of the pure oxide surface by hydroxyl-terminated Zn atoms develops when hydrogen is added to the sputtering gas.

Details of Zn *2p* and O *1s* core line deconvolution are showed in Figure 9.2. Zn $2p_{3/2}$ peak was fitted with two components: the first located at 1021.4 *eV* corresponding to zinc bound to oxygen in the zinc oxide lattice and the second, shifted by 1.1 *eV* towards high binding energies with respect to the first component, attributed to zinc hydroxide, situated at 1022.6 *eV* [4,5]. As for the O *1s* core line, the main component at 530.2 *eV* is attributed to oxygen linked to Zn in the zinc oxide lattice. The second component, placed at 531.2 *eV*, corresponds to oxygen in the zinc hydroxide contamination; finally components #3 and #4 at higher BEs (532 *eV* and 532.6 *eV* respectively) are associated with either adsorbed molecular H_2O or C-O bondings like O-C-O or O=C-O [4,6].

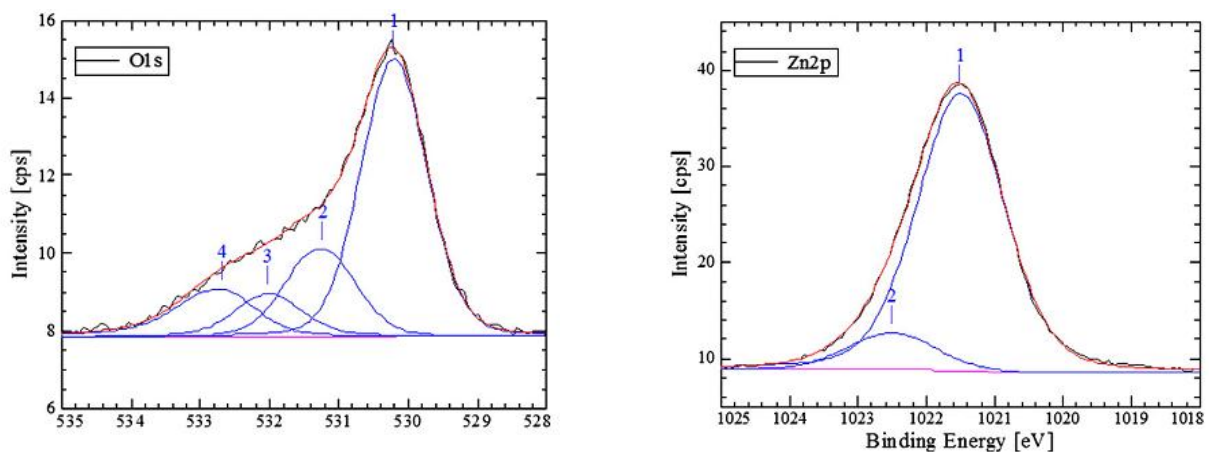

Figure 9.2 XPS core lines of Zn $2p_{3/2}$ and O *1s* corresponding to ZnO thin film deposited in Ar-H_2

The stoichiometry of ZnO films was investigated. In Figure 9.3 the O/Zn atomic ratio is plotted as a function of the hydrogen quantity introduced in Ar plasma during the deposition of ZnO films. In pure-Ar the O/Zn ratio is close to the stoichiometric value (O/Zn=0.96). The addition of H_2 in discharge leads to a decrease until a value of O/Zn=0.66 for 3%H_2. A minimum of O/Zn ratio is observed at 16%H_2 (O/Zn=0.57), followed by an increase for further increase of H_2 content in discharge. Two regions were delimited in Figure 9.3 (named I and II) and further explanations on the stoichiometric ratio behavior with the hydrogen concentration added in the gas mixture are given in the next sections of this chapter.

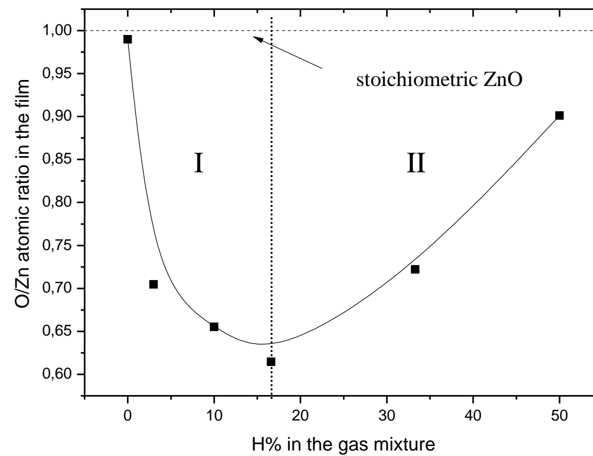

Figure 9.3 O/Zn atomic ratio for ZnO films as a function of H_2 added in Ar plasma

9.4 Hydrogen effect on the film structural properties

XRD diffraction patterns performed for ZnO thin films prepared in Ar-H_2 atmosphere showed that all the films crystallized in the characteristic hexagonal würtzite type phase of ZnO, independently on the gas mixture used in the sputtering process.

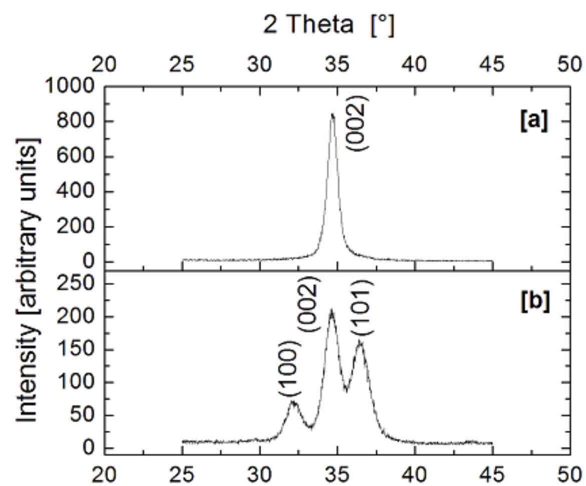

Figure 9.4 Diffraction patterns of ZnO films deposited in pure Ar [a]
and in Ar-H_2 plasma (10% H_2) [b]

Nevertheless, as can be seen from the X-ray Diffraction patterns presented in Figure 9.4, while samples deposited in pure Ar plasma present a preferred orientation along the (002) axis, the ZnO films sputtered in Ar-H_2 atmosphere exhibits multiple growth directions. Three distinct peaks appear at $2\Theta = 32.2°$, $34.6°$ and $36.4°$ which correspond to (100), (002) and (001) directions of the hexagonal ZnO structure [6].

Films crystallinity is affected as well when hydrogen is introduced in discharge. Crystallites size values (D), calculated according to the Scherrer's equation, are plotted in Figure 9.5 showing that even little hydrogen addition in the sputtering gas is sufficient to observe a decrease in the grains dimension. For the film prepared in Ar plasma $D \sim 16$ nm, while for 3%H_2 added in Ar plasma $D \sim 7$ nm, without major changes when increasing the hydrogen concentration in the gas mixture.

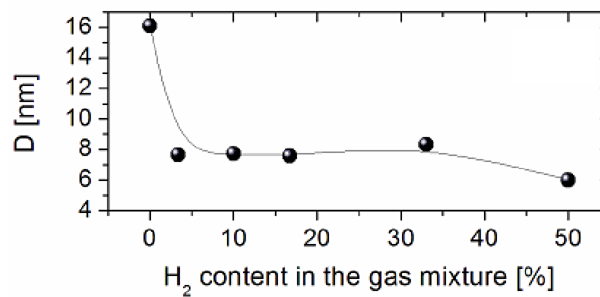

Figure 9.5 Variation of the crystallites dimension versus the H_2 added in Ar plasma

The scanning electron images presented in Figure 9.6 closely reflect the above described structural changes. Films deposited in pure Ar discharges show a rather rough surface with large grains. On the contrary, a smoother surface profile is obtained when hydrogen is present in the gas mixture, with grains of visibly reduced dimensions.

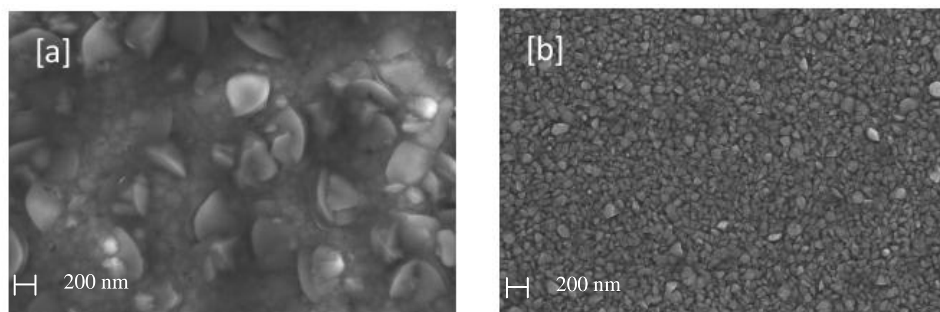

Figure 9.6 Top-view images of ZnO films deposited in Ar [a] and in Ar-H_2 plasma (10% H_2) [b]

9.5 Hydrogen effect on the plasma composition

Various plasma chemical species were monitored by Optical Emission Spectroscopy (OES) as a function of the different hydrogen concentrations added in Ar plasma. In Figure 9.7 a typical spectrum acquired during the sputtering of ZnO films in Ar-H_2 plasma is shown. We can observe in particular the emission signals for Ar, OH, Zn(I) and H (spectral lines of the Balmer series H_β at 486.1 *nm* and H_α at 656.5 *nm*) [7,8]. In Table 9.1 the identified spectral lines and bands are listed. Oxygen emission lines in its atomic or ionic states have not been detected.

The emission line of Zn(I) at 481 *nm* showed only small intensity fluctuations when varying hydrogen concentration in the plasma. On the contrary, significant variations in OH and H_α signals were observed in function of the Ar-H_2 ratio in the gas mixture, as can be seen from the Figure 9.8. The two lines present quite an opposite trend. In particular, H_α line intensity constantly increases with increasing hydrogen concentration in Ar plasma, while OH signal reaches a maximum at 3%H_2 and then decreases. Two regions can be identified in Figure 9.8 (named I and II), similar to the graph corresponding to the stoichiometric ratio O/Zn.

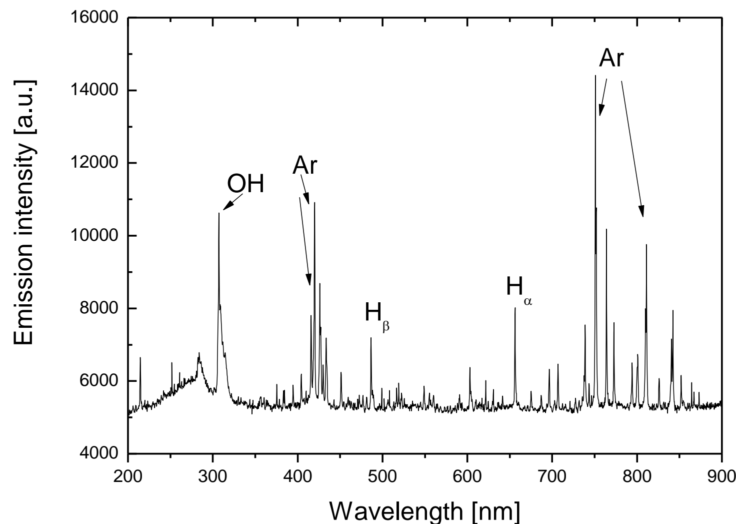

Figure 9.7 OES spectrum from RF sputtering discharge of a ZnO target in Ar-H_2 [10%]

Table 9.1 Identified OES spectral lines and bands in the deposition plasma of ZnO

Species	λ (nm)	Transition	
H	656.3	3d-2p	H_α
	486.1	4d-2p	H_β
Ar	811.5	4p-4s	
	750.4	4p’-4s’	
Zn	481.05	4s4p $^3P_2$ - 5s $^3S_1$	Zn(I)
OH	306	$A^2\Sigma – X^2\Pi$	

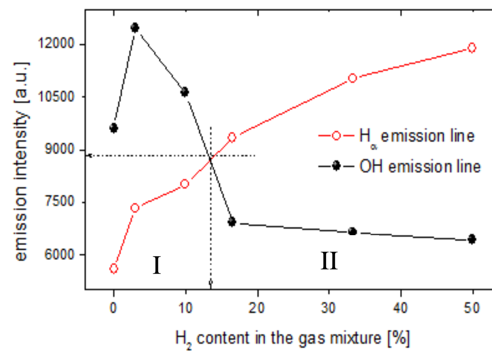

Figure 9.8 OH and H_α lines intensities variation as a function of H_2 in Ar-H_2 plasma

The detection of OH signal in pure-Ar plasma is normally attributed to water vapor present in the plasma, coming mainly from the reactor walls. On the other hand, such OH source cannot account for the above described trend, which is actually a sign of more complex reactions involved in the sputtering process in the presence of hydrogen.

An explanation can be drawn on the base of the results of a recent investigation on RF Ar-H_2 glow discharges performed in the same experimental conditions by Laidani *et al.* [9]. They got evidences that a pure physical sputtering of an unaltered target is not representative of the process in most of the Ar–H_2 plasmas. With hydrogen addition to an Ar discharge new ions are likely to be created, besides Ar^+: ArH^+ and hydrogenic ions such as H_2^+, H_3^+ and H^+. While Ar^+ density was found to decrease as a function of H_2 addition to the plasma, as one could expect, that of ArH^+ rises sharply to a maximum for very low concentrations of H_2 (only 3%), and then decreases like Ar^+. The effect on the sputtering process is substantial. In particular it was proved that the sputtering of the target in the 3-16% H_2 range is mainly driven by ArH^+ ions which determine a reduction of the cathode: the process can be defined in this case as a reactive sputtering. For higher hydrogen concentration the discharge is characterized on the contrary by high density of hydrogenic ions which do not provoke a chemical composition change in the target but provide chemical assistance at the sputtering process by Ar^+ ions.

The above explained model fits with the observed trends of the discharge species, as shown in Figure 9.8. At low hydrogen concentrations in fact, ArH^+ ions can lead to a reduction of the ZnO target through oxygen atoms displacement in the form of OH species. As a consequence the OH line emission intensity is found to sharply increase. On the other hand, when hydrogen is added in higher concentration in the gas mixture (above 16%) the sputtering process becomes gradually driven by Ar^+ ions. This causes the observed reduction of the OH line signal.

9.6 Hydrogen effect on the film electrical properties

The conductivity of ZnO thin films was measured by a four-point probe. In Figure 9.9 the evolution as a function of the hydrogen content in Ar plasma is shown. A pronounced change in the films electrical behaviour with increasing H addition is evident from data shown in the plot. In particular, films deposited in pure Ar and with low H_2 concentration in the plasma were found to be perfectly insulating. Measurable conductivity values were on the other hand obtained when hydrogen percentage exceeded the 6%. Above this concentration threshold ZnO conductivity increases, entering the values range typical of metallic materials.

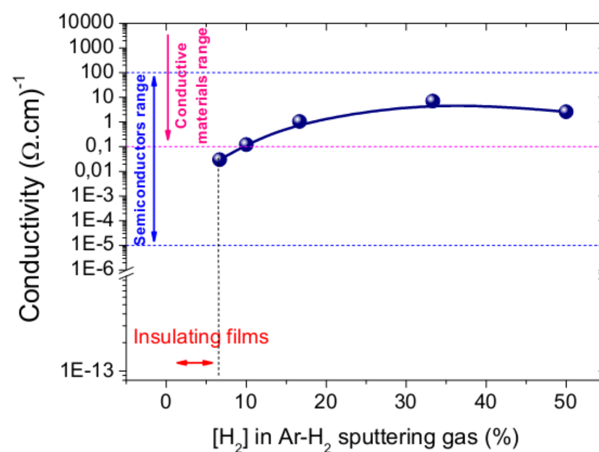

Figure 9.9 ZnO films conductivity variation in function of hydrogen concentration in the gas mixture

In Figure 9.10 the obtained conductivity was plotted as a function of the OH and H_α emission intensities. This allows us to describe the ZnO films electrical behavior with respect to the sputtering process variations induced by H addition in the plasma.

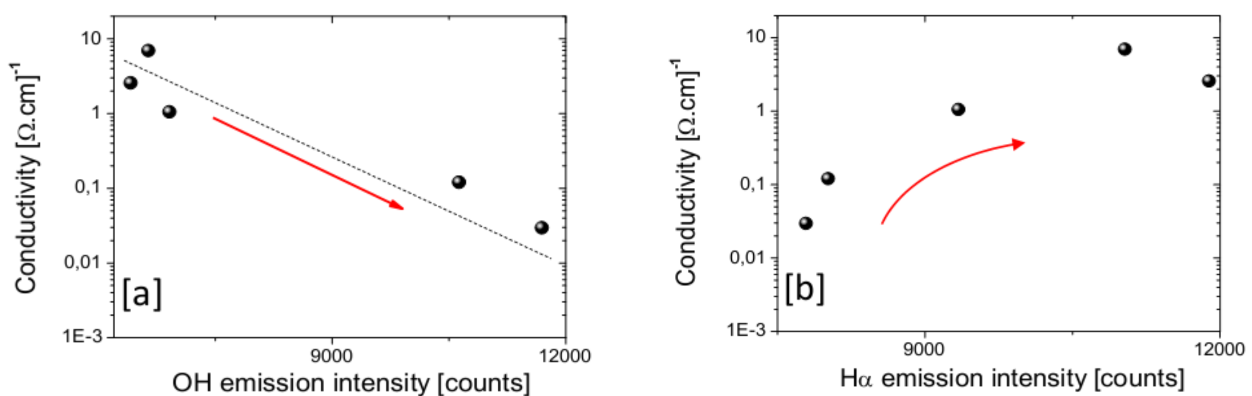

Figure 9.10 ZnO films conductivity variation versus OES H_α (a) and OH (b) signal intensity

As can be seen, an inverse dependence of films conductivity on the OH and H_α plasma species was obtained. In particular, the conductivity enhancement scales with the increase in the atomic hydrogen signal. An opposite trend is found versus OH signal variation. In other words, ZnO films conductivity appears to be related to the increase of atomic hydrogen radicals formed in the plasma as a consequence of hydrogen addition in the gas mixture.

A correlation was found between conductivity of ZnO films and the chemical structure. ZnO contamination by OH species was measured with XPS and IR spectroscopy. An example of a FTIR spectra corresponding to C–H and O–H stretching bands measured on ZnO films is shown in Figure 9.11.

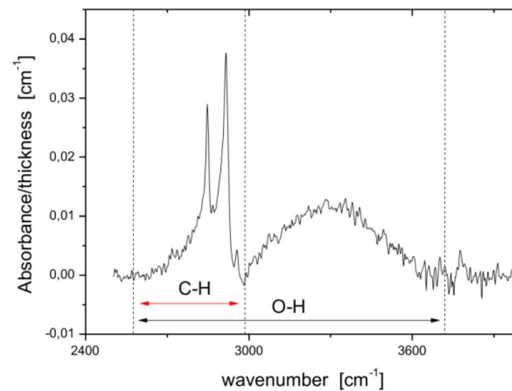

Figure 9.11 FTIR spectra corresponding to C–H and O–H stretching bands measured on ZnO films

In Figure 9.12 (a) the conductivity is plotted versus the amount of Zn involved in Zn-OH bonds, derived by the deconvolution of XPS Zn *2p* core line and in Figure 9.12 (b), the conductivity is drawn versus the estimated amount of hydrogen involved in OH bonds in the films, as derived from IR OH band integration. In both cases a correspondence is found between the development of hydroxyl groups and the improvement of the electrical properties of the films.

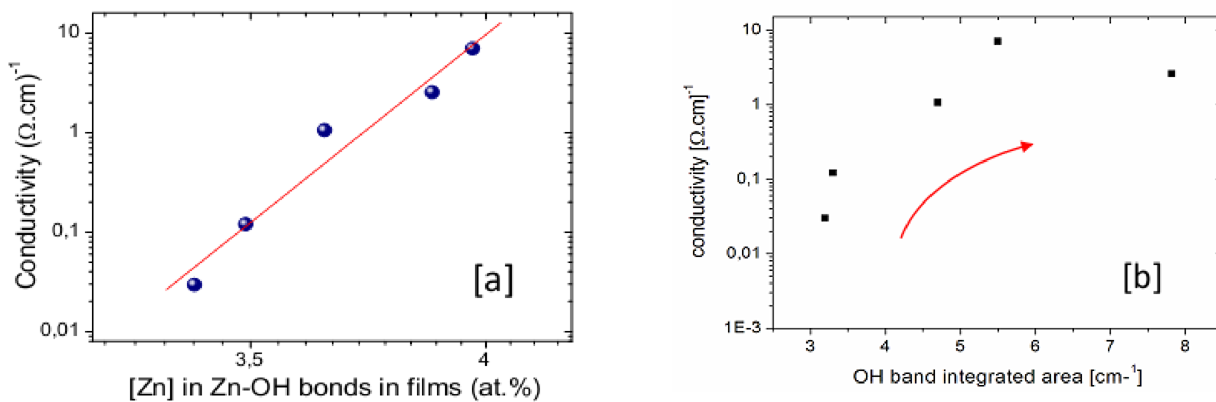

Figure 9.12 ZnO films conductivity as a function of the percentage of Zn involved in OH bonds, determined from XPS data [a] and as a function of the OH band integrated area from ATR-FTIR [b]

If we consider this result in combination with what obtained from OES (Figure 9.8), a conclusion can be drawn: the electrical conductivity, which is observed in ZnO films for H_2>6%, finds a correlation with intentional hydrogen incorporation in the crystal structure, possibly in the form of hydroxide species. The real nature of the electrically active defects induced in ZnO structure through OH bond formation is still under investigation.

9.7 Hydrogen effect on the film optical properties

A high level of transparency of the films is maintained when hydrogen is added in Ar plasma. In Figure 9.13 the transmittance and absorption coefficient spectra for ZnO films prepared in pure-Ar and when 10% H_2 is added in discharge is shown. A transmittance value of ~80% in the visible region is observed for both ZnO films.

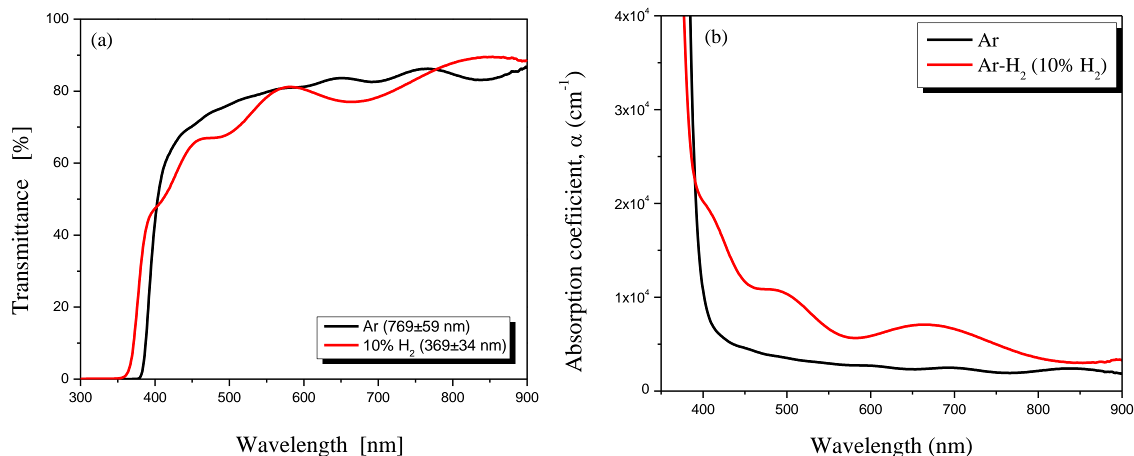

Figure 9.13 (a) Transmittance and (b) absorption coefficient for ZnO thin films prepared in pure-Ar and Ar-H_2 atmosphere (10% H_2)

The band gap of ZnO films prepared in pure-Ar and the one prepared with 10% H_2 added in Ar plasma was determined from the Tauc plot and the corresponding values are 3.08 *eV* and 3.11 *eV* respectively.

9.8 Concluding remarks

By combining XPS, ATR-FTIR and OES data correlations were established between conductivity and its variations with intentional hydrogen incorporation in the crystal structure, detected in the form of hydroxide species.

Optical emission spectroscopy offered a valuable and helpful tool for discerning the alterations in the discharge reactions resulting from different H_2/Ar ratios in the gas mixture. Marked structural and chemical modifications were observed in the films, together with a pronounced change in their electrical behaviour which become conductive for $H_2 > 6\%$. The films transparency was on the other hand maintained.

9.9 References

1. E. V. Lavrov, J. Weber, F. Börrnert, C. G. Van De Walle, R. Helbig, Physical Review B, 66 (2002) 165205
2. C. G. Van De Walle, Phys. Stat. Sol. (b) 229 (1) (2002) 221
3. S. F. J. Cox *et al.*, Physical Review Letters 86, 12 (2001) 2601
4. S. Ben Amor, M. Jacquet, P. Fioux, M. Nardin, Appl. Surf. Sci. 255 (2009) 5052
5. L.S. Dake, D.R. Baer, J.M. Zachara, Surf. Interface Anal. 14 (1989) 71
6. N. Asakuma, T. Fukui, M. Toki, K. Awazu, H. Imai, Thin Solid Films 445 (2003) 284
7. M. Neuhauser, S. Barwulf, H. Hilgers, E. Lugscheider, M. Riester, Surface and Coatings Technology 116-119 (1999) 981
8. N. Joshy, J. Isaac, M.K. Jayarai, Journal of Applied Physics, 103 (2008) 123305
9. N. Laidani, R. Bartali, P.Tosi, M. Anderle, Journal of Physics D : Applied Physics, 37 (2004) 2593

10. Concluding remarks and perspectives

The aim of the work presented in this thesis was a study of the doping processes of thin oxide films, TiO_2 and ZnO, two cheap, chemically stable and non-toxic materials. Two main objectives were pursued in this work: (i) the optimization of the film deposition and doping conditions for a potential replacement of indium tin oxide (ITO) and (ii) the understanding of the factors dominating the doping process as well as the limitations of the latter.

The approach was to explore three doping methods of the films: intrinsic doping, extrinsic doping and, with the aim to combine the benefits of both, intrinsic-extrinsic co-doping. Since the structural defects (such as oxygen vacancies) are at the basis of the intrinsic doping, a control of their formation was searched through the variation of the film growth process conditions. Niobium was selected for the extrinsic doping of the TiO_2 films.

The first step was the study of TiO_2 films deposited in Ar-O_2 and Ar-H_2, in order to understand the limitations of doping by intrinsic defects. A control over the intrinsic defects by changing the parameters (oxygen and hydrogen concentration in the gas mixture, cathode self-bias voltage) during the deposition or by post-growth annealing in vacuum treatment was searched. Doping with intrinsic defects of TiO_2 films gave high values of conductivity, but not enough to allow the use of these films as replacement of ITO as a transparent conductor. The best intrinsically-doped films in terms of optical and electrical properties were TiO_2 films deposited in Ar-O_2 gas mixture.

Another low-cost material investigated as possible candidate for replacing ITO was zinc oxide (ZnO). A first step was to investigate the mechanisms behind the hydrogen incorporation in ZnO structure. A first conclusion from this study is that hydrogen inclusion in the gas mixture leads to an increase in the conductivity values, but the intrinsic doping of these films is not enough for obtaining electrical properties similar to the one of ITO.

The second step was to understand the mechanisms behind the extrinsic doping of TiO_2 by niobium, by varying different parameters in the deposition of the films like the concentration of Nb or the cathode self-bias voltage. Higher conductivity values were obtained for extrinsic-doped TiO_2 films in comparison with the un-doped TiO_2 films prepared in Ar-O_2 gas mixture. The best performance in terms of optical transparency and conductivity, which raised the films at ITO level, was obtained for a narrow concentration range of Nb. All Nb concentrations above 2.3 at.% were ineffective in doping. From this study it was understood that well-doped films (high carrier density) means also an anatase-to-rutile transformation “inhibited”. In the films of this thesis, when the anatase-to-rutile transformation occurs, it was accompanied by reduced crystallite sizes, which leads also to a reduction of carrier mobility in these films. It was also observed that Nb doping increased the vacancies in the films, most likely due to a charge compensation effect.

In order to combine the benefits of both intrinsic and extrinsic doping of TiO_2 to obtain higher performance films, a third approach was adopted in the deposition: TiO_2 and Nb co-sputtering in Ar-O_2 and Ar-H_2 gas mixtures. However and contrarily to the expectations, no effective Nb-doping effect on the electrical properties of the films prepared with such processes was found. Even if the conductivity values were high, they keep far from the ITO value. The doping efficiency loss in TiO_2-Nb films grown in Ar-O_2 and Ar-H_2 plasmas are attributed to: (i) a conductivity loss due primarily to an unvaried carrier density (only a very limited increase was obtained with Nb incorporation in the case of Ar-O_2 gas mixtures and no effect at all was obtained in the case of Ar-H_2 gas mixture, while in the films prepared in Ar plasma, nearly four orders of magnitude improvement brought about by Nb was observed) and (ii) the structure distortion introduced by the presence of defects like oxygen vacancies or Ti-OH and/or Ti-H bonds expected to influence the incorporation of Nb or the carrier trapping.

In view of their application in transparent charge collectors (electrodes), the studied materials were also characterized for their work function. It was evidenced that, if the processes in Ar-O_2 and Ar-H_2 to grow the films were ineffective or limiting for any doping effect enhancement of TiO_2-Nb films, nonetheless they provided a method for a better control of the work function of the materials. In particular, the Ar-O_2 plasma allowed to obtain high values, useful properties for application as electrode material for next generation photovoltaics. A combination of different processes aiming first to obtain the TCO performance and high work function can be envisaged to reach the conductive transparency of ITO and even to exceed its work function property.

In conclusion, the results in this thesis demonstrate that RF sputtering, a suitable technique for coating in large area substrates and easily transferred in industry, allowed to obtain transparent and conductive titanium oxide films. Process conditions were properly defined to obtain a figure of merit close to that of commercial ITO. This work helped a better understanding of the factors determining the strength and the limitations of the processes underlying the creation of the high conductivity, still keeping low optical absorption in visible. On the other hand, the usefulness of many characterization techniques, such as XPS and PAS, is evidenced and the joint use of different techniques of analysis proved to be powerful in providing important and complete information about the material structure and its influence on the film performance.

The results suggest many routes to get further improvement of the electrical and optical performance of the oxides. Doping levels equivalent to the ones obtained in this thesis or even higher should be searched at low temperatures, this would extend the application of these materials as transparent electrodes or charge collectors also on heat-sensitive substrates, such as flexible polymers and textiles. Further, the double effect of Nb as (i) dopant enhancing the carrier density and (ii) worsening factor of crystallinity and thus carrier mobility (reducing crystallite size) should be carefully investigated in order to overcome the contrasting influence on electrical conductivity. The range of energetic conditions during the film deposition should be extended, in order to efficiently modify the atomic mobility and to control the crystallinity from which depends the carrier mobility, without sacrifying optical transparency.